Enhanced light-matter interaction in atomically thin semiconductors coupled with dielectric nano-antennas

Luca Sortino

Department of Physics and Astronomy
University of Sheffield

This dissertation is submitted for the degree of
Doctor of Philosophy

December 2019

To my grandfather, a farmer who taught me polynomial equations

Declaration

I hereby declare that except where specific reference is made to the work of others, the contents of this dissertation are original and have not been submitted in whole or in part for consideration for any other degree or qualification in this, or any other university. This dissertation is my own work and contains nothing which is the outcome of work done in collaboration with others, except as specified in the text and Acknowledgements.

Luca Sortino
December 2019

Acknowledgements

I would like to acknowledge the people that helped me in this work and that I met in these years passed in UK and around Europe. First to Prof. Sasha Tartakovskii who gave me the opportunity to grow and study in his group, and to the Marie Skłodowska-Curie Actions for founding this project. Then, the invaluable help from the postdocs at the beginning of my PhD, in particular Stefan, Scott, Tillman and Eugene. The LDSD group and the 2D material group, in particular to Armando and Panaiot who helped in the lab over a lot of the experiments. Then all the others with whom I shared time and struggles: Tom, Pampos, Alessandro, little Sasha, Gau, Dom, Joe, Catherine, Alastair, Giuseppe, Armanda, Rahul, Kyriakos, Onakr, Joel, Ben, Abdul and many others. In particular for this thesis work I need to thank Javier Cambiasso for his amazing fabrication skills, without them this thesis wouldn't have been possible. The group of Riccardo Sapienza and in particular Sandro Mignuzzi, who performed the FDTD simulations for the GaP nano-antennas. Matthew Brooks for the strain topography theoretical model and the time spent to work on it here in Sheffield. And of course to all the Spin-Nano gang, with which we have experienced some great times around our meetings in Europe. I also acknowledge the groups that hosted me in my visiting periods, first at TU Dortmund, in particular Daniel Smith and Prof. M. Aßmann for the time spent with me at the streak camera setup; the group at the University of Basel led by Prof. R. P. Warburton, and Sigurd with whom I have enjoyed the long time on the open cavity setup, but even the Basler carnival. I need to knowledge all the people I talked to in the various conferences and meeting, and whoever managed to gave some good insight in my work and in the way to survive this PhD. On this topic, the people with whom I have shared the climbing time which helped to overcome many difficult moments and to clear the mind, in particular Paolo and Edo. From this experience, I need to thank Elena for the happiness she brought me, without her all this would have been far more difficult to overcome. And finally to my family and friends that have been far but close enough to not feel alone. This whole thesis is a work over just three years, during which I understand that the best things are always the ones where you spend time and effort to make them grow before being able to see the results. Hard work will always pay off, but we're meant to balance it with care.

Abstract

By confining strong electromagnetic fields at their surfaces, nano-structures with sub-wavelength dimensions can enhance the light-matter interaction of closely coupled emitters. While these phenomena have been extensively studied for plasmons in metals, recently high-refractive-index dielectrics have gained attention as they exhibit optical Mie resonances offering a low-loss platform to overcome plasmonic quenching mechanisms. Between atomically thin semiconductors, the family of transition metal dichalcogenides (TMDs) exhibits promising optical properties, such as tightly bound excitons and a transition to direct bandgap in the single layer form, with favourable integration with nano-photonic structures. Most of the efforts so far have been given to plasmonic structures, while coupling 2D-TMDs with dielectric nano-antennas is mostly unexplored.

In this work, we transferred single and double layer TMD WSe_2 onto an array of high-index gallium phosphide (GaP) dimer nano-antennas, leading to a strong enhancement of WSe_2 photoluminescence (PL) at room temperature. We show that this is a result of an increased absorption and enhanced spontaneous emission rate, provided by the strongly confined optical mode of the nano-antennas, as well as an emission redirection. Further manifestation of the strong photonic confinement is observed in the enhanced Raman scattering signal and polarization dependent PL.

Moreover, the nano-structures displace the 2D semiconducting layers in the out-of-plane direction, allowing the strain-tuning of the local WSe_2 band structure. We model the strain topography in a mechanical picture and show a co-location of largest tensile strain and of the maximum photonic enhancement. This concurrence let us directly probe the strain-induced WSe_2 band structure renormalization from the distinct spectral signatures. In monolayers we observe a tuning of the excitonic resonance above 50 meV. For bilayers, an indirect bandgap semiconductor, high level of strain results in the transition to direct bandgap. By studying the cryogenic PL emission at liquid helium temperatures, we confirm that the strain-induced potential acts as a trap for photo-generated excitons. Finally, we show that this approach can be exploited for the deterministic positioning of strain-induced bright single-photon emitters

at the nano-antenna location, opening to the coupling between single 2D quantum emitters and dielectric nano-resonators.

These results highlight dielectric nano-structures as a platform to improve light-matter interaction in 2D semiconductors and for nano-scale positioning of 2D quantum emitters.

Publications and conference presentations

Publications

- **L. Sortino**, P. G. Zotev, S. Mignuzzi, J. Cambiasso, D. Schmidt, A. Genco, M. Aßmann, M. Bayer, S. A. Maier, R. Sapienza, A. I. Tartakovskii.

  "Enhanced light-matter interaction in an atomically thin semiconductor coupled with dielectric nano-antennas"

  Nature Communications 10, Article number: 5119 (2019) IF: 11.880

- **L. Sortino**, M. Brooks, P. G. Zotev, A. Genco, J. Cambiasso, S. Mignuzzi, G. Burkard, S. A. Maier, R. Sapienza, A. I. Tartakovskii.

  "Dielectric Mie resonators for strain engineering in two-dimensional semiconductors"

  (*Under submission*)

- B.G. Freestone, J. A. Smith, G. Piana, R. C. Kilbride, A. J. Parnell, **L. Sortino**, D. M. Coles, O. B. Ball, N. Martsinovich, C. J. Thompson, T.I. Alanazi, O. S. Game, A. I. Tartakovskii, P. Lagoudakis, D. G. Lidzey

  "Low-dimensional emissive states in non-stoichiometric methylammonium lead halide perovskites"

  Journal of Materials Chemistry A, 7, 11104–11116 (2019) IF: 10.733

- A. Catanzaro, A. Genco, A. Kozikov, **L. Sortino**, C. Louca, D. Gillard, E. Alexeev, K. S. Novoselov, A. I. Tartakovskii

  "Resonant electronic and excitonic hybridisation in transition metal dichalcogenides alloys heterobilayers"

  (*Under preparation*)

Conference presentations

- TMD-UK — Bath, UK, Sep 2016

  "Electrically pumped single-defect emitters in van der Waals heterostructures"

- NOEKS 16 — Dortmund, DE, Oct 2016

  "Electrically pumped single-defect emitters in van der Waals heterostructures"

- TMD-UK 17 (poster) — Sheffield, UK, Jul 2017

  "Optical stability of colour centres in hexagonal boron nitride under red excitation"

- TMD-UK 18 — Sheffield, UK, July 2018

  "Purcell effect, Raman enhancement and strain-induced quantum emitters in an atomically thin semiconductor coupled to dielectric nanoantennas"

- ICPS 2018 — Montpellier, FR, Aug 2018

  "Purcell effect, Raman enhancement and strain-induced quantum emitters in an atomically thin semiconductor coupled to dielectric nanoantennas"

- SpinQubit4 (poster) — Konstanz, DE, Sep 2018

  "Purcell effect and Raman enhancement in an atomically thin semiconductor coupled to dielectric nanoantennas"

- Flatlands 2018 — Liepzig, DE, Sep 2018

  "Purcell effect, Raman enhancement and strain-induced quantum emitters in an atomically thin semiconductor coupled to dielectric nanoantennas"

- POEM 2019 (*Invited*) — London, UK, Apr 2019

  "Coupling atomically thin semiconductor with dielectric nano-antennas: radiative enhancement and strain-engineering"

- TMD-UK 19 (poster) — Sheffield, UK, Jul 2019

  "Dielectric nano-antennas for on-chip strain engineering of two-dimensional semiconductors"

- NANOP19 — Munich, DE, Sep 2019

  "Enhanced light-matter interaction in an atomically thin semiconductor coupled with dielectric nano-antennas"

Table of contents

List of figures

Chapter 1

Introduction

This chapter will introduce the main topic of this thesis work. The first section will give a brief history on the research of two dimensional materials, one of the most exciting discoveries in the field of nanotechnology in the last decade. The second part will introduce the light-matter interaction engineering with optical cavities, followed by a perspective on the field of quantum information with single photon sources. An outline of the thesis is given at the end of the chapter.

1.1 Two-dimensional materials

Materials with reduced dimensionality exhibit peculiar physical behaviours due to confinement of electrons in one or more dimensions, with size comparable to the spatial extent of the relative wavefunction. The appealing feature of accessing novel quantum physics made such nano-structures one of the most flourishing field in condensed matter physics. During the last decades, a vast research has been carried out on zero (0D) and one dimensional (1D) systems, such as quantum dots and nanowires, which have seen a rapid progress both in their physical understanding and synthesis, with prospects of scalable quantum technologies. Two dimensional (2D) confinement instead, have been studied mainly in thin semiconducting layers, or quantum wells, grown between materials with higher bandgap energy, leading to the formation of a confined 2D electron gas. The isolation of graphene in 2004 by A. Geim and K. Novoselov in Manchester [1, 2] marked the first report on the stability of a free standing two dimensional crystal, although predicted to be impossible by Landau and Peierls [3]. While being achieved with the simple idea to use an adhesive tape to peel off single atomic layer from a graphite crystals, this approach paved the way for numerous discoveries

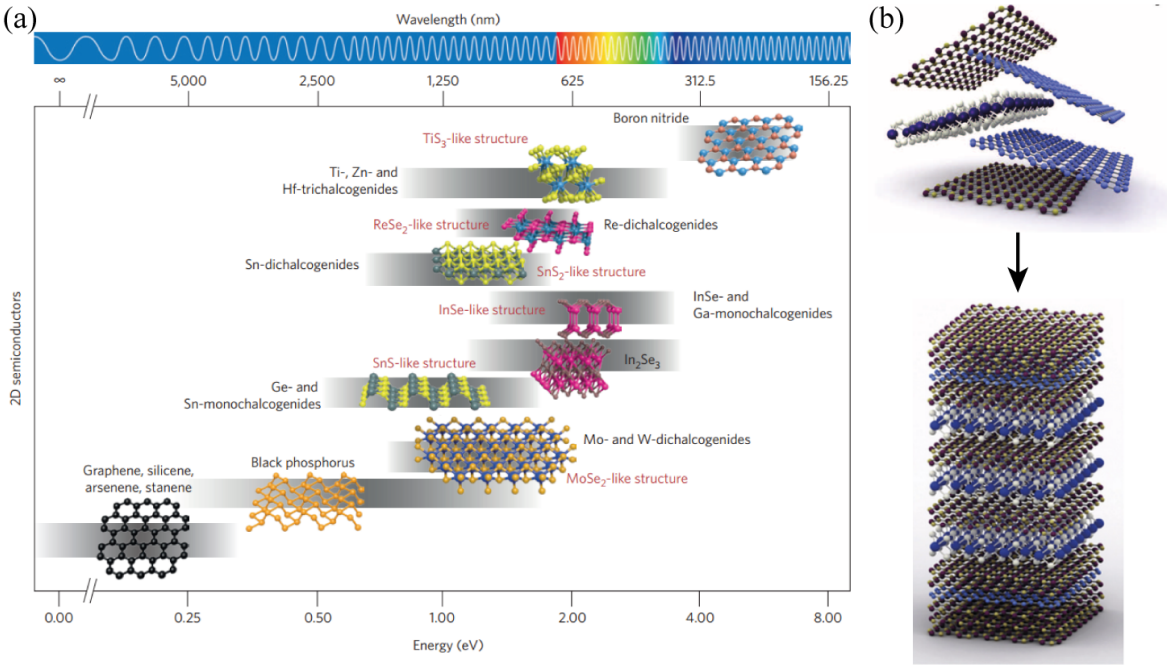

Fig. 1.1 (a) Comparison between two-dimensional semiconductors families and relative bandgap energies. The large number of available atomically thin crystals covers most of the electromagnetic spectrum, leading to a broad variety of opto-electronic applications offered by these materials. Adapted from Ref.[4]. (b) Schematic of a van der Waals heterostructure. The lack of lattice mismatch allows the arbitrary stacking of different 2D layer, which can combine or merge single layers properties, foreseen as a novel platform for development of quantum devices. Adapted from Ref.[5].

in the physics of 2D materials and opened to entirely new fields of research in material science, leading to the award of the Nobel prize in Physics in 2010.

In the last decade, a host of 2D materials beyond graphene have been synthesized and isolated, providing a wide range of substances [6, 7] with properties ranging from metallic to insulating (Fig.1.1a). These new materials exhibit peculiar physical properties, such as unprecedented mechanical strength and charge transport, together with exotic physical behaviours, from superconducting to topological phases. An additional advantage of 2D materials is their promising integration approaches on arbitrary substrates and in current electronic and photonic architectures [8–11]. Two dimensional semiconductors rapidly became the forefront of this research due to unique opto-electronic properties and appealing technological applications, for instance in the miniaturization of current processors [12]. Moreover, the numerous catalogue of 2D materials offer a wide variety of intrinsic electronic and mechanical properties which can be manipulated by creating tailored devices by stacking different 2D layers on top of each other, in the so-called van der Waals heterostructures

(Fig.1.1b) [5, 13, 14]. This approach enabled the fabrication of entirely new optoelectronic devices [15], excitonic phases [16] and meta-materials [17]. The lack of a lattice mismatch between different 2D crystals allows to build an almost infinite combinations of layers, which could benefit numerous applications and open to novel physical systems. Indeed, more exciting degrees of freedom and fundamental physics have been recently demonstrated in 2D heterostructures. The arbitrary staking of different 2D layers opened to the control of twist angle between two adjacent layers, leading to the discovery of unconventional superconductivity in graphene [18] and Moiré physics [19, 20]. Additionally, ferromagnetic behaviour in novel 2D semiconductors [21, 22], topological materials [23] and two-dimensional single photon emitters [24, 25] hold promises for the development of novel quantum materials and to overcome current technologies.

1.2 Light-matter interaction engineering

The underlying physics of absorption and emission of light have been a long-standing question until the mathematical formulation of Maxwell's equations, giving a classical description to light-matter interaction. However, it was only with the advent of quantum mechanics, and more specifically quantum electrodynamics by Dirac [26], that a more profound understanding of the physical mechanism behind light emission and absorption was achieved.

Every luminescent emitter, such as atoms or molecules, can be approximated to a fundamental two level quantum system that absorbs and emits light via the electronic transition between a ground $|g\rangle$ and an excited state $|e\rangle$, separated by an energy equal to $\hbar\omega_0$, where $\hbar$ is the reduced Plank's constant. A photon with frequency ω_0 can be absorbed by the two level system, in analogy with an energy transfer in a coupled oscillator model, promoting the electronic transition between the two states. At this stage, the electron in the excited state will spontaneously decay to the ground state, in a process which can be either radiative, i.e. emitting light, or non-radiative, preventing the emission of a photon by transferring the excitation to non emitting states.

It was only in 1946 that Purcell [27] demonstrated that the spontaneous emission of light is not an intrinsic properties of atomic matter, but rather related to the environment the emitter is experiencing, and more precisely to the local photonic density of states. This observation opened the way towards the control of spontaneous emission decay, quantified by the Purcell factor (F_P), and the engineering of light-matter coupling by modifying the photonic environment around an emitter.

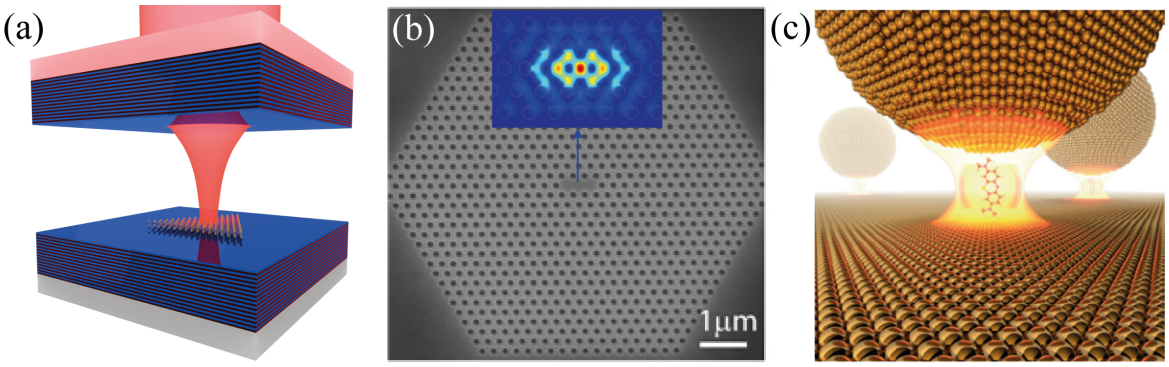

Fig. 1.2 (a) Fabry Perot optical cavities, composed of two distributed Bragg mirrors which confine light in the gap between them where an emitter is placed. (b) Photonic crystal cavity, consisting of a suspended slab of dielectric material with a hole pattern. By removing one or more central holes, a defect is created and light is concentrated in a diffraction limited volume. Inset: electric field intensity at the central defect of the photonic crystal structure. (c) Illustration of a single molecule embedded in the nano-scale gap between a gold nano-particle and a gold surface. Adapted from Ref.[29].

To enhance light-matter interaction, the emitter is embedded in a photonic structure, or optical cavity [28], which confines light in at least one dimension. Low dimensional semiconductors host stable hydrogen-like quantum systems, called excitons, which are composed by an electron and a hole, held together by the reciprocal attracting Coloumb force. Similarly to an atom or a molecule, an exciton behaves as an oscillator at optical frequencies, thus absorbing and emitting light. Following the progress in epitaxial growth techniques, semiconductors nano-structures became one of the most studied systems for the integration in optical cavities. The most studied platforms to improve the light-matter coupling in semiconductors are high quality factor (Q) cavities, such as photonic crystals and Fabry-Perot cavities (Fig.1.2a-b).

While being the forefront of research, high-Q factor cavities requires long and expensive fabrication processes and their Purcell factors are limited due to the confinement of light in diffraction limited volumes [30]. An alternative approach for the control of light-matter coupling at the nano-scale have been found in the use of plasmonic resonances in metals [31] or Mie resonances in dielectrics nano-structures [32]. These systems can overcome the optical mode volume limitation of high-Q factor cavities due to the confinement of light in ultra-small volumes beyond the diffraction limit (Fig.1.2c). In the last decades most of the effort have been devoted to the study of nano-scale light-matter interaction with plasmonic optical nano-antennas. These systems can confine light at the surface of metal nano-particles by coupling photons to the plasma oscillations excited in the metal conduction

band electrons, from which the term plasmonics. In more recent years, it has been understood that losses in plasmonic systems play a detrimental role which can hamper the use of such systems for certain applications. The discovery of Mie resonances in high-index dielectrics ($n > 2$) opened the way to overcome such limitations, while at the same time exhibiting novel photonic effects, for instance the presence of both electric and magnetic responses, which could lead to novel photonic and quantum applications.

1.3 Quantum information processing with single photons

In the classical world, a bit of information is usually regarded as some variable which can only take the values of 0 or 1. On the other hand, a quantum state, or *qubit*, can be found at any time in a superposition of the two states, described by their linear combination. This property, characteristic of the quantum world, opened the study of tasks impossible to be produced by classical systems, described by the quantum information processing.

Storing and manipulating data with qubits leads to even more applications when entangled sates comes into the picture. Entanglement is a unique feature of quantum systems, one of the most counter-intuitive properties of nature, which held a long debate on the veracity of quantum mechanics, started by the famous EPR paradox [33]. As example, a qubit register, an ensemble of n qubits analogue to the classical processor register, can be in an entangled state and store simultaneously all of the 2^n combination available, while a classical one can posses only one of such states. By exploiting the properties of entangled systems it would be possible to realize powerful quantum simulators, i.e. computers, rationalized by the Di Vincenzo criteria [34], and to scale them up to quantum entangled networks, or the quantum internet [35]. The implementation of quantum systems in current technologies could lead to improvements in many fields beyond information and computing tasks, such as secure communication, with the quantum key distribution protocols, or advances in metrology for more accurate sensors, offering ways to beat the current resolution limits in analytical techniques.

Many physical systems have been studied as qubit candidates, for example photons, trapped atoms, Josephson junctions, colour centres in crystals and semiconductors quantum dots. With the advent of photonic quantum technologies [36] and the demonstration that an architecture for quantum computing could be created by the use of linear optics [37] and silica-on-silicon waveguide quantum circuits [38], a physical systems involving the quantum properties of light became a promising platform for the development of on-chip quantum technologies.

Since information can be initiated, stored and read in the polarization state of a photon, the fundamental building blocks of these systems are single photon sources (SPEs) [39]. A single particle of light emitted into a dielectric waveguides can be used to compute on chip operations through single photon interference and detection [40]. While the first single photon emission were reported for trapped atoms in opto-magnetical fields back in the 1970s [41], in the last years solid state sources, and in particular self assembled III-V semiconductor quantum dots [42], have shown to be the most reliable and scalable candidate for the realization of efficient single photon emitters [43]. Moreover, they are well suited for the integration with photonic structures, which have been a fundamental step to achieve the current high-performances exhibited by solid state systems [44].

Only recently, single photon emission has been demonstrated in two-dimensional materials, opening to entire new prospects for the integration of atomically thin SPEs in quantum technologies and photonic architectures.

1.4 Thesis outline

This thesis work tries to tie all the previously described topics into a single system, achieved by coupling a 2D transition metal dichalcogenides (WSe_2) with high-refractive index gallium phosphide (GaP) nano-antennas. This approach results in an enhanced light-matter interaction, obtained by the interplay of the exceptional mechanical and optical properties of 2D semiconductors, together with the low-losses offered by novel dielectric nano-photonic structures. The choice of WSe_2 opens also to the possibility of positioning single photon emitters at cryogenic temperature, by stretching the thin semiconductor membranes on top of the dielectric nano-structures.

Chapter 2 will introduce the fundamental physical properties of 2D transition metal dichalcogenides. The discussion will move from the electronic properties to their optical response, the latter dominated by the presence of strongly bounded excitons. In particular, the optical properties of the dark-excitons in WSe_2 and the luminescence dynamics of 2D excitons will be discussed. The chapter will also describe the effects of mechanical deformations on the band structure and exciton motions in 2D semiconductors, owing to their large mechanical strength. The chapter will conclude with an overview on the optical properties and positioning approaches of single photon emitters embedded in atomically thin WSe_2.

In Chapter 3 an introduction on the properties of optical antennas is given, moving from the description of nano-structured metals to those of high-index dielectrics nano-resonators.

The chapter will then give the theoretical basis of light-matter interaction, with a focus on the main physical properties, and figures of merit, of luminescent emitters interfaced with optical nano-antennas, relevant for the discussion of the experimental results.

The experimental methods are discussed in Chapter 4 and will focus on the 2D materials isolation and transfer, nano-antenna fabrication and optical spectroscopy techniques employed to obtain the results described in the remaining chapters.

The experimental work will start from Chapter 5, where I will describe the enhanced light-matter interaction, at room temperature, between the 2D confined excitons in single and double layer of WSe_2 coupled to GaP nano-antennas. The analysis of a large number of samples, via different spectroscopy techniques, is discussed. A complementary theoretical description of the systems, via numerical calculations performed by S. Mignuzzi from the group of R. Sapienza at the Imperial College London, is given in the Appendix A.

The unique mechanical properties of 2D semiconductors and the photonic enhancement allows to study the evolution of WSe_2 band structure under strain, as discussed in Chapter 6. Here I describe the strain-induced band structure engineering in single and double layer WSe_2, as a result of the effect of the local deformation induced by the nano-antenna, resulting in the modulation of the excitonic resonance under optical excitation. Moreover, I will also give evidence of the confinement of excitons in a distortion potential, supported by the theoretical description developed by M. Brooks from the University of Konstanz, as described in Appendix B.

In the final Chapter 7 I will discuss the positioning of strain-induced WSe_2 single photon emitters on dielectric nano-antennas, at cryogenic temperature. By analysing many samples by means of time- and polarization-resolved spectroscopy, I observed the emergence of characteristics traits in the emission spectra which can attributed to quantum confined excitons in strain potentials, together with the observation of the strain tuning of the single photon emission as expected from the strain model developed in Chapter 6.

Chapter 2

2D Transition Metal Dichalcogenides

The first studies on transition metal dichalcogenides (TMDs) dates back to the end of 1960s [45] with earlier reports on their layered crystal structure [46]. Following the rise of graphene and 2D materials, TMDs have seen a rapid growth in the research interest becoming one of the most studied family of two-dimensional semiconductors [47–49]. TMDs exhibit a variety of properties from insulating, metallic and semiconducting, to more exotic phases such as topological semi-metal and superconductors. This work will focus on the semiconducting group IV TMDs, which exhibits appealing properties such as a transition to direct bandgap in the monolayer, large excitonic binging energies and coupled spin-valley physics. This chapter will cover all the relevant physical properties of group IV TMDs for the experimental results discussed in the later chapters, and with a particular focus on the properties of WSe_2 being the host of two dimensional single photon emitters.

2.1 Crystal structure

Similarly to graphite, Group IV TMDs are layered crystals in the form MX_2, where M is a transition metal (mainly W and Mo) and X is a group VI chalcogen (S, Se and Te). The crystal structure is formed by single atomic layers, with strong in-plane covalent bonding, held together by weak out-of-plane van der Waals forces between each other (Fig.2.1a).

A single TMD layer is only three atoms thick ($\approx$0.7 Å), with an $X-M-X$ coordination, where a plane of transition metal atoms reside between two covalently bonded planes of chalcogen atoms (Fig.2.1b). In case of bulk single crystals, each TMD layer is rotated by 180 degrees from each other, restoring the crystal inversion symmetry which is broken in the single layer form.

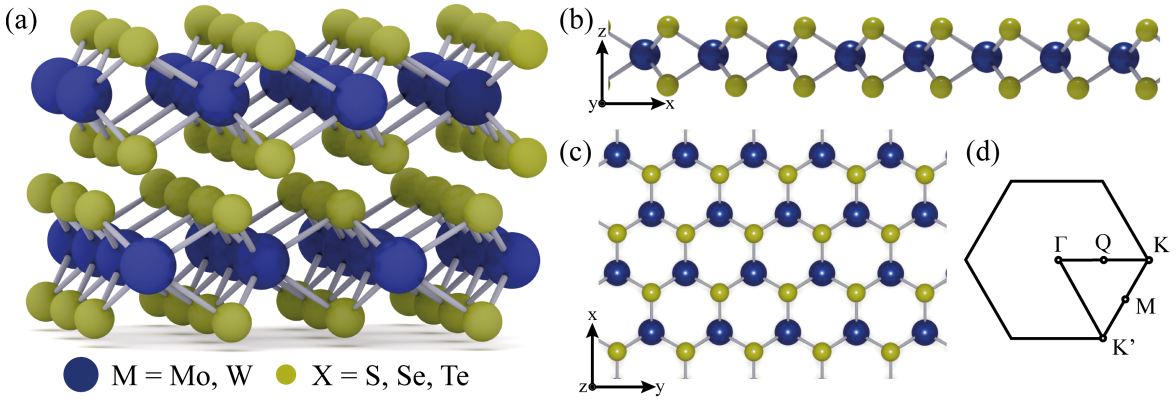

Fig. 2.1 (a) Schematic view of the crystal structure for a double layer $2H-$TMD. (b) Side view and (c) top view of a single layer $2H-$TMD exhibiting the hexagonal symmetry, analogous to graphene. (d) Two dimensional hexagonal Brillouin zone, with the main symmetry points in the momentum space.

Only two structural phase are found in Group IV single layers, defined by the transition metal coordination. The thermodynamically stable is the semiconducting $2H-MX_2$ phase where the metal coordination is trigonal prismatic, and the crystal shows an honeycomb structure analogous to graphene (Fig.2.1c), replicated in the electron momentum space (Fig.2.1d). The second phase is the $1T-MX_2$, which exhibits an octahedral coordination giving rise to a centred honeycombs structure. In this work we consider only the semiconducting $2H$ phase since is the one obtainable from the mechanical cleavage of single crystals under ambient conditions.

Depending on the phase and the metal oxidation state, TMDs can exhibit different electronic behaviours. For example, while $2H-MX_2$ phase is semiconducting, a metallic behaviour is found for the $1T-MX_2$ phase. This is due to the significant contribution on the electronic properties by the transition metal d shell electrons. The orbital band is split into two larger bands for the $1T$ phase, and in three for the $2H$ phase. The Fermi level, defined by the electron counts, can be either lying inside a band, giving rise to a metallic behaviour, or in the gap between the orbital bands, leading to semiconducting properties [50].

2D-TMDs posses many favourable properties for next generation devices, for instance their high carrier mobilities makes them a good candidates for future transistors [51] and photo-detectors [52], while their large excitonic binding energy would find applications in light emission and absorption operations. Moreover, the surface of a monolayer lacks in dangling bonds, one of the detrimental problem in semiconductor technologies. 2D-TMDs are also robust inorganic materials, showing stability over months in air which can be extended by encapsulation with hexagonal boron nitride. Similarly to graphene, single TMD

layers are the most stretchable semiconductors up to date, with elastic thresholds up to 10% [53], opening routes for band gap engineering via strain, unlikely achievable in current bulk semiconductors.

2.2 Electronic properties

Due to the strong quantum confinement of electrons in the out-of-plane direction, dramatic changes are found in the electronic properties of 2D-TMDs when moving from bulk down to a single atomic layer. While known to be indirect bandgap semiconductors for decades, in their monolayer form TMDs exhibit a transition to direct bandgap [54] leading to profound consequences in their optical properties [55, 56] (Fig.2.2a). This effect can be related to the orbital contribution in the TMD band structure [57]. As shown in Figure 2.2b, for a MX_2 TMD the valence band maximum is related to a combination of in-plane $d_{x^2-y^2} + d_{xy}$ orbitals of the metal atoms and p_z chaclogen orbitals, while the conduction band minimum is prevalently formed by the d_{z^2} orbitals. As a bulk material, TMDs are indirect bandgap semiconductors since the valence band maximum is located at the Γ point while the conduction band reaches a minimum at the K point, resulting in the lower energy state being formed at different point in the momentum space. In single layers, the strong confinement of electrons in the out of plane dimension, together with the different contribution of out-of-plane orbitals lacking the near neighbours interactions, shifts the valence band maximum from Γ to K. This shift results in a direct bandgap transition at the K point, leading to improved optical properties, both for emission and absorption processes, due to the lack of a phonon-assisted recombination required to compensate the momentum mismatch in case of indirect transitions. Note, the conduction band at the K point is only slightly perturbed compared to bulk since the metal orbitals lie at the middle of the atomic layer, and thus are less affected by the removal of the neighbouring layers.

Following the presence of an hexagonal crystal symmetry in a single TMD layer, the theoretical framework developed previously for the graphene band structure shows many analogies and has been used as a starting point in the description of TMDs electronic properties. For a single TMD layer, the electronic dispersion close to the K point can be described with the following Hamiltonian in the $\mathbf{k}\cdot\mathbf{p}$ approximation [59]:

$$H_0 = at(\tau k_x \sigma_x + k_y \sigma_y) + \frac{\Delta}{2}\sigma_z \tag{2.1}$$

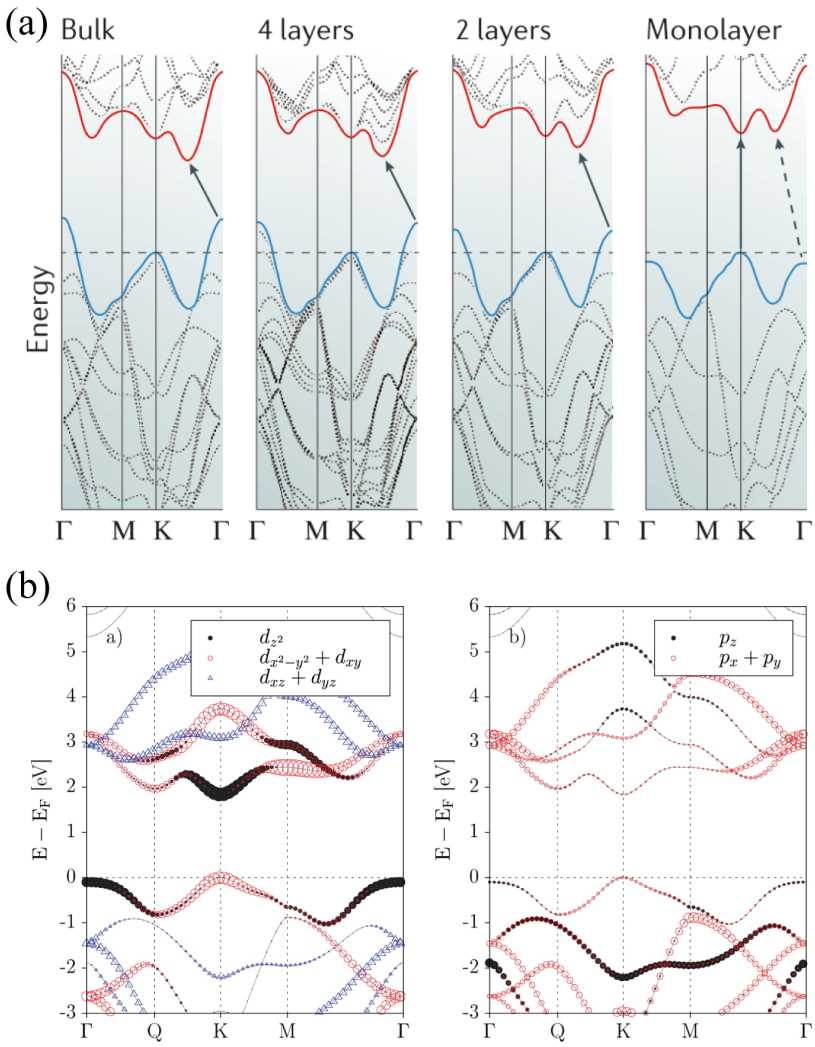

Fig. 2.2 (a) Evolution of the band structure from bulk to single layer MoS_2, a transition from indirect to direct bandgap is seen in case of single atomic layers. Adapted from Ref.[55]. (b) *d* and *p* orbital contribution to the valence and conduction band for a MX_2 TMD. Adapted from Ref.[58].

where a is the interatomic distance, t the hopping integral and τ the valley index (± 1). Similarly to graphene, k_x and k_y define the two dimensional momentum space, while σ denotes the Pauli matrices. Here, the main difference with graphene Hamiltonian lies in the presence of a finite energy gap at the Fermi surface, described by the factor Δ. Although TMDs do not exhibit the characteristic Dirac fermionic physics of graphene [60, 61], the Hamiltonian in Equation 2.1 shows analogies with that of staggered graphene [62]. In this framework, the effect of an out-of-plane distortion leads to the generation of opposite properties in different valleys, via the introduction of an additional magnetic moment. The

band structure at the K point deviates from the relativistic linear dispersion characteristics of flat graphene and acquires a finite band gap (Δ) and a parabolic profile at the Dirac point, with two degenerate minima at the K and K' valley.

2.2.1 Spin-orbit and valley properties

Two dimensional TMDs posses even more attractive electronic properties when spin is considered. From first principle calculation, a giant spin-orbit (S-O) coupling arises when approaching the single layer limit, introducing a splitting in the energy levels of different spin orientation [63]. This is a consequence of the presence of heavy transition metal atoms in the chemical structure of TMDs. Interestingly, this S-O induced splitting reaches values up to 400 meV in the valence band of TMDs, making them promising candidate for hole spin manipulation and spintronics applications. Moreover, this effect is increased in the case of WSe_2 due to the larger S-O coupling than Mo-based TMDs.

A single layer of TMD exhibits is accompanied with an intrinsic broken inversion symmetry, restored in its bilayer form. When this lack of symmetry is coupled to the high S-O interaction, electron spins are locked at opposite valley and, whether they are in the K or K' valley, become associated with a valley pseudo-spin (Fig.2.3a). This pseudo-spin constitutes a novel degree of freedom, which can be manipulated optically [64].

From this symmetry considerations, the TMD Hamiltonian in Equation 2.1 then obtains an additional factor:

$$H_0 = at(\tau k_x \sigma_x + k_y \sigma_y) + \frac{\Delta}{2}\sigma_z - \lambda\,\tau\frac{\sigma_z - 1}{2}s_z \tag{2.2}$$

where, s_z is the Pauli matrix for spins and 2λ is the spin splitting in the valence band. In this picture, electrons with different spins are locked at the K or K' valley, leading to a peculiar valley exciton physics and valleytronics applications [65, 66].

This effect can be explained by considering the curvature of the Berry phase of electrons and its effects on their properties [68]. Since the nature of electrons in TMD is that of massive Dirac fermions, the curvature of the Berry phase ($\Omega(k)$) in the conduction/valence band can be written as [59]:

$$\Omega_c(k) = -\Omega_v(k) = -\tau\frac{2a^2t^2\Delta'}{[\Delta'^2 + 4a^2t^2k^2]^{\frac{3}{2}}} \tag{2.3}$$

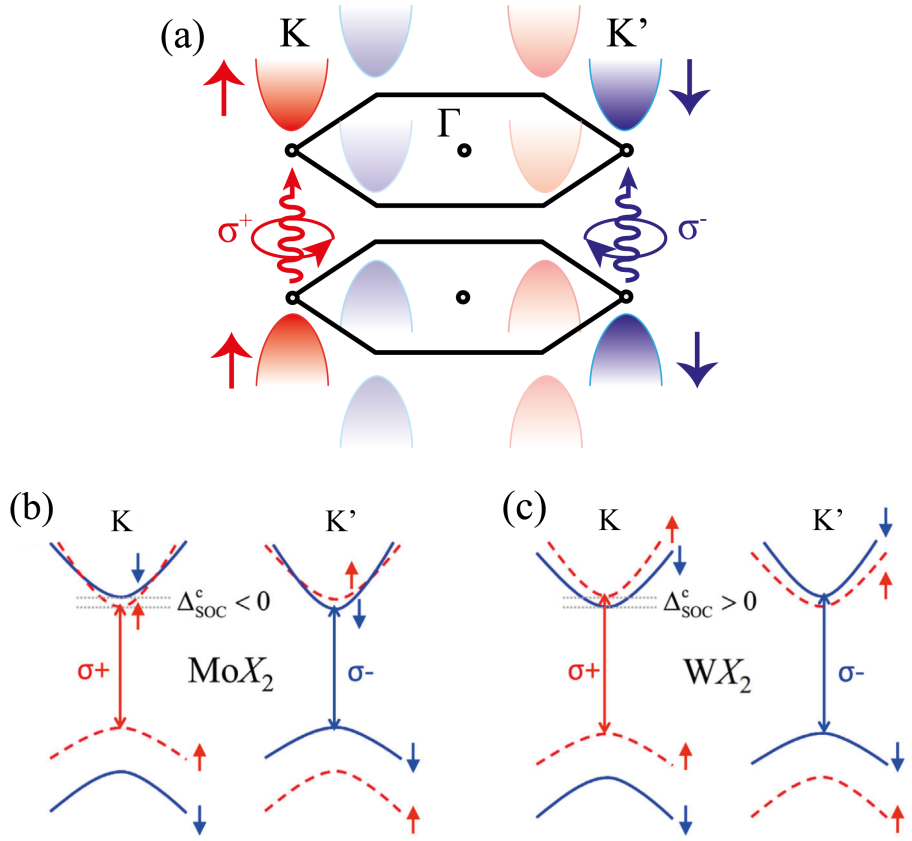

Fig. 2.3 (a) Spin-valley coupled optical selection rules for a single layer TMD. The contrasting properties, at K and K' point in the momentum space, results in the locking of different spin at opposite valleys associated with a valley pseudospin. The spin locking leads to peculiar optical selection rules which couples the circular polarization $\sigma^+(\sigma^-)$ to a spin polarized electronic transition. (b,c) Spin-orbit interaction (Δ_{SOC}) values for the conduction band minimum of Molybdenum (b) and Tungsten (c) single layer TMDs exhibiting an opposite value of Δ_{SOC} leading to a spin-allowed (b) or spin forbidden (c) ground state. Adapted from Ref.[67]

The curvature is constant around the K point and changes sign between the valence and conduction band. More interesting, it becomes spin dependent through the factor $\Delta' = \Delta - \tau\sigma_z\lambda$. The spin-valley coupling gives rise to an intrinsic magnetic moment associated with the electron with different valley index [69], inducing valley Hall effects [70] and precise optical selection rules [71, 72]. If a TMD monolayer is excited with circular polarized light, the optical selection rules ($\Delta m = \pm 1$) couples the intra-band transition associated with $\sigma^+(\sigma^-)$ polarization to different valley index. Since the optical fields couples only to the orbital part of the electron wavefunction, the spin is conserved in the intra-band transition and the valley optical selection rules are translated into spin dependent selection rule, which

let selectively excite a single spin orientation and create spin polarized electrons population (Fig.2.3a). This optical coherence is one of the most appealing features of 2D-TMDs, however the role of phonons and local disorder can have a disruptive impact on the properties of these materials by increasing the valley degeneracy.

The S-O interaction is also a fundamental aspect in the optical response of 2D-TMDs, resulting in contrasting properties when looking at TMDs made from different transition metals. As shown in Figure 2.3b, in Molybdenum based TMDs (MoX_2) the S-O splitting in the conduction band is associated with a negative sign, leading to a spin-allowed lower energy state. This state can efficiently couple to light and is then defined as *bright*. Contrary to Mo, in Tungsten based TMDs (WX_2) the S-O splitting acquires a positive sign (Fig.2.3c). This effect leads to a spin-forbidden ground state which cannot couple to light and thus is called *dark*. This leads to the accumulation of a large dark excitons reservoir that is not allowed to recombine directly via a momentum direct transition. This effect have fundamental consequences in the PL response of each material, for instance in an inverted trend of the luminescence intensity as a function of temperature. Due to the small S-O splitting of the conduction band ($\approx$ 20 meV), thermal energy can be large enough to promote a spin-flip process allowing to a more efficient population of the bright state in WX_2 monolayer at higher temperatures [73, 74].

2.3 Optical properties

Although the isolation of single layers TMD crystals was demonstrated 20 years before the mechanical exfoliation process [75], the effect of quantum confinement on the optical properties of 2D-TMDs remained unexplored for some times. Only in 2010 two independent groups [55, 56] demonstrated an increase of 10^4 in the radiative efficiency, or quantum yield, in exfoliated single MoS_2 layers compared to bulk material. This enhancement in the optical response results from the combination of a transition from indirect to direct gap and strong excitonic effects, enhanced by the quantum confinement, leading to bright luminescence and strong absorption even at room temperature [76].

2.3.1 2D Wannier-Mott Excitons

In semiconductors, the absorption and emission of light is mediated by an electron-hole pair, or *exciton*, created via the intra-band electronic transition between the valence maximum and the conduction band minimum. An exciton can be described as an hydrogen-like system

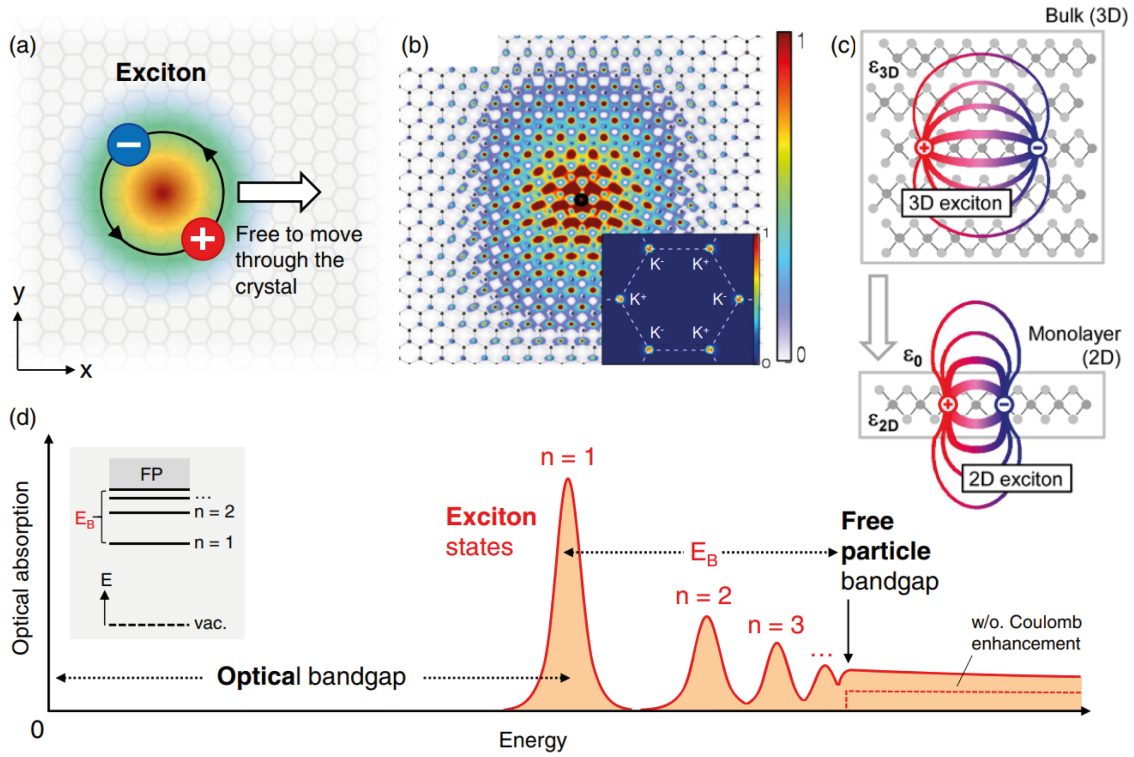

Fig. 2.4 (a) Schematic representation in real-space of a 2D Wannier-Mott exciton, as a bound electron-hole pair free to move in the crystal. (b) Squared modulus of the electron wavefunction calculated for a monolayer MoS_2. The inset shows the same wavefunction represented in the momentum space, with both K and K' exciton states. (c) Schematic of the reduced dielectric screening for a 2D exciton by different dielectric constants ε_{3D} and ε_{2D}. Adapted from Ref.[77]. (d) Illustration of the optical absorption of an ideal 2D semiconductor. A series of exciton transitions are found below the free particle band gap, with a continuum absorption in the energy range exceeding E_B. The inset shows the hydrogen like energy level scheme of the exciton states, designated by their principal quantum number n. Fig.a,b,d are adapted from Ref.[67].

where the two particles are held together by their mutual Coulomb attraction (Fig.2.4a). In this picture the excitonic energy states, in a 3D medium with dielectric permittivity ε_r, are given by the Bohr eigenstates:

$$E_{n,\boldsymbol{K}} = E_g - \frac{E_B}{n^2} + \frac{\hbar^2 \boldsymbol{K}^2}{2M} \tag{2.4}$$

where E_g is the energy gap and $M = m_c^* + m_v^*$ is the exciton effective mass, derived from the electron (m_c^*) and holes (m_v^*) effective masses, and $\boldsymbol{K}^2 = (\boldsymbol{k}_x^2 + \boldsymbol{k}_y^2 + \boldsymbol{k}_z^2)$. The exciton binding

energy (E_B) is calculated for the lowest transition, at the direct recombination point at $k = 0$, and is equal to:

$$E_B = \frac{\mu^* e^4}{32\pi^2\hbar^2\varepsilon_r^2} \tag{2.5}$$

here μ^* is the reduced effective mass equal to $1/\mu^* = m_0/\mu = 1/m_c^* + 1/m_v^*$. The exciton is then associated with an electron-hole separation, r_n, calculated from the Bohr model as:

$$r_n = \frac{\varepsilon_r}{\mu^*} n^2 a_H = n^2 a_X \tag{2.6}$$

where a_H is the Bohr radius for the hydrogen atom and a_X is the exciton Bohr radius. When a_X exceeds the lattice constant, excitons are described as Wannier-Mott excitons. Being that such electron-hole pair can move through the crystal, the exciton kinetic energy enters the equation in the third term of Eqn.2.4, where $\boldsymbol{K}$ is the wave vector relative to the two particle system's centre of mass.

The Wannier excitonic wavefunction takes the following form:

$$\phi(\boldsymbol{K}, n, l, m) = N^{-1/2} e^{i\boldsymbol{K}\cdot\boldsymbol{R}} \phi_e(\boldsymbol{r}_e)\phi_h(\boldsymbol{r}_h)\phi_{n,l,m}^{env}(\boldsymbol{r}_e - \boldsymbol{r}_h) \tag{2.7}$$

where N is the normalization factor, $e^{i\boldsymbol{K}\cdot\boldsymbol{R}}$ is the periodic wave describing the Wannier-type exciton motion in the crystal, in analogy with the Bloch description, where $\boldsymbol{R} = (m_e\boldsymbol{r}_e + m_h\boldsymbol{r}_h)/(m_e + m_h)$ is the centre of mass. The wave-packet relative for the electron and hole are defined by $\phi_{e,h}(\boldsymbol{r}_{e,h})$, while the envelope function $\phi_{n,l,m}^{env}(\boldsymbol{r}_e - \boldsymbol{r}_h)$ describes the relative motion of the electron and hole, maintaining the same meaning as in the hydrogen atom model, as per the quantum number n, m, l relative to the exciton angular momentum.

In 2D semiconductors the excitons are confined in the two-dimensional plane defined by the layer thickness and their wavefunction spreads over numerous unit cells, with $a_X \approx 1$ nm (Fig.2.4b). They can be treated as Wannier-Mott states with an in-plane confinement. The exciton momentum, now $\boldsymbol{K} = (\boldsymbol{k}_x + \boldsymbol{k}_y)$, remains a good quantum number to describe the 2D exciton properties, while the motion in the z-dimension is now quantized. Besides the effect on the excitonic density of states, the quantization changes the exciton binding energy, the Rydberg series and the oscillator strength. The exciton dispersion relation in two dimension becomes:

$$E_{n,\boldsymbol{K}} = E_g - E_Q - \frac{E_B}{(n-1/2)^2} + \frac{\hbar^2(\boldsymbol{k}_x^2+\boldsymbol{k}_y^2)}{2M} \tag{2.8}$$

where E_Q is the quantization energy and the main quantum number n is replaced by $n-1/2$ [78]. The oscillator strength of a 2D exciton increases as the excitonic Bohr radius is reduced from the three dimensional case, due to the increment of the electron and hole overlap and their attraction as the dimensionality is reduced.

Since excitons confined in a 2D semiconductors can be treated as in-plane dipole emitters, the lack of a surrounding medium as in bulk semiconductors leads to a reduced dielectric screening of the excitonic field lines, which naturally spread outside the two dimensional layer (Fig.2.4c). This effect, unique to 2D semiconductor, results in large exciton binding energies, in the order of 0.5 eV [79], and non-hydrogenic Rydberg series of states [77] (Fig.2.4d). Following these properties, the optical response of single layers is dominated by the excitonic states and not the band-edge transition [80], yielding to strong light-matter interaction at the excitonic resonance [81, 76].

The presence of disorder in 2D materials has been shown to heavily impact the electronic and optical properties of 2D atomic layers (Figure 2.5) [84, 85]. The picture of an exciton confined in a 2D plane described in the previous paragraphs can exist only for a perfect crystals, the local fluctuations in the layer thickness, strain, defects and substrate effects are

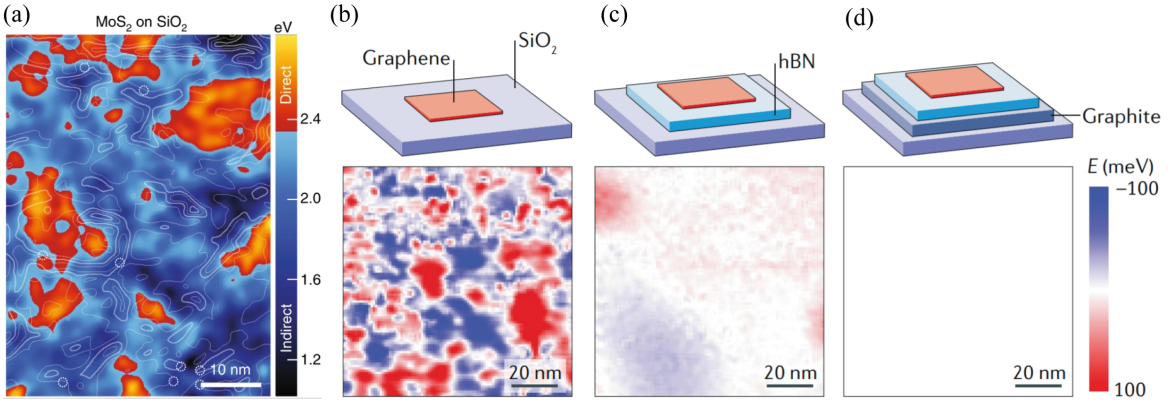

Fig. 2.5 (a) Scanning tunnelling spectroscopy map of the bandgap energy fluctuations in a monolayer of MoS_2 deposited on an SiO_2 substrate. Adapted from ref.[82]. (b-d) Schematic of the structures (top) and relative charge fluctuations (bottom) for a graphene sheet deposited on bare SiO_2 substrate (b), on hexagonal boron nitride (hBN) and SiO_2 (c) and on a hBN/Graphite/SiO_2 structure. The reduction in charge fluctuations is related to the increased homogeneity of the supporting substrate. Adapted from ref.[83].

all sources of deviation from the ideal case. As shown in Figure2.5a, the local disorder in a single layer of TMD is found to be in the range of few tens of nanometres when deposited on bare SiO_2 substrate. These inhomogeneity can be reduced by using different supporting substrates (Figure2.5b) for instance hexagonal boron nitride (hBN), which exhibits a flat surface and low residual charges, and have been shown to greatly improve the quality of encapsulated TMD samples [86, 87].

For an exciton, a first effect of disorder is the appearance of localized states which can be either related to the trapping of a single carrier, or the whole exciton, in a confinement potential. This difference is determined by the ratio between the size of the exciton Bohr radius and that of the disorder potential. A localized state can be described by an envelope function centred at the defect position ($\mathbf{r}_0$) which decays exponentially with a length ξ. Moreover, a major effect of disorder is the breaking of the translation symmetry of the crystal, thus the excitonic wave vector is no longer a good quantum number. The exciton wavefunction is then modified as a superposition of wavefunctions with different $\mathbf{K}$'s and its dispersion broadens in the momentum space:

$$\phi^{loc}(\boldsymbol{r}) = \sum_{\boldsymbol{K}} c_{\boldsymbol{K}} \phi_{\boldsymbol{K}}(\boldsymbol{r}) e^{-|\boldsymbol{r}-\boldsymbol{r}_0|/\xi} \tag{2.9}$$

Even thought the disorder plays a fundamental role in the formation of excitons the large binding energy of allows the stabilization of more complex 2D exciton species. For instance, charged excitons, or *trions*, have been shown to be stable up to room temperature [88–90], while at cryogenic temperature the presence of multiple excitonic species, such as biexcitons [91] and charged biexcitons [92], have been demonstrated. Figure 2.6 shows the low temperature photoluminescence spectrum of a monolayer of WSe_2 deposited on a planar GaP substrate. Here, it is possible to identify the neutral exciton (X), trion (X^T) and biexction (XX) species at high excitation energies (yellow trace). The biexcitonic emission appears at lower energies than the neutral or charged excitons and shows a super-linear dependence in its PL emission intensity, while for neutral exciton this dependence is linear (Inset Fig.2.6).

It is also worth to mention that in 2D heterostructures, where two different semiconductors layers are coupled in artificial bilayers leading to a Type 2 heterojunction, different carriers can be confined in opposite layers resulting in the presence of interlayer excitons [93]. This novel excitonic phase exhibits promising physical properties, such as an out-of-plane dipole moment and long radiative lifetimes, which could be used for engineering new quantum phases in 2D heterostructures [16].

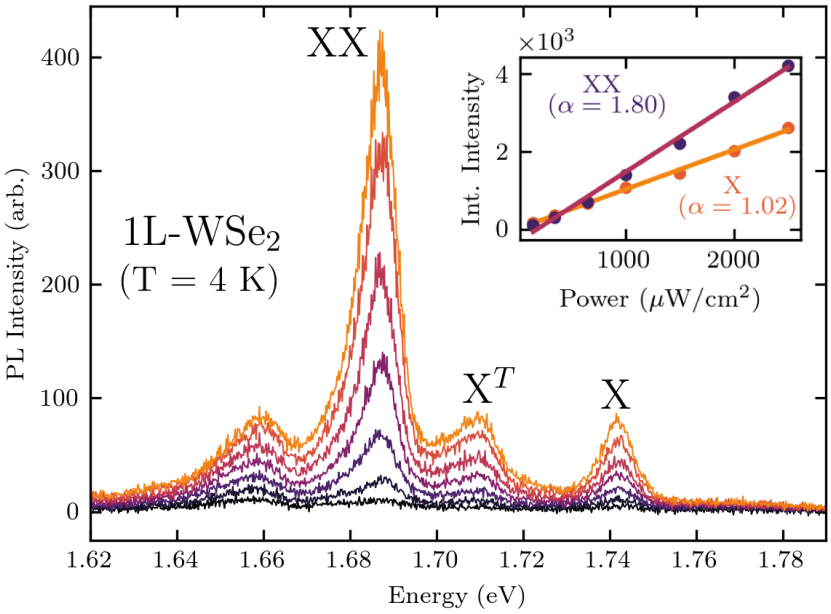

Fig. 2.6 Photoluminescence spectra of monolayer WSe_2 deposited on GaP, collected at T = 4 K and under increasing excitation power (black to yellow) with a 532 nm continuous wave laser. The main emission peaks are labelled for the neutral exciton (X), trion (X^T) and biexction (XX). Inset: power dependence of the neutral exciton (X) and biexction (XX) emission intensity, showing a super-linear power dependence for the biexcitonic peak.

2.3.2 Dark excitons in W-based TMDs

The large binding energy of excitons, and the peculiar spin-valley ordering discussed in section 2.2.1, leads to a precise hierarchy of spin-allowed (bright) and spin-forbidden (dark) excitonic state in the band structure of 2D-TMDs. Dark exciton states exhibit large binding energies [80], making them an attractive platform to observe exciton-spin physics. Moreover, they are of extremely importance in the understanding of the fundamental optical response of WX_2 TMDs [94].

As shown in Figure 2.7a, for a WSe_2 single layer the lowest lying energy state of the direct exciton is spin-forbidden. The splitting between bright and dark states (Δ) have been experimentally measured to be in the order of 40-50 meV [95] and are accompanied with a fine structure splitting, at zero magnetic field, of approximately δ =0.6 meV. This effect results in the splitting of the dark excitons in two states where one is a completely dark state, while the second is a "grey"exciton which can be detected in luminescence experiments due to the weak coupling to the z component of light [96]. These states have been measured by collecting the in-plane light emission of WSe_2, showing lifetimes up to two order of

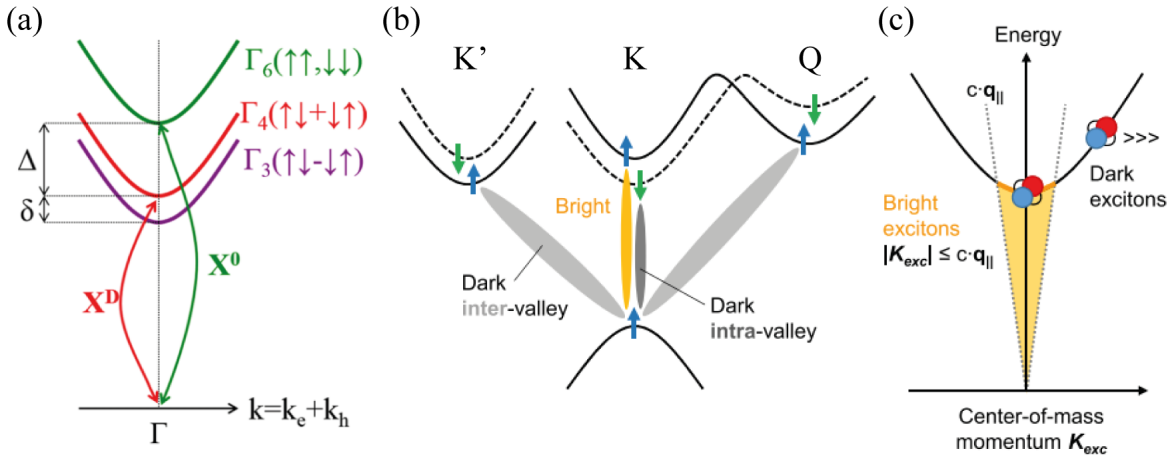

Fig. 2.7 (a) Spin-dark states in the direct exciton transition for WX_2 2D-TMDs, the notation is related to the group theory analysis of the excitonic state's symmetry, leading to the description of the spin-orbit splitting (Δ) between bright (X^0) and dark excitons (X^D). Moreover, the dark exciton state also shows a fine structure splitting at zero field (δ). Adapted from Ref.[96]. (b) Schematic of the momentum-dark exciton states in the multiple valley band structure of WX_2 2D-TMDs. (c) Schematic representation of the exciton momentum dispersion in a two-particle picture. The parabolic dispersion is related to the excitonic centre-of-mass momentum (K_{exc}). The excitons with small momentum are contained in the light cone, defined by the free-space photon dispersion $c \cdot \mathbf{q}_k$, and are considered bright, excitons with larger momentum are outside of the cone, hence dark. Fig.b-c are adapted from Ref.[67].

magnitudes longer than bright neutral excitons [95]. Furthermore, the presence of dark excitonic states in W-based TMDs have been demonstrated with different techniques, for instance the use of strong magnetic fields [97] or by coupling the dark emission to plasmonic systems [98, 99].

Additionally to spin-dark states, the presence of multiple valleys in the TMDs band structure give rise to momentum-dark excitons transition which can be intra-valley, if located at the direct K point, or inter-valley, if the recombination takes place between other conduction band minima at the K' or Q point (Fig.2.7b). Another way to create dark excitons is the generation of electron-hole pairs with large centre of mass momentum ($\mathbf{K}$), as shown in Figure 2.7c. Here we take into account the dispersion of the excitonic energy in a two-particle picture. The bright excitons (related to the inter-valley transition) are the ones associated with small momentum which reside into the light cone, defined by the free-space photon dispersion $c \cdot \mathbf{q}_k$ (where c is the speed of light). The excitons with larger momentum resides outside of the cone and are considered dark.

On importance for the experimental results discussed in later chapters, recent reports [94, 100, 101] have indicated that the optical response of single and double layer WSe_2, at cryogenic temperature, is strongly correlated to phonon-assisted recombinations of momentum-dark excitons and, discussed in section 2.5, a similar picture could be responsible for the appearance of single photon emitters in WSe_2.

2.3.3 Photoluminescence dynamics of 2D excitons

As discussed in the previous section, the bright excitons within the light cone can be directly created via the absorption of a photon and will spontaneously decay via coupling to a continuum of photon states. On the other hand, in case of dark excitons with a larger momentum outside of the light cone, the coupling to light is forbidden making them optically inactive. This effect have a direct consequences on the radiative lifetime of 2D excitons observed in experiments.

The intrinsic radiative decay time for bright excitons (τ^0_{rad}) in 2D semiconductor quantum wells is defined as [102, 103]:

$$\tau^0_{rad} = \frac{1}{2\Gamma_0} = \frac{\hbar\varepsilon}{2k_0}\left(\frac{E_{X^0}}{e\hbar v}\right)^2 (a_B^{2D})^2 \tag{2.10}$$

where Γ_0 is the spontaneous decay rate, k_0 is the light wave-vector, E_{X^0} is the neutral exciton transition energy and a_B^{2D} the 2D exciton Bohr radius. From both first principles calculations [104] and experimental results [103], the radiative time of bright excitons in 2D-TMDs at cryogenic temperatures is in the order of $1/2\Gamma_0 \approx 1$ ps. At low temperature this fast relaxation process dominates while at a finite temperature, and longer times than the exciton-exciton and exciton-phonon interaction, the photoluminescence decay can be orders of magnitude larger than the intrinsic lifetime value. This lifetime is given by the average decay rate of a thermalized exciton population [102]. The resulting effect at high temperature is that longer luminescence decay, up to nanosecond scale, are observed experimentally [103]. When taking into account a finite temperature, only the excitons in the light cone can decay radiatively, leading to an effective decay time defined as:

$$\tau^{eff}_{rad} = \frac{3}{2}\frac{k_b T}{E_0}\tau^0_{rad} \tag{2.11}$$

where k_bT is the thermal energy and E_0 the exciton kinetic energy.

At high temperature, the presence of non-radiative processes can dominate the overall luminescence decay process. In case of 2D semiconductors, the evolution of the excitonic population is given by the following rate equation [103]:

$$\frac{dN}{dt} = -\frac{N}{\tau} - \gamma\frac{N^2}{2} \tag{2.12}$$

where τ is the sum of the radiative and non-radiative decay processes ($\tau = \tau_{rad}^{eff} + \tau_{nr}$) and γ is the exciton-exciton annihilation rate, a non-radiative Auger process which is dominant in the luminescence decay of 2D semiconductors at room temperature [105, 106]. From experiments, the value of the exciton-exciton annihilation rate is found to be $\gamma = 0.35$ cm^2/s [105]. In Figure 2.8 is shown the evolution of the decay for different values of the γ coefficient (Fig.2.8a) and of the initial excitonic population (Fig.2.8b, at fixed $\gamma = 0.35$ cm^2/s). As it can be seen, the main impact of these effects on the luminescence decay are found in the

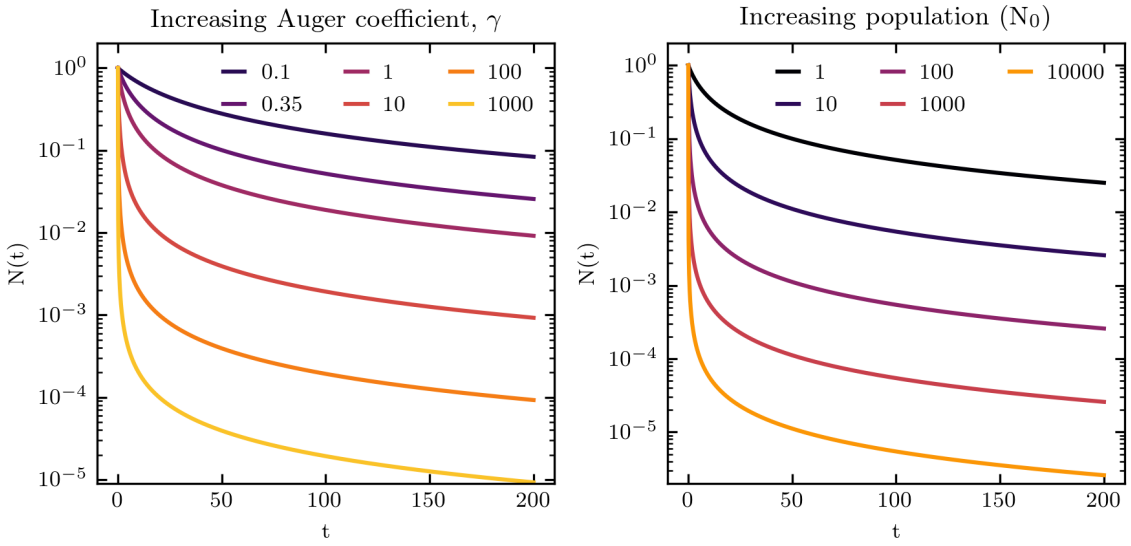

Fig. 2.8 Evolution of the decay rate for a 2D excitons population in the thermal regime, calculated by solving equation 2.12 in case of (a) an increasing exciton-exciton annihilation processes (from experiments $\gamma = 0.35$ cm^2/s [105]) and (b) an increased initial excitonic population (N_0). The overall radiative lifetime, neglecting any changes in the non radiative losses, is set to $\tau = 1$ ns.

modification of the fast decay component, while the longer decay, related to the thermalized exciton population at finite temperature, does not exhibit any substantial modification.

2.4 Strain effects in 2D semiconductors

The control over lattice distortions, or strain-engineering, is a valuable tool for tailoring semiconductors electronic band structure, with improvement for optical properties and carrier mobilities [107]. For common crystalline materials the applicable strain before fracture is limited to $< 1\%$ and mainly introduced via crystal lattice mismatch in controlled growth processes. The intrinsic flexibility of two dimensional materials [108] opens the way to demonstrations of novel physics [109, 110] and flexible electronics [10]. Following these results, two dimensional semiconductors have recently emerged as a promising platform to overcome bulk crystalline semiconductors mechanical limitations [111, 112]. Moreover, the reduced dimensionality offers additional degrees of freedom than bulk counterparts. For instance, the possibility to introduce in-plane or out-of-plane deformation of the 2D membrane, the creation of localized [113] or periodic [114] strain profiles and anisotropic responses to the applied deformations [115–117].

The effects of strain on the electronic properties of semiconductors can be ascribed to two main effects on the crystal structure, namely the piezoresistivity and piezoelectricity [107]. While the first is observed in any semiconductor systems, and related to resistivity modification by strain, the latter is found only in non-centrosymmetric crystals from the stress-induced changes in the charge polarization. For TMD monolayers, the lack of inversion symmetry leads to an intrinsic piezoelectric effect [118] which has been demonstrated experimentally in MoS_2 [119, 120].

2.4.1 Band structure modification

Owing to their large deformation thresholds, an appealing effect of strain application in 2D-TMDs is the possibility to continuously tune their bandgap energy via a controlled deformation [121, 113]. This effect is related to the changes in the overlap between p_z chalcogen and d_{z^2} transition metal orbitals [122, 123]. Fig.2.9 shows the relative changes in the real and reciprocal space of the unit cell under tensile strain, and the relative band structure evolution under uniaxial tensile strain for mono and bilayer WSe_2. For a monolayer WSe_2 (Fig.2.9b) the most prominent effect of tensile strain is the reduction of the energy bandgap at the K point, due to the lowering of the conduction band minimum and the simultaneous

increase in the valence band maximum. On the other hand, under compressive strain the conduction band minimum at the K valley is lifted at higher energy, while a concomitant reduction at the Q point leads to a transition to indirect bandgap. Note, for both compressive and tensile strain the valence band maximum in monolayer WSe_2 is expected to lift in its energy leading to a electron and hole confining potential, an opposite behaviour than most 2D-TMDs [124].

As shown in Figure 2.9c, for a bilayer WSe_2, where the lowest energy transition is indirect, at high value of tensile strain it is possible to observe a transition to direct bandgap [125, 126]. This is due to the stronger reduction of the K valley energy, than at the Q point, leading to a crossover of the conduction band minimum and the onset of a momentum direct lowest energy recombination process.

When the crystal symmetry is reduced by strain, some degeneracies in the band structure are lifted and band splitting can occur. This effect is expected to cause a valley hybridisation in 2D-TMDs, leading to the mixing of opposite valley states and lower protection of the pseudospin degree of freedom, thus modifying the valley selective optical selection rules, as described in section 2.2.1, yielding lower degrees of valley polarization.

2.4.2 Exciton funnelling effect

As consequence of localized nano-scale deformations, the large bandgap re-normalization in strained 2D-TMDs [57] can lead to the formation of an inhomogeneous profile in their band-structure. This spatial distribution of strain translates into a potential gradient seen by the 2D excitons, which can concentrate most of the population into the strained area, or push it away, via the funnelling effect [127]. Figure 2.10a-b show the expected deformation potential and exciton energy profiles in case of an indentation type of deformation, similar to that obtained with an AFM tip or by stretching the 2D layer on top of a nano-pillar. As discussed in the previous section, the calculated biaxial strain profile in Figure 2.10a is directly correlated to a reduction of the bandgap and replicated in the local exciton energy profile (Fig.2.10b).

As shown in Figure 2.10c, three types of funnelling mechanisms have been proposed [127], depending on the relative valence/conduction band bending under strain and on the relative exciton binding energy. For a Type I funnelling mechanism, the simultaneous lowering of the conduction band and lift in the valence band leads to the confinement of excitons in the strained area. In case of Type II and Type III, both the conduction and valence band are reduced under strain and the accumulation of charges is discriminated by

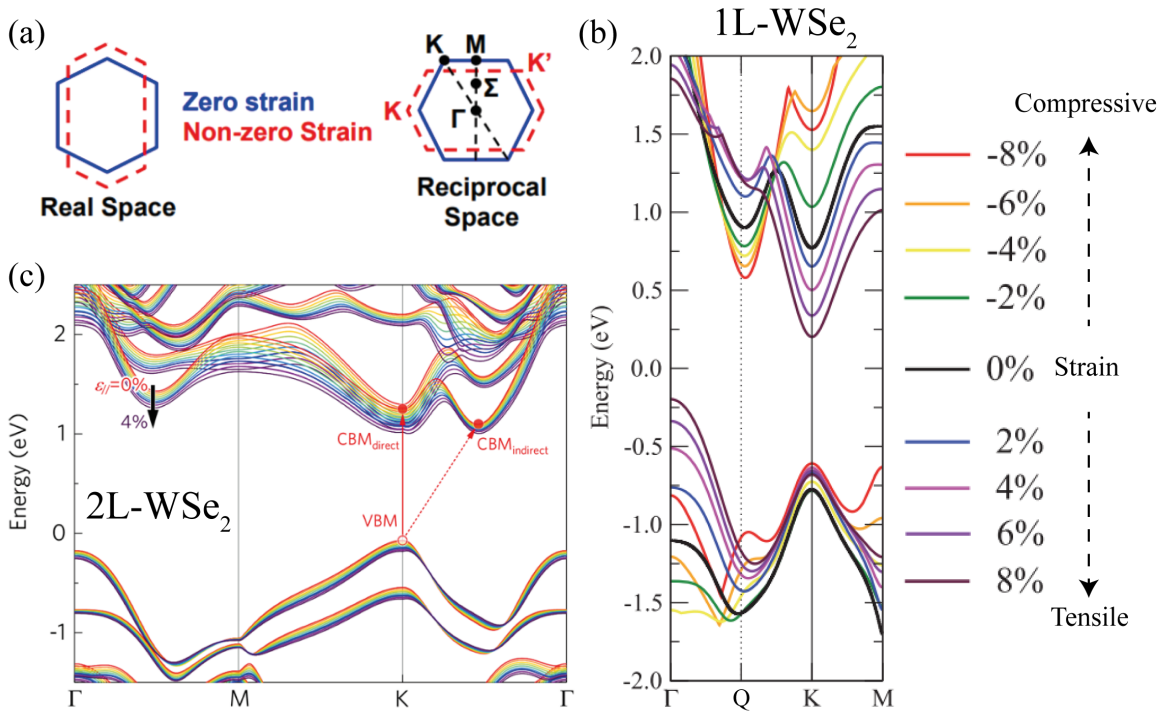

Fig. 2.9 (a) Effect of uniaxial strain on the hexagonal crystal structure of 2D-TMDs for both the real and reciprocal space. Adapted from Ref.[125]. (b) Evolution of the band structure under compressive and tensile strain for monolayer WSe_2. For tensile deformations, the bandgap at the K point is reduced. For compressive strain instead, the bandgap at the K point is increased and the Q valley reduced its energy leading to a transition to indirect bandgap at high strain levels. Note, for the valence band the application of strain always induces a lift in its energy. Adapted from Ref.[57]. (c) Evolution of bilayer WSe_2 band structure under uniaxial tensile strain exhibiting a stronger reduction in energy of the conduction band minimum (CBM) at the K point, leading to a transition to direct bandgap under high deformation values. Adapted from Ref.[126].

the exciton binding energy. In case of weakly bounded excitons, charge separation due to the build-in potential will occur and different carriers will drift in opposite directions (Type II). For strongly bounded excitons (Type III), the band profile will lead to the diffusion of the electron-hole pair in the strained area, in analogy to the Type I mechanism.

For most 2D-TMDs, it is expected that both the electron and hole will experience a funnelling mechanism and become trapped in the deformation potential. While Type III is the expected mechanism for MoS_2, the Type I picture is the one associated with strained WSe_2, due to the lift in the valence band maximum under strain.

In other 2D semiconductors, such as black phosphorous and HfX_2, the funnelling mechanism is inverted, and is expected to deplete charges from the strained area. This effect leads

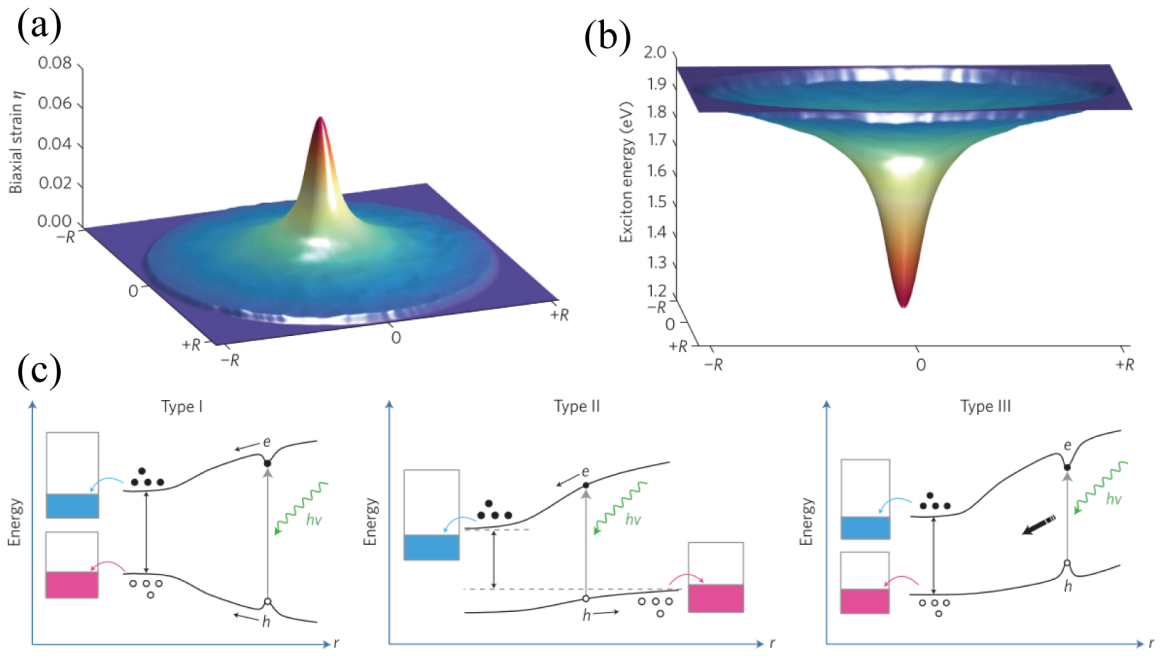

Fig. 2.10 (a) Calculated biaxial strain profile on a MoS_2 monolayer for an indentation type of deformation. (b) Local exciton energy profile relative to the deformation shown in Fig.a. (c) Classes of excitonic funnelling mechanism from the different band structure bending and exciton binding energy in a strained semiconductor layer. Figures adapted from Ref.[127].

to an inverse funnelling operation which can be used, in principle, to improve the charge collection in strained 2D devices [128, 129].

2.5 Single photon emitters in WSe_2

Solid-state single photon emitters (SPEs) [43] emerged as the most promising candidate for quantum information processing and quantum technologies, with the forefront of research is in III-V semiconductor quantum dots (QDs) [130, 44], with prospects of commercialization and scalable systems. Two dimensional SPEs are a novel entry in this field, offering appealing features such as an ease in photon extraction, due to the lack of bulk material around, and favourable integration on arbitrary substrates.

The first reports of quantum light in 2D-TMDs happened in a short time by a few research group working on monolayer WSe_2 [25, 131–134]. Since then, quantum emitters have been observed in mono and multilayer WS_2 [135, 136] and QD-like features in single layer $MoSe_2$ [137, 138]. Other two dimensional families exhibit the presence of single photon emitters such as GaSe [139] and hexagonal boron nitride crystals [24], the latest showing

quantum emission up to room temperature. While their nature is still under debate, single photon operation have been demonstrated in electroluminescent devices [135, 140–142], waveguides [143, 144] and coupled to Fabry-Pérot [145] and plasmonic optical cavities [146]. Moreover, the evidence of a biexciton cascade emission [147] could lead to the development of entangled photon pairs from 2D SPEs.

Although the role of a single defect as the source of quantum emission is still under debate [148, 149], it has been understood that disorder and localized strain plays a fundamental role for the deterministic localization of WSe_2 SPEs, leading to the demonstration of nano-scale positioning with various approaches.

2.5.1 Optical properties

At cryogenic temperatures and under low power excitation, in single and double layer WSe_2 optical spectra it is possible to observe highly localized narrow line emitters (Fig.2.11a), red-shifted from the neutral exciton energy by 50-200 meV, which area associated with single photon emission characteristics (Fig.2.11b).

As shown in Figure 2.11c, photoluminescence excitation (PLE) experiments show an hydrogen-like progression of the SPE energy levels, confirming that SPEs are formed from free exciton states [25, 132]. This observation leads to the comparison of such localized emitters with bound excitons states in colour centres and potential wells. Polarization measurements on these single emitters show linearly polarized emission, as in the case of single dipoles, and the PL intensity under increasing power exhibits a saturation behaviour, both indications of a two level quantum system (Fig.2.11d-e). The luminescence decay lifetimes vary drastically between different SPEs, however all of them are found to be orders of magnitude longer than that direct excitons, confirming the picture of a localized bound exciton state. Note, that the intrinsic radiative lifetime of such emitters is still an open question, with reports of luminescence decays from few nanoseconds up to < 200 ns [151]. This might indicate very long radiative lifetimes for 2D SPEs, although more experimental and theoretical investigation is required for a complete understanding.

An indication of the excitonic confinement is also derived by the presence of a fine structure splitting (FSS) in certain SPEs, related to the exchange interaction between the electron-hole pair under anisotropic potentials and from the Zeeman interaction between the carriers [152]. This degeneracy can be lifted with the application of an external magnetic field, as shown in Figure 2.11f. Polarization measurement at zero field show that the two FSS lines are orthogonally-polarized, with a near unity degree of polarization, although this is not

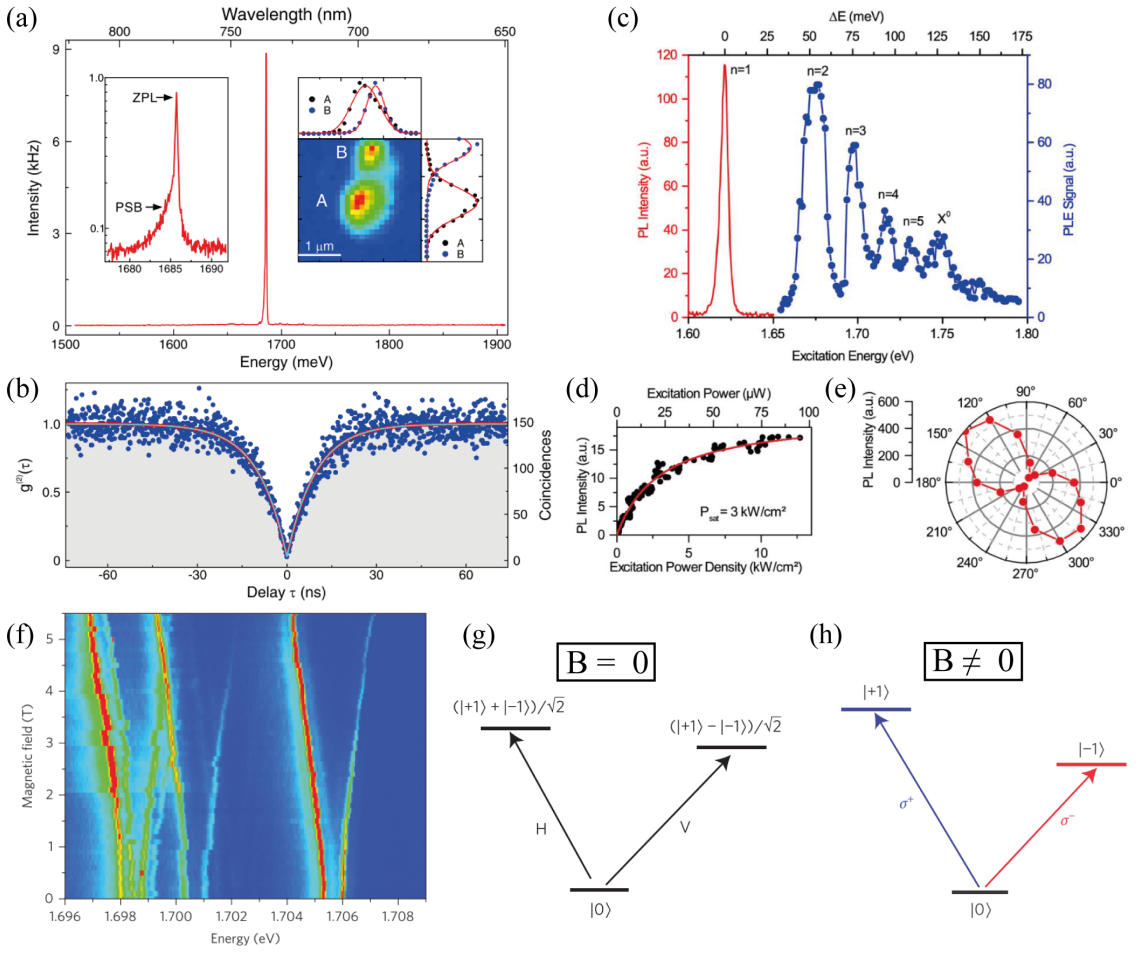

Fig. 2.11 (a) Single photon emitter in monolayer WSe_2 at cryogenic temperature, showing a zero phonon line (ZPL) and a phonon sideband (PBS). (b) Autocorrelation function ($g^2(t)$) under resonant excitation, showing a nearly perfect single photon emission. (c) PLE spectrum of a localized exciton exhibiting an hydrogen like series of states. (d) Saturation curve of the SPE PL intensity as a function of increasing power. (e) Polar plot showing the linear polarized emission from a SPE with dipole-like patter. (f) Magneto-optical studies of multiple SPEs, exhibiting a Zeeman spitting under increasing magnetic field. (g-h) Optical selection rules of the SPE emission. Under no magnetic field ($B = 0$) the SPEs show a mixing of two degenerate states leading to a cross polarized doublet emission in an horizontal and vertical basis. By applying a magnetic field ($B \neq 0$), the state degeneracy is lifted and the doublet becomes circularly polarized. Fig.a-b are adapted from Ref.[150], Fig.c-e from Ref.[25] and Fig.f-h from Ref.[133].

always the case [150]. The application of an external magnetic field, perpendicular to the layer surface, shifts the doublet polarization from a linear to a circular basis (Fig.2.11g-h). This effect is related to the presence of an in-plane anisotropy, due to symmetry breaking, which hybridizes the $\sigma^+(\sigma^-)$ states connected to the valley excitons. The Zeeman interaction with the external field can lift this anisotropy, restoring the circular polarization states [133].

Two dimensional SPE show a large variance in their emission properties, even between emitters from the same monolayer. For WSe_2, three main categories of emitters can be identified from the FSS characteristics [150]: SPEs with FSS of about 0.6-0.7 meV with large g-factors ($\approx 7-10$), SPEs with smaller FSS and small g-factor, and finally emitters that doesn't show any FSS even under high magnetic field. It has been demonstrated that the FSS can be controlled with the application of an external electric field [153], in analogy with the symmetry breaking from the application of a magnetic field. Moreover, confined excitons retain a g-factors with values close to that of the fundamental dark (bright) excitonic transition in WSe_2 ($MoSe_2$), indicating a correlation with the intrinsic band structure character of the 2D host [94].

2.5.2 Nano-scale positioning of single photon emitters

It took over a decade of work to deterministically position quantum emitters in epitaxially self-assembled III-V semiconductor QDs. For 2D-TMDs instead, in less then a year after the first reported SPEs, few groups demonstrated the deterministic positioning of quantum emitters in both monolayers and bilayers WSe_2 (Fig.2.12a).

Different techniques have been adopted, such as etched holes on silicon [154], gapped gold nanorods [155] and arrays of dielectric pillars [156, 157]. All these approaches concern the nature of the substrates on which the TMD will be transferred, rather than a direct chemical or physical treatment of the material. Only recently, the use of He ion irradiation have been demonstrated to create SPEs in MoS_2 [158].

The deposition of monolayers is usually performed with an all dry-transfer process using a viscoelastic PDMS stamp (Fig.2.12b), described in section 4.1.3. If the substrate presents steps or out-of-plane structures the monolayer can easily fracture, due to the built up compressive strain in the polymer during the deposition procedure, and in its following release, leading to a low control on their optical properties and stability. The best quality of SPEs have been reported for WSe_2 deposited on the high aspect ratio pillars [157]. This approach shows improvement on the SPEs properties such as increased spectral stability and

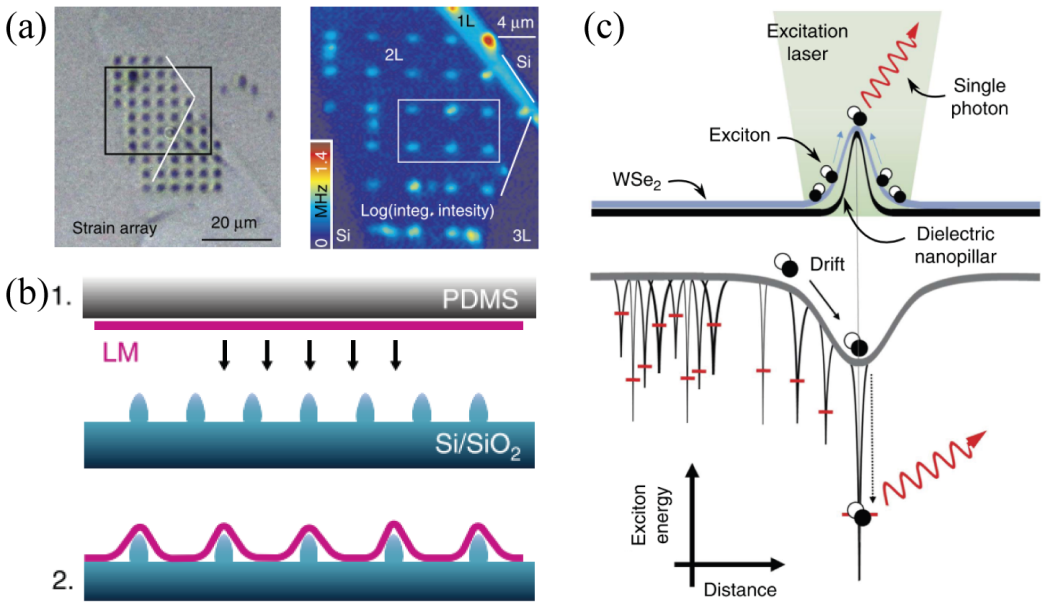

Fig. 2.12 (a) Left: Image of a transferred WSe_2 bilayer on top of an array of dielectric nano-pillars. Right: PL mapping of the same sample revealing an increased PL intensity (range 700-860 nm), for both mono- and bilayer, when on top of the nano-pillars. (b) Schematic of the PDMS transfer methods for the positioning of single photon emitters on an array of nano-pillars. (c) Schematic of the funnel effect as a possible explanation for the nano-scale positioning of single photon sources in the strained 2D semiconductors. Fig.a-c are adapted from Ref.[156], Fig.b from Ref.[157].

reduced linewidths, all enhanced when increasing the pillars height. An explanation for this effect can be related to the role of increasing strain on the material electronic properties.

A possible explanation for the appearance of strain-induced SPEs has been related to the exciton funnelling effect [127]. As shown in Figure 2.12c, the strain profile of an indented layer creates a local energy minimum that leads to a quick funnelling of a free exciton in the potential well, resembling that of an artificial atom. In a TMD monolayer the local strain profile, introduced by the pillar, traps a single exciton which then recombines on a localized state, for instance a defect, giving rise to the single photon emission [159]. However, the exact nature of this process is still under debate, with theoretical proposal of strain-induced bound states [160] or localized inter-valley defect excitons [161] as the source of anti-bunched light.

Chapter 3

Light-matter interaction with optical nano-antennas

In the first part of this chapter an overview of the main properties of optical antennas is given, discussing plasmonic nano-structures and novel high refractive index dielectric nano-resonators. The second part of the chapter will describe the fundamental physics of light-matter interaction in optical cavities, with focus on the main figure of merit relevant for the discussion of the experimental results in this work.

3.1 Optical antennas

As schematically shown in Figure 3.1, an antenna is a device which can transmit or receive electromagnetic radiation [162, 163]. In analogy with radio or microwave counterparts, an optical antenna can convert a freely propagating optical radiation into localized energy, in its near-field region, and vice versa transducing this energy into a modified radiation pattern in the far-field, described by the reciprocity theorem [164]. The requirement of sizes comparable with the operational wavelengths impose nanometre size devices for antennas operating in the visible range. The controlled fabrication of the design of nano-structures has been achieved only in recent decades, with the progress of nano-scale fabrication techniques, such as electron beam lithography and focused ion milling.

The principle of operation of an antenna is the confinement of the free electrons in a metal into a finite volume. The confined charges oscillate in reaction to an applied AC field leading to a periodic response which, if left alone, can be described in terms of a damped harmonic oscillator. The damping of the excitation is related to the loss of energy via Ohmic resistance, or via the emission of the electromagnetic radiation. This fluctuation of the charge

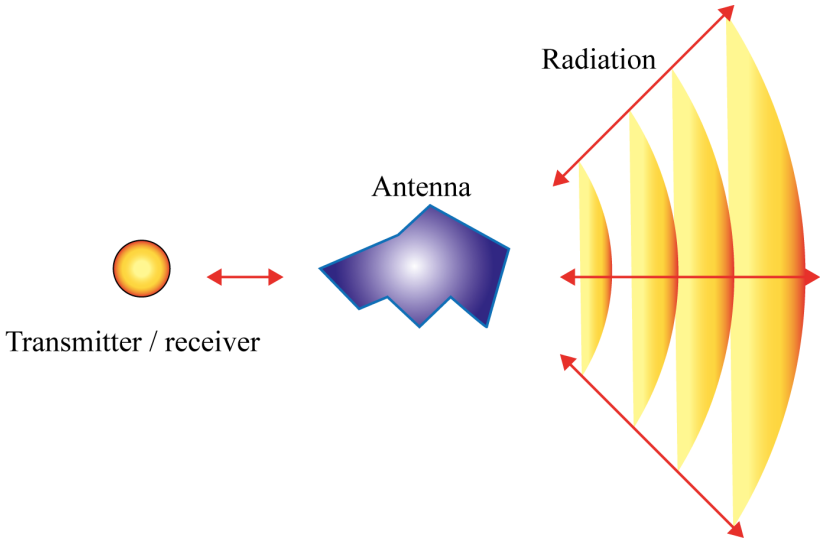

Fig. 3.1 Design of an optical antenna, where the interaction between a transmitter (receiver), represented by a dipole, and the electromagnetic radiation is mediated by the optical antenna.

distribution is replicated in the transmitted electromagnetic far-field in a remote point of space, far from the antenna itself.

The concept of optical nano-antennas was born in the field of near-field optics and microscopy [165], where it was firstly understood that a metal nano-particle could be used as a nano-scale probe in order to overcome the resolution limit of far-field techniques, which relies on the focusing of light with standard optics. This approach led to the development of the so-called “tip-enhanced”spectroscopy techniques [166].

In the last decades, the field of plasmonics emerged as one of the most flourishing branches in nanophotonics [31, 167, 168], focusing on the study of the interaction between light and the free conduction electrons in noble metals. When reducing the size of a metal, and approaching higher and higher frequencies, its behaviour deviates from that of a perfect conductors due to the finite mass of electrons. The free electron gas in the metal conduction band behaves like a plasma and the interaction with the electromagnetic fields give rise to two main excitations, described by quasi-particles states, namely the surface plasmon polaritons (SSP) and localized surface plasmon resonances (LSPR). An illustration of these phenomena is given in Figure 3.2.

SSP are electromagnetic excitations of the free electron gas, which can propagate at the interface between a metal and a dielectric, such as air or vacuum, generating an increased electric field strength in the near-field region. The SSP is associated with an evanescent field component that decays exponentially in the perpendicular direction to the propagation wave-front. These excitation have been extensively studied in the waveguiding light at

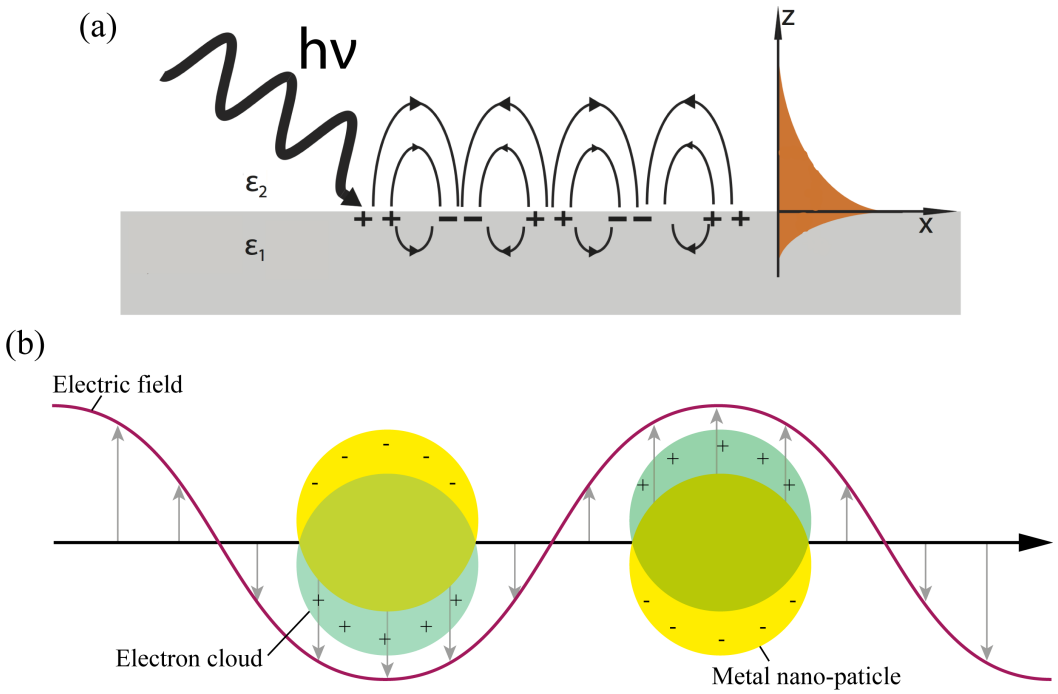

Fig. 3.2 (a) Schematics of a surface plasmon polaritons, an electromagnetic excitations at the interface between a metal (ε_1) and dielectric (ε_2). This excitation can propagate along the surface of the metal in the x direction, while the evanescent field component decays exponentially in the z-direction of the propagation wave-front. (b) Localized surface plasmon resonance of a metallic nano-particle under an oscillating electric field. The free electron cloud shifts in response of the field, giving rise to a dipole-like response.

the nano-scale far below the diffraction limit [169]. The existence of such excitations in 2D materials [170] has opened to even more exciting research and applications, as the confinement of light into a single atomic sheet of graphene, corresponding to a confinement of $\lambda/10000$ [171].

In case of a metal nano-particle with size comparable to the wavelength of the incident light, the oscillating nature of the field induces a response in the free electron cloud of the particle giving rise to LSPR (Fig.3.2b). These are non propagating excitations associated with optical resonances which can fall in the visible range, as in the case of silver and gold nano-particles, while at the same time leading to an electric field amplification in the near-field region of the nano-particle. The LSPR are naturally excited in optically driven nano-particles and can be described by the Mie theory, as discussed in section 3.2.2. These excitations are the fundamental principle of operation of the so-called plasmonic nano-antennas [172] and have been at the centre of the interest for enhancing fluorescence and non-linear effects, such as Raman scattering and second harmonic generation. Moreover, the LSPR can also

be excited by the field produced by a closely coupled dipole emitter, such as molecules or quantum dots, leading to a change in its emission properties, as described in the second part of this chapter.

3.1.1 Plasmonic nano-antennas

Since optical antennas allow the confinement of light far below what is achievable with conventional optics, leading to an increased strength in the electric field at the antenna surface together with an efficient redirection of radiation in the far-field, interfacing quantum emitters in the vicinity of an metallic nano-antenna offers an efficient route to improve the light-matter interaction at the nano-scale. Despite exhibiting low Q factors (< 10), when compared with high-Q factor cavities metal nano-antennas have more affordable fabrication approaches and exhibit a broader bandwidth, i.e. a broad cavity resonance, resulting in an easier spectral coupling than for narrow cavity resonances. For these reasons the use of plasmonic nano-antennas have been extensively investigated in the last decades [167]. Some examples of nano-fabricated gold plasmonic nano-antennas on dielectric substrates are shown in Figure 3.3a-c.

Different geometries have been employed, due to the fact that the resonances of a plasmonic nano-antenna can be tailored by modifying the shape, size or material used. While the first studies focused on spheres or nano-rods (Fig.3.3a), which at first were synthesized via chemical approaches, the use of nano-lithography techniques opened to a finer control and more complex design for modifying the antenna properties. For instance, the presence of corners or protrusions leads to the confinement of stronger fields at the antenna surface, as in the case of triangular particles, usually placed in a bow-tie geometry (Fig.3.3b). The emission properties of a nano-antenna can also be tailored not only by varying the geometry of the antenna itself, but via the coupling to different resonant structures in close proximity. Unidirectional emission from coupled emitters can be achieved as in the case of a Yagi-Uda antenna [174], the geometry of which is shown in Figure 3.3c.

An effective way to improve the near-field enhancement is that of placing two nano-antennas close enough to create ultra-small gaps, in the order few to tens of nanometres, leading to a strong confinement of light and field intensity in the region between them. This approach offers a great opportunity for increasing the light-matter coupling strength due to a reduction of the optical mode volume and increased field strength. The effect of the gap mode on the optical properties of a nano-antenna is shown in Figure 3.3d,e. Here, the authors used two photon luminescence spectroscopy (TPL) to probe the local density of

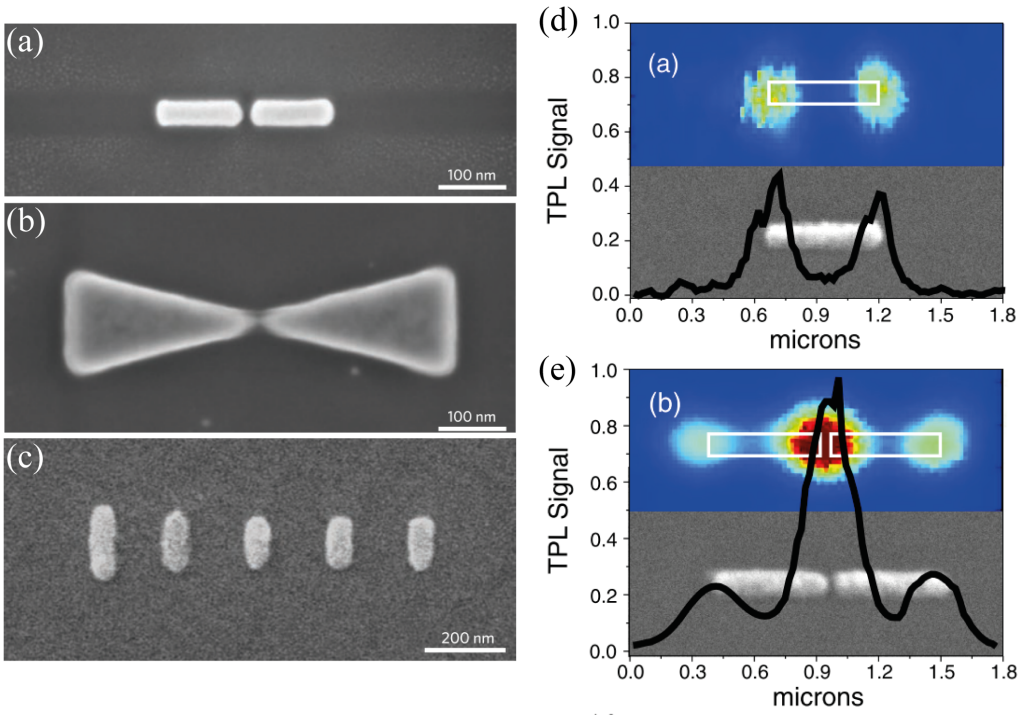

Fig. 3.3 (a-c) Examples of nano-fabricated plasmonic nano-antennas made of gold on dielectric substrates. Closely coupled antennas in the form of nanorods (a) or in a bow-tie geometry (b) are extensively used in studying the nano-scale light-matter interaction due to enhanced field in their gap region. Other geometries as the Yagi-Uda antennas (c) are actively used to achieve unidirectional emission of the light emitted by coupled luminescent emitters. Adapted from Ref.[163]. (d-e) Two photon luminescence (TPL) signal as a probe of the local density of states for a single (d) and coupled (e) gold nano-rods (length = 500 nm, gap = 40 ± 10 nm). The profile shows the TPL intensity as a function of the position along the nanorod long axis, closely replicating the expected optical mode spatial extent. Adapted from Ref.[173].

states for different geometries of nano-rods antennas [173]. For a single gold nano rod, the luminescence profile shows that the signal intensity, as a function of the antenna position, is concentrated at the opposite edges of the rod, as it would be expected from the oscillation of the free electron gas confined in the elongated structure (Fig.3.3d). In case of coupled nano-rods, distanced by a gap of about 40 nm, the resulting signal shows a maximum at the centre of the structure, tightly confined in the gap region (Fig.3.3e). Due to the dipolar character, this gap "hotspot"can be excited more efficiently by illuminating the structure with a plane wave with polarization aligned along the dimer antenna long axis. Moreover, by reducing the distance between the two antennas, the confined optical mode in the gap region exhibits an increment in the electric field strength, together with a reduction in the effective

volume. However, this approach is limited mostly by the resolution of the fabrication process and by the precision in positioning the emitters at the location of the nanometre sized gap.

The description of this coupling effect between close resonant nano-structures can be derived from an hybridization model, similar to that of molecular orbital theory [164]. The overlap of the wavefunction associated with each single antenna is taken into account for the creation of a bonding and anti-bonding state. The former is usually the one detected in spectroscopic experiments, while the latter is a dark state since the out of phase oscillation of each single antennas cancels out the far-field component of the emission.

Even smaller sized gap can be created in case of the so called nano-patch antenna [175], where the luminescent emitter is placed onto a metal surface and a nano-particle is deposited onto the sample. With this approach, the thin gap between the particle and the metal surface results in the formation of ultra-small cavity volumes, leading to large Purcell factors [176] and strong coupling up to room temperature [29, 177]. However, this approach have severe limitations for the integration in current optoelectronic devices.

3.1.2 High refractive index nano-resonators

Although metals have been studied for decades, it has been understood that the losses from the presence of a free electrons have a large impact on their performances, limiting the use of plasmonics for certain applications [178]. For noble metals these losses are either connected to the absorption of the excitations by the free electron gas (Ohmic losses) or from the transformation of the incident radiation into thermal energy under increasing excitation power (thermal losses).

Moreover, metals show a proximity quenching mechanism which is one of the main loss channel, related to the depletion of a quantum emitter excitation in the free electron gas, and is highly dependent on the emitter's distance from the metal surface [179]. To overcome this problem, most of the plasmonic devices require the deposition of a dielectric passivation layer [167], few nanometres thick, adding an additional step in the fabrication process, and at the same time moving away the emitters from the electric field maximum, is located at the metal surface, thus limiting the overall coupling. Additional drawbacks occur from inter-band transition, for instance in gold and sliver when approaching visible/near-infrared wavelengths, and from the incompatibility with complementary metal-oxide-semiconductor (CMOS) fabrication processes.

Recently, a novel approach to nanophotonics emerged by exploiting the optical resonances of high refractive index dielectric nano-structures [32]. As for plasmonics particles, even in

dielectric nano-structures with high enough refractive index ($n > 2$) the Mie theory [180] predicts the presence of electromagnetic resonances at optical wavelengths (see section 3.2.2), which has been observed experimentally [181, 182]. Contrary to noble metals, these resonances are not related to oscillations of free charges but rather to bound electrons displacement currents inside the nano-particle itself (Fig.3.4a).

One main difference between using metals and dielectrics to manipulate light-matter interaction at the nano-scale is that high-index nano-antennas can support the presence of different electromagnetic resonances. While metallic nano-particles only exhibit electrical modes, high-index nano-structures also support strong magnetic resonances at optical frequencies [183, 181, 184] (Fig.3.4b). This is due to the fact that for plasmonic excitations in metals the transient electric (TE) modes are damped in the free electron gas, resulting in the presence only of the transient magnetic (TM) modes, where the electric field is parallel to the propagating wave-front [31]. This difference allows the excitation of magnetic "hotspots", as in the gap between dielectric dimer structures, which is impossible to achieve in the case of noble metals (Fig.3.4c).

The use of high-index dielectrics have been shown to be a valuable platform for the enhancement of fluorescence in coupled quantum emitters [187] and improvement in the spectroscopic analysis when compared with plasmonic structures [188–190]. Moreover, high-index dielectrics exhibit the absence of thermal quenching from Joule heating [191, 186], particularly important for biological sensing [192] (Fig.3.4d). High-index dielectrics have little optical absorption since most of the materials are completely transparent to the resonance wavelength, leading to reduced optical losses. High-index dielectrics are commonly used in the fabrication of semiconductors structures and the variety in the available materials properties offer a large number of compounds for different applications [193]. For some of these, such as the semiconductor gallium phosphide (GaP), the absorption coefficient can reach values close to zero at visible wavelengths, resulting in ultra-low optical losses, appealing for surface enhanced spectroscopy [194].

The presence of electrical and magnetic dipole responses have also great advantage for the research and realization of complex nano-photonic effects. For instance, the possibility to achieve multipolar resonances with equally weighed electric and magnetic multipoles excited in an individual particle can lead to unidirectional scattering and highly directional emission [195, 182] or to novel photonic effects, such as toroidal electromagnetic modes and non-radiating anapoles [196].

The limitations of dielectric nano-antennas are mainly related to their lower near-field concentration, resulting in a decreased electric field intensity, when compared with that of

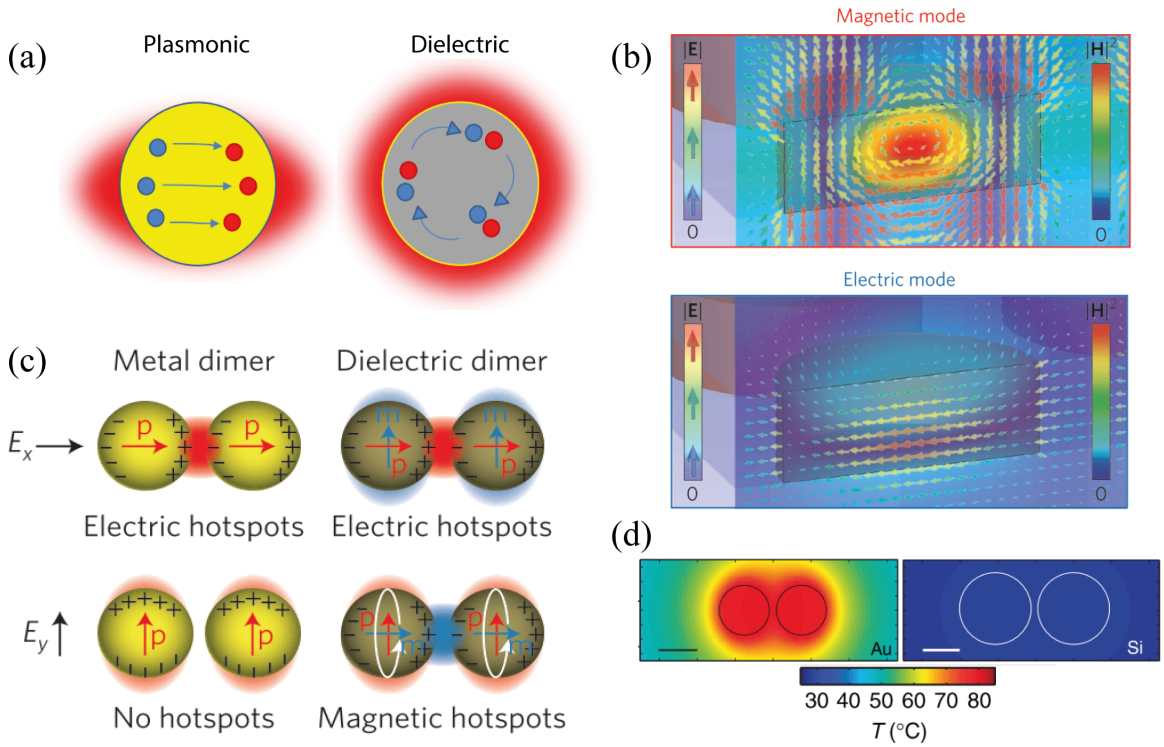

Fig. 3.4 (a) Schematics of the fundamental physical mechanism inducing electromagnetic resonances in metal (yellow) and dielectric (grey) nano-particles. While metals rely on oscillations of the free electron gas, dielectrics optical resonances stems from bound electrons displacement currents inside the nano-particle. (b,c) Electric and magnetic modes for a nano-disk (b) and a dimer configuration (c). Although the electromagnetic modes are confined inside the nano-structure, the use of coupled particles can lead to the arbitrary excitations of electrical or magnetic hotspots in the dimer gap, the latter absent in case of noble metal nano-particles. (d) Temperature map for a gold dimer (left) and a silicon dimer (right) taken under the same excitation density. In case of a dielectric nano-antenna the thermal losses are completely absent. Fig.3.4b is adapted from Ref.[185], Fig.3.4c from Ref.[184] and Fig.3.4d from Ref.[186].

analogous plasmonic nano-antennas. This effect is related to the characteristics of high-index dielectric to have their optical mode spreading throughout the volume of the resonant nano-structures, thus providing less confinement. This is in contrast with metallic nano-particles which instead push the electric field outside of the metal, enabling a stronger field enhancement at their surface, and thus exhibiting larger Purcell factors of closely coupled emitters.

However, these limitation on the Purcell effect can be circumvent firstly from the fact that dielectrics does not need a spacer at their surface to compensate for proximity quenching and moreover from the use of inverse-designed structures [197] or nano-particle clusters

[198], which can be an efficient approach to improve the spontaneous emission rate of closely coupled emitters in dielectric nano-phonics systems. Additionally, effects such as surface lattice resonances [199] or bound states in the continuum [200] could be used for boosting the quality factors and non-linear effects in arrays of sub-wavelength dielectric resonators.

Although the promising properties of dielectric nano-antennas have been reported, the main applications are currently focusing on the field of metasurfaces [201, 202] for flat optical components and for next generation integrated photonic devices [203]. The integration of quantum emitters with high-index dielectrics nano-antennas is still a young field of research, where novel effects can be achieved with the use of novel active materials integrated as a gain medium for photonic applications [30].

3.2 Emitter-cavity interaction

A general schematic of a two level emitter interacting with an optical cavity is shown in Figure 3.5. Here the main parameters to consider when describing the light-matter interaction are the decay rate of the emitter, γ, the decay rate of the cavity, κ, and the emitter-cavity coupling rate, g. In case of an atom-field interaction two distinct regimes can be distinguished from the magnitude of the coupling rate, which can estimated as:

$$g = \frac{\mu}{\hbar}\sqrt{\frac{\hbar\omega_0}{2\varepsilon_0 V}} \tag{3.1}$$

where μ is the dipole matrix element, ω_0 the frequency of the transition and V is the volume of the cavity, i.e. the spatial extent of the confined electromagnetic radiation. If the dissipation rate exceeds the coupling rate ($g << \gamma, \kappa$) the emitter-cavity interaction is described in terms of weak-coupling regime. The emitter decay in the ground state with a rate γ but the presence of the cavity modifies the local density of optical states (LDOS) and, following the Fermi golden rule, the resulting decay rate and Purcell factor can then be calculated, as discussed in section 3.2.1.

In case the coupling rate is larger than the combined decay rates of the emitter and cavity ($g >> \gamma, \kappa$) the system is in the strong coupling regime. Here, the energy released by the emitter is reabsorbed before it can escapes the cavity, and the energy oscillates between the emitter and cavity and this cyclic transfer of energy is known as a Rabi cycle. The spectrum of the emitter is then associated with an energy splitting, leading to the formation of half-light half-matter quasi-particles known as polariton. Looking at equation 3.1 it is straightforward

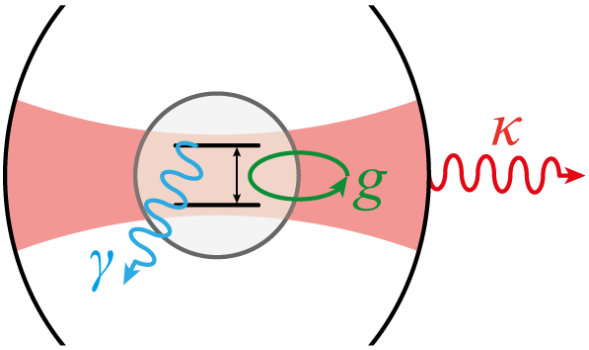

Fig. 3.5 Schematics of the physical rates which determine the dynamics of an emitter-cavity system. The photon decay rate of the cavity κ, the non-resonant emitter decay rate γ and the emitter-cavity coupling parameter g.

to observe that a way to increase the coupling strength of an emitter-cavity system is to reduce the interaction volume, obtainable in nano-photonic structures with effective volumes below the diffraction limit.

3.2.1 Spontaneous emission decay and Purcell factor

As discussed in the previous section, the main evidence of the weak coupling regime is a change in the spontaneous emission decay rate, due to the modification of the local density of photonic states. This result is also known as the Purcell effect [27], quantified via the Purcell factor $F_P = \gamma/\gamma_0$ which can be directly determined in experiments by measuring the radiative lifetime of an emitter inside ($\tau = 1/\gamma$) and outside ($\tau_0 = 1/\gamma_0$) the optical cavity.

The spontaneous emission rate, for a dipole emitter between an initial $|i\rangle$ and final state $|f\rangle$, is given by the Fermi's golden rule:

$$\gamma = \frac{2\pi}{\hbar^2} |\langle i|\hat{H}_I|f\rangle|^2 \delta(\omega_i - \omega_f) \tag{3.2}$$

where $\hat{H}_I = -\hat{\mu}\cdot\hat{E}$ is the interaction Hamiltonian in the dipole approximation and the delta function defines the discrete set of states available for the emitter to radiate into.

For high quality factor (Q) cavities, with an optical mode confined in an effective volume V_{eff}, the delta function is replaced by a Lorentzian spectrum, of width $\Delta\omega = \omega/Q$ centred

on the cavity resonance, and the spatial profile is set by the eigenfunction of the cavity field. Within this approximation the LDOS for a dipole, normalized over the LDOS of the surrounding medium with index n, simplifies the Purcell factor to the following equations:

$$F_P = \frac{3\lambda_0^3}{4\pi^2 n^3}\frac{Q}{V_{eff}} \qquad V_{eff} = \frac{\int \varepsilon |E|^2 dr}{max(\varepsilon |E|^2)} \tag{3.3}$$

From this formula it is clear that the Purcell factor scales linearly with higher quality factors and smaller cavity volumes. However, this approximation fails to describe the density of photon states of an emitter in case of non-resonant and lossy cavities, as in the case of plasmonic nano-antennas, and when the dipole is not placed at the maximum of the confined electric field amplitude [204].

A more rigorous description of the emitter-cavity interaction is given by introducing the partial (i.e. directionally dependent) local density of states $\rho_\mu(\boldsymbol{r}_0, \omega_0)$, which represent the number of electromagnetic modes, per unit frequency and per unit volume, available for the emitter to radiate into [165]. With this approach the total decay rate can be rewritten as:

$$\gamma = \frac{\pi\omega_0}{3\hbar\varepsilon_0}|\boldsymbol{\mu}|^2 \rho_\mu(\boldsymbol{r}_0, \omega_0) \tag{3.4}$$

where $\boldsymbol{\mu} = \mu \cdot \boldsymbol{n}_\mu$ is the dipole moment with $\boldsymbol{n}_\mu$ the unit vector of the dipole orientation. The partial LDOS is evaluated from the imaginary part of the Green's dyadic function, $\overleftrightarrow{G}$, as follow [165]:

$$\rho_\mu(\boldsymbol{r}_0, \omega_0) = \frac{6\omega_0}{\pi c^2}[\boldsymbol{n}_\mu^T \cdot \mathrm{Im}\{\overleftrightarrow{G}(r_0, r_0; \omega_0)\} \cdot \boldsymbol{n}_\mu] \tag{3.5}$$

The Green's dyadic function is a tensor which is evaluated at the dipole origin $\boldsymbol{r}_0$ and related to the electric field generated by the emitter, at the location of the emitter itself (Fig.3.6). In a classical picture this self-generated field, or back-action, is dependent on the field polarization the emitter generates and from the interaction with the surrounding environment, which can be described as the backscattered field by the dielectric environment, creating a net field (E_S) at the emitter position [197] . In case of an emitter close to a dielectric volume (V), the sources that produce the scattered fields are the induced currents, j(r'), in the dielectric medium (ε_r) surrounding the emitter itself [205]. The spontaneous emission rate is

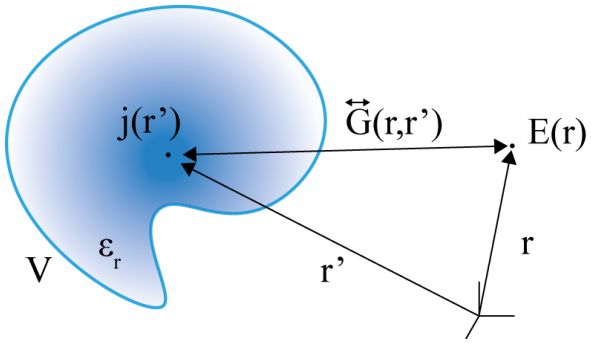

Fig. 3.6 Illustration of the Green's dyadic function. The Green's function renders the electric field at the point **r** generated by a single point source j at the point **r'**. Being dependent on the orientation of the point source, the Green's function is a tensor, accounting for on all the possible orientation of the point source. In case of a dipole emitter at the position **r** the Green's function can give the field generated inside a dielectric medium of volume V and permittivity ε_r at position **r'**, responsible for the back-action on the dipole self-generated field.

then proportional to the electric field that the emitter generates at its location and the overall enhancement, neglecting any non-radiative process, is defined as:

$$\frac{\rho}{\rho_0} = \frac{\gamma}{\gamma_0} = 1 + \frac{6\pi\varepsilon_0}{|\boldsymbol{\mu}|^2}\frac{1}{k^3}\,\mathrm{Im}\{\boldsymbol{\mu}^T \cdot \boldsymbol{E}_S(\boldsymbol{r}_0)\} \tag{3.6}$$

here $\rho_0 = \omega_0^2/(\pi^2 c^3)$ is the local density of electromagnetic modes for a black body radiation, and γ_0 the free space spontaneous decay, defined as:

$$\gamma_0 = \frac{\omega_0^3 |\boldsymbol{\mu}|}{3\pi\varepsilon_0 \hbar c^3} \tag{3.7}$$

3.2.2 Optical resonances of a dielectric nano-particle

The analytical solution to the problem of a spherical particle illuminated by a plane wave was already solved analytically by Gustav Mie in 1908 [180]. In analogy with the light reflected or transmitted by a material slab, a nano-particle can be described as an obstacle for the incoming electromagnetic wave (Fig.3.7a). In this picture, the scattered wave can be seen as the reflected wave, while the extinction is related to the amount of energy transferred through the particle. Their difference determines the amount of energy absorbed by the particle, while the resulting internal field is responsible of the optical resonances. The Mie theory, as described by Bohren and Huffman [206], starts from the time-harmonic dependent equation of the electromagnetic field:

$$\nabla^2 \boldsymbol{E} = -\omega \varepsilon_0 \varepsilon_r \mu \boldsymbol{E} \tag{3.8}$$

$$\nabla^2 \boldsymbol{H} = -\omega \varepsilon_0 \varepsilon_r \mu \boldsymbol{H} \tag{3.9}$$

from here we look for a solution in the case of a spherical particle of radius a and dielectric permittivity $\varepsilon = n^2$, where n is the particle material index of refraction, surrounded by a non-absorbing medium with index of refraction n_m. To obtain the solutions the incident, scattered and internal field are first expanded into an infinite series of spherical harmonics and the relative coefficients are calculated by satisfying the boundary conditions defined by the surface of the sphere [206]. From a classical point of view, the scattering, extinction and absorption cross-section can be approximated as the ratio of the power density (W) over the incident (I_i) power, giving rise to each relative phenomena.

The relative cross-section can be calculated as:

$$\sigma_{scatt} = \frac{W_s}{I_i} = \frac{2\pi}{k^2} \sum_{n=1}^{\infty} (2n+1)(|a_n|^2 + |b_n|^2) \tag{3.10}$$

$$\sigma_{ext} = \frac{W_e}{I_i} = \frac{2\pi}{k^2} \sum_{n=1}^{\infty} (2n+1)\,\mathrm{Re}(a_n + b_n) \tag{3.11}$$

$$\sigma_{abs} = \frac{W_a}{I_i} = \sigma_{ext} - \sigma_{scatt} \tag{3.12}$$

where $k = \dfrac{2\pi n_m}{\lambda}$ is the wavevector of the incoming light, and the sum terms represent the multipolar resonances ($n = 1$ dipolar, $n = 2$ quadrupolar, ...). The scattering coefficients a_n and b_n represent the electric and magnetic response, respectively. Figure 3.7b shows the electric and magnetic field lines of the first three modes, depicting the dipolar and multipolar characteristics of the internal field of a spherical nano-particles, taken from the original work of Mie.

The scattering coefficients are determined by the following equations:

$$a_n = \frac{m\psi_n(mx)\psi_n'(x) - \psi_n(x)\psi_n'(mx)}{m\psi_n(mx)\xi_n'(x) - \xi_n(x)\psi_n'(mx)} \tag{3.13}$$

$$b_n = \frac{\psi_n(mx)\psi_n'(x) - m\psi_n(x)\psi_n'(mx)}{\psi_n(mx)\xi_n'(x) - m\xi_n(x)\psi_n'(mx)} \tag{3.14}$$

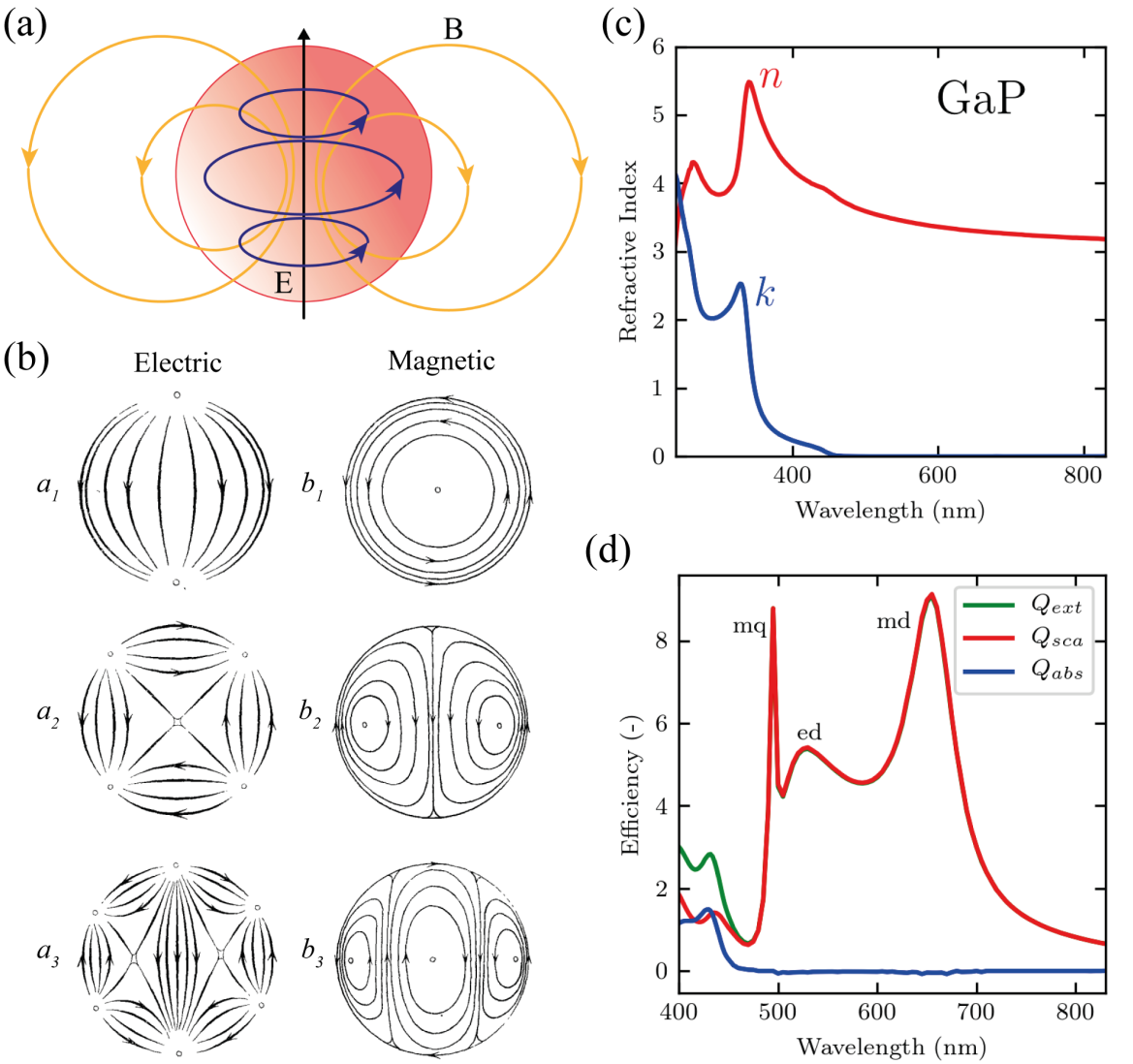

Fig. 3.7 (a) Schematic of the electromagnetic resonances for a dielectric nanoparticle. E is the electric field (blue), B the magnetic field (orange). In black the direction of the incoming light wave-vector, normal to its plane of propagation. (b) Electric and magnetic resonances of a nano-particle as reported by the original paper of Gustav Mie [180]. (c) Complex refractive index of gallium phosphide (GaP). (d) Calculated Mie efficiency factors for a GaP sphere in air with a radius of 100 nm. The main scattering peaks are labelled as for the magnetic dipole (md), electric dipole (ed) and magnetic quadrupole (mq).

here m is the relative refractive index ($m = \frac{n}{n_m}$) and x the size parameter ($x = ka = \frac{2\pi n_m a}{\lambda}$). The functions $\psi_n(z) = z j_n(z)$ and $\xi_n(z) = z h_n^{(1)}(z)$ are the Riccati-Bessel functions, where $j_n(z)$ is the spherical Bessel function of the first kind and $h_n^{(1)}(z)$ is the spherical Bessel function of the third kind, also called Hankel function of the first kind ($h_n^{(1)}(z) = j_n(z) + i y_n(z)$). The prime indicates the differentiation with respect to the argument. It can be seen that as m tends to one, i.e. there is no particle, the scattering coefficient vanish.

For small particles compared to the incident wavelength, the scattering response is composed of many peaks appearing in the resonance spectrum. In Figure 3.7d is shown the calculated Mie scattering cross-sections for a GaP nano-particle with a radius of 100 nm, in air. The broad peaks correspond to the magnetic (md) and electric (ed) dipolar resonance, while at higher frequencies it can be seen that a sharp peak appears in the scattering spectrum, related to higher order resonances, in this case to the magnetic quadrupole resonance (md).

A useful figure of merit to describe the scattering properties of a nano-particle are the relative efficiencies, or efficiency factors, for the scattering, extinction and absorption cross-section. These are defined as the relative cross-section normalized over the particle area:

$$Q_{ext} = \frac{\sigma_{ext}}{G} \qquad Q_{scatt} = \frac{\sigma_{scatt}}{G} \qquad Q_{abs} = \frac{\sigma_{abs}}{G} \tag{3.15}$$

$$Q_{scatt} = Q_{ext} - Q_{abs} \tag{3.16}$$

here G is the particle cross-sectional area, projected on the plane perpendicular to the incident wave vector, which takes the value of $G = \pi a^2$ for a spherical particle.

A shown in Eq.3.16, the scattering efficiency is controlled mainly by parasitic absorption in the nano-particle. In case of a non-absorbing material, i.e. the refractive index is real, we have that $Q_{scatt} = Q_{ext}$. This is an important feature to increase the efficiency of a particle, and the choice of GaP is justified being one of the most effective material for this task, following that the extinction coefficient drops to values close to zero at visible wavelengths, as shown in Figure 3.7c.

The main limitations of the Mie theory stems from the fact that it is rooted in the context of classical electrodynamics and limits the analytical solution only to spherical particles. Since the modern fabrication of nano-antennas can yield various geometries, from disks to

more complex designs, most of the studies are carried out with calculations with numerical analysis software. Moreover, the Mie theory fails to describe the properties of particles when drastically reducing their sizes, where quantum mechanical effects are prominent, together with a lack in the description of surface phenomena such as the non-sharp boundary at a particle interface with the surrounding medium or surface effects and doping.

3.2.3 Near-field enhancement

The absorption of light from a quantum emitter can be described in terms of a frequency dependent absorption cross-section. For weak excitations, the rate at which an emitter is excited is proportional to the square of the absolute value of the electric field $\mathbf{E}$ along the axes of the dipole moment $\boldsymbol{\mu}$. The power received by the emitter can be written as [162]:

$$W_{exc} = \frac{\omega}{2} \mathrm{Im}\{\alpha\} |\mathbf{n}_\mu \cdot \mathbf{E}|^2 \tag{3.17}$$

where α is the emitter's polarizability. Formally, the absorption cross-section is the geometrical area of interaction which usually correspond to a surface area of the interaction, normal to the plane of the incident wave. In case of a two-level system, in the absence of an antenna the absorption cross-section show a theoretical limit of $\sigma_{abs} = 3\lambda^2/(2\pi)$. In case of the presence of a strong electric field, as at the surface of an optically driven nano-antenna, the absorption cross-section of a luminescent emitter is increased, directly leading to an enhancement of its excitation rate. The overall absorption cross-section resulting from the interaction with the near field region of the nano-antenna can be written as:

$$\sigma = \sigma_0 \frac{|\mathbf{n}_\mu \cdot \mathbf{E}|^2}{|\mathbf{n}_\mu \cdot \mathbf{E}_0|^2} \tag{3.18}$$

where $\mathbf{E}$ and $\mathbf{E}_0$ are the field at the nano-antenna surface and without the antenna, respectively, and σ_0 the absorption cross-section without the antenna. This near-field enhancement at the surface of the nano-antenna leads to an higher excitation rate of the emitter, which results in a more efficient preparation of the emitting state. If this higher efficiency in the state preparation is then associated with an increased spontaneous emission rate, via the Purcell effect, the results is an overall increment of the light extracted from a quantum emitter coupled to the antenna near-field.

3.2.4 Directional emission

A nano-antenna acts as a near-field concentrator of light which can modify the far field pattern of the emitted radiation. This property is quantified by the directivity (D) of the antenna, defined as:

$$D(\theta,\phi) = \frac{4\pi p(\theta,\phi)}{W_{rad}} \tag{3.19}$$

where $W_{rad} = \pi r^2 I Q_{scatt}$ is the total power radiated in the far-field in the solid angle defined by the distribution p, dependent on the spherical coordinates (θ,ϕ).

In case of both magnetic and electric dipole moments, the directivity of a nano-antenna can be tailored reach high values of the forward to backward ratio, which can lead to a near-unity directional emission. As shown in Figure 3.8, this effect is related to the relative orientation and magnitude of the electric and magnetic dipole moment, for instance in a dielectric nano-particle. The destructive interference of the interacting dipoles, also known as the Kerker condition [207], can cancel out the back scattered wave in the far-field, resulting in a highly directive source which leads to an overall improvement of the light emission efficiency.

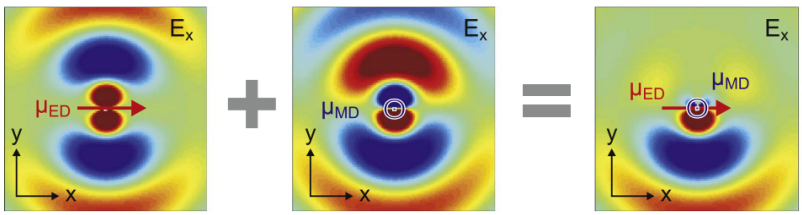

Fig. 3.8 Schematic of the Kerker condition. The interaction between an electric dipole (μ_{ED}) and a perpendicular magnetic dipole (μ_{MD}), of same frequency and amplitude, results in the destructive interference of the scattered wave in one direction, and the constructive interference in the other direction yielding a near unity directivity. Adapted from Ref.[208].

3.2.5 Photoluminescence enhancement factor

With the figures of merit described up to now, we can now address the experimental study of optical nano-antennas coupled with luminescent dipole emitters. From experiments, three enhancement effects occur in an optically driven nano-antenna [209] and their product determines the overall intensity extracted from an emitter (I) as a function of its position ($\mathbf{r}$):

$$I(\boldsymbol{r}, \omega_{pump}, \omega_{em}) \propto P_{pump}(\boldsymbol{r}, \omega_{pump}) \cdot q(\boldsymbol{r}, \omega_{em}) \cdot \eta_{NA}(\boldsymbol{r}, \omega_{em}) \tag{3.20}$$

where $\omega_{pump}, \omega_{em}$ are the excitation and emission frequency, respectively.

The first factor (P_{pump}) is the excitation enhancement of the emitter, directly proportional to the near-field enhancement at the pump frequency, as discussed in section 3.2.3. This factor is dependent on the wavelength used to excite the structure, its polarization and the beam profile.

Once the emitter is in the excited state, it will spontaneously decay with an enhanced emission rate which is described by the quantum efficiency, or quantum yield, defined as:

$$q(\boldsymbol{r}, \omega_{em}) = \frac{\gamma_r}{\gamma_r + \gamma_{nr}} \tag{3.21}$$

where γ_r is the radiative decay rate and γ_{nr} is the non-radiative decay rate. The quantum efficiency defines the number of photon emitted over the photons absorbed and, as described in section 3.2.1, can be enhanced via the Purcell effect which directly improves the spontaneous decay rate γ_r. Note, that for an emitter with near-unity intrinsic quantum efficiency ($\gamma_{nr} \approx 0$, $q \approx 1$) the intensity of photon extracted cannot be improved. On the contrary, for a poor quantum efficiency emitter ($q \ll 1$) the overall efficiency can be increased up to $1/q_0$. This is important in the case of 2D-TMDs, where the quantum yield in exfoliated materials are usually below 0.1% [210].

Finally, the property of an antenna to redirect the amount of light in the upper hemisphere can result in an increased collection efficiency, the third factor in Equation 3.21, defined as:

$$\eta_{NA}(\boldsymbol{r}, \omega_{em}) = \int p(\boldsymbol{r}, \omega_{em}; \theta, \phi) \sin\theta d\theta d\phi \tag{3.22}$$

where the subscript *NA* indicates the integration over the numerical aperture of the collection optics used in the experimental setup.

3.2.6 Surface enhanced Raman scattering

An additional effect of confined fields at the surface of optically driven nano-particles is the enhancement of non-linear effects of closely coupled emitters, such as the Raman scattering intensity.

The Raman process describes the inelastic scattering between a photon and a fundamental vibration mode of a crystal lattice, or rotation modes in molecules. The process can be described from the absorption of a photon at frequency ω and subsequent emission of another photon with different frequency ω_R, with an energy offset from the first photon equal to the vibrational frequency ω_{vib}:

$$\omega_R = \omega \pm \omega_{vib} \tag{3.23}$$

if $\omega_R > \omega$ it is referred to Stokes Raman scattering, instead if $\omega_R < \omega$ is called anti-Stokes Raman scattering, as shown in Figure 3.9.

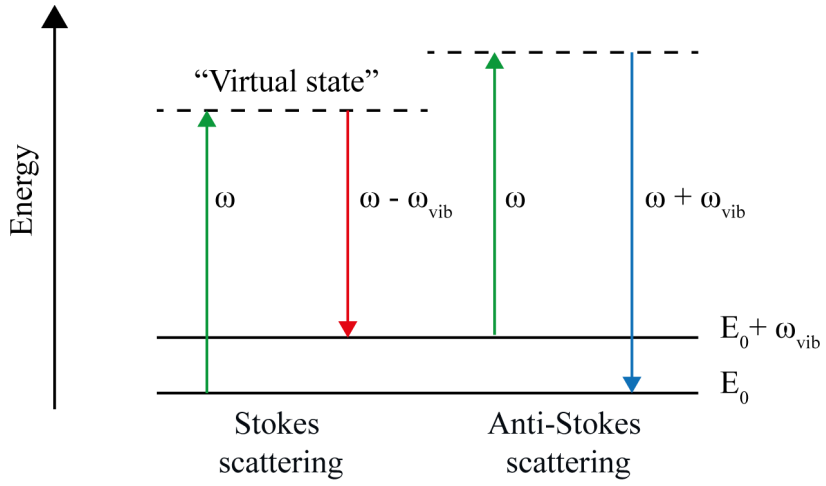

Fig. 3.9 Schematic of the Raman scattering process

The Raman effect is an extremely weak process where the Raman scattering cross-section is usually more than ten orders of magnitudes smaller than that associated with the fluorescence processes. It is then fundamental to find approaches to enhance the interaction between the optical probe and the vibrational modes. The most common example is given by the Surface enhanced Raman scattering (SERS) [211] where the presence of a strongly confined field at the surface of metal or dielectric [212] nano-particles can give rise to a enhancement of the Raman signal up to 10^{12} [213].

For Stokes processes the power of the scattered beam can be approximates as [31]:

$$P(\omega_R) = N\sigma_{RS}I(\omega) \tag{3.24}$$

Where N is the number of active scatterers under the excitation spot, σ_{RS} is the Raman cross-section and $I(\omega)$ is the intensity of the excitation source. The enchantment of the

scattered signal power is directly correlated to the changes in the cross-section ($\sigma_{SERS} > \sigma_{RS}$) which can be ascribed to two main effects, the electronic or chemical contributions, and more importantly to the excitation of stronger electromagnetic fields via localized plasmons resonances and the crowding of field lines. The Raman scattering enhancement factor can be expressed as $L(\omega) = |E_{loc}(\omega)|/|E_0|$, and the total power in case of SERS becomes:

$$P(\omega_R) = N\sigma_{SERS}L(\omega)^2L(\omega_R)^2I(\omega) \tag{3.25}$$

being that $\Delta\omega = \omega_R - \omega$ is small, the overall Raman scattering enhancement is proportional to the fourth power of the electric field as $R = |E_{loc}(\omega)|^4/|E_0|^4$.

Chapter 4

Experimental Methods

This chapter covers all the experimental techniques used in this work. The first section describes the methods used to isolate single and few layers of two-dimensional materials and the transfer methods on arbitrary substrates. The second section will describe the procedure for fabrication of dielectric nano-antennas. The last part will discuss the experimental methods used in the optical and time resolved spectroscopy studies of 2D-TMDs photoluminescence and single photon emission.

4.1 2D materials fabrication methods

The layered nature of crystals such as graphite allows the mechanical cleavage of single atomic sheets via repeated exfoliation processes with adhesive tape. This process, so-called "Scotch tape method", or mechanical exfoliation, was firstly used for the isolation of single graphene sheets and other 2D crystals [2]. Since then, new attractive methods for large scale production have been developed, such as chemical vapour deposition [214] and liquid exfoliation [215], yet the preferred way to obtain high quality 2D crystals in most of the research laboratories remains the exfoliation of single bulk crystals. After the isolation and identification of single 2D layers, the material is then transferred on arbitrary substrates or assembled in vertical heterostructures [216]. In this work, we carried out the transfers with poly-dimethylsiloxane (PDMS) as it is the fastest and more reliable way to obtain large single layers of 2D-TMDs and to transfer them on top of non-planar patterned substrates. As comparison it will be also discussed the transfer technique based on poly-methylmethacrylate (PMMA).

4.1.1 Mechanical exfoliation

The atomically thin materials used in this work are exfoliated from commercially available bulk single crystals (HQ Graphene) with the use of an adhesive tape (Nitto® BT-150E-CM) chosen for the low glue residues left on the exfoliated crystals.

Figure 4.1 shows a schematic of the mechanical exfoliation process. A bulk layered crystal is placed on a clean adhesive tape and, with the use of the tape protective PET film, a gentle pressure is applied in order to make the crystal surface adhere to the tape. The adhesion forces are strong enough to break the weak interlayer bonding and, after careful removal of the crystal, the first few layers from its surface are left on the tape. This process is repeated until a good coverage of the tape is obtained. From this residues, few additional exfoliation processes are done by employing a new, clean tape. This procedure allows to break even more the interlayer bonding between the residual material, and to obtain thinner crystals. The tape is then pressed onto a substrate in order to transfer the remaining material. Most commonly the 2D layers are transferred on top of a polymeric films or silicon oxide

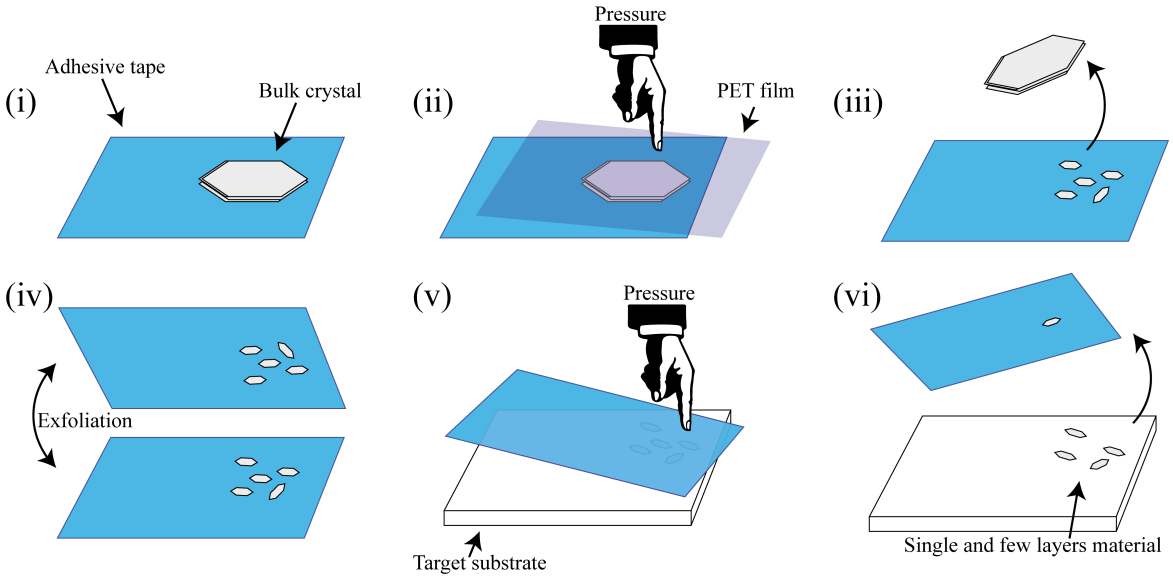

Fig. 4.1 Mechanical exfoliation process for layered crystals. (i-ii) The bulk crystal is placed on a adhesive tape and press onto it by using a protective film. (iii) The adhesion force will strip the first few crystal layers, after the removal of the bulk crystal, leaving them onto the tape. (iv) This process is repeated with a new tape in order to break even more the interlayer forces between the exfoliated crystals. (v) After few peeling, the remaining material is pressed onto a polymeric or silicon substrate and transferred from the tape to the substrate. (vi) The single and few layers of material left onto the substrate are then identified with an optical microscope, in order to be transferred onto arbitrary substrates.

substrates, specifically chosen for the transfer method used or for the assembly of van der Waals heterostructures. In our case we used PDMS (Gel-Pak® 4, approximately 1x1 cm size sheets deposited on a glass slide) since in our experience is the best way to obtain large single crystals with clean material surfaces, when not directly in contact with the polymeric substrate. At this stage, the polymer is searched with the use of an optical microscope for identification of single layer crystals, as discussed in the following section.

4.1.2 Photoluminescence imaging

In order to unambiguously identify the thickness of single and double layer TMDs we use a photoluminescence (PL) imaging technique in a commercial optical microscope, as introduced in Ref.[217] and shown in Figure 4.2. The most common approaches to identify single and few layers of 2D materials relies on their optical contrast and visibility on the relative target substrate [218]. Instead, the principle of operation of this PL technique exploits the high quantum efficiency of mono and bilayer of TMDs at room temperature.

By using the same white light source used to acquire the bright-field images of the sample (Fig.4.2b), it is possible to excite simultaneously the luminescence of 2D-TMDs. To isolate the signal coming from the atomically thin layers, the white light source is filtered with a 550 nm shortpass filter (550SP) in the excitation path, removing the infra-red and near-infrared part of the emission spectrum. The PL signal produced by the TMDs is then isolated with a 600 nm longpass filter (600LP) in the collection path. The resulting image on the microscope CCD camera is shown in Figure 4.2c. Here, it is possible to identify the single and double

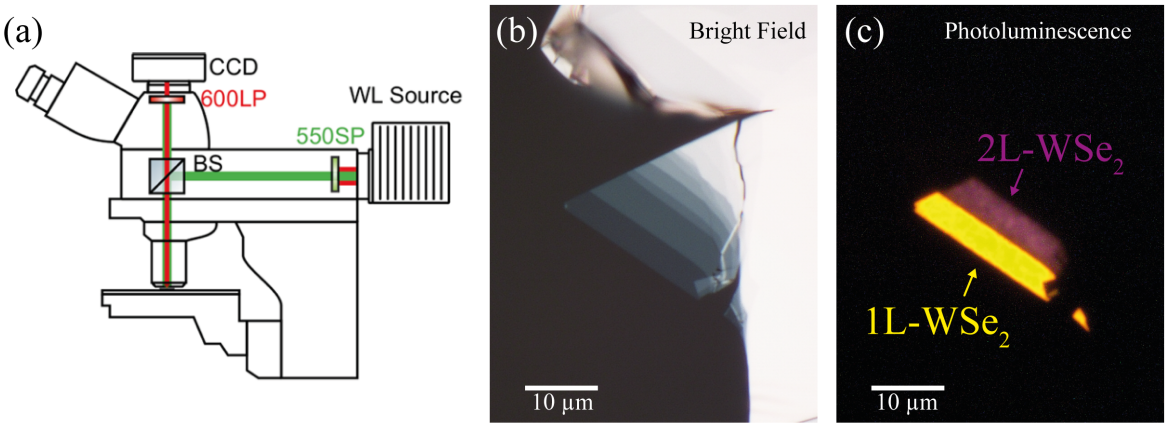

Fig. 4.2 (a) Schematic view of the PL imaging setup in a commercial optical bright field microscope. Adapted from Ref[217]. (b) Bright field image of an exfoliated WSe_2 sample on PDMS. (c) Photoluminescence signal isolated from single and double layer WSe_2.

layer from the relative emission intensity and colour. The colour is an artefact of the filters placed before the microscope CCD camera pixels. For the room temperature PL emission of WSe_2 we observe in yellow the PL emission for monolayers (peaked at around 750 nm) and in purple for bilayers (broad PL emission at 750-800 nm).

4.1.3 2D crystals transfer methods

One fascinating feature of 2D materials is the possibility to deterministically transfer single layers on arbitrary substrates and to stack them one on top of each other to create novel and engineered devices. Most of the 2D crystal transfer techniques can be carried out on a small optical table with a modified optical microscope, long working distance objectives and few chemicals, as shown in Figure 4.3. Two sets of micro-manipulator are used for alignment of the exfoliated material and the target substrate, held on a rotation/heater stage used for fine alignment in the assembly of 2D heterostructures. A vacuum pump is connected to the micro-manipulators in order to improve the stability of the transfer arm, fixing the glass slide to the end of the arm and to keep the target transfer attached to the rotation stage. The glass slide with the 2D crystals is then carefully brought into contact with the target substrate. The transparency of the polymer allows the optical access with the optical microscope, which is used to observe the real-time progress of the transfer process.

The 2D crystal transfer methods can be described in two main categories: the wet transfer methods, based on the use of chemicals, such as acetone, to dissolve the polymer membrane

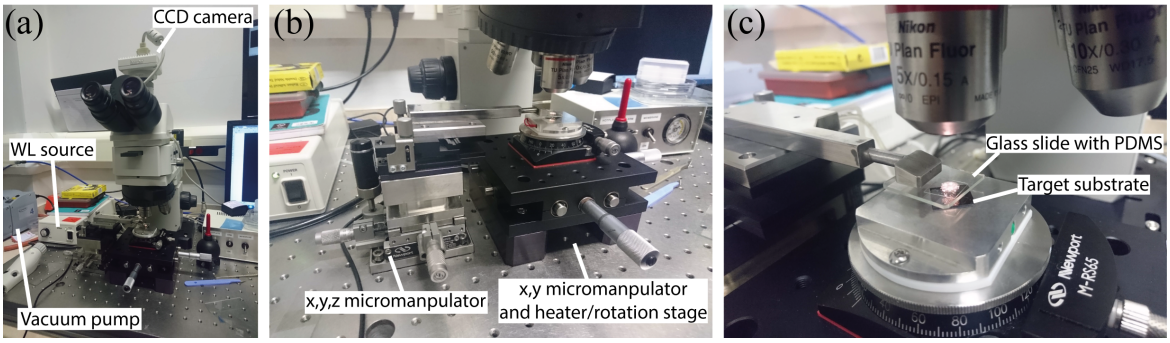

Fig. 4.3 (a) Modified optical microscope for the transfer of 2D materials. (b) A three axis manipulator with a vacuum holder is used to align the exfoliated material to a substrate positioned on a rotation and heater stage with a two axis micro-manipulator for finer alignment. (c) Close up of the transfer stage. A glass slide with the polymeric film with exfoliated crystal is aligned to a target silicon substrate. the transparency of the glass slide and polymer allows the optical access during the whole transfer process.

used in the transfer, and the dry transfer methods, where the 2D material is deposited on the target substrate by just peeling it off the polymer film.

PMMA transfer technique

In a wet transfer technique a sacrificial layer of poly-methylglutarimide (PMGI) is spun onto a silicon wafer and covered with another layer of PMMA before the exfoliation process. Once a suitable 2D layer is isolated, the area around the crystal is scratched with a dental pick in order to expose the underlying PMGI layer. By adding DI water in small drops the PMGI layer is dissolved, leaving the PMMA membrane floating on water. The sample is then placed in a becker full of DI water to let the membrane float. The membrane is then picked up from the water surface with a metallic support which will hold the membrane for the following alignment and transfer process. If the target substrate have adhesion forces stronger than the PMMA, it is possible to dry-peel the 2D crystal off the PMMA film. Otherwise, the membrane is collapsed onto the target substrate and eventually washed away in an acetone bath.

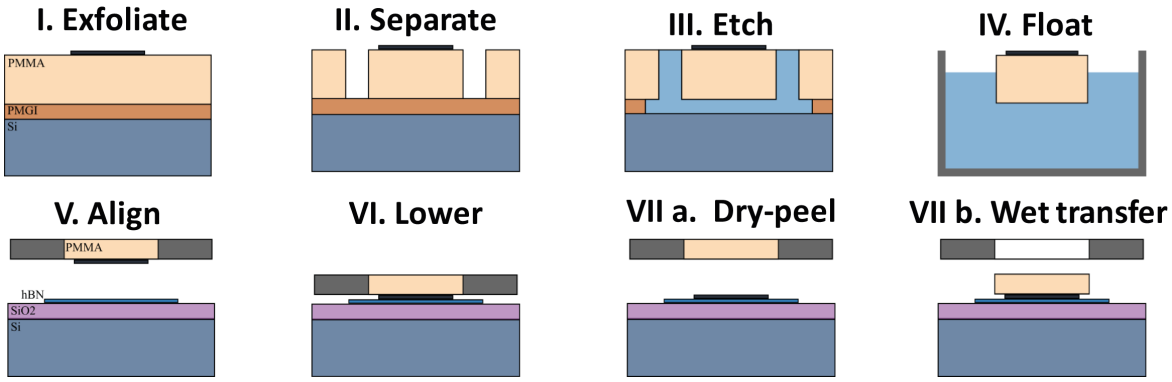

Fig. 4.4 Schematic of a PMMA wet transfer technique. After etching of the PMGI sacrificial layer, the PMMA membrane is used in a transfer setup to either dry-peel off the 2D crystal or collapsed onto the target substrate and washed in a wet transfer process with an acetone bath.

PDMS all-dry transfer technique

Since use of chemical can be detrimental for the optical properties of 2D semiconductors, all-dry transfer techniques are more suitable to preserve the high optical quality of exfoliated materials. The most developed technique uses a visco-elastic stamp (PDMS) to transfer the 2D material on arbitrary substrates [219] (Fig.4.5a). Here, the exfoliated material is aligned to the target substrate, and pressed onto it. In order to release the crystal, the peeling

procedure is done in a slow and controlled way, in order to use the visco-elastic properties of PDMS to detach the 2D layer and transfer it onto the substrate.

Due to its elastic properties, the use of PDMS allows a finer control in the deposition of materials on top of patterned substrates presenting out-of-plane nano-structures. This advantage proved to be critical in the deposition of integer layers on top of pre-patterned nano-structures, such as the optical nano-antennas used in this work. The control on the force applied during the compression of the layer onto the substrate, and on the velocity and direction of the contact edge, are crucial in the release of integer 2D layers on top of different nano-structures. This can be achieved with careful alignment of the exfoliated crystals and some experience in the transfer procedure. The use of very large (>100 μm lateral size) exfoliated material proved to be the most effective way to transfer and release undamaged 2D crystals on top of nano-structures (Fig.4.5b).

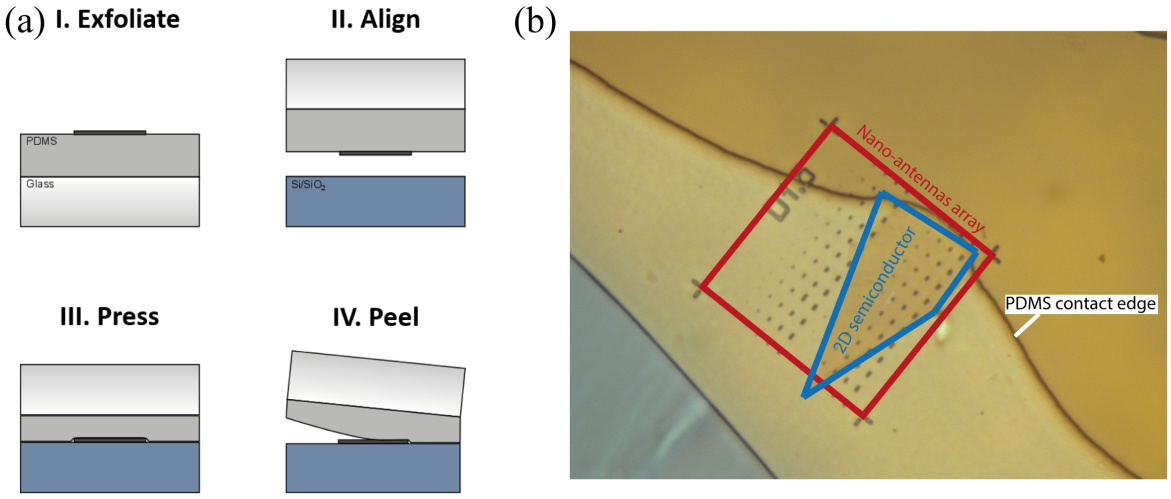

Fig. 4.5 (a) Schematic of the PDMS dry transfer process. (b) Optical image during the peel-off process of a large exfoliated single 2D crystal on top of a GaP dimer nano-antennas array (200 nm height) with lateral size $\approx$ 100 μm.

4.2 Optical nano-antennas fabrication

As discussed in Chapter 3, the fabrication of optical nano-antennas in the visible range are strongly connected with the advances in nano-scale fabrication processes. This is due to the fact that the quality of their resonances is strongly affected by the deviation of the sub-wavelength dimensions and geometry of the fabricated nano-structures from the ideal case, for instance in the shape of the walls or edges. One of the advantages of optical nano-antenna over high quality factor cavities is the low cost and easier fabrication processes. For instance they offer bottom-up fabrication techniques, which are mainly achieved through chemical methods as those used in the synthesis of gold nanoparticles and colloidal quantum dots. This approach allows to achieve a controlled shape and high crystal quality of the antennas, but lacks the important requisite of controlling their disposition on a substrate, thus requiring additional nano-manipulation tools such as AFM or pre-patterned hole arrays. Top-down approaches are more suitable for a controlled design and location of the fabricated antennas, and are appealing methods for industrial and scalable technologies. The main routes of top down fabrication involve the use of electron beam lithography or focused ion beam milling, offering nano-scale precision in designing the structures, with resolution down to tens of nanometres.

4.2.1 GaP dimer nano-antennas

The GaP dimer nano-antennas used in this work are fabricated by J. Cambiasso from the group of Stefan Maier at Imperial College London, with a top-down process [194] as shown in Figure 4.6. The fabrication steps are as follow:

- (i) The nano-antenna fabrication starts from an undoped, crystalline GaP(100) wafer.
- (ii) A thin layer of 40 nm of SiO_2 is sputtered on the GaP wafer at a rate of 0.2 Å s^{-1}, to be used as a mask in later steps.
- (iii) A PMMA layer is spin-coated at 3000 rpm for 1 min, acting as a positive resist in the lithographic step.
- (iv) Electron beam lithography is used to define the antenna size and geometry. The electron beam acceleration voltage was 20 kV, working distance 10 mm and aperture 10 μm. The exposed PMMA is developed in a standard MIBK:IPA 1:3 solution for 30 s and rinsed in clean IPA.

- (v) 40 nm of Au are thermally evaporated under high-vacuum at a rate of 2 Å s^{-1}.
- (vi) The sample is then submerged in acetone for the lift-off of the PMMA mask.
- (vii) The SiO_2 layer not covered by Au is removed with CHF_3 reactive ion etching.
- (viii) The thin SiO_2 layer left acts as a mask, protecting the GaP in the following Cl_2 etching step which removes the exposed GaP material.
- (ix) The remaining Au and SiO_2 residues are removed with a wet etching process based on hydrofluoric acid (HF) and rinsed in acetone and water.
- (x) Finally, the resulting nano-antenna rise from the substrate, with diameter size and position determined by the lithography process and height by the etching procedure. The resulting nano-structure is then used as a target substrate for the transfer of the exfoliated 2D material.

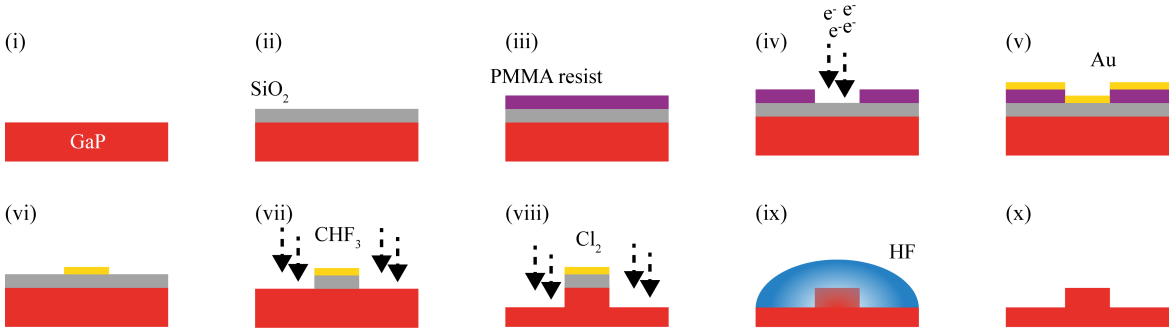

Fig. 4.6 The fabrication of GaP dimer nano-antenna starts from a commercial available GaP wafer (i) which is firstly covered with SiO_2 (ii) acting as a protection mask in the later etching steps. After defining the nano-antenna geometry via an electron beam lithography step (iv), the wafer is exposed to different etching processes (vii-ix) in order to remove systematically the exposed material and masks, leading to the realization of the final nano-antenna structure (x).

4.3 Optical spectroscopy

All the photoluminescence (PL) and Raman scattering experiments have been carried out in home-built setups in Sheffield. Figure 4.7 shows the schematic top view of the optical table and experimental setup used. As excitation sources, diode lasers at different wavelengths are coupled to single mode optical fibres. Continuous wave excitation is obtained at 405, 450, 532, 638, 685 and 725 nm. A 638 nm pulsed diode laser (PicoQuant LDH, pulse width 90 ps) is used as the excitation source for time resolved PL analysis. The ultra-low frequency Raman scattering setup and the μ-PL setup are coupled in free space to a grating spectrometer. The bath cryostat μ-PL setup instead is coupled with single mode fibres to the excitation sources and, for collection, to the same spectrometer.

The light coming from all the optical setups is focussed onto the slit of a dual-exit 0.75 metre focal length spectrometer (Princeton Instruments SP2750) which either directs the light for detection to a high-sensitivity liquid nitrogen cooled charge-coupled device (CCD, Princeton Instruments PyLoN BR-eXcelon), or allows the filtering from a second slit exit aperture. This signal is collected in a single/multimode fibre and directed to single photon avalanche photodiodes detectors (APD) for time correlated single photon counting (TCSPC), or connected to two APD in a Hanbury-Brown-Twiss (HBT) geometry interference experiment.

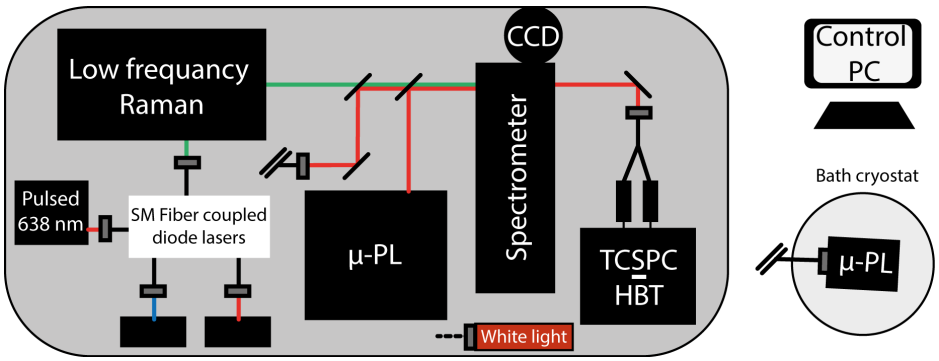

Fig. 4.7 Schematic of the optical spectroscopy setups and disposition. The optical table (grey) host a multi chromatic excitation scheme, obtained with single mode fibre coupled diode lasers. A Raman and μ-PL setups are coupled in free space to a spectrometer/CCD system for the detection of light. A bath cryostat is placed at the side of the optical table and host a fibre coupled μ-PL setup to access the samples kept at cryogenic temperature. The collected light is then directed with a single mode fibre to the same spectrometer for analysis. The output signal at the exit slit of the spectrometer is directed to avalanche photodiode detectors, used for time resolved PL analysis and autocorrelation experiments. All is controlled and automated from a control computer (PC).

4.3.1 μ-Photoluminescence setup

For photoluminescence analysis with sub-micron resolution, we used an homebuilt optical setup in back reflection geometry, with programmable stepper motorized stages which allow to move the sample in the x,y plane with spatial resolution down to 0.31 μm. A schematic of the setup is shown in Figure 4.8.

The samples are placed in a flow cryostat (Oxford instruments) and held under high vacuum, at either room or liquid helium temperature. As excitation source, a laser coupled to a single mode fibre is filtered with a short pass filter (SPF) to clean the low energy side of the laser spectrum. The light then passes through a Glan-Thompson linear polarizer (LP) followed by a half-wave plate mounted onto a motorized rotation stage ($\lambda/2$), allowing the control of the linear polarization angle of the excitation source. With a 50:50 beam splitter (BS) the light is directed downwards in a long-working distance infinity corrected objective (Mitutoyo 100x, numerical aperture (NA) = 0.7) which focusses the light onto the sample. The objective is mounted on a motorized vertical positioner, with single step resolution of 0.021 μm. A multimode fibre coupled white light source (Thorlabs SLS201L) is used to image the sample by projecting the light on a CMOS camera sensor (Thorlabs). The sample is mounted onto stepper motor x,y stages (STANDA-8MTF) which allows the automated two-dimensional mapping of the sample surface. For polarization detection, a half-wave plate on a motorized rotation stage and a linear polarizer are inserted in the collection path. Before reaching the spectrometer slit, the light from the sample is filtered with a longpass filter (LPF) to remove any residual laser signal. The light is then focussed on the slit of the spectrometer and analysed after a 300 grooves/mm grating projects the signal on the CCD sensor.

4.3.2 Liquid helium bath cryostat setup

To study the low temperature PL emission for prolonged time a gas exchange, liquid helium bath cryostat offers a sustainable way to hold a sample at cryogenic temperatures of 4.2 K, compared to a helium flow cryostat, as long as the evaporated helium inside is replenished periodically. As shown in Figure 4.8b the bath cryostat consist in a tank (Cryo Anlagenbau Gmbh) containing approximately 75 litres of liquid He. The evaporated He is collected in a compressor and recycled. A microscope stick, with a cage structure (Attocube) and a window for the optical access, host the optical components and the sample. The sample is placed onto piezoelectric nano-positioners (Attocube ANP101 models), working with a stick-slip mechanism, used for scanning and aligning the sample to the optical path. The cage is then

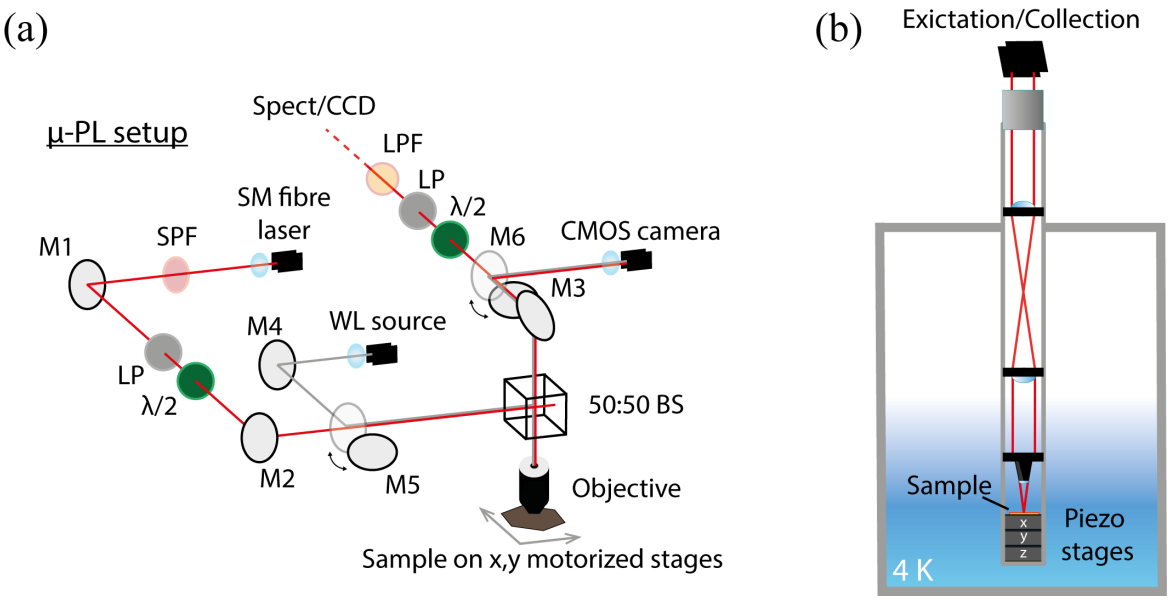

Fig. 4.8 (a) Schematic of the μ-PL setup. (b) Schematic of a liquid helium bath cryostat and optical cage system to access the sample on piezoelectric nano-positioners.

inserted into a cylindrical vacuum tube and pumped down to 10^{-4} mbar, with an oil-free vacuum pump, before inserting a small amount of He gas from a bladder. The He gas allows a more uniform thermal exchange between the sample and the liquid He bath, compared to high vacuum. The whole tube is then carefully inserted in the cryostat, in direct contact with the liquid He bath. During the temperature changes the nano-positioners are grounded to avoid charge accumulation and capacitance breakdown. An optical breadboard with a μ-PL setup, analogous to the one described in Figure 4.8a , is placed on top of the insert tube to carry out the optical analysis using single modes optical fibres to excite and collect the PL signal.

4.3.3 Raman spectroscopy

All Raman spectra are collected at room temperature in a μ-Raman set-up, with samples placed in vacuum in a flow cryostat. Figure 4.9 shows a schematic of the optical setup. A single mode 532 nm laser (Cobolt 04-01) is used as excitation source. To control the linear polarization degree both in the excitation and collection path, two linear polarizes (LP) are mounted on motorized rotation stages. This way it is possible to use a cross polarized detection to remove the Rayleigh scattered laser signal. An Optigrate Bragg notch filter (BNF) is used to to inject/reject the laser beam into an infinity corrected objective (Mitutoyo 50x NA=0.55) with the use of an mirror placed at $\approx$ 45 degrees (M2). As shown in Figure 4.9b,

the Bragg filter is used to reject most of the laser light from the collection beam path with both an angular and spectral filtering. In order to collect signal at ultra-low frequencies from the laser line, the Rayleigh scattered laser signal is suppressed using three Optigrate Bragg notch filters in the collection path. Each single filter can act as an effective optical density of 3 at the laser wavelength. The Raman signal is then collected in the same spectrometer/CCD system as for PL spectroscopy with the use of two gratings (1800 g/mm or 2400 g/mm). With this setup the ultra-low frequency modes of 2D-TMDs can be collected. As a reference, Figure 4.9c shows the shift in the low-frequency Raman shear mode resonance in bulk and bilayer WSe_2 [220].

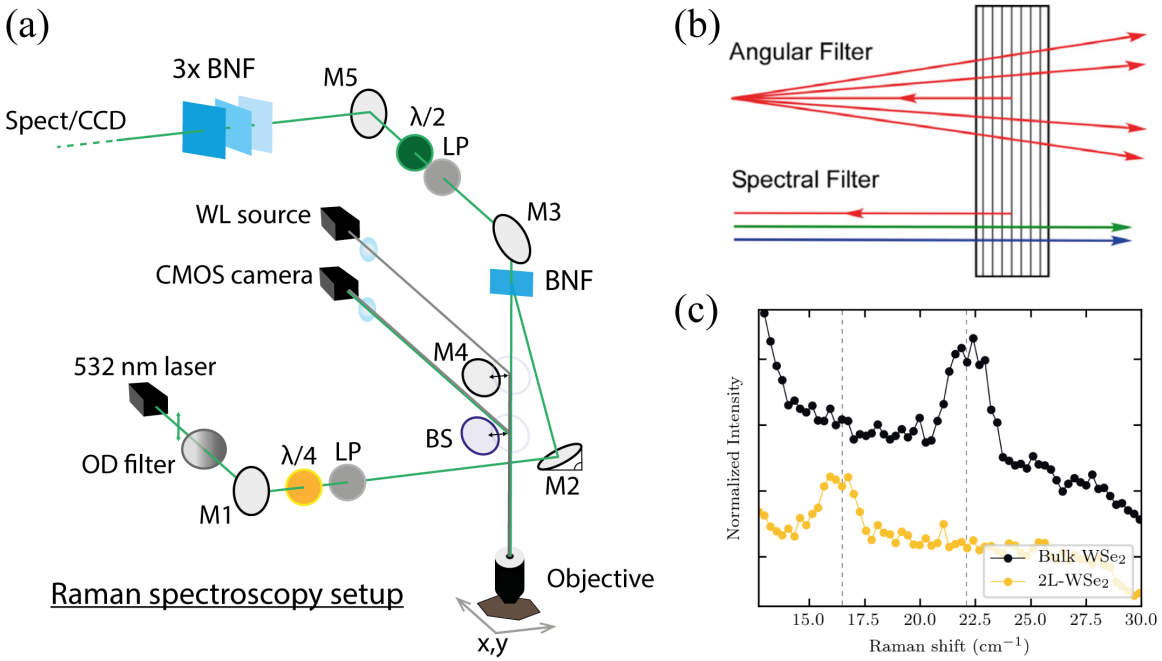

Fig. 4.9 (a) Schematic of the ultra-low frequency Raman spectroscopy setup. (b) Principle of operation of the Bragg notch filter (BNF). The angular rejection is obtained by tilting the filter relative to the laser beam. The spectral filtering is related to the design and fabrication of the right Bragg condition. (c) Dependence of the ultra-low frequency Raman shear modes on the number of layers in WSe_2. In bulk crystals the signal is found at around 22.5 cm^{-1}, for bilayer the shear modes resonance blueshifts around 16 cm^{-1}, closer to the laser line at 0 cm^{-1}

4.4 Time resolved spectroscopy

Time correlated single photon counting (TCSPC) is the most common technique used to access the time domain in optical spectroscopy experiments, for the measurement of excited states lifetime and single photon interference experiments. An important parameter in time resolved studies is the timing resolution achievable. Current TCSPC electronics can detect signals below 30 ps resolution, however the limiting factors are related the pulse width of the excitation source and the detector response time. For diode lasers, pulse widths below 100 ps are usually obtainable, while for higher resolution mode-locked lasers with femtoseconds pulse width are commonly employed. In the detection of fast signals, the detector instrument response function (IRF) is crucial. The most common and reliable detectors used in time resolved spectroscopy are single photon avalanche photodiode, which can achieve time resolutions below 50 ps. In order to detect ultra-fast signals, a streak camera can be used as detector with >1 picosecond time resolution. Nowadays the most advanced streak camera systems are used with femtosecond tunable Ti:Sapphire laser and can reach sub-picosecond time resolution.

This section will cover the basic principles of the electronics involved in the TCSPC detection of single photons used for the study of luminescence time dynamics. The autocorrelation measurements in a Hanbury-Brown-Twiss interference experiment is also discussed. The streak camera measurement reported in Chapter 5 were performed at TU Dortmund, under the assistance of Prof. M. Aßmann, and a brief schematic of the experimental setup and principle of operation are given at the end of this section.

4.4.1 Time correlated single photon counting

For a more complete understanding of luminescence phenomena, the use of time domain spectroscopy offers a valuable tool for studying the dynamics of excited states. Consider a two level electronic transition between a ground and excited state. In Figure 4.10a is shown the instrument response function (IRF, in black) and a luminescence decay signal (orange) collected for a single photon emitter, as discussed in Chapter 7. The intensity at $t = 0$, just after the excitation pulse, is directly related to the excited state initial population n_0. This population will then spontaneously decay back to the fundamental ground level following the rate equation:

$$\frac{dn(t)}{dt} = (\Gamma_0 + k_{nr})n(t) \tag{4.1}$$

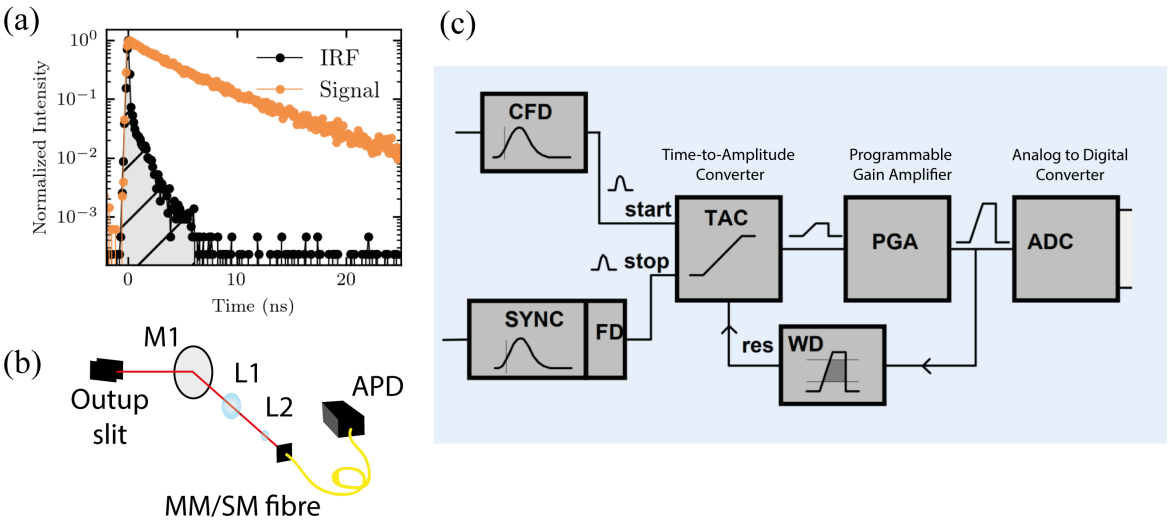

Fig. 4.10 (a) Example of a instrument response function (IRF, in black) of an APD triggered with a 90 ps pulsed diode laser, the . The fluorescence signal (orange) exhibits a single exponential decay, indication the presence of a single transition in the sample excited with the ps pulsed source. (b) Schematics of the collection setup used to direct the light filtered from the spectrometer to the APD detector. (c) Schematics of the TCSPC electronic components.

where Γ_0 is the spontaneous emission rate and k_{nr} the sum of all non-radiative decay rates. The solution of this equation yields a single exponential decay profile, in the form of $n(t) = n_0 e^{-t/\tau}$, where $\tau = (\Gamma + k_{nr})^{-1}$.

The acquisition of a luminescence lifetime decay is intrinsically an averaged and statistical process, due to the fact that a large number of emitters, and excitation cycles, gives rise to the overall signal curve. The single photon detection event happens at different times, relatively to the excitation pulse, leading to the formation of a decay trace when acquired for long integration times. If the PL decay curves can be fitted with single or bi-exponential decay functions, in the form $y = y_0 + A_1 e^{-t/\tau_1} + A_2 e^{-t/\tau_2}$, indicating the presence of one or two recombination processes, the τ value can be directly related to the effective decay time of the photoluminescence signal [221]. This way, it is possible to correlate the dependence of the extracted decay and amplitude coefficients to the studied system temporal dynamics, and relate it to the variables used during the experimental analysis (e.g. temperature, power, bias, etc.).

Figure 4.10b shows the schematic of the collection setup used to direct the light signal to an APD detector. After filtering through the spectrometer exit slit, the light is focussed with two lenses. The first lens (L1) focusses the broad signal scattered by the spectrometer grating

on a second lens (L2), with matching numerical aperture to that of the single/multimode fibre used to direct the signal to a fibre coupled APD detector. In this work, the pulse signal from the APD (ID100-MMF50, time-resolution of ∼40 ps) is read using a photon counting card (Becker and Hickl SPC-130). A ≈90 ps pulsed diode laser (PicoQuant LDH) with wavelength 638 nm is used as the excitation source with MHz repetition rates. Overall, the instrument response function obtained shows full width at half maximum of 150-200 ps (Fig.4.10a) due to the broadening of the signals in the fibre used for light collection. The tail in the IRF response is due to the release of trapped carriers in the APD, which are released at later times after the excitation pulse detection.

In Figure 4.10c is shown a schematic of the electronic components used in a TCSPC card. The trigger signal form the pulsed laser and the APD detector are fed to the start and stop circuit in the photon counting card. The detector pulse triggers the constant fraction discriminator (CFD) which extract the precise timing of the detection process. The reference signal from the pulsed laser is delayed, and stops the measurement (SYNC). Between the start and stop signal, the time to amplitude converter (TAC) accumulates a voltage which is then fed into a gain amplifier (PGA) and eventually converted to a digital input stored in the memory of the photon counting card. The voltage readout will discriminate the time of arrival of a single photon from the excitation pulse. This process, repeated thousand of time per seconds, is then translated into an histogram over the time window defined by the TAC, resulting in the rise of a luminescence decay trace as shown in Figure 4.10a.

4.4.2 Photon-correlation measurements

From quantum mechanic perspective, any light pulse can be described as a sum of plane waves in which every mode is a solution of the quantum harmonic oscillator equation, with finite frequency ω and a photon state $|n\rangle$, or Fock state, which represents the exact number of photon present in the state. A $|0\rangle$ state can be seen as the vacuum state, where no photon is present. From this description it is possible to understand the differences in the photon statistic emission of different light source, and why single photon emitters are purely a trait of quantum nature.

Thermal light sources, such as common lamps, are an ensemble of independent emitters exhibiting large fluctuations in the overall emission intensity over time, following the independent nature of the ensemble emission processes. As shown in Figure 4.11a, the photon emission statistic for such systems follows a Bose-Einstein distribution, due to the bosonic nature of photons. Here, the most populated state on average is that of $|0\rangle$ photons. Even

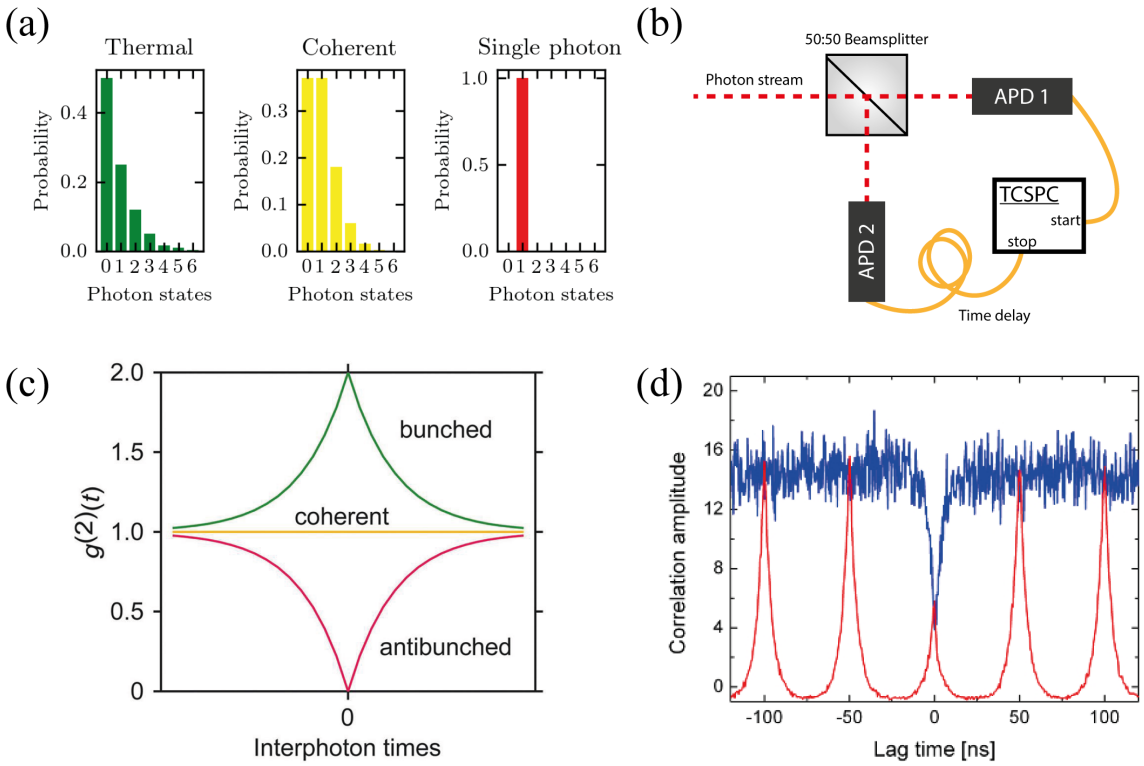

Fig. 4.11 (a) Photon emission statistic for different kind of light sources. (b) Schematic of an Hanbury-Brown-Twiss interference experiment setup. The photon stream from the light source is divided by a 50:50 beamsplitter and directed at two APD detectors connected to a TCSPC photon counting card. (c) Theoretical expectation values of the second order correlation function $g^{(2)}$ for the light sources shown in Fig.4.11a. (d) Reference example of an experimental $g^{(2)}$ value for a single photon emitters under continuous wave excitation (blue) and for 50 ns pulsed excitation (red). Adapted from Picoquant website.

in the case of coherent light, such as lasers, which exhibits reduced fluctuation in intensity, the photon emission statistics follows a Poissonian distribution, with a large probability of finding $|0\rangle$ photon states.

From these considerations, no classical system can reproduce the sub-Poissonian statistics of a single photon source, which would naturally shows a single value peaked at $|1\rangle$ photon.

A valuable parameter to determine the single photon emission from a luminescent source is the second-order correlation function, defined as:

$$g^{(2)}(\tau) = \frac{\langle E^*(t)E^*(t+\tau)E(t+\tau)E(t)\rangle}{\langle E^*(t)E(t)\rangle\langle E^*(t+\tau)E(t+\tau)\rangle} = \frac{\langle I(t)I(t+\tau)\rangle}{\langle I(t)\rangle\langle I(t+\tau)\rangle}$$

where $E(t)$ and $I(t)$ are the electric field and intensity at time t.

By realizing a Hanbury-Brown-Twiss interference setup (Fig.4.11b), it is possible to obtain a direct measurement of the second-order correlation function due to its dependence on the light intensity, which is then proportional to the detection efficiency. A light beam is directed to a 50:50 beam-splitter which splits the signal and sends it to two different photon counting modules, connected to a correlation card. The TCSPC electronics measure the time delay between coincidences events, equal to the time between simultaneous photon detection by the two APD detectors.

Following the detection at $t = 0$ by the first detector, the probability of having a detection at $t = \tau$ by the second detector is directly correlated to the nature of the light source. As shown in Figure 4.11c, if we take into account a perfectly coherent source, where the light intensity is constant for every τ, it is clear that $g^{(2)}(\tau)$ will always be 1 since $I(t) = I(t+\tau)$ for every τ . For a thermal or chaotic source, the value at zero time will always be $g^{(2)}(0) > 1$, meaning that there is a high probability that we can detect a second photons at short time from the first, as depicted in the high probability of finding multiphoton states in its statistics.

For a single photon source, instead, the detection of a second photon will always happen at longer times. Hence, the second-order correlation function at $t = 0$ must be $g^{(2)}(0) < 1$, while showing a rise in coincidences at longer times, approaching the value of 1. The light which shows this patter is called *antibunched* and is a commonly used parameter in the determination of a single photon state purity, i.e. how much the value of $g^{(2)}(0)$ is close to zero . This effect is easily understood by picturing a two level systems. When the first photon is detected, the system is now in the ground state and is not able to emit another particle of light instantaneously but have to be excited again by the next laser pulse, thus inducing a dead time between subsequent emissions. For an ideal single photon source it will always be that at zero time delay $g^{(2)}(0) = 0$.

Experimentally it is possible to determine the purity of a single photon sources by looking at the value of the correlated detection at $t = 0$, and a general indication of a single photon state is that the central dip reaches a value of 0.5. As shown in Figure 4.11d, in case of a continuous wave excitation the single photon purity is calculated from the dip of the autocorrelation function at zero time delay. For pulsed excitation, a maximum of correlation events is found at a time equal to the repetition rate of the laser. For the central peak at $t = 0$, a reduction in the relative intensity, below 0.5, is the indication of a single phonon state.

4.4.3 Streak camera

A streak camera offers the possibility of measuring ultra-fast phenomena with picosecond time scales and simultaneously imaging the space and time coordinate of the signal in a two dimensional plane.

The basic principle of operation of a streak camera is shown in Figure 4.12a. The light beams arriving on the horizontal silts of the camera are projected onto a photo-cathode, which converts the photons in a number of electrons proportional to the light intensity. The electrons are then accelerated and sent between two parallel charged electrode plates. A high voltage sweep potential, synchronized with the excitation trigger pulse, is applied to the electrode plates deviating the electron at slightly different angles based on the time of arrival between the plates. With this approach, the electrons (photons) arriving between the sweep electrodes are deflected in the vertical direction with larger angles for those arriving at later times. The deflected electrons are sent to a MCP (micro-channel plate) which multiplies the signal and projects it on a phosphor screen where the streak camera image is formed.

In this work we used a Hamamatsu streak camera detector and excited the sample at 711 nm with a Ti:Sapphire femtosecond pulsed laser (Coherent Mira, $\approx$ 200 fs pulse width at 76 MHz). A schematic of the optical setup used is shown in Figure 4.12b. The excitation laser is filtered with two short pass filters in the excitation path and two longpass filters in the collection path before reaching the streak camera slit. The sample PL signal is also directed in a spectrometer for alignment. The polarization angle of the excitation source is controlled with a half-wave plate before reaching the 50:50 beamsplitter. An infinity corrected objective (Mitutoyo 100x NA=0.7) focuses the light on the sample which is held in a cryostat under high-vacuum. Figure 4.12c shows the image trace acquired on the streak camera sensor for a free space collection. Here, the decay trace can be extracted by integrating the long tail present in the signal image.

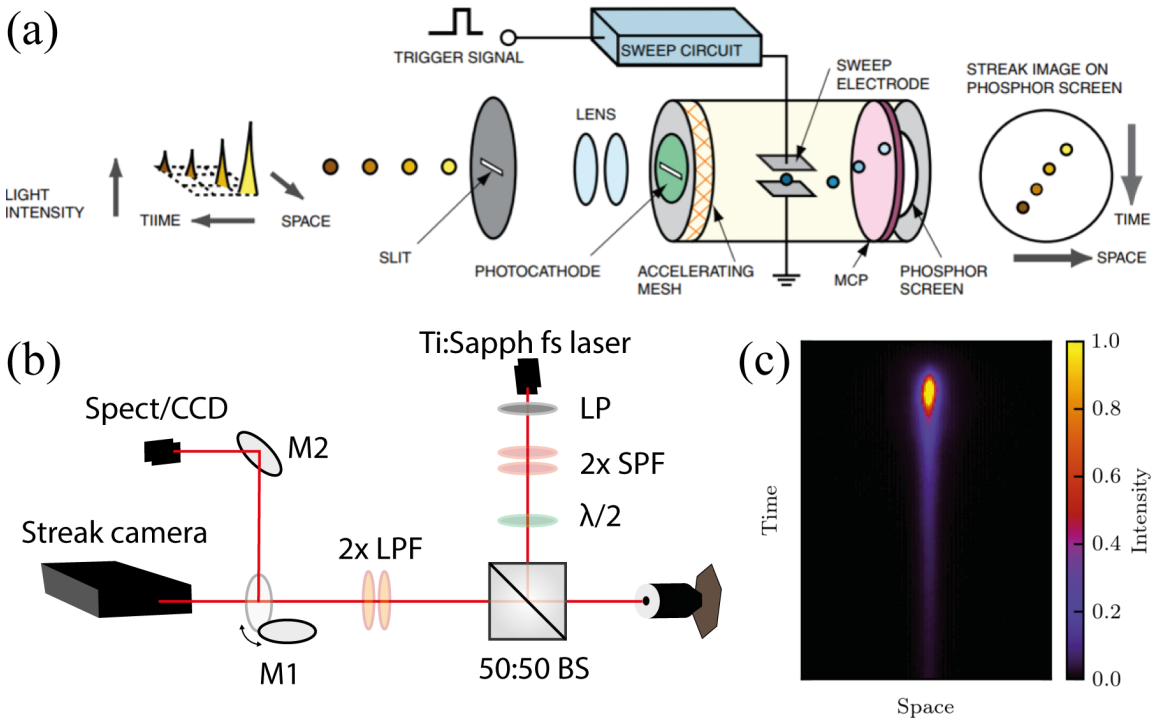

Fig. 4.12 (a) Operating principle of a streak camera. The signal is sent to an horizontal grating and accelerated. A sweep circuit with two charged plates deviated the electrons towards a phosphor screen that records the time and space information of the relative signal. (b) Schematics of the optical setup used in this work. (c) Image of the recorded signal trace on the streak camera sensor.

Chapter 5

Enhanced light-matter interaction in 2D-WSe_2 coupled with dielectric nano-antennas

5.1 Motivation

Unique structural and optical properties of two-dimensional semiconductors enable in principle their efficient coupling to photonic cavities having the optical mode volume below the diffraction limit. This has been demonstrated by coupling TMDs with plasmonic nanostructures, which exhibit strong energy dissipation limiting their potential applications in devices. An alternative approach for realisation of nano-cavities is employing high refractive index dielectrics, attractive owing to negligible non-radiative losses

In this chapter, we realize low-loss high-index gallium phosphide (GaP) dimer nano-antennas with sub-wavelength volumes coupled to mono- and bilayer TMD WSe_2. We observe a photoluminescence (PL) enhancement exceeding 10^4 compared with WSe_2 placed on planar GaP, and trace its origin to a combination of enhancement of the spontaneous emission rate, favourable modification of the PL directionality and enhanced optical excitation efficiency, all occurring as a result of WSe_2 coupling with strongly confined photonic modes of the nano-antennas. Further effect of the coupling is observed in the PL polarization dependence and in the Raman scattering signal enhancement exceeding 10^3.

These findings reveal dielectric nano-antennas as a promising platform for engineering light-matter coupling in two-dimensional semiconductors.

5.2 Introduction

Monolayer semiconducting TMDs such as WSe_2 exhibit bright excitonic luminescence and strong absorption at room temperature with potential for photonic applications [67, 112]. An important property favouring integration in devices is their compatibility with a wide range of substrates. So far, photonic device demonstrations include monolayer TMDs coupled to nano-cavities in photonic crystals [222, 223], nanobeam waveguides [224] and to microdisk cavities [225]. TMD monolayers and van der Waals heterostructures [5] comprised of vertically stacked atomic layers of TMDs, hexagonal boron nitride and graphene have been integrated in Fabry-Pèrot microcavities [226, 227]. These devices provide photonic modes with relatively high quality factors, Q, in the range of 100s to 1000s. Despite the coupling to TMD monolayers via the relatively weak evanescent field, lasing in hybrid TMD-dielectric cavities has been observed [222, 224, 225]. Moreover, the strong light-matter interaction regime has been realized in optical microcavities [226, 227] and photonic crystals [223], where atomic layers of 2D TMDs were placed at the anti-node of the photonic mode.

Most of these devices relied on confining electromagnetic fields in diffraction-limited volumes, $V_{eff} \gtrsim (\lambda/n)^3$, in order to increase the spontaneous emission rate by the Purcell enhancement factor F_p, which scales as Q/V_{eff}. Whereas the high Q has been readily realized, V_{eff} provided by these structures is relatively large, leading to modest values of F_p. Most of these devices also show a reduction of the light intensity compared with bare TMD monolayers, explained by the presence of fast non-radiative processes in the currently available TMDs, where the quantum yield is typically below 0.1% [210].

The effective volume of the optical mode can be reduced below the diffraction limit in plasmonic meta-materials and nano-cavities [31]. Such structures have been extensively researched for confining and guiding light on the nano-scale, shaping incoming radiation in a fraction of a wavelength, and modifying optical properties of nanoscale light emitters [209]. By coupling TMDs to plasmonic structures, large PL enhancements [228], strong light-matter coupling [177], brightening of the dark excitonic states [99], and modification of optical properties of quantum emitters in WSe_2 [146] have been achieved. However, high optical losses due to the absorption in the metal remain the main obstacle for further development of hybrid TMD-plasmonic devices [186, 229]. Special care had to be taken to overcome optical losses in metallic plasmonic structures by introducing a few nm dielectric spacer separating the TMD layer [230]. This turns out to be particularly important to suppress quenching for quantum light emitters [146, 231].

Recently, it has been shown that high-refractive-index dielectric nano-antenna can provide confined optical modes with strongly reduced mode volumes [32]. The main advantages of such structures are low non-radiative losses induced in the coupled light emitting material [186, 194, 188]. Furthermore, it has been shown that such nano-antennas can be designed in principle to provide Purcell values of thousands [197]. Despite the low $Q < 10$ in the currently realised antennas, coupling to such confined modes still results in high Purcell enhancement factors, as was recently shown experimentally for dye molecules coupled to GaP high-refractive-index ($n > 3$) nano-antennas [194], similar to those used in our study (Fig.5.1a). These observation relied on the low losses in such nano-antennas allowing emitters to be placed in their close proximity and experience strong electric fields of the sub-wavelength-confined modes. In contrast, plasmonic structures requires a spacer separating the emitters in order to prevent quenching [31]. Moreover, dielectric nano-antennas can surpass plasmonic structures for light-emitting application providing minimal losses, especially important for quantum applications, together with the absence of free or hot electrons and being often CMOS compatible. On the other hand, modified directionality of PL was shown for monolayer MoS_2 coupled to a Si nanowire [232]. Si nano-particles coupled to WS_2 were explored for the realization of strong coupling [233]. Finally, multilayer TMDs themselves were used to fabricate high-index nanodisks, whose resonant response could be tuned over the visible and near-infrared ranges [234].

Here, we report large enhancements of the PL and Raman scattering intensity in mono- (1L) and bilayer (2L) WSe_2 placed on top of cylindrical GaP nano-antennas (Fig.5.1a), compared with WSe_2 on the planar GaP. Upon illumination, the nano-antennas scatter radiation which is strongly confined around the pillar edges. This confinement effect is observed in a broad spectral range, overlapping with the optical response of both mono- and bi-layer WSe_2. Our approach exploits the extreme ability of the atomically thin layers of TMDs to stretch and conform with the nano-structured surfaces and therefore favourably align themselves with the confined optical mode (Fig.5.1b-d). Our interpretation of the observed PL enhancement shows that it arises from a combination of the Purcell enhancement, efficient redirection of the emitted PL in the space above the substrate, and larger absorption of light in the 2D layer related to the enhancement of the optical field in the confined mode. Similarly to experiment, our model shows increase of the PL enhancement as the pillar radius reduces. Supporting our interpretation, time-resolved measurements show the shortening of the PL life-time consistent with a spontaneous emission decay enhancement. We further confirm the photonic effect of the nano-antennas by demonstrating linearly polarized PL and enhanced Raman scattering in the coupled WSe_2. Our findings show an effective approach to

engineering light-matter coupling at the nanoscale, by exploiting the low-loss optical modes of the dielectric nano-antennas together with the unique mechanical and optical properties of 2D semiconductors. This work opens the way for utilization of 2D semiconductors as a novel active medium in the emerging field of photonic meta-surfaces [201].

5.3 Results and discussion

The calculated spatial distribution of the electric field around the cylindrical double-pillar GaP nano-antennas (Fig.5.1a, referred to as 'dimers') is shown in Figures 5.1b and c. Light

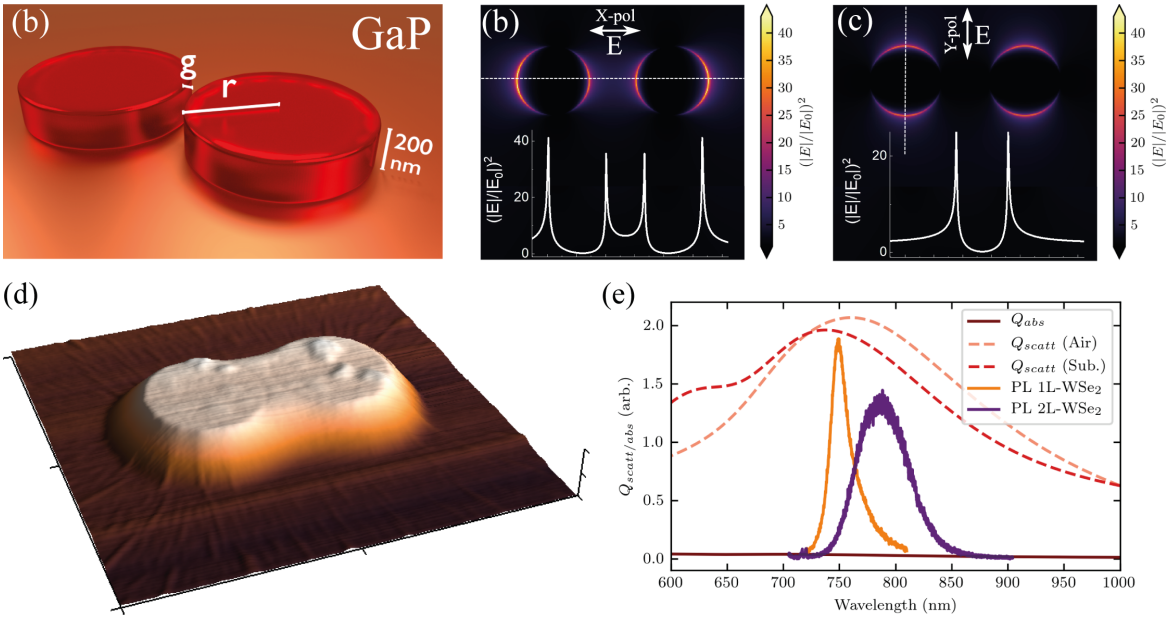

Fig. 5.1 (a) Schematic view of a GaP dimer nano-antenna with a height h = 200 nm, gap width g and pillar radius r. (b,c) Calculated relative intensity $(|E|/|E_0|)^2$ of the light scattered by a GaP dimer (r = 50 nm, h = 200 nm, g = 65 nm). E (E_0) is the electric field amplitude of the scattered light by (normally incident on) a GaP dimer. The polarization of the normally incident wave is shown with arrows and is either along X (b) or Y (c) axes. $(|E|/|E_0|)^2$ is calculated at the height of 200 nm, corresponding to the top surface of the dimer. The inset shows the variation of $(|E|/|E_0|)^2$ along the horizontal and vertical dotted lines. (d) Atomic force microscopy (AFM) image of a GaP nano-antenna (r = 500 nm) covered with a monolayer WSe_2. (e) Simulated scattering (Q_{scatt}) and absorption (Q_{abs}) efficiency integrated over numerical aperture NA=0.9 for a GaP nano-antenna (g = 35 nm, r = 100 nm) illuminated with a plane wave. Pink (red) dashed line Q_{scatt} for light scattered upwards in air (downwards into the substrate). Room temperature PL spectra are shown for 1L-WSe_2 (orange) and 2L-WSe_2 (purple).

at a pumping wavelength of 685 nm polarized linearly along (X) and perpendicular (Y) to the line connecting the centres of the pillars is used. $(|E|/|E_0|)^2$ is shown for the plane containing the surface of the dimer, i.e. 200 nm above the planar substrate. Here E and E_0 are the electric field amplitudes of the wave scattered by the pillars and the normally incident wave, respectively. The two-dimensional distribution in the plane is shown as a colour-map. In the small volume within the dimer gap an enhancement is only observed for the X-polarization [194, 187]. The graphs shown with white lines present the variation of $(|E|/|E_0|)^2$ along the horizontal and vertical dotted lines, revealing strong maxima at the edges of the pillars. For the X-polarization, at this height of 200 nm, these maxima are stronger than the $(|E|/|E_0|)^2$ values in the gap. They are also stronger than the enhancement values at the pillar edges in the Y -polarization. In Appendix A.4 we provide the profiles for both magnetic and electric fields at an height of 100 nm, i.e. the antenna half height. While the magnetic field is contained inside the pillars, the electric field is instead confined at their surface and strongly enhanced inside the gap region.

Atomic force microscopy (AFM, Fig.5.1d) shows that the transferred atomically thin layer of WSe_2 closely follows the shape of the dimer, thus strongly overlapping with the volume of the confined optical mode.

As shown in Figure 5.1e the spectral response of the nano-antenna is very broad, extending well into the visible and near-infrared ranges, and fully overlapping with the PL profiles of both 1L and 2L-WSe_2. In Appendix A.1 we provide the scattering resonances, under the two different orientations of the excitation source, and for nano-antennas with different radius.

5.3.1 Photoluminescence imaging

Figure 5.2a shows a PL image of 1L and 2L samples deposited on an array of GaP nano-antennas and measured using an optical microscope. The image is recorded with a short-pass filter in the unpolarized white light path illuminating the sample, and a long-pass filter in the imaging path using the technique described previously in Section 4.1.2.

Bright PL replicating the shape of the dimers is visible for both 1L (yellow) and 2L (purple), whereas the PL from WSe_2 on planar GaP is very weak (dark areas around the pillars). A comparison of the intensities in the PL and dark field microscopy images is shown in Figure 5.2b, where the intensities are measured along the dotted line shown for one of the nano-antennas in Figure 5.2a. The PL enhancement is observed most strongly around the edges and in the gap of the nano-antenna, where, as seen in the dark field profile, most of the light is scattered by the pillars.

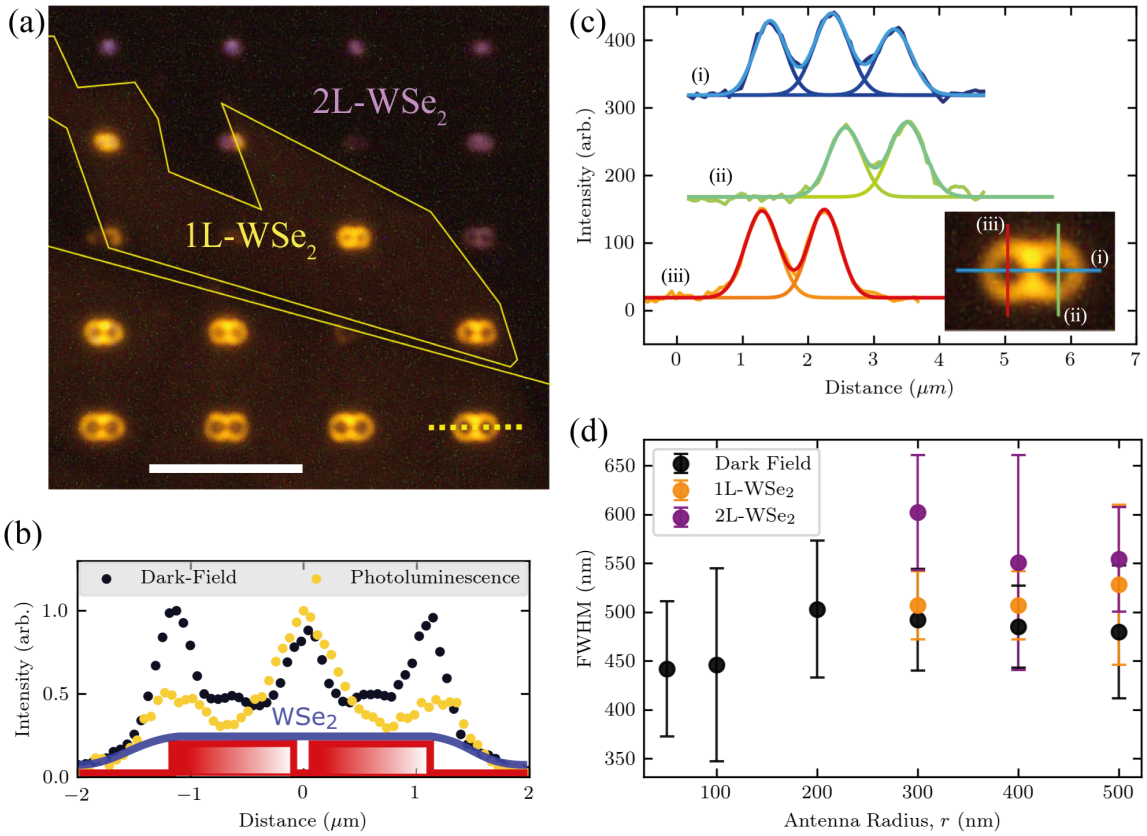

Fig. 5.2 (a) Optical microscope image showing PL from a GaP dimer nano-antennas array covered with 1L- and 2L-WSe_2 illuminated with unpolarized, broad white light excitation. Scale bar is 10 μm. The yellow lines show the boundaries between 1L- and 2L-WSe_2. PL from 1L (2L) sample shows as false yellow (purple) colour in the image. (b) Intensity profiles extracted from a dark-field (black) and PL (yellow) microscope images for a dimer with r=500 nm. Both profiles are measured along the dashed line in Fig.4.2a. The intensity profiles are overlaid with the schematic of a dimer. (c) PL imaging profiles for a single GaP dimer nano-antenna covered with 1L-WSe_2. The PL is highly localized at the nano-antenna edges, showing full-width half maximum (FWHM) values close to the optical microscope resolution. (d) FWHM of the PL and dark-field (DF) profiles for different radii nano antennas, extracted as in Fig.c. Contrary to DF imaging, for nano-antennas with $r < 300$ nm it is no longer possible to clearly resolve distinct peaks in the respective PL profile.

Further comparison of the PL profile is shown in Figures 5.2c-d. Here it is possible to observe that the linewidth of the PL profiles closely resembles that of the experimental resolution of the optical microscope (≈400-450 nm). We then compare the PL signal spatial extent to that of the scattering response observed under dark-field imaging (Fig.5.2d). We found that while it is still possible to extract the scattering peaks for small nano-antennas in dark-field imaging, the PL peaks are no longer resolved when moving to antennas with

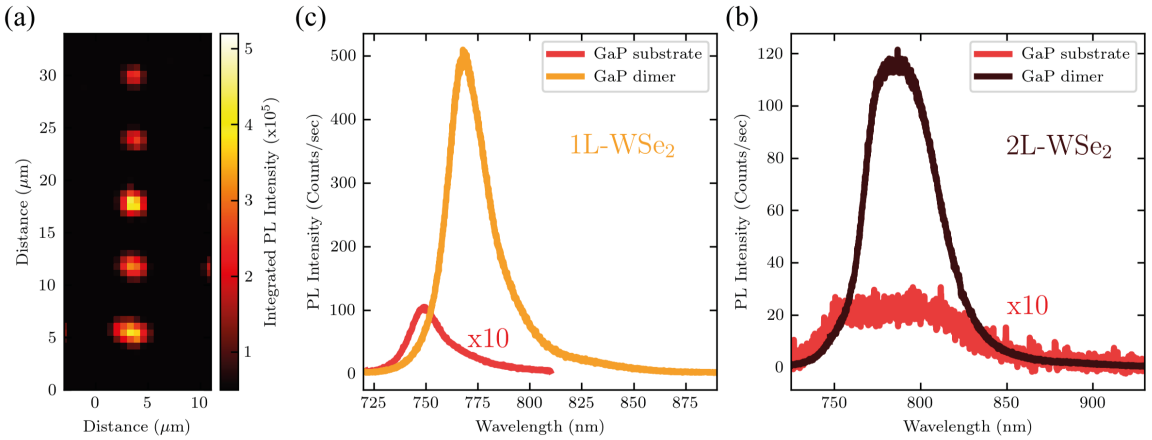

Fig. 5.3 (a) Sub-micron resolution PL map of a row of GaP dimer nano-antennas covered with 1L-WSe_2, with radius from 500 nm to 100 nm (bottom to top). (b,c) PL spectra for 1L-WSe_2 (orange) and 2L-WSe_2 (black) placed on top of GaP nano-antennas with r = 300 nm and 100 nm, respectively. Spectra in red are measured on 1L- (a) and 2L-WSe_2 (b) placed on the planar GaP. Their intensity is multiplied by 10.

radius below 300 nm. The less defined PL profile can be ascribed to the mobility of 2D WSe_2 excitons and their diffusion along the antenna, leading to a broader and less defined linewidth at small distances.

5.3.2 Photoluminescence enhancement

We have additionally carried out detailed room temperature PL measurements in a micro-PL setup (described in Section 4.3.1) for both 1L and 2L-WSe_2 placed on GaP nano-antennas. We use a laser with wavelength λ =685 nm, which is below the GaP absorption edge and is absorbed only in the WSe_2 layer. Figure 5.3a shows a sub-micron resolution PL map for a row of nano-antennas covered with 1L-WSe_2, with radius from 500 to 100 nm (from bottom to top). A strong PL intensity is found at the antenna location but, contrary to Figure 4.2a, here the resolution is limited by the laser spot size ($r \approx 1\mu$m). In Figures 5.3b and c are shown the PL spectra for 1L and 2L-WSe_2 coupled to GaP nano-antennas with r =300 nm and 100 nm, respectively, and compare them with PL from the 2D layers placed on the planar GaP. Strong enhancement of PL intensity exceeding 50 times for WSe_2 placed on nano-antennas is observed. Lower PL intensity for 2L-WSe_2 is a consequence of its indirect bandgap, in contrast to the 1L-WSe_2 having a direct band-gap. The effect of strain present in WSe_2 placed on the nano-pillar is evident in the PL redshift for 1L and in the spectral modification for 2L samples.

5.3.3 Experimental enhancement factor

We compare the observed PL intensity for WSe_2 coupled to the nano-antennas (I_{on}) to that of the uncoupled WSe_2 on planar GaP (I_{off}) by introducing the PL enhancement factor [176, 228, 190, 209], $\langle EF \rangle$, defined as:

$$\langle EF \rangle = \frac{I_{on}}{A_{dimer}} \left(\frac{I_{off}}{A_{laser}} \right)^{-1} \qquad (5.1)$$

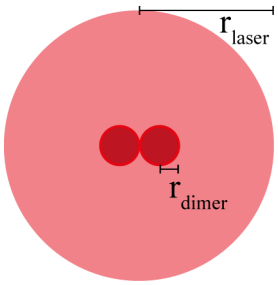

Here we take into account the significant difference between the PL collection area $A_{laser} = \pi r_{laser}^2$, defined by the excitation laser spot of 3.5 μm diameter, and the geometrical area for a given dimer, $A_{dimer} = 2 \times \pi r_{dimer}^2$. We expect that A_{dimer} is larger than the actual area from where the enhanced PL is collected (effectively edges of the pillars and dimer gap), and than the effective interaction area (A_{eff}), defined as the area at the top surface of the pillars that participate in the excitation enhancement (see Appendix A.2 for more details). Thus, $\langle EF \rangle$ calculated in this way is expected to be a lower bound estimate of the observed effect.

Figure 5.4a shows the $\langle EF \rangle$ values extracted from the experimental data for different nano-antennas. $\langle EF \rangle$ for 1L-WSe_2 exhibits an increase from 10^2 for the large $r = 500$ nm pillars to nearly 10^4 for $r = 50$ nm, whereas the variation is more significant for the 2L samples, where $\langle EF \rangle$ changes from ≈ 30 to $4 \cdot 10^4$. Such large $\langle EF \rangle$ values are comparable with the highest reported in plasmonic/TMDs systems [228].

As we show below, the observed enhancement is the consequence of the interaction of WSe_2 with the optical mode of the nano-antenna. The extremely efficient overlap between the 2D layers and the optical mode field maxima are important for enhancing the interaction with the nano-antennas. Figure 5.4a shows that there is a variation of $\langle EF \rangle$ between the antennas of the same size. There are several factors that can cause this. (i) Non-uniformity of the coupling between WSe_2 and the nano-antennas, caused by a variety of factors such as local contamination from the polymer used for the WSe_2 transfer, local deformation of WSe_2, local presence of water, etc. (ii) Non-uniformity of the structural properties of the nano-antennas. For example, the size of the gap may vary. The quality of etching may also vary, for example producing side-walls of the pillars, which are not perfectly vertical etc.

A smaller value of $\langle EF \rangle$ for the 2L sample for the nano-antennas with the large radii is probably due to its higher rigidity compared with 1L. As the radius becomes smaller the 2L conforms more closely with the shape of the nano-antenna, and in addition the increased strain in the crystal may lead to the indirect to direct bandgap crossover [125], yielding larger values of $\langle EF \rangle$.

In order to compare the results with our model, we introduce an effective enhancement factor $\langle EF \rangle_{eff}$ defined as the product of three factors, as described in section 5.3.3:

$$\langle EF \rangle_{eff} \propto \frac{\gamma_{exc}(\lambda_{exc})}{\gamma^0_{exc}(\lambda_{exc})} \cdot \frac{q(\lambda_{em})}{q^0(\lambda_{em})} \cdot \frac{\eta(\lambda_{em})}{\eta^0(\lambda_{em})} \tag{5.2}$$

Here $\gamma_{exc}/\gamma^0_{exc}$ is the ratio of the excitation rates at a wavelength λ_{exc}, for an emitter coupled to the antenna (γ_{exc}) and placed on the planar substrate (γ^0_{exc}). $\gamma_{exc} \propto (|E|/|E_0|)^2$, for which the spatial distribution is shown in Figures 5.1b-c. Their ratio would account for the enhancement of the incident radiation leading to stronger light absorption in WSe_2. We find that an additional increase in the $\gamma_{exc}/\gamma^0_{exc}$ ratio arises due to the reduction of the γ_0 for a dipole placed 0.5 nm above the planar GaP substrate, compared to the value in free-space. The dependence of this ratio on the pillar radius r is shown in Figure 5.4c for an electric dipole placed 0.5 nm above the top surface of the pillars (see more details on the numerical calculations in Appendix I). The dipole is placed at the edge of one of the pillars just outside the gap between the two pillars. As shown in the inset in Figure 5.4d and in Appendix A.5, this is the position where the coupling to the optical mode of the dimer is maximized. The data in Figures 5.4b-e, showing the individual contributions of the different terms to the overall enhancement in Eq.5.2, are calculated for this position of the dipole.

The second term describes the enhancement of the quantum yield (q/q_0) for an emitter at a wavelength λ_{em}. This is achieved through the enhanced rate of spontaneous emission [190] described by the Purcell factor $F_p = \gamma_r/\gamma^0_r$, where γ_r and γ^0_r are the rates of spontaneous emission for the emitter coupled to the antenna and placed on the planar GaP, respectively. In our model we consider the limit of a low quantum yield for the emitter, i.e. the non-radiative decay $\gamma_{nr} \gg F_p\gamma_r$, which leads to $q/q_0 = F_p(\gamma_r + \gamma_{nr})/(F_p\gamma_r + \gamma_{nr}) \approx F_p$. The dependence on r for this term is shown in Figure 5.4d.

The third term η/η^0 describes the improved collection efficiency for WSe_2 PL on top of the nano-antennas (η) compared to planar GaP (η_0), as the emitted radiation is coupled to our detector using collection through numerical aperture NA=0.7 (see Appendix A.3). The dependence on r of η/η^0 is shown in Figure 5.4e.

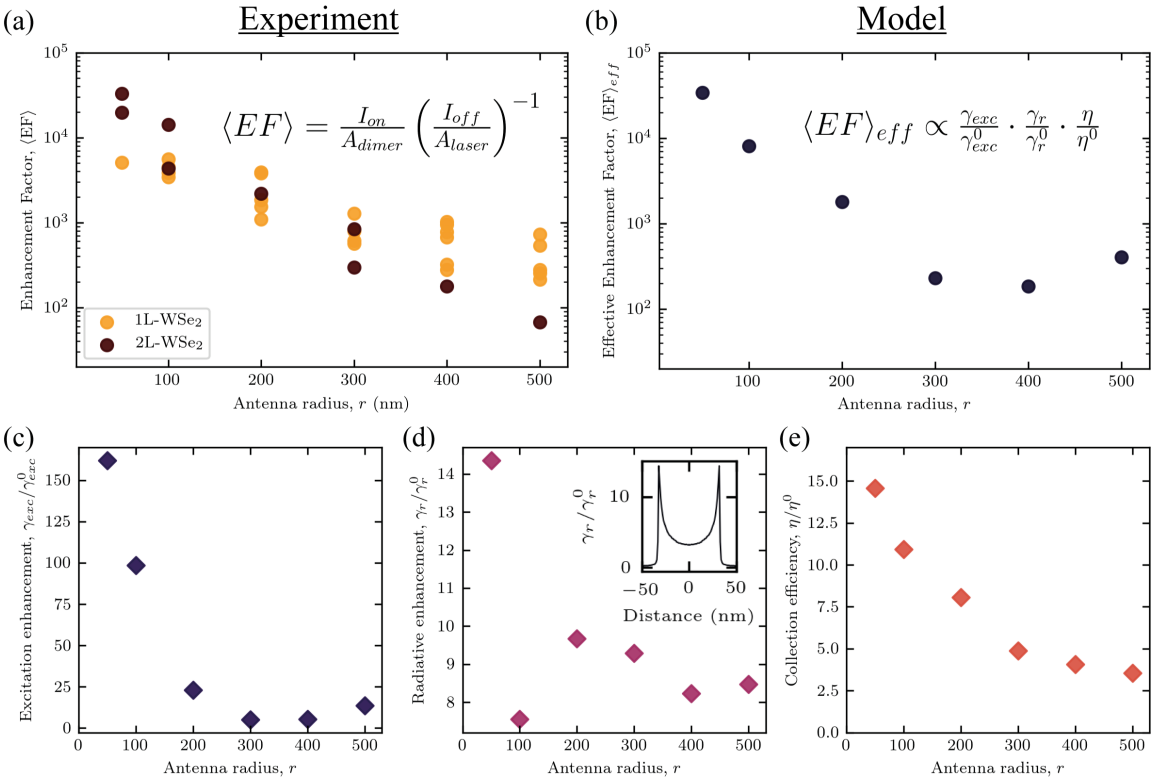

Fig. 5.4 (a) Experimental PL enhancement factor, $\langle EF \rangle$, as a function of the antenna radius, for 1L-(orange) and 2L-WSe_2 (black). (b) Dependence on r of the calculated effective enhancement factor, $\langle EF \rangle_{eff}$, defined as the product of the parameters in (c), (d) and (e) (see Eq.5.2 and the formula on the graph). (c-e) Results of simulations showing various parameters determining the observed PL enhancement in a dimer as a function of the pillar radius (see Appendix 1 for further details). The values shown in the figures correspond to the behaviour of an oscillating electric dipole placed at the edge of the gap between the two pillars, 0.5 nm above the top of the pillar, and aligned along the line connecting the centres of the pillars [see inset in (d)]. (c) Enhancement of the excitation, $\gamma_{exc}/\gamma^0_{exc}$, dependent on the electric field intensity at the antenna surface and on planar GaP substrate, $(|E|/|E_{GaP}|)^2$. (d) Enhancement of the radiative recombination rate, γ_r/γ^0_r. Inset shows variation of this ratio as a function of the dipole position above the dimer gap. (e) Enhancement of the light collection efficiency, η/η^0. The values plotted in (b)-(e) are calculated for the dipole placed at the position where γ_r/γ^0_r reaches the maximum.

Figure 5.4b shows the calculated values of the effective enhancement factor $\langle EF \rangle_{eff}$ taking into account the above three mechanisms [209, 190]. The dependences of $\langle EF \rangle_{eff}$ and $\langle EF \rangle$ are in a good qualitative agreement, suggesting that our model captures the main contributing factors.

5.3.4 Polarization dependent luminescence

We find further evidence for the sensitivity of the WSe_2 coupling to the optical mode of the dimer in polarization resolved PL measurements.

The spatial asymmetry of the dimer nano-antenna and the enhanced field in the gap between the two pillars is expected to lead to a polarization-dependent response [187, 194], as predicted by the electromagnetic field profiles under different polarization orientation of the exciting source (Fig.5.1b-c). Such behaviour is found in PL of WSe_2 coupled to nano-antennas, as shown in Figure 5.5. Figure 5.5a shows the case for a nano-antenna with $r = 400$ nm and a gap $g = 65$ nm. It is observed that the integrated PL signal is 20% stronger when excited with an X-polarized excitation compared to the Y-polarized (X and Y are selected as in Figure 5.1b-c). A similar modulation is observed in dimers with other values of r (Fig.5.5b).

The origin of this behaviour is further revealed when considering touching pillars with no gap. The image in Figure 5.5c shows the dark-field microscope images of dimers without (top) and with (bottom) a lithographically defined gap. The graphs in Figure 5.5c show the extracted scattering intensities along the line connecting the centres of the pillars, revealing the absence (left) or the presence (right) of the gap. Figure 5.5d shows the integrated PL intensity for WSe_2 coupled to such dimers measured in our micro-PL set-up. In the dimer with a gap, the PL is modulated by 20% when varying the polarization of excitation, exhibiting higher intensity for X-polarized laser, which is due to the excitation of the optical mode in the gap between the pillars. A negligible polarization dependence is observed in the dimer with no defined gap, emphasizing nearly equal coupling of WSe_2 to the X- and Y-polarized optical modes.

5.3.5 Radiative decay enhancement

The theoretical interpretation in Figure 5.4 demonstrates that partly the PL enhancement originates from the enhanced radiative decay rate in WSe_2. We have been able to demonstrate this experimentally by measuring PL dynamics in WSe_2.

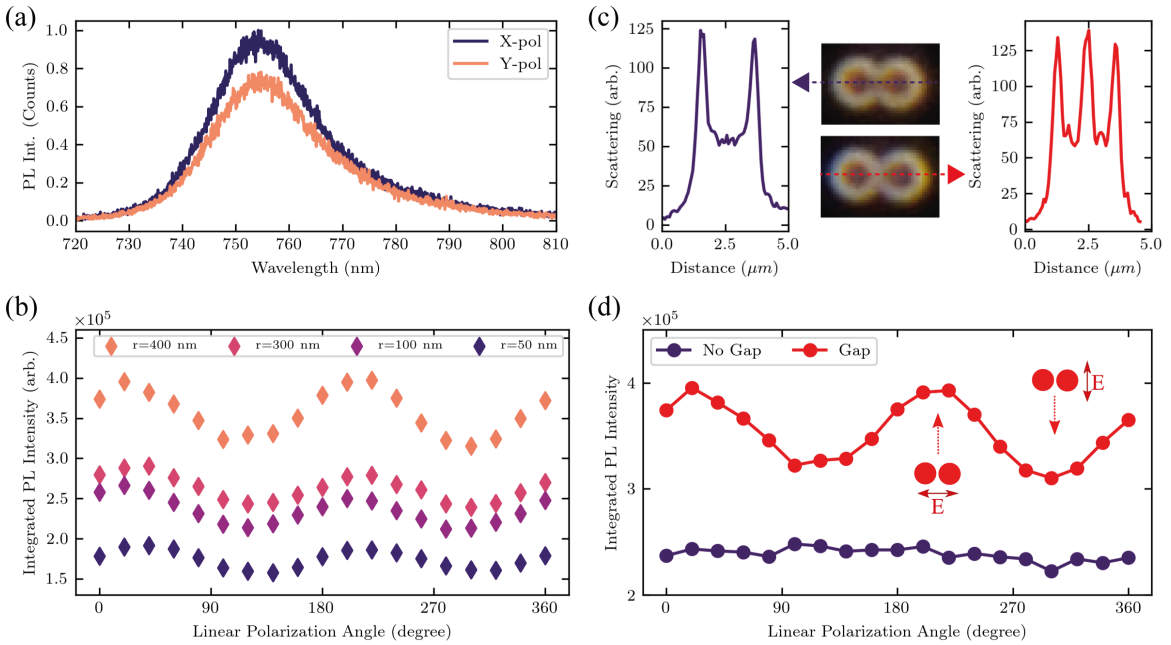

Fig. 5.5 (a) Photoluminescence spectra for 1L-WSe_2 on a GaP nano-antenna (g = 65 nm, r = 400 nm), for a laser excitation linearly polarized along X- and Y-axes of the dimer. (b) WSe_2 Integrated PL intensity as a function of the angle of the linear polarization of the excitation laser for nano-antennas of different radii and the same gap width of g = 65 nm. (c) Dark-field microscopy images and related scattered light intensity profiles for two GaP nano-antennas (r = 400 nm) covered with 1L-WSe_2. The scattered light intensity profiles are taken along the long axes of the dimer as shown by the dotted lines. The top (bottom) images and left (right) graphs correspond to the dimers without (with) a gap. (d) Comparison of 1L-WSe_2 PL intensity as a function of the orientation of the linearly polarized excitation for the nano-antennas in Figure 5.5c. Red (purple) shows the dependence for the dimer with (without) a gap.

Figure 5.6 shows the PL decay for a 1L-WSe_2 placed on the planar GaP (purple) compared to the emission when it is coupled to a nano-antenna with $r = 200$ nm (orange). The curves are measured using a TCSPC setup (described in Section 4.4) with a 90 ps pulsed laser excitation at 638 nm and 80 MHz repetition rate, and detection with an avalanche photodiode detector. The corresponding instrument response function (IRF) is shown in Figure 5.6 as a grey shaded area. For these measurements, we used a low excitation density (0.2 W/cm^2) to avoid non-radiative exciton-exciton annihilation, resulting in faster PL decays [105, 67]. For low pumping powers, single exponential decay is usually observed, reflecting the radiative recombination dynamics of the thermalised exciton population and the lack of exciton-exciton annihilation effects [103, 235].

Such behaviour is observed in Figure 5.6 for the 1L-WSe_2 on the planar GaP, which shows a single-exponential PL decay with a lifetime of $\tau_{GaP} \approx 1.3$ ns. Here, the measured PL decay is comparable to the expected radiative lifetime predicted theoretically [104], in the order of few nanoseconds, and confirmed in luminescence lifetimes experiments [105] in case of small non radiative decays for monolayer WSe_2. The estimate of WSe_2 lifetimes of 4 ns, presented in Ref.[104], is comparable to the one found in our experiments. Thus, the radiative decay shown in Figure 5.6 for the WSe_2 on planar GaP substrate provides an upper limit for the exciton non radiative channels, yielding longer decay times, in the order of few nanoseconds, and with a single exponential decay profile, all as a results of the negligible extrinsic non-radiative processes present at ultralow excitation.

The PL decay measured for WSe_2 coupled to a dimer is dominated by a fast component with a lifetime $\tau_{dimer} \approx 0.2$ ns. This is very similar to the fast component in the instrument response function (IRF) of $\tau_{IRF} \approx 0.16$ ns. We thus conclude that the measured $\tau_{dimer} \approx 0.2$ ns is a resolution-limited value. We interpret the shortening of the PL lifetime as a consequence of the Purcell enhancement of the radiative rate. A conservative lower-bound estimate

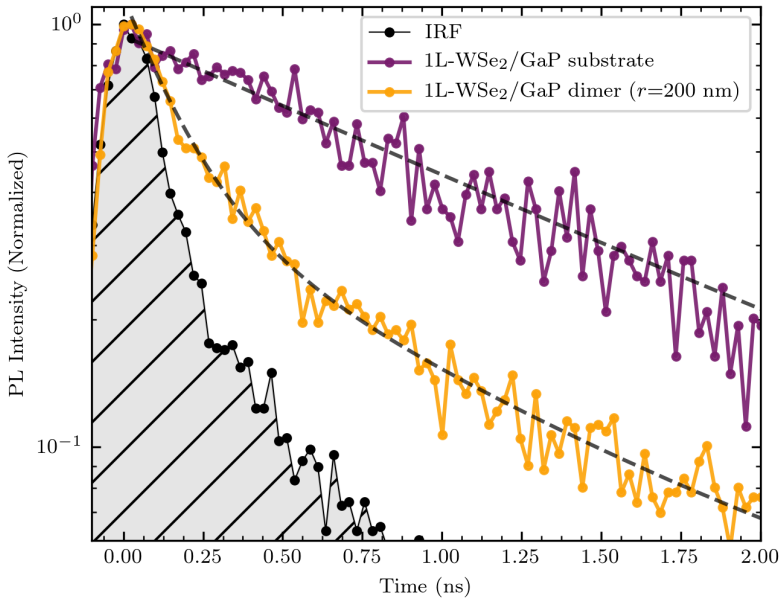

Fig. 5.6 PL decay traces for a WSe_2 monolayer placed on a planar GaP substrate (purple) and coupled to a nano-antenna with $r = 200$ nm (yellow). Grey shows the instrument response function (IRF). The PL signal is measured with a 90 ps pulsed laser, under low excitation power of 0.2 W/cm^2, to avoid exciton-exciton annihilation processes. Resolution-limited dynamics are measured for WSe_2 coupled to a dimer. Dashed black lines show results of the fitting with mono- and bi- exponential decay functions.

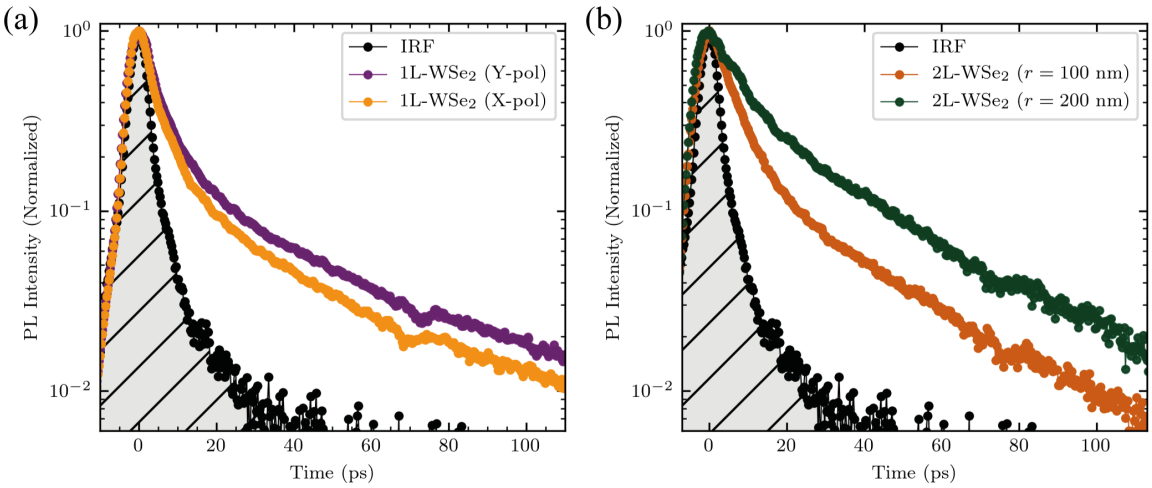

Fig. 5.7 (a) Dependence of 1L-WSe_2 lifetime coupled to a GaP nano-antenna ($g = 65$ nm, $r = 500$ nm) for X- and Y-polarization excitation geometries. (b) 2L-WSe_2 photoluminescence lifetime dependence on the nano-antenna size (collected under X-polarized excitation). For smaller antenna ($r = 100$ nm) a reduction in the fast component is consistent with an increased electric field intensity at the nano-antenna surface, leading to stronger bi-exponential character in the PL decay profile.

of the Purcell enhancement factor is therefore ≈6. This is in a good agreement with the theoretical predictions, for which we should take into account the spatial variation of the Purcell enhancement in the WSe_2 coupled to the mode.

In order to improve the temporal resolution (down to 2.4 ps in our case), we probed the photoluminescence decay with the use of a streak camera setup and a 200 fs pulsed laser (see Section 4.4 for a full description of the technique and setup used). Figure 5.7 shows a ultrafast bi-exponential PL decay for 1L and 2L-WSe_2 coupled to the GaP nano-antenna measured in this way. Both curves in Figure 5.7 show a double-exponential decay, caused by the fast exciton-exciton annihilation processes due to the high power density used in the measurement (see the discussion given in Section 2.3.3). In order to achieve a satisfactory signal-to-noise ratio, we had to use a high excitation laser power density corresponding to an average power of 3.4×10^3 W/cm^2, introducing non-linearities in the response of the excitonic population. Due to the low signal intensity of the WSe_2 on planar GaP we cannot extract an estimate of the Purcell factor measured this way. However, these results obtained at room temperature further confirms that a radiative decay enhancement results from the coupling with the optical modes at the nano-antenna surface, and cannot be ascribed to the enhanced non linearities in the 2D exciton population.

To further confirm that the antenna near-field enhancement impacts on the TMD luminescence properties we collected the PL decays for different excitation polarization angles, shown in Figure 5.7a. The geometry of a dimer nano-antenna can be used to shrink light to small volumes, as in the small gap between the two nano-pillars. By exciting the antenna with a polarization aligned to the dimer axis (X-pol) it is possible to obtain an increase in the scattered *E* field intensity when compared to exciting the antenna with polarization angle perpendicular to the dimer axis (Y-pol), as seen in Figure 5.1b-c. Figure 5.7a shows the decays extracted from 1L-WSe_2 coupled to a 500 nm radii antenna for the two different polarization geometries. The PL decays show a reduction of the PL lifetime when changing the polarization angle of the excitation pump, as expected from an increased spontaneous emission decay when in X-polarized geometry [187]. In this case we observed an limited values for the fast component in the order of 1 ps, while for the long component of the decay we could extract lifetimes in the order of 20-30 ps.

We probed also the dependence of the radiative lifetimes as a function of the nano-antenna size by collecting the PL decay from 2L-WSe_2 coupled to antennas with radius of 100 nm and 200 nm, shown in Figure 5.7b. An increment of the fast component of the decay trace when on smaller nano-antennas (from 8.4 ps to 6.5 ps) is consistent with an enhanced excitation rate and increased non-linear exciton dynamics in 2D-WSe_2. The long component of the decay shows lifetimes in the order of 40 ps.

From the reduction of the room temperature lifetimes of WSe_2 excitons, we give an interpretation of the faster decay as a consequence of the the strongly localized field at the nano-antenna surface. The effect of the confined electric field, on scale on the order of tens of nanometres, results in a more efficient excitation of the higher momentum dark excitons, together with localized exciton states, leading to the overall reduction of the room temperature lifetimes to sub-ns decays. This can be described as a spread of the light cone in the momentum space, leading to a more efficient excitation of the dark excitons, and relative enhancement of the radiative recombination rate.

5.3.6 Surface enhanced Raman scattering

Further evidence for the efficient interaction of WSe_2 with the nano-antennas is obtained from the observation of the enhanced Raman scattering response. This effect, typically observed for nano-structured metals [31] and dielectric nano-particles [212], is related to the surface localization of the electromagnetic field and, while being linearly dependent on the

laser intensity, it shows a dependence to the fourth power of the confined electric field at the nano-antenna surface.

We collected the Raman scattering signal for both 1L and 2L-WSe_2 coupled to GaP nano-antennas, as shown in Figures 5.8a and b, where both samples are excited with a laser at λ =532 nm. The Raman scattering spectra of atomically thin WSe_2 show a pronounced peak at 250 cm^{-1} composed of two degenerate modes, the in-plane E' for 1L and E^1_{2g} for 2L WSe_2, and out-of-plane A'_1 for 1L and A_{1g} for 2L WSe_2.

Additionally to the degenerate peak at 250 cm^{-1}, in a bilayer sample it is possible to resolve at 310 cm^{-1} the B^1_{2g} mode, which is instead absent in bulk and monolayer but becomes Raman active in few layers samples [236].

Figure 5.8a,b further compare the Raman spectra measured for WSe_2 on the planar GaP with the spectra collected on nano-antennas with different radius. We show a notable enhancement of the signal, but while the overall Raman signal decreases with decreasing r, its relative strength per unit nano-antenna area is significantly enhanced. To demonstrate this enhancement, in analogy with the discussion in section 5.3.3, we define the Raman experimental enhancement factor, $\langle EF \rangle^{Raman}$:

$$\langle EF \rangle^{Raman} = \frac{(I^{fit}_{Raman} - I^{fit}_{ref})}{A_{dimer}} \left(\frac{I^{fit}_{ref}}{A_{laser}} \right)^{-1} \tag{5.3}$$

The Raman signals are analysed by fitting the two WSe_2 Raman peaks with Gaussian functions, following a background subtraction. The 250 cm^{-1} peak intensities extracted in this way are used to calculate the Raman enhancement factor in Eq.5.3. In this equation I^{fit}_{Raman} is the Raman intensity for WSe_2 coupled to a dimer and I^{fit}_{ref} is for the reference WSe_2 on the planar GaP. We determined experimentally that $A_{laser} = 16.8\ \mu m^2$ in the micro-Raman set-up. Figure 5.8c shows the experimental extracted $\langle EF \rangle^{Raman}$, exhibiting an increment when reducing the nano-antenna radius, reaching values up to 10^3 in dimers with $r = 50$ nm. Interestingly, these are values comparable with previous experiments on GaP nano-particles [237].

5.4 Conclusions

The reported enhancement in the PL emission and Raman signal intensities, and shortening of the radiative lifetime in 2D WSe_2 coupled to GaP nano-antennas, shows that nano-structured high-index dielectrics can be an efficient alternative to plasmonic structures as a platform to engineer light-matter interaction at the nano-scale.

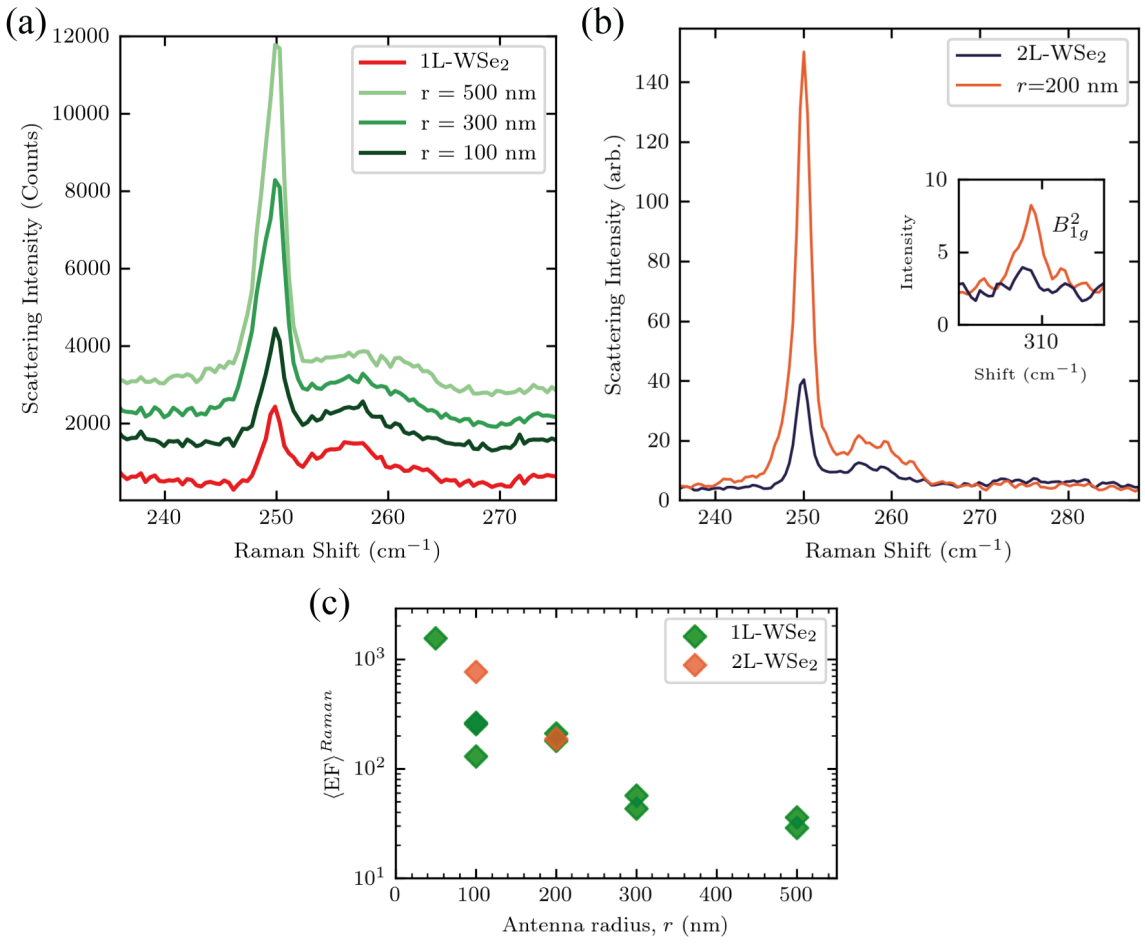

Fig. 5.8 (a) Raman scattering spectra for 1L-WSe_2 placed on GaP nano-antennas (green) and on the planar GaP (red). (b) Raman scattering spectra for 2L-WSe_2 on a r=200 nm GaP nano-antenna (orange) and on the planar GaP (blue). (c) Experimental Raman enhancement factor, $\langle EF \rangle^{Raman}$ (see Eq.5.3), obtained (after background subtraction) for the 250 cm^{-1} peak in 1L- and 2L-WSe_2 coupled to nano-antennas with different radius.

Importantly, we show that the coupling to nano-antennas can be used to significantly enhance the quantum yield in TMDs via the enhancement of the radiative decay rate, emphasizing the potential of this approach for light-emitting applications. The PL enhancements, which we report are of the order or exceed those recently reported in TMDs coupled to metallic plasmonic nano-antennas, showing the viability of our approach in a broader nano-photonics context. Our approach could be expanded to arrays of dielectric nano-structures, or meta-surfaces, an emerging field of nano-photonics [201] and for integration with novel van der Waals nano-photonics structures made from multilayer TMDs [234], with potential in a wide range of applications, such as quantum optics, photovoltaics and imaging.

This approaches can also be implemented in the field of strain-induced single photon emitters [157, 156] for applications exploiting quantum light generation.

Chapter 6

Dielectric nano-antennas for strain-engineering in 2D-TMDs

6.1 Motivation

Transition metal dichalcogenides are two-dimensional semiconductors with large deformation thresholds, offering a promising route for control of their optical and electronic properties via strain [111]. However, most optical cavities require flat interfaces to efficiently confine light, hindering the possibility to implement strain in TMDs interfaced with nano-photonic devices.

In this chapter, we demonstrate that a gallium phosphide (GaP) nano-antenna, described in Chapter 5, can be used to tune the optical properties of mono- and bilayer TMD WSe_2 via strain. The nano-structures vertically displace the atomically thin layers from the planar substrate, while providing sub-wavelength optical modes enhancing the local PL emission.

We describe the position-dependent strain topography with a continuum-mechanical theoretical description [124] and show that strain can be controlled by tailoring the nano-antenna radial dimension. Furthermore, from our model we calculate the distortion potential induced in the TMD band structure under the local deformation introduced by the nano-structure, which is expected to result in the exciton funnelling effect [127].

We provide experimental evidences of the strain-tuning, in agreement with our model, by observing the optical response of stretched TMDs at room temperature and we show exciton confinement into strain-induced potential wells at cryogenic temperature, consistent with the description provided by our theory.

These results are relevant for both all-dielectric or metallic nano-photonic structures and provide a novel approach to control strain in two dimensional semiconductors, opening to an additional degree of freedom in engineering light-matter interaction at the nano-scale.

6.2 Introduction

Single atomic layers of TMDs, only three atoms thick, are the most flexible semiconductors up to date, exhibiting large elastic thresholds ($>10\%$) [53] offering a unique possibility to engineer their electronic band structure via strain [123, 238, 57, 239]. This approach have been successfully applied for tuning the optical properties [121, 113, 240–242], together with carrier mobilities [243], charge transport [244, 129] and piezoelectric response [120, 244]. Moreover, by relying on the carefully design strain patterns introduced in 2D-TMDs by underlying nano-structures, artificial periodic arrays [114] and quantum emitter positioning [156, 157] have been demonstrated.

While first applications of strained 2D semiconductors in electronic devices have been achieved [243, 245], the use of strain in TMDs integrated with nanophotonic systems have not been reported [246]. This can be related to the fact that most high-quality factor optical cavities, such as Fabry-Pérot and photonic crystal cavities, although offering a reliable platform to improve light-matter interaction, limit the application of strain in 2D semiconductors since they mostly employ planar interfaces [247]. An alternative approach to engineer light-matter interaction at the nano-scale relies on resonant nano-antennas [167, 163], which can overcome high-quality factor optical cavities due to the confinement of strong electromagnetic fields at their surfaces. With this approach, dielectric nano-structures with sub-wavelength dimensions improve the light-matter interaction of closely coupled luminescent emitters, such as excitons in a 2D semiconductor [248], as described in Chapter 5.

Common approaches for introducing strain in a 2D crystal relies on a mechanical bending apparatus or piezoelectric substrates [111]. While the first offers a reliable way to introduce strain in the 2D membrane, they cannot be implemented in current technologies [121]. Piezoelectric substrates instead have widespread applications in semiconductor industry, as in surface acoustic wave (SAW) sensors, but can offer very small amount of deformation ($< 1\%$). Here, we demonstrate that a single nano-antenna can be used to introduce an out-of-plane deformation in a 2D semiconductor, resulting in tensile strain of 1-3 %, by displacing the layer from the substrate, while at the same time obtaining an enhancement of the PL emission efficiency from the strained area.

We transferred single (1L) and double (2L) layers of WSe_2 on top of gallium phosphide (GaP) nano-antennas [194] (Fig.6.1) and describe the strain topography with a continuum-mechanical theoretical model [124]. The full description of the model developed by M. Brooks (University of Konstanz) is given in Appendix B.

The co-location between the tensile deformation in WSe_2 and the nano-antenna confined field maxima, both located at the topmost edge of each dimer nano-antenna (Fig.6.1b,e), allows to observe the strain-induced band structure renormalization from the relative signatures in the enhanced 2D-WSe_2 PL emission. From our theoretical description and experiments, we demonstrate that by tailoring the nano-antenna radial dimension it is possible to modify the amount of tensile strain induced in the TMD layers. With this approach, we observe the tuning of WSe_2 monolayer excitonic resonance exceeding 50 meV, corresponding to strain values above $> 1\%$. In bilayers, we found larger strain than in monolayers under the same deformation geometry, due to a higher rigidity (see Appendix B Eqn.B.2), resulting in the transition to direct bandgap at high strain values, which we estimate to be $> 3\%$.

Moreover, from the calculated topography model we extracted a distortion potential profile induced in the WSe_2 band structure, and predict an inhomogeneous landscape which can trap excitons into strain-induced potential wells at the nano-pillar edges, where tensile strain is maximized (see Appendix B Fig.B.1). This behaviour is confirmed in the cryogenic PL signal of 2L-WSe_2 which exhibits a clear localization in the neutral exciton PL emission, consistent with the predicted potential shape.

Our findings present dielectric nano-antennas as a valuable tool for tailoring the optical properties of 2D semiconductors via strain and for the confinement of 2D excitonic species into strain-induced potential wells, where strong interaction with the confined optical modes is achieved.

6.3 Results and discussion

6.3.1 Strained 2D-WSe_2 topography on GaP dimer nano-antennas

Figure 6.1a shows a schematic section of a WSe_2 single layer (0.7 nm thick) transferred on top of a GaP dimer nano-antenna (200 nm tall) with a radius r. Owing to its elasticity, the thin semiconductor crystal stretches from the substrate up to the topmost edge of the nano-antenna, resulting in a local compressive (orange) or tensile (blue) stress, following to the large height mismatch.

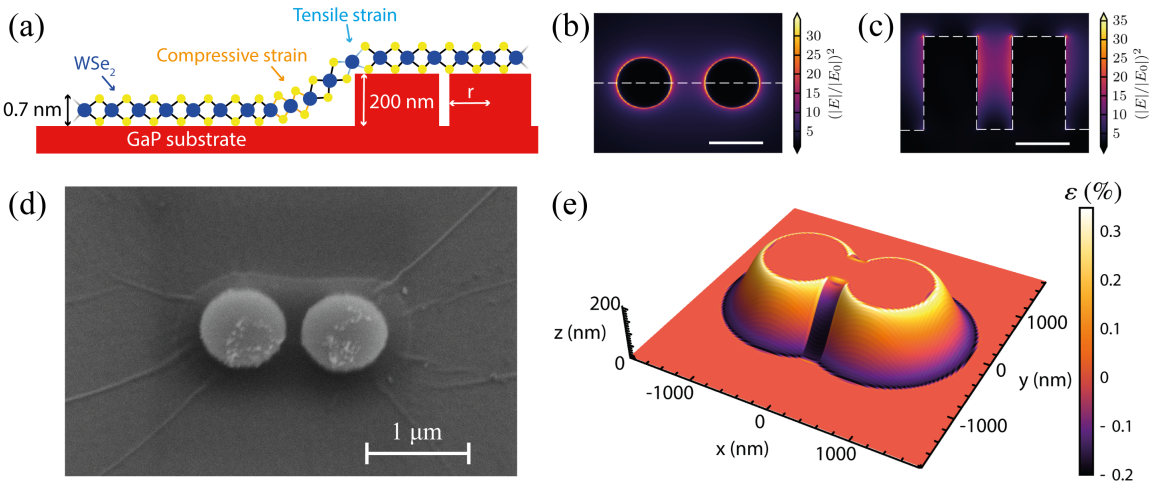

Fig. 6.1 (a) Schematic of a GaP dimer nano-antenna (in red) with a transferred single layer of WSe_2 on top. The WSe_2 layer stretches above the dimer nano-structure (200 nm height) without fracturing. The area of high compressive (tensile) strain is highlighted in orange (blue). (b,c) Intensity of the scattered electric field (E) over the incident field amplitude (E_0) for a GaP dimer nano-antenna (r = 50 nm) under unpolarized excitation. Scale bar: 100 nm. The top view field distribution is calculated at the topmost edge of the dimer (H=200 nm), the side view along the dashed line connecting the centre of the two pillars. (d) Secondary electron microscope (SEM) image of a 400 nm radius GaP dimer nano-antenna covered with 2L-WSe_2. (e) Theoretical modelling of the WSe_2 strain (ε) topography on top of a dimer nano-structure with $r = 500$ nm.

Under illumination, the dimer nano-antenna exhibits confined optical resonances leading to a strongly increased scattered near-field amplitude [248]. Figures 6.1b-c show the electric field distribution, $(|E|/|E_0|)^2$, for a GaP dimer nano-antenna under unpolarized excitation, where E is the field scattered by the nano-antenna and E_0 the electric field of the plane wave illuminating the dimer. Due to the antenna geometry, the maxima of the scattered field intensity, i.e. of the largest light-matter coupling, are located at the edges of each nano-pillar (Fig.6.1b) and inside the gap region between them (Fig.6.1c). As seen from the electron microscopy image (SEM) shown in Fig.6.1d, the atomically thin semiconductor layer stretches atop the resonant nano-structure, without compromising its integrity, fully overlapping with the confined optical modes at the nano-antenna edges.

We describe the nano-scale distortions in the 2D layer with a continuum-mechanical theoretical approach [124] by modelling the pressure experienced by the stretched semiconductor in the out-of-plane direction (see Appendix B). From the relative displacement of the WSe_2 layer from the substrate, we calculated the height topography, $\zeta(r)$, by using an appropriate pressure model [124]. From the analytically calculated function for a single

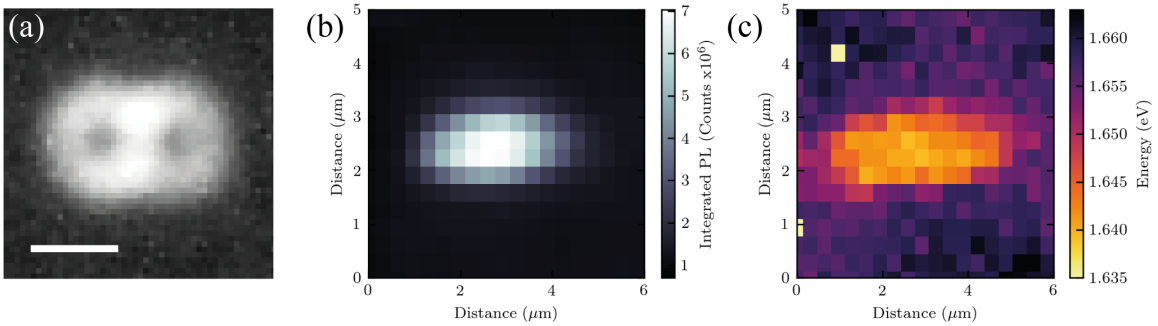

Fig. 6.2 (a) Real space photoluminescence imaging of a GaP nano-antenna ($r = 300$ nm) covered with 1L-WSe_2, exhibiting an enhanced emission intensity located where the maximum of tensile strain and photonic enhancement are expected. Scale bar 600 nm. (b) Sub-micron resolution mapping of 1L-WSe_2 PL intensity on a GaP nano-antenna ($r = 300$ nm). (c) Relative emission intensity energy maxima of 1L-WSe_2 exciton resonance, extracted from the same PL map shown in Fig.6.2b. A clear emission energy red-shift is related to the strain-induced reduction of 1L-WSe_2 bandgap energy under tensile stress.

pillar we interpolate the low-symmetric dimer structure and obtain a numerical solution of the height topography. From this estimate, the spatial strain distribution introduced in the deformed 2D semiconductor can be calculated (see Appendix B for more details). The strain topography resulting from our numerical calculations for a 1L-WSe_2 stretched onto a dimer nano-antenna ($r = 500$ nm) is shown in Fig.6.1e. Here, a maximum of tensile strain is located at the topmost edge of each nano-pillar, at $z = 200$ nm, which correspond to the strongest near-field enhancement offered by the underlying nano-antenna optical modes. As expected, a main region of compressive strain is located where the 2D layer meets the substrate, at $z = 0$, and a similar trend is found in the dimer gap region.

6.3.2 Strain-tuning in monolayer WSe_2

A microscope image of 1L-WSe_2 PL emission on top of a single GaP dimer nano-antenna, with $r = 300$ nm, is shown in Figure 6.2a (see section 4.1.2 and Ref.[217] for more details). Here, it is possible to resolve the spatial distribution of the PL signal which closely resembles that of the dimer nano-antenna scattered field amplitude (Fig.6.1b).

We studied the emission from the same nano-antenna in a μ-PL mapping setup, as shown in Figure 6.2b. The sample is excited at $\lambda_{exc} = 685$ nm, below the absorption edge of GaP, and light is absorbed only by the WSe_2 layer. As expected, a large enhancement in the overall PL intensity is correlated with the location of the nano-antenna. Here, the resolution is limited by our excitation spot size ($r \approx 1$ μm).

As shown in Figure 6.2c, we extracted the emission peak maxima from the relative position in the PL map and found a prominent red-shift of the exciton emission peak on the nano-antenna, as expected from the reduction of the optical bandgap in 2D-WSe_2 under mechanical deformation. As discussed in Chapter 2, for WSe_2, and for most single layer TMDs [57, 238], the direct optical transition is located at the K(K') point of the Brillouin zone and expected to reduce its energy under increasing tensile strain (Fig.6.3b), leading to the observed red-shift of the excitonic resonance.

From our theoretical description we have shown a dependence of tensile strain maximum, located at the nano-pillar edges, on the nano-antenna size (as shown in Fig.B.1a). We found that reducing the nano-pillar radius allows to introduce an increased amount of strain in the 2D layer. This trend is confirmed experimentally. Figure 6.3a shows the normalized 1L-WSe_2 PL spectra for the TMD coupled to nano-antennas of different radii, and compare them to that of WSe_2 on planar GaP substrate (where the excitonic resonance peak is marked by a dashed line). When reducing the nano-pillar radius, the larger red-shift in the excitonic resonance confirms that the semiconducting layer is experiencing an increased strain, as predicted by our model.

By using an experimental gauge value for the WSe_2 A exciton red-shift under mechanical stress (-49 ± 2 meV/%)[249], we extracted the uniaxial tensile strain magnitude from the exciton resonance energy found for coupled WSe_2 on the nano-antenna with different radius. The extracted strain values are shown in Figure 6.3c. We find tensile strain values up to 1.3% from the exciton resonance energy as the nano-antenna radius is decreased. This value is comparable to the estimate of our theoretical model (see AppendixB). In case of nano-antennas with radius of 50 nm, we observe that the resulting strain magnitude is lower than expected. This effect can be attributed to the non-uniform coverage of the antenna surface by the monolayer and from disorder (wrinkles, folding, etc.) in the WSe_2 layer. The agreement of our model with the experimental results let us expect that such description will work even in the case for strained bilayer WSe_2.

6.3.3 Direct bandgap transition in bilayer WSe_2

As schematically shown in Figure 6.4a, contrary to the monolayer case a WSe_2 bilayer is an indirect bandgap semiconductor. It exhibits two main recombination pathways at room temperature, a direct and indirect transition, respectively at the K and Q point of the conduction band [123]. For unstrained 2L-WSe_2 (black dashed line) the lowest energy

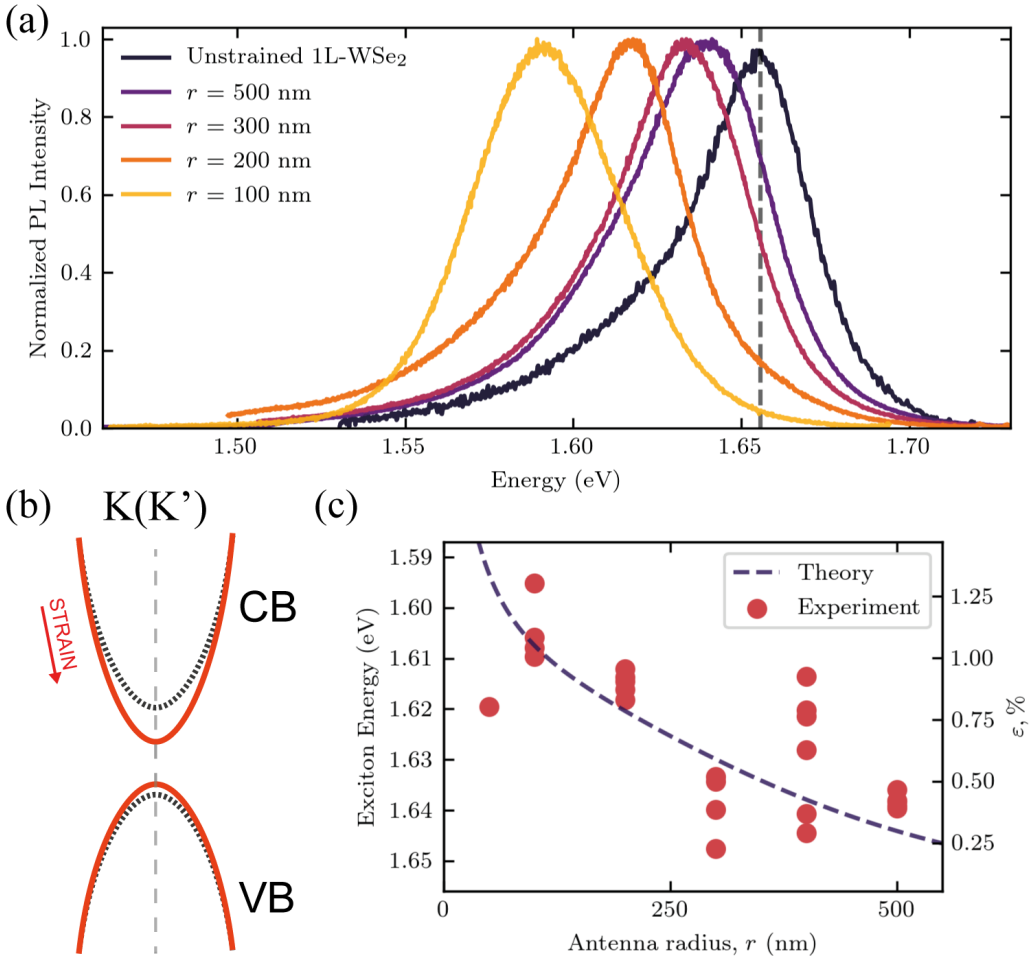

Fig. 6.3 (a) Normalized 1L-WSe_2 PL emission as collected on top of different dimer nano-antennas with variable radius (r). When reducing the nano-antenna dimension, a shift of the emission peak to lower energy correspond to an increasing amount of tensile strain introduced in the 2D layer. (b) Schematics of the band structure re-normalization under tensile strain (red) from unstrained 1L-WSe_2 (dashed black line). The direct optical recombination, located at the K/K' point of the Brillouin zone, is reduced in energy under increasing tensile deformation. (c) Uniaxial strain values extracted from the maxima of 1L-WSe_2 emission on top of nano-antennas with different radius, by using an experimental gauge factor from Ref.[249], and compared with the calculated expected values (dashed line) from our model (see Appendix B).

transition is the phonon-assisted recombination between the conduction band minimum at the Q point and the valence band maximum at the K point in the momentum space.

Under tensile stress (solid colour lines) the reduction in the energy of both the K and Q point minimum follows from the changes in the inter-atomic distance, i.e. the orbitals overlap, as expected in 2D-WSe_2 under strain (see section 2.4). As discussed in section 2.2, the transition metal d_z orbital are the main component in the conduction band minimum at the K point in momentum space, and the modification of their overlap via strain is expected to have a large impact on the optical properties [57]. Following this picture, we expect a stronger band-shift at the K point compared to the one at the Q valley, which instead is mainly formed by the in-plane orbitals which are less sensitive to low strain levels. This effect has been previously related to a transition from indirect to direct band-gap in strained 2L-WSe_2 [125, 126].

Figure 6.4b shows the PL spectrum of the unstrained 2L-WSe_2 placed on the planar GaP substrate. In contrast to what was found for monolayers, the bilayer spectrum exhibits a broad luminescence which can be fitted with two emission peaks. As previously discussed, these features have been attributed to the indirect ($E_{Indirect} = 1.63$ eV) and direct ($E_{Direct} = 1.55$ eV) optical transitions [123, 250].

In analogy with the analysis carried out for WSe_2 monolayers, we collected the PL emission of the strained bilayer on top of the nano-antennas with different radii. The normalized PL spectra as a function of the nano-antenna radius are shown in Figure 6.4c.

In case of a strained bilayer, the presence of two nearly degenerate transition leads to a more difficult derivation of the strain from the PL spectra. However, we observe a clear reduction in the overall linewidth when the 2D layer is deposited on the nano-antennas, an effect which can be related to the reduction of the exciton-phonon coupling in WSe_2 under strain [249]. By comparing the spectral shape to that of the unstrained case, we observe that the higher energy side of the spectrum exhibits a shift to lower energies as we reduce the nano-antenna radius. We ascribe this effect to the reduction of the energy of the $K \rightarrow K$ transition, as previously found in the monolayer case. Moreover, the PL spectral profile exhibits an abrupt change in its shape when the 2L-WSe_2 is deposited on top of a GaP dimer nano-antenna with $r = 50$ nm. This spectral shape and peak position resemble those reported in Ref.[125, 126] and attributed to a transition to direct bandgap, occurring due to the shift of the high-energy E_{Direct} peak.

From our theoretical model, we predict strain values $> 3\%$ for 2L-WSe_2 on top of nano-antennas with $r = 50$ nm (see AppendixB). This value is comparable with the reported direct gap transition threshold observed in encapsulated WSe_2 bilayer samples [126].

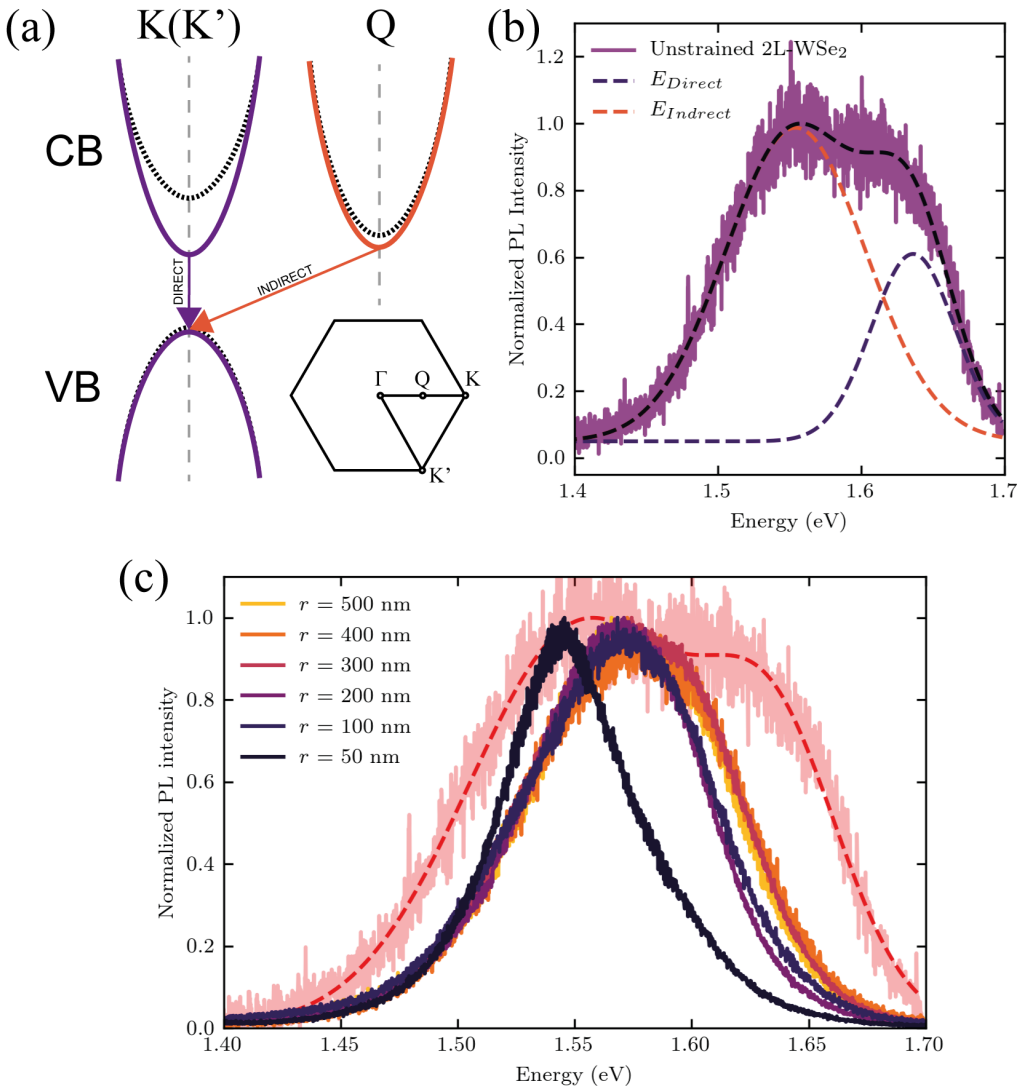

Fig. 6.4 (a) Schematic of the band structure re-normalization under tensile deformation for unstrained 2L-WSe_2 (dashed line). In colour, the relative changes under increasing strain of the two optical recombination processes. (b) Unstrained 2L-WSe_2 PL emission spectra on planar GaP substrate. In orange the emission peak associated with the indirect transition $Q \rightarrow K$ ($E_{Indirect}$), in purple the one related to the direct transition $K \rightarrow K$ (E_{Direct}). (c) Normalized 2L-WSe_2 PL spectra collected GaP nano-antennas with different radius. Contrary to the monolayer case, the spectral shape of 2L-WSe_2 under strain exhibits a reduction in the high energy side of the spectrum, with a district shape in the case of nano-antennas with $r = 50$ nm where a transition to direct bandgap is observed.

Note, that under the same deformation geometry we found that in the bilayer case a higher strain is introduced in the semiconducting layer due to a larger rigidity and a larger mass of the layer. In the bilayer this induces a stronger bandgap tuning. A similar effect has been observed in 1L- and 2L-MoS_2 under strain [244].

To elucidate the relative role of the competing valleys in the transition to the direct bandgap, we extracted the relative emission peaks positions for 2L-WSe_2 deposited on nano-antennas with different radius (Fig.6.5a). We observe that the high-energy peak shifts to lower energies as the radius is reduced, corresponding to higher strain values. We have extracted the relative energy difference between the two peaks, $\Delta E_{D-I} = E_{Direct} - E_{Indirect}$, as a function of the nano-antennas radii. As shown in Figure 6.5b, for unstrained bilayer on GaP substrate we found the largest difference between the direct and indirect peaks $\Delta E_{D-I} \approx 80$ meV. When stretched above the nano-antennas, ΔE_{D-I} exhibits an initial reduction form the unstrained values, further exhibiting a shift of > 30 meV when approaching the smallest nano-antenna.

Figures 6.5c-d show the position of the indirect and direct optical transition as extracted from the PL spectra on nano-antennas with different radius. When reducing the size, i.e. increasing strain, the $E_{Indirect}$ does not exhibits a clear shift in its position when compared to the unstrained case (red dot). On the other hand, we found a large shift of the E_{Direct}, of approximately 100 meV from the unstrained case. This behaviour confirms predominant role of the $K \rightarrow K$ optical recombination pathway in the transition to direct bandgap in 2L-WSe_2 under strain.

6.3.4 Exciton confinement in strain-induced distortion potentials

Owing to their large sensitivity to strain, controlled nano-scale deformations, such as those obtained by tip indentation [244] or substrate pattering [114], lead to the control of exciton motion in 2D semiconductors by means of band structure re-normalization [127, 128].

As discussed in Chapter 2, for WSe_2 the application of tensile strain results in the simultaneous reduction of the conduction band minimum and lift in the valence band maximum at the K point [239]. This effect leads to a Type I funnelling mechanism [124, 127] where the inhomogeneous strain gradient efficiently confines the excitonic population into potential wells. Moreover, this effect is expected to induce single photon emitters in strained WSe_2 at low temperatures [156].

From our strain topography model, it is possible to calculate the deformation potential gradient even for complex geometries of the TMD/nano-antenna system. We found that

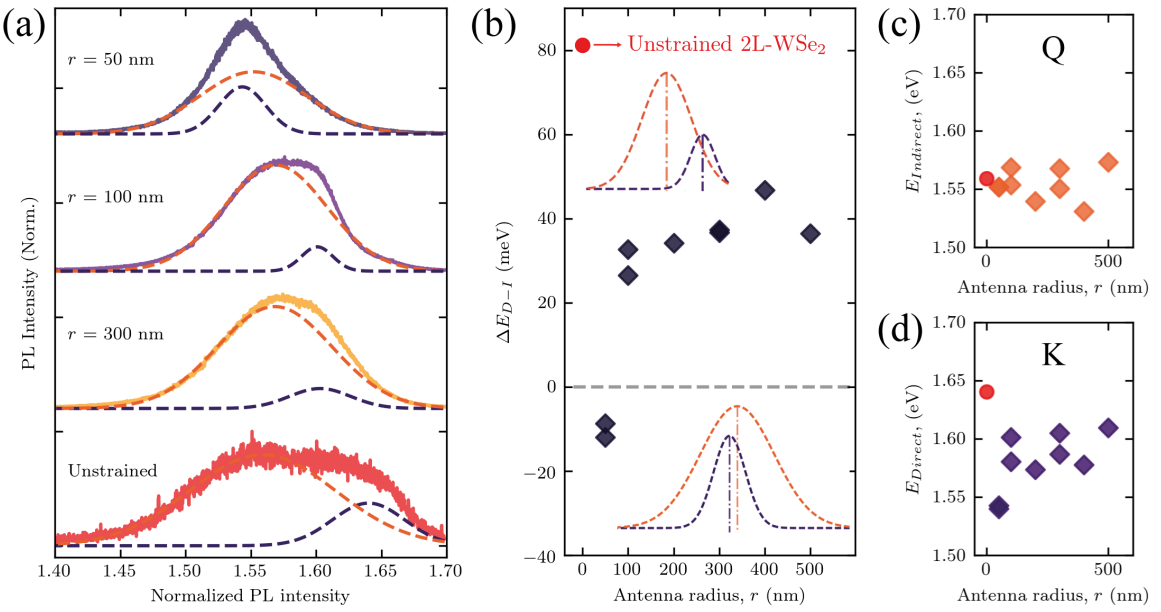

Fig. 6.5 (a) 2L-WSe_2 PL spectra for nano-antenna with different radius, fitted with two Gaussian functions relative to the direct (purple) and indirect (orange) exciton transitions. (b) Energy difference ($\Delta E_{D-I} = E_{Direct} - E_{Indirect}$) between of the two emission peaks maxima, as a function of the antenna radius. In red the value extracted from unstrained 2L-WSe_2 on flat GaP. The dashed line marks the transition to direct bandgap. (c,d) Direct and indirect recombination PL peak position extracted from the spectra on different radius nano-antennas (in red for unstrained 2L-WSe_2). While no evident changes are seen for the $E_{Indirect}$ peak (c), a stronger modulation in the E_{Direct} position (d) confirms that the transition to direct bandgap is related to the energy reduction of the conduction band minimum at the K point in the 2L-WSe_2 band structure.

strain-induced potential wells are located at the nano-pillars edges, where tensile strain is maximized. Instead, when strain becomes compressive, i.e. where the layer touches the substrate, we observe the presence of potential barriers due to the opposite effect which leads to an increase of the bandgap energy (see Fig.B.1 in Appendix B).

In order to elucidate the role of strain confinement, we probed the spatial dependence of the PL emission of 2L-WSe_2, at cryogenic temperature, due to its larger strain sensitivity that in monolayers, leading to deeper potential wells which can trap excitons more efficiently. Figure 6.6a shows the profile of strained 2L-WSe_2 (dashed line) on top of a dimer nano-antenna with $r = 500$ nm (red squares). The TMD profile is calculated for a cross section along the $x-$axis (as defined in Fig.1e), where $x = 0$ is the centre of the dimer gap, and we correlate the local strain deformation to the changes in the energy of the conduction band minimum (V_{cb}), calculated for the K valley. A reduction in V_{cb} is located at the nano-pillars

edges where tensile strain is maximum, resulting in confinement potential wells for carriers (shaded areas). Where the layer touches the substrate, strain becomes compressive resulting in an increase of V_{cb}. In such a potential landscape, excitons are pushed towards the nano-structure edges, concentrating the population at the strongest light-matter interaction points offered by the nano-antenna optical modes.

Figure 6.6b shows a reference PL spectrum of 2L-WSe_2, at 4 K, collected on planar GaP (black) and on a dimer nano-antenna ($r = 500$ nm, in orange). The position of the neutral exciton (X^0) on the planar GaP substrate (Inset Fig.6.6b) is found to be at 1.7 eV, approximately 45 meV higher than the position of the strained exciton on the nano-antenna (X), at 1.655 eV. Following the previous description of the strain-induced modulation of the band structure at room temperature, from this energy shift we extract a value of $\approx 0.9\%$ of tensile strain, consistent with our theoretical model predictions (see Fig.B.1a). As discussed in section 2.3.2, the low temperature PL emission of atomically thin WSe_2 is dominated by a broad side-band, reflecting the presence of a hierarchy of momentum-indirect recombination pathways due to the complex bright/dark sates ordering present in 2L-WSe_2 band structure [94]. The strained exciton emission, arising from the direct optical recombination process, is located at higher energy than the momentum-dark indirect transitions which appear as phonon replicas in the lower energy side of the PL spectrum. Together with localized bound excitons [154], these phonon assisted recombination processes lead to the formation of a low-energy side-band in the cryogenic PL emission of atomically thin WSe_2 [94, 101].

Figure 6.6c shows a one-dimensional hyper-spectral PL image of 2L-WSe_2 on top of four GaP nano-antennas ($r = 500$ nm and increasing gap size between 100 and 150 nm , left to right). The PL image is collected by scanning our collection/excitation spot along the nano-antenna x-axis (see Fig.6.1e for the axis denomination), while on the figure vertical axis we report the spectral distribution of the collected PL emission.

An increased PL intensity correspond to the enhanced 2L-WSe_2 emission when on top of the dimer nano-antennas (orange), with negligible signal when on flat GaP (black areas in between). The spatial distribution of the strained exciton PL emission, two order of magnitude less intense than the side-band, exhibits a clear localization in the two maxima, less evident in the broad emission band between 1.53-1.6 eV and appearing again below 1.53 eV. As expected from our deformation potential model, this localization corresponds to the outer edges of the underlying nano-structure, i.e. the strain-induced potential well locations.

Figure 6.6d shows the integrated PL intensity as a function of the position for the free exciton emission, in black, compared with that of the phonon side-band, in purple. The profile relative to the direct optical transition exhibits a clear localization in two distinct

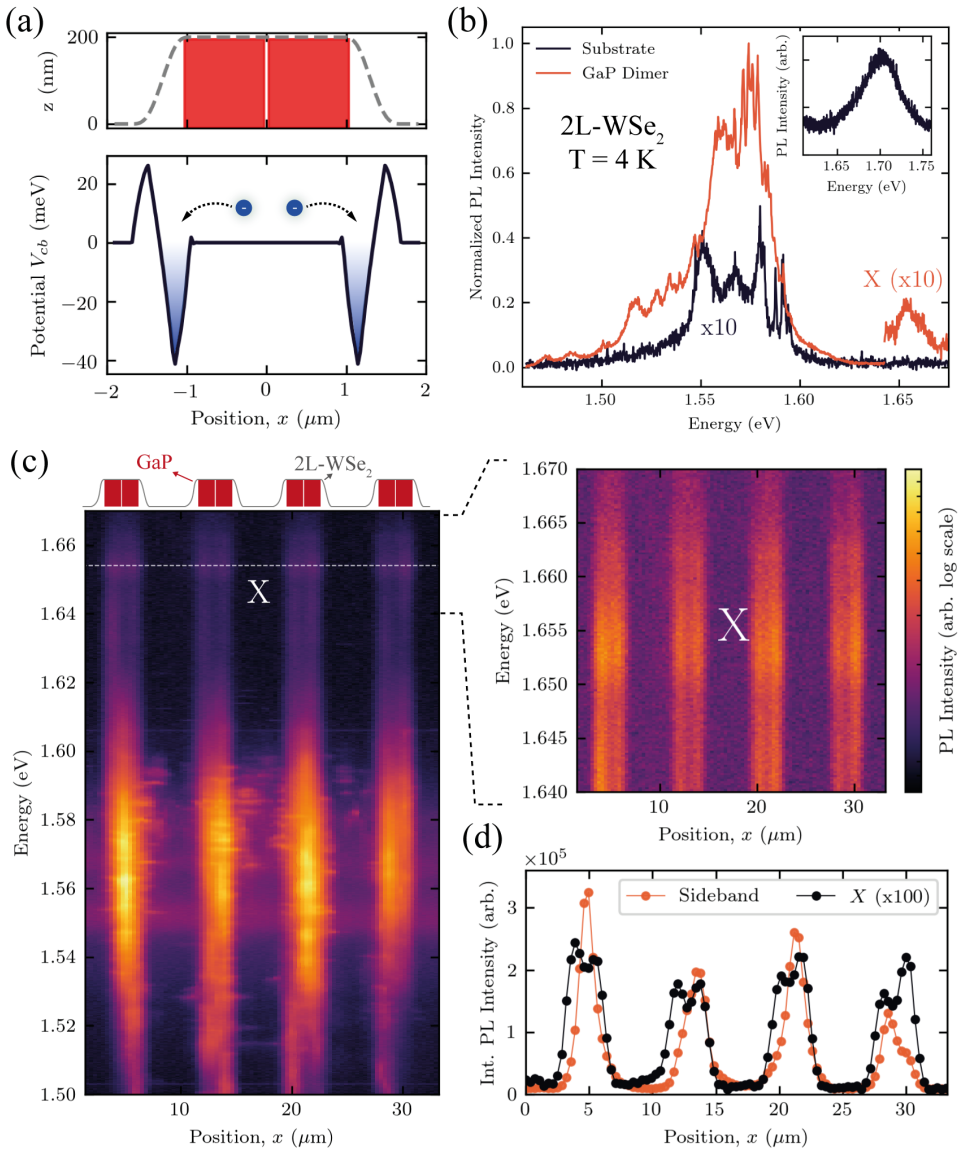

Fig. 6.6 (a) Cross-section, along the dimer central x-axis, of the profile for 2L-WSe_2 (dashed line) on top of a dimer nano-structure (in red, H = 200 nm, r = 500 nm) and the relative strain induced potential profile (V_{cb}), calculated for the K point of the conduction band. (b) 2L-WSe_2 PL emission at a temperature of 4 K, collected on top of the dimer nano-antenna (r = 500 nm, in orange) and in the area between them (black). The PL profile is dominated by the phonon related side-band, red-shifted from the strained exciton peak at 1.655 eV. Inset: 2L-WSe_2 neutral exciton emission on planar GaP substrate (1.7 eV). (c) One-dimensional hyper-spectral imaging of 2L-WSe_2 PL deposited on top of four dimer nano-antennas (r = 500 nm) distanced $\approx$ 10 μm. The spatial distribution of the neutral exciton shows a clear localization in two distinct emission maxima, as predicted by the calculated distortion potential profile in Fig.4a. (d) Integrated PL intensity profile, as a function of the x-axis position, for the neutral exciton (integration limits: 1.65-1.66 eV) and for the phonon side-band (integration limits: 1.56-1.58 eV).

maxima, with negligible signal intensity in between the nano-antennas. For the side-band, we found a similar enhancement at the nano-antenna sites, with signatures of a preferential localization where the neutral exciton emission exhibits a maximum.

Note, as we have showed in Chapter 5, a maximum in the PL emission intensity is expected at the dimer gap region due to the increased coupling and field strength, arising from the hybridization of the optical modes of each single nano-pillar [248]. This effect is observed in the spatial distribution of the 2L-WSe_2 side-band emission, while the free excitons show a preferential recombination at the outer edges of the nano-antenna. Moreover, as the dimer gap width of the underlying nano-structure is increased (left to right in Fig.6.6c), hence the field strength at the centre of the nano-antenna is reduced, we observe a more pronounced localization at the outer part of the structure even in the sideband emission. This effect allows to rule out the photonic enhancement as the source of the localized PL emission. Instead, we ascribe this spatial distribution of the strained excitons PL to the distortion potential wells at the outer edges of the nano-antennas, induced by the tensile strain in the 2D layer as predicted by the calculated potential profile shown in Figure 6.6a.

The PL spectrum of 2L-WSe_2 at low temperature is highly sensitive to the layer morphology and environment. The dominance of the side-band in 2L-WSe_2 cryogenic PL have been recently interpreted as the result of phonon mediated momentum-indirect recombination processes, and intra-valley scattering between competing valleys, which can be heavily modified by the local topography [94]. Following this interpretation, a more pronounced spatial confinement of the free excitons can be ascribed to the their ability to diffuse under a strain gradient, providing evidence of the exciton funnelling effect in strained 2D semiconductors.

6.4 Conclusions

In summary, we have demonstrated the strain-tuning of the electronic band structure in 2D semiconductors by employing pre-patterned dielectric nano-antennas, acting as a deformation centres. This work opens the way for strain as an additional degree of freedom in the light-matter engineering with 2D materials. By coupling with the optical modes confined at the surface of the nano-antenna, we obtain an enhancement in the 2D-TMDs PL emission from the strained area. This effect results in the observation of the strain-induced band-structure renormalization from the signatures in the TMDs optical spectra. We obtained a tuning of WSe_2 monolayers excitonic resonance exceeding 50 meV, corresponding to $\approx 1.3\%$ of tensile strain. For bilayers, we predict a higher level of strain than monolayers and observe a transition to direct bandgap when our model predict $\approx 3\%$ of tensile strain.

Moreover, we show at cryogenic temperature the presence of confined excitons into strain-induced potential wells, as predicted by our theoretical model, an evidence of the exciton funnelling effect in 2D semiconductors. These results could find applications for studying 2D excitonic species in confined potentials and advances in positioning of strain-induced WSe_2 quantum emitters[157, 156], as well in Bose-Einstein condensation of interlayer excitons in TMDs heterostructures[16]. Additionally, our continuum-mechanical theoretical approach can be expanded to describe the strain distribution and resulting distortion potential for 2D-TMDs coupled to low-symmetric and more complex nano-structures geometries. Note, that this approach does not discriminate the material of the structure itself but the geometry, thus is relevant even for plasmonic nano-antennas. These results open the ways for designing optically active nano-photonic platforms interfaced with strained 2D materials and their heterostructures, with prospects in photodetection, light emission and photovoltaics applications.

Chapter 7

2D-WSe_2 single photon emitters positioning on GaP nano-antennas

7.1 Motivation

Single photon emitters (SPEs) in mono and bilayer WSe_2 can be deterministically created on top of nano-structures, opening a route for control over their optical properties. This property has been previously related to strain-induced gradients in the local WSe_2 band structure [156, 157], where photo-generated excitons are trapped into potential wells. However, SPEs obtained with the current approaches exhibit reduced quality than other more mature technologies, such as diamond colour centres or III-V semiconductors quantum dots, showing low emission intensity and a difficult reproducibility of the emitters characteristics.

In this chapter, we show that GaP nano-antennas can be used to act both as a positioning site for SPEs in monolayer WSe_2 and an optical cavity, improving the overall photon collection efficiency. We observe bright photoluminescence intensity from the SPEs at the nano-antenna location, with count rates up to 30 kHz at saturation, more than one order of magnitudes larger than those reported for plasmonic nano-structures [146]. Moreover, we observe reproducible characteristics in their emission properties, demonstrating a finer control than previous approaches [155, 154, 157, 156].

We analysed a large number of emitters in terms of time- and polarization-resolved luminescence and, based on the previous works described in section 2.5, we ascribe these emitters to two classes of SPEs. The first, with emission energy between -50 to -100 meV to that of neutral exciton, exhibits a single emission peak with fine structure splitting (FSS), long radiative decay lifetimes and a specific rise time, related to the capture of a free neutral exciton into a localized state. A second class of emitters exhibits a large number of peaks at

lower energies, between -100 and -150 meV, all showing the same polarization axis, no fine structure splitting and faster recombination.

We describe these trends in terms of quantum confined WSe_2 excitons in finite potential wells, where the size and depth of the strain-induced distortion potential determines the two different kind of emission. Moreover, consistent with the discussion given in Chapter 6, we observe a dependence of the SPEs emission energy with the strain introduced in the WSe_2 layers. Although the current fabrication methods of polymer transfer lack a fine control over the position and emission properties of strain-induced SPEs in WSe_2, we observe the reproducibility of the SPEs spectral features described in our analysis. This work establish an efficient route to improve their optical properties and hold promise for their integration in photonic devices.

7.2 Introduction

Quantum emitters integration with on-chip photonic architectures offers potential applications in quantum optics and quantum information processing [251]. The discovery of strain-induced SPEs in single- and double-layer WSe_2 opened the way to harness the unique mechanical properties of 2D semiconductors. However, WSe_2 SPEs exhibit large variations in the optical properties and low photoluminescence intensities, owing to the lack of control over their fabrication process.

Most of the peaks in monolayer WSe_2 PL emission at cryogenic temperature have been identified [92, 252] (see Fig.2.6), but relatively little is still understood about the localized states giving rise to the single photon emission. Many theoretical approaches have been proposed to explain the presence of such SPEs in the cryogenic PL spectra of W-based TMDs, for instance due to the presence of dark-momentum states [94], localized inter-valley defects [161], trapping potential wells [159] or single structural defects [149, 151]. While their nature is still under debate, localized strain textures introduced with SiO_2 and polymer pillars [156, 157], were found to play a fundamental role for the deterministic positioning of SPEs on the nano-scale.

Here, we use high-index ($n > 3$) dielectric GaP nano-antennas (height $= 200$ nm, radius $= 150, 200, 250, 300$ nm and gap width ≈ 50 nm) with a transferred monolayer WSe_2 on top, in analogy with the work described in the previous chapters. The sample is kept at cryogenic temperatures in a gas exchange cryostat, in the setup described in section 4.3.2. We observe the presence of bright single photon emitters where the TMD layer stretches on top of the nano-antennas, with bright PL count up to 30 kHz at saturation (Fig.7.1a). We attribute such

large improvement in the overall PL efficiency to an efficient coupling to the optical modes of the nano-antennas, in analogy with what described in Chapter 5. We studied a large number of emitters in polarization- and time-resolved spectroscopy. From this analysis we ascribe distinct features in the SPE PL spectra to the free exciton funnelling into finite potential wells, leading to the creation of bound exciton states.

In agreement with a particle in a box model, as recently reported in a theoretical analysis [159], when the distortion potential have small extent in the real space relative to the free exciton Bohr radius, the SPE emission is centred at higher energy closer to the free neutral exciton peak. These emitters exhibits long decay lifetimes (> 10 ns) accompanied with a rise times (< 1 ns), which are reminiscent to a behaviour of an impurity bound exciton state [253]. Moreover, these emitters usually present a fine structure split doublet at zero field, of 0.6-0.8 meV, related to a symmetry breaking due to the anisotropy of the confinement potential, similarly to what seen in III-V semiconductors quantum dots [254].

On the other hand, a second class of SPEs exhibit a manifold of peaks at lower emission energies which we attribute to a larger confinement potential spatial profile, hence accommodating a higher number of states. All these emitters share the same polarization axis and are accompanied with faster lifetimes (< 10 ns), ultra-fast rise times at excitation powers close to saturation, and the absence of a FSS, Indicating faster capture rate than the first class of emitters.

We show the reproducibility of such SPEs emission characteristics for nano-antennas with three different radii, confirming that these trends are not only dependent on the local disorder or fabrication methods but are correlated to the intrinsic nature of the quantum emission. Moreover, we observe a persistent tuning of the emitters emission energy as a function of the nano-antenna radius, which can be attributed to the tuning of the band structure in WSe_2 layers under increasing tensile strain, as recently reported for different experimental approaches [255, 256].

7.3 Results and discussion

7.3.1 Nano-scale positioning of bright WSe_2 quantum emitters

Figure 7.1a shows a PL spectrum of a monolayer WSe_2, collected on top of a GaP dimer nano-antenna ($r = 300$ nm). As expected, due to the strain in the 2D layer the WSe_2 emission shows the presence of narrow peaks at cryogenic temperatures, recently shown to correspond to single photon emitting centres [25]. We observe at high energy a bright single peak (at

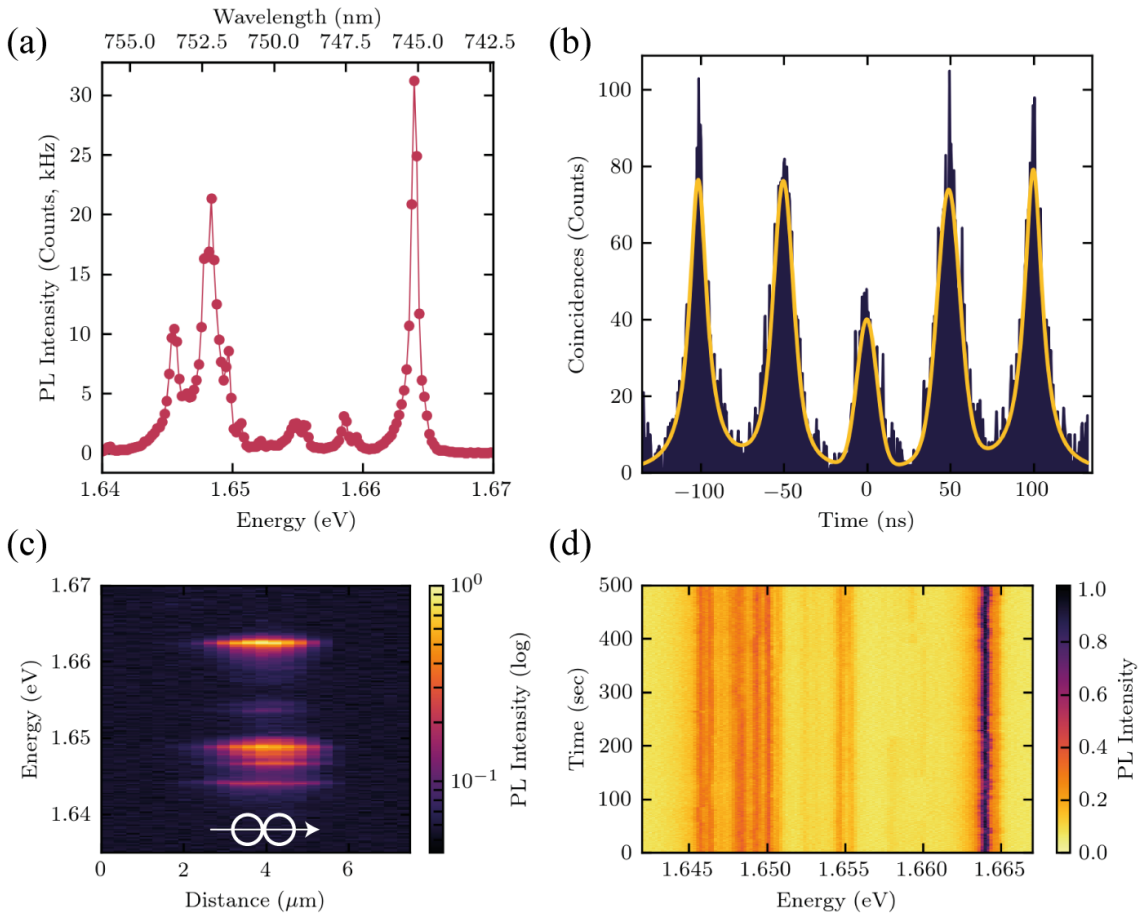

Fig. 7.1 (a) Photoluminescence emission of a strained monolayer WSe_2 on top of a GaP nano-antenna ($r = 300$ nm). The spectrum is acquired at 4 K with 638 nm, 80 MHz pulsed excitation at 500 nW. The spectral profile exhibits a higher energy peak (with fine structure splitting) and a series of side peaks at lower energy. (b) Photon correlation measurement on the high energy peak, showing a reduction in the peak at zero delay indicating a single photon emission. (c) PL linear scan above the nano-antenna position along the axis connecting the dimer nano-pillars, exhibiting a spatial correlation between the emission lines shown in Fig.7.1a. The white inset shows the scan direction relative to the dimer nano-antenna. (d) Spectral wandering of the emitter in Fig.a showing the stability of spectral emission over time, as expected form highly strained quantum emitters.

1.665 eV, which we labelled 'main') which is accompanied with a series of low energy peaks, labelled 'satellite' peaks, below 1.65 eV. The PL emission intensity for the main peak reaches high count rate up to 30 kHz under non-resonant pulsed (80 MHz) excitation, with linewidths down to 260 μeV.

We probed the photon emission statistics of the high energy peak in Figure 7.1a with photon autocorrelation measurements, in a Hanbury-Brown-Twiss setup (described in section 4.4.2). As shown in Figure 7.1b, it is possible to see that the central peak, at zero time delay, shows a clear anti bunching dip in the coincidence counts, confirming the nature of single photon emission from the bright WSe_2 peak. The presence of a residual background from 2D excitons and a closely spaced FSS doublet, as shown in Figure 7.4, can be related to the high multi-photon events recorded at $t = 0$.

The SPE emission lines show a spatial correlation with the nano-antenna position, with no PL signal detected from the free exciton of WSe_2 monolayer surrounding the area around the antenna, due to the low excitation power used. This is shown in Figure 7.1c, acquired by scanning our excitation/collection spot along the axis connecting the dimer nano-pillars (white line) where it is possible to observe a clear correlation between the antenna position and the localized emitters. While the resolution of the system is not high enough to discriminate the position of each single peak, we observe small shifts in the relative emission intensity as a function of the position, which led us to conclude that the manifold of peaks is not related to a single bound state, but rather the presence of multiple potential wells in the inhomogeneously strained WSe_2 monolayer. Although the relative position is not resolved, we observe that all these lines exhibit low spectral wandering, as shown in Fig.7.1d, and stability over months at cryogenic temperature. These results are consistent of an improved stability for strain-induced SPEs deterministically created on top of high aspect ratio nano-pillars made of high-quality semiconducting material GaP. In our sample the single pillar aspect ratio is between 0.66 and 0.33, higher than in previous works [156, 157].

7.3.2 SPE emission intensity saturation

Following the high efficiency extraction of SPEs luminescence signal, we investigated the power dependences for the two classes of emitters using a pulsed diode laser at 638 nm and 80 MHz repetition rate. As shown in Figure 7.2, we collected the PL emission as a function of the excitation power, for both the main peak (Fig.7.2a-b) and the satellite peaks (Fig.7.2c-d). The integrated PL intensity signal is fitted with the following saturation curve function:

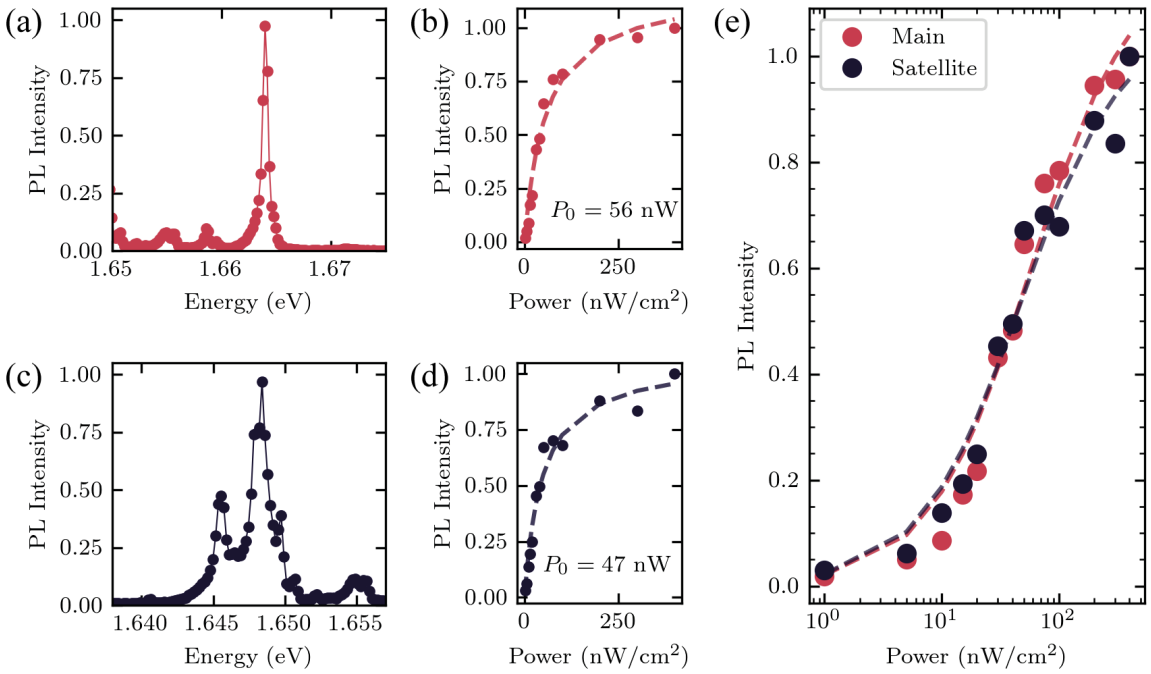

Fig. 7.2 (a,b) PL emission spectra of the high energy main peak (a) and relative integrated intensity curve as a function of the excitation power (b). (c,d) PL emission spectra of the lower energy satellite peaks (c) and the relative integrated intensity curve as a function of the excitation power (d). (e) Comparison of the two integrated intensity curved in Fig.b,d with a logarithmic scale for the x-axis. A change of linear slope is shown for the threshold power at 10 nW.

$$I = I_{sat} \frac{P_{exc}}{P_{exc} + P_0} \tag{7.1}$$

where I_{sat} is the integrated intensity value at saturation, P_{exc} the excitation power and P_0 is the normalized power value, defined as the excitation power at which the integrated PL intensity becomes half of I_{sat}.

As shown in Figure 7.2b and d, P_0 found for the two class of emitters shows similar values, with a faster saturation in the case of the satellite peaks. We then compare both PL intensity dependence as a function of power as shown in Figure 7.2e. At low power densities, below 10 nW, both emitters show a slow increment in the PL intensity. This situation changes as we approach higher excitation power, closer to P_0, where a clear shift in the linear slope is found above 10 nW. Interestingly, while the PL intensity does not show large differences

between the two class of emitters, the main discrepancies between the two classes arise when looking at the relative time resolved luminescence, as described below.

7.3.3 Power dependence of the decay and rise time of SPEs luminescence

To gain more insight of the nature of the quantum emission, we probed the photoluminescence dynamics for both the main peak at the higher energy (Fig.7.3a) and of the satellite peaks at the lower energy (Fig.7.3b) as a function of the excitation power.

As shown in Figure 7.3, for low power densities it is possible to observe that in the luminescence traces a clearly resolvable rise time is present in the signal of both classes of emitters. This delayed luminescence is related to the formation time of the quantum emitter state, dependent on the diffusion and subsequent capture of a single neutral exciton into a strain-induced distortion potential well, in analogy with time resolved spectroscopy of impurity bound excitons in diamond [253] and nitrides [257].

We fit the luminescence decay traces with a combined exponential growth and decay function, defined as:

$$I = \begin{cases} I_0 + A_d + A_r\left(e^{-\frac{t_c}{t_r}} - e^{-\frac{t}{t_r}}\right) & t \leq t_c \\ I_0 + A_d e^{-\frac{t-t_c}{t_d}} & t > t_c \end{cases} \tag{7.2}$$

where t and A are the time and coefficient for the rise time (subscript r) and decay time (subscript d), while t_c is the onset time, i.e. the point where the luminescence decay starts. Such separate treatment of the rise and decay time is possible because t_r is found to be two orders of magnitude shorter than t_d. As shown in the inset of Figure 7.3a, we found that the onset of the decay is reduced at higher excitation powers, corresponding to a decrease in the rise time, i.e. a faster capture rate of the neutral exciton. The values of the fit parameters extracted from the data shown in Figure 7.3 are reported in Table 7.1.

From the comparison between the two types of SPEs, it is clear that the main peak exhibits a longer rise and decay time, leading to a delayed luminescence present at even high power densities (10^3 nW). This indicates that the emission is related to trap states, where relaxation to lower energy leads to a slow build up of the population. In case of the satellite peaks, the rise time becomes very short, below resolution, at already intermediate power (10^2 nW), similar to those found for the main emission for power densities of one order of

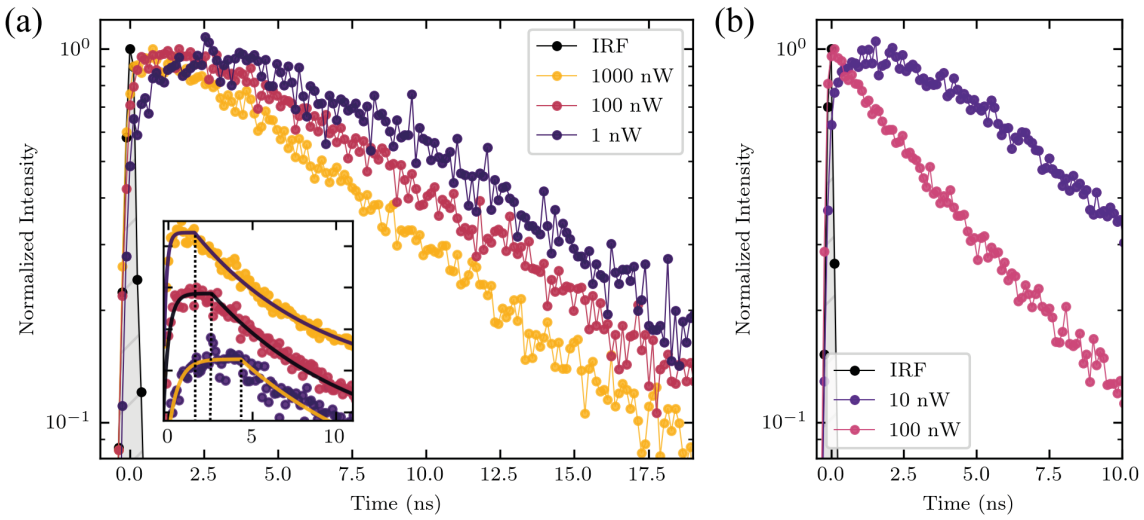

Fig. 7.3 (a) Luminescence decay trace for the main emission peak (Fig.7.2a) for increasing excitation power. The decay shows a clear rise time in the luminescence, leading to a delayed decay of the luminescence signal. This delay can be interpreted as the formation time of the confined state, correlated to the capture of a single exciton in the distortion potential well. Inset: reduction of the rise time as a function of increasing power. The solid line is the fit of the experimental data with Equation 7.2. (b) Luminescence decay trace for the satellite emission peaks (Fig.7.2b) for different excitation power. While for low pump intensity the decay show a delayed luminescence, at higher power the emission shifts to a single exponential decay. The fitting values for both figures are reported in Table 7.1.

Power (nW)	t_r^{main} (ns)	t_d^{main} (ns)	t_c^{main} (ns)	t_r^{sat} (ns)	t_d^{sat} (ns)	t_c^{sat} (ns)
1	0.58	9.8	4.3	-	-	-
10	-	-	-	0.33	7.1	2.7
100	0.33	8.7	2.6	-	4.2	-
1000	0.24	7.3	1.9	-	-	-

Table 7.1 Rise time (t_r), decay time (t_d) and onset time (t_c) for the PL decay traces for the main peak (t^{main}) and satellite peaks (t^{sat}) shown in Fig.7.3

magnitude higher. From this difference, the satellite peaks could be described in terms of larger potential traps, where a faster capture and release of the excitation is expected.

Both luminescence traces in Figure 7.3 show a reduction in the rise time with increasing power, which we relate to a higher exciton density and consequently faster rate of the trap state filling, or exciton capture. In the case of the satellite peak emission, the rise time vanishes, indicating a more efficient capture of the free excitons. Even in the decay times we observe a reduction for increasing powers, with a more pronounced effects in the case of the satellite peaks. This reduction can be explained by taking into account the larger non-

radiative recombination pathways for instance exciton-exciton annihilation, in the case of a higher excitonic population, or residual charges, which are crucial effects in the luminescence dynamics of 2D semiconductors [105].

The luminescence decay values extracted from the two different SPE classes show long lifetimes, with larger values for the higher energy emitters, as expected in the case of more confined excitonic species. Although the luminescence of these SPEs is high, the emitters are accompanied with longer radiative lifetimes than for those reported in literature (in the order of 1-10 ns). However, the radiative lifetime of SPEs in WSe_2 is still an open question, with reports of luminescence lifetimes which can reach values up to more than 200 ns [151]. This issue hinders a clear definition of a Purcell enhancement factor in these confined systems, which would be highly dependent on the SPE confinement potential well and the emitter position relative to the maximum of the field at the surface of the nano-antenna. All these factors requires a high spatial resolution and a finer control of the SPE position than what our experimental and fabrication techniques offer.

7.3.4 Polarization properties

As previously described in section 2.5, localized SPEs in WSe_2 exhibit unusual polarization characteristics. While no complete understanding exist, confined excitons in WSe_2 exhibit various polarization properties for example the presence, or absence, of a FSS even under high magnetic field [150]. This variance in the presence of observable FSS supports the idea that strain has a fundamental impact on the potential well shape and depth. In analogy with self-assembled quantum dots in III-V semiconductors, the splitting in the emission line of a confined exciton is caused by a combination of the underlying anisotropy of the crystal, which can be heavily modified by the local strain [258], together with the effects of spin-orbit interaction and the electron-hole exchange interaction [152].

Figure 7.4 shows the polarization properties of the WSe_2 SPE previously described in Figure 7.1. Here, we illuminate the sample with a linearly polarized pulsed excitation, kept constant during all the measurements, while the light emitted by the SPE is detected with a rotating halfwave plate in the collection part, as described in Chapter 4. As shown in Figure 7.4a, under perpendicular polarization detection angles, at 90 degrees difference (here arbitrarily labelled H and V selected where the relative intensity is maximized), the main peak at higher energy shows the presence of a FSS doublet with a splitting of ≈ 720 μeV, consistent with previous reports [133]. The inset in Figure 7.4a shows the polar plot of the PL intensity for the two peaks, marked by the lines of the same colour in the PL spectra, as a

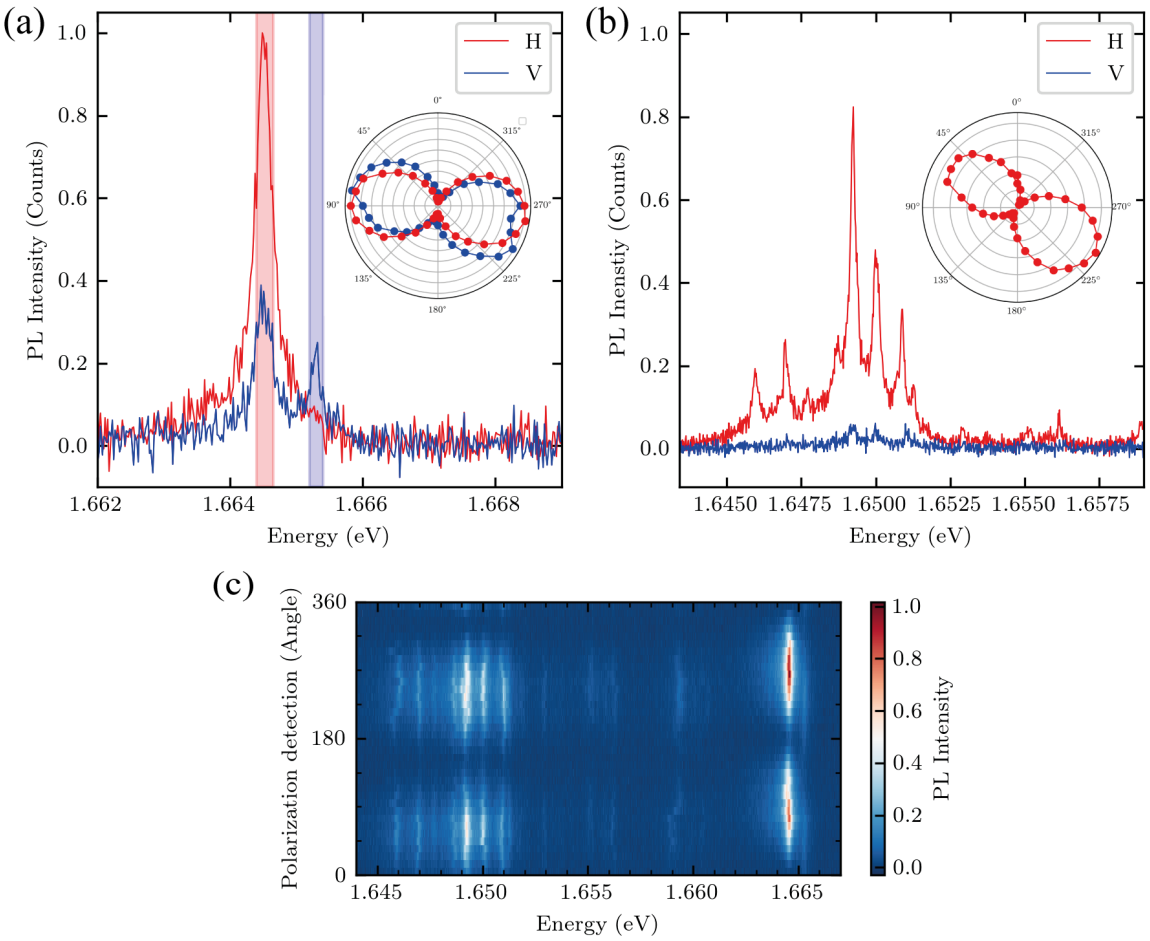

Fig. 7.4 (a) Polarization properties of the main SPE peak. The sample is excited with a linearly polarized laser beam, and the detection is done by collecting the emitted light in a horizontal (H) and vertical (V) geometry, as a function of the half-wave plate rotation angle in the collection path. The main peak exhibits a doublet, with a fine structure splitting of $\approx 700\ \mu$eV. The inset shows the polar plot of the normalized PL intensity of the two peaks (as indicated by the dashed lines) as a function of the half wave plate detection angle. The two peaks shows a relative polarization angle difference of about 15 degrees, ascribed to strain effects. (b) Polarization of the satellite peaks, showing a near unity degree of linear polarization and the same polarization axis for all the different emission peaks. (c) PL intensity as a function of the detection angle for the full SPEs emission spectrum. Slight changes in the relative orientation of the polarization axis can be due to the different amount of strain experienced by each emitter.

function of the halfwave plate detection angle. Here, we found a small shift in the relative polarization axis angle of the two emission lines of approximately 15 degrees.

When looking at the manifold of emission peaks present in the lower energy side of the SPE spectrum (Fig.7.4b), we found the absence of any fine structure splitting. Moreover, the peaks all share the same polarization axis (Inset Fig.7.4b) with a near unity degree of linear polarization. Figure 7.4c shows the PL emission of the full SPE spectrum as a function of the polarization detection angle. We observe slight differences in the polarization orientation for the two classes of emitters, and in other samples even between emitters with similar peak energies, which might indicate the role of a variation in the local strain magnitude, and relative changes in the confinement potential geometry. Moreover, strain-induced changes in the crystal symmetry of the 2D membrane can be responsible for the rotation of the polarization axis of confined excitons (due to folding, wrinkles etc.), in analogy with the description in self-assembled quantum dots [259]. From this trends, we conclude that these states are confined to a larger potential well than the main peak which, following a particle-in-a-box model, can host a larger number of bound states. Moreover, the absence of the FSS can be related to the fact that in large size potentials the mutual exchange interaction of the carriers is not strong enough to introduce the FSS.

7.3.5 Reproducibility in SPEs emission characteristics

In this section we show that the properties of strain-induced SPEs described so far (on antenna with radius of $r = 300$ nm) are replicated in emitters positioned on top of nano-antennas with different geometry. For both antennas with radius of $r = 250$ nm (Fig.7.5) and $r = 200$ nm (Fig.7.6), we could observe similar optical properties to those found in the SPE on top of $r = 300$ nm. A high energy peak with the clear FSS doublet is followed at lower energy by a manifold of peaks that share the same polarization axis and no FSS. As discussed luminescence lifetimes show a similar pattern, with longer decay values for the high energy peak and shorter decays for the low energy peaks. Note, we probed also many other antennas covered with 1L-WSe_2 and observed a variety of peaks which falls in one or the other class. We present here only those that exhibit SPEs of both classes. More rigorous statistics of these emitters are given in the following section.

In the case of antennas with $r = 250$ nm (Fig.7.6), we observed a single isolated peak exhibiting a low saturation power ($P_0 = 26$ nW) and an increase in the linewidth, from 500 to 700 μeV, under increasing power (Insets Fig.7.5a). Interestingly, as we rotate the polarization detection angle, a manifold of peaks appears at lower energies (Fig.7.5b), while the isolated

peak disappears. The radiative lifetimes show a similar trend to the ones described in Fig.7.3, where the high energy peak exhibits a longer decay time than the ones found for the satellite peaks at lower energies (Fig.7.5c). Moreover, even the polarization characteristics are reproduced, the satellite peaks all share the same polarization axis, with a near unity degree of linear polarization (Fig.7.5d), while the main peak at higher energy exhibits a cross polarized doublet (Fig.7.5e).

These spectral features are found to be replicated also in SPEs located on top of a nano-antennas with $r = 250$ nm (Fig.7.6). Even here, the PL spectrum (Fig.7.6a), time resolved luminescence (Fig.7.6b) and relative polarization characteristics (Fig.7.6c-f) reproduce the ones reported so far in Figure 7.3 and 7.5.

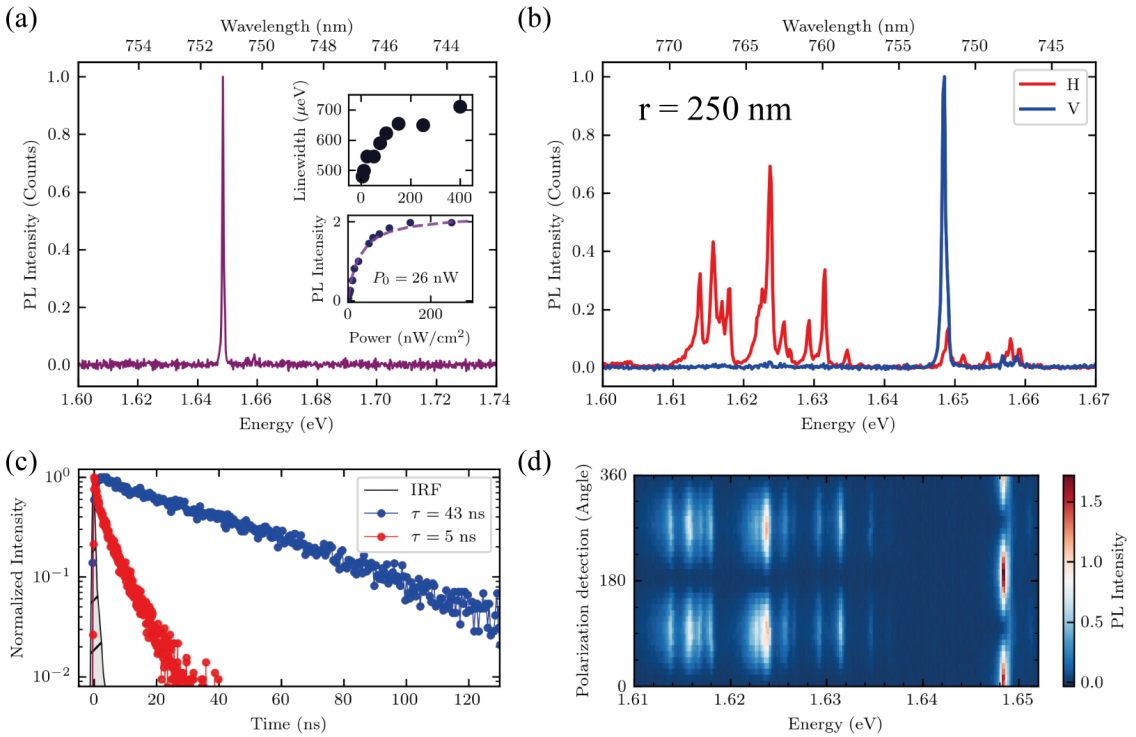

Fig. 7.5 (a) WSe_2 SPEs on top of a nano-antenna with $r = 250$ nm, showing a single isolated peak, power saturation of 26 nW and a linewidth of approximately 500 μeV which increases to 700 μeV at saturation. (b) PL spectrum at different detection angles, shifted by 90 degrees, exhibiting the appearance of a manifold of peaks at lower energies. (c) Luminescence decay traces for the main (blue) and the satellite peaks (red), confirming a longer lifetime values for the FSS peak. (d) Polarization plot of the PL intensity as a function of the polarization angle, the the satellite peaks at low energy shows a similar polarization axis, while the main peak below 1.65 eV shows cross polarized polarization axis (as shown in Fig. b).

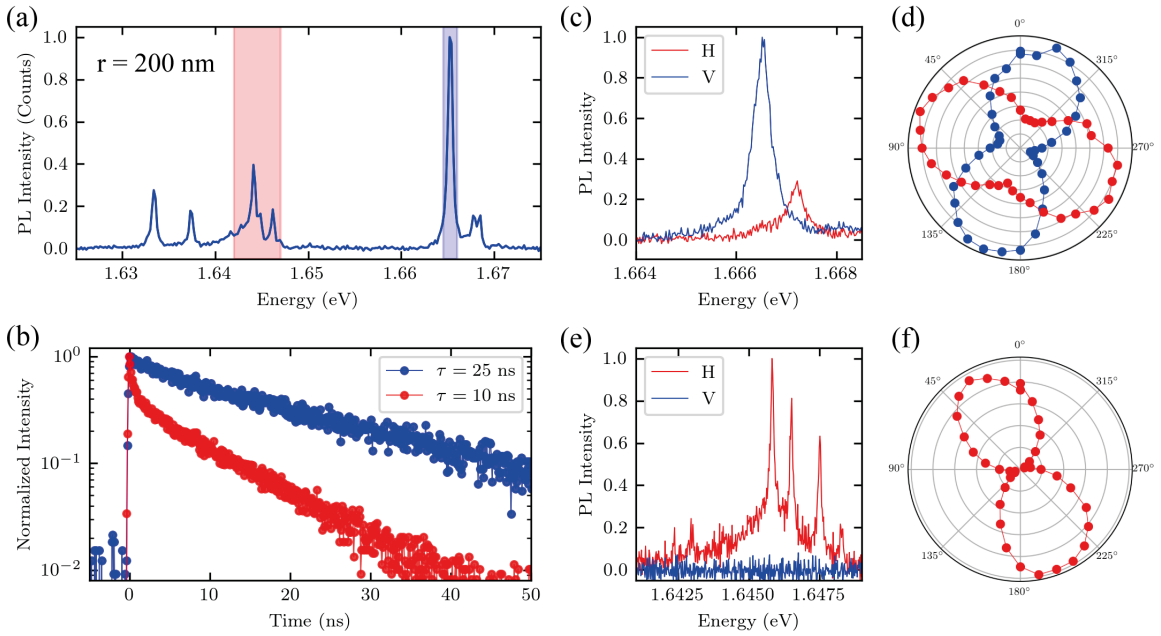

Fig. 7.6 (a) WSe_2 PL spectrum collected on top of a $r = 200$ nm GaP nano-antenna. The narrow peaks exhibit a similar structure to that observed for other SPEs. (b) Luminescence decay traces for the two class of emitters, corresponding to the same colour of the shaded areas in Fig.a. (c-d) Polarization properties of the high energy peak, showing a FSS doublet (c) for perpendicular polarization detection angles, which exhibits a difference of approximately 90 degrees between the two peaks (d) . (e-f) Polarization properties of the low energy side of the SPE spectrum, with a manifold of collinear peaks in the PL emission (e) with a near unity degree of linear polarization (f).

Although the control of the TMD layer deposition does not allow us to discern the relative changes in the 2D semiconductor nano-scale morphology, the reproducibility in the optical properties of SPEs led us to believe that these are linked to a similar confining potential.

7.3.6 Strain dependence of SPEs luminescence

Following the description given in Chapter 6, we looked at the cryogenic PL emission of the WSe_2 SPEs to find if the strain tuning of the WSe_2 band structure, observed at room temperature, is detectable from the localized emitters properties. In Figure 7.7 are shown the position of the SPE emission energy in strained WSe_2 as collected on different radius nano-antennas, and at low power densities.

As evidenced in the dispersion of the SPE emission energies (black dots) we observe a gradual red-shift in the energy as we approach smaller radius nano-antennas. This behaviour is consistent with the red-shift of the neutral exciton energy under increasing strain (crosses),

related to a rigid shift in the band structure of WSe_2 when approaching higher strain values as described in the theoretical model in Appendix B.

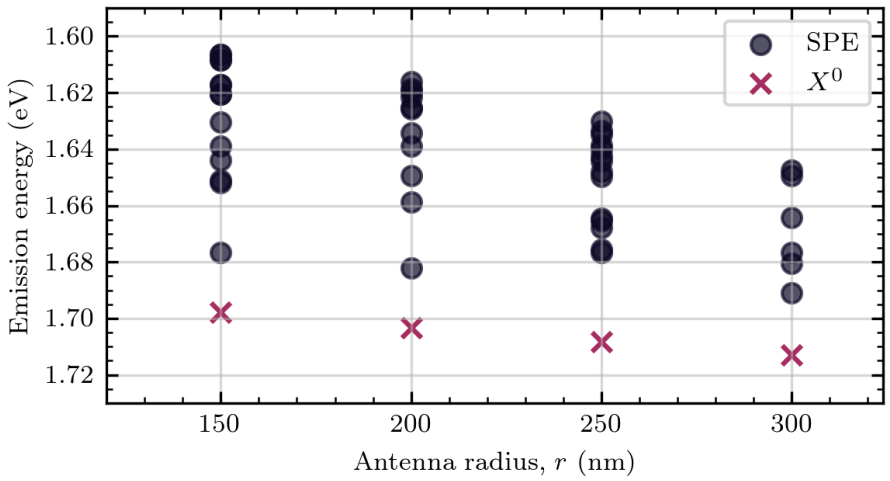

Fig. 7.7 Strain-dependence on the emission energy of monolayer WSe_2 single photon emitters. The localized narrow emitters collected on different GaP nano-antennas (black dots) show a dependence on the antenna radius. In agreement with the red-shift of the neutral exciton (X^0) for smaller radius nano-antennas (purple crosses), related to an increased strain value introduced in the semiconducting membrane, we expect a rigidly shift of the emission energy to lower values for increasing tensile strain. The neutral exciton emission energies are calculated from the unstrained value (see Fig.2.6) and obtained by interpolating the theoretical curve, described in Appendix B, with the experimental gauge of -49 meV/% under tensile strain for the neutral exciton at room temperature [249].

7.3.7 WSe_2 quantum emitters statistics

We now address the statistics of the strain induced WSe_2 SPEs collected in our experimental work. With this effort we try to give a more broad understanding on the nature of these quantum emission by correlating the various properties described in the previous sections.

As shown in Figure 7.8a, we collected a large number of localized emitters and plot the relative SPEs emission energy as a function of the distance from the unstrained bright exciton energy (E_{X^0}). The distribution shows a maximum in its occurrence at -100 meV, corresponding to approximately 1.65 eV, in analogy with what was found in previous studies [156].

As discussed in section 2.3.2, the band structure of atomically thin WSe_2 have a fundamental dark energy state (X^D, dashed line in Fig.7.8a) located at approximately -40 meV

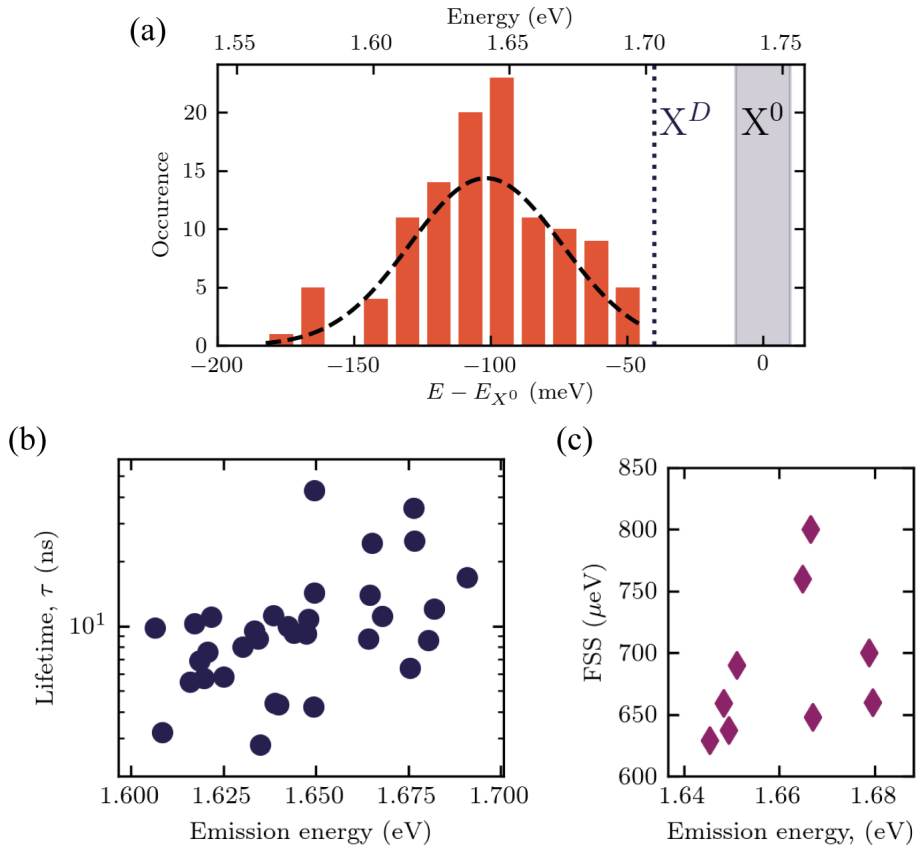

Fig. 7.8 (a) Statistics of the emission energy for a large number of quantum emitters found in strained single layer WSe_2 on top of GaP dimer nano-antennas. The energy is also given as a function of the distance from the unstrained bright exciton energy (X^0, where the grey shaded area defines the linewidth of ≈ 9 meV) and that of the dark exciton energy (X^D). The SPEs distribution shows a maximum at -100 meV from the neutral exciton energy. (b) Lifetimes values of WSe_2 SPEs excited with low power densities (< 200 nW). The emitters above 1.65 eV shows an increased lifetime value compared to the ones below this energy value. (c) Statistics of the fine structure splitting (FSS) energy found at zero magnetic field for various SPEs. No fine structure split emitter is found at energy lower than 1.65 eV.

from the bright exciton energy (X^0, grey shaded area in Fig.7.8a) [96]. We found that all the SPEs in strained WSe_2 on GaP nano-antennas appear below the dark exciton energy which, if we take into account the strain-induced shift, it would be fount at lower energies, in analogy to the behaviour of the neutral exciton. This cut-off in the SPEs emission energy could be related to the recombination of dark excitons via phonon assisted processes or to the presence of additional momentum-dark transitions in the WSe_2 band structure, for instance due to inter-valley coupling. The disorder introduced by strain could reduce the valley degeneracy and lead to inter-valley mixing and, consequently, a way for the dark exciton reservoir to recombine more efficiently. From this picture, if we take into account the shift of the X^D energy due to strain, which in our case we observe up to 1.3% in monolayers (see Chapter 6) and corresponding to a red shift of ≈ 65 meV [249], the maximum of the SPEs distribution at -100 meV could be related to the tuning of the dark exciton energy level via strain.

Figure 7.8b reports the luminescence decay lifetimes for many SPEs, all excited with low power densities (< 200 nW). The distribution shows that for the SPEs above 1.65 eV the lifetimes value tends to be longer, up to few tens of ns, while for those below this value the observed lifetimes are found to be faster, and hardly exceed the value of 10 ns.

Furthermore, the appearance of a FSS in the SPE spectra could be linked to a strong confinement and help in the description of the reported lifetimes. As shown in Figure 7.8c, the values for all the SPEs collected on different radius nano-antennas which exhibits the FSS, show a tendency in the FSS appearance to be related to higher energy SPEs. We note that no FSS doublet is observed in SPEs emitting at energies below 1.65 eV, leading us to believe that the higher energy side of the emission statistics in Figure 7.8a, and the longer lifetimes in this range in Figure 7.8b, can be related to emitters confined in small potential wells. On the other hand, the SPEs in the lower energy side of the distribution in Figure 7.8a experience broader potential wells. This picture is consistent with a particle-in-a-box model, as recently described in a theoretical model for confined excitons in WSe_2, where a larger width of the confined potential is predicted to shift the SPEs emission energy at lower frequencies [159]. Moreover, the shared polarization axis in the emission of the second class of SPEs, could be attributed to the local nano-scale deformations in the WSe_2 layer which selectively orient the exciton polarization along a certain direction of the crystal.

7.4 Conclusions

In conclusions, we have shown the positioning of strain-induced SPEs in 2D -WSe_2 on dielectric nano-antennas. Moreover, the confined optical modes at the nano-antenna surface

lead to an increased photon extraction of the SPEs PL emission, allowing to access the optical signatures of the underlying nature of these quantum emitters.

By accessing bright luminescence at ultra-low power densities, we resolved recurring optical properties in the emission spectrum of the strain-induced SPEs which can be explained in terms of localized excitons into strain-induced distortion potentials. The presence of a growth in the emission intensity of many SPEs, as shown in time resolved luminescence experiments, let us conclude that these narrow emission lines are related to the capture of free neutral excitons, as previously shown in PLE experiments [25], by confinement potential in analogy with the process of exciton trapped by impurities in bulk materials.

Moreover, by looking at the differences in their time and polarization resolved optical properties we are able to distinguish two classes of emitters. The first class appears at higher energies (between -50 and -100 meV from the neutral exciton luminescence) and exhibits long radiative decay times (> 10 ns) and are commonly associated with a fine structure splitting at zero magnetic field. These properties are related to excitons confined in potential wells with narrow spatial extent. The second class of emitters appears at lower emission energies, exhibits faster decay lifetimes and no FSS. Moreover, these emitters exhibit a manifold of peaks which all shares the same polarization axis. These emitters can be ascribed to excitons confined in laerger potential wells, leading to faster exciton capture rates and hosting a larger number of bound states. This can be deduced from the dependence of the energy states in an infinite potential well model, where the confined particle energy states scales as $E_n \propto 1/L^2$, where L is the potential well width.

Quantum emitters in 2D semiconductors are an attractive platform to study the physics of excitonic species in confinement potential. However, the deterministic creation of such states is dependent on a multitude of degrees of freedoms, such as strain, disorder or contaminations. These factors are tightly linked to the local 2D crystal morphology at the nano-scale, which turn out difficult to control precisely. The optical proprieties of such states will remain poorly understood unless a more deterministic way of fabrication, and theoretical understanding, is developed. Here we have shown that the use of dielectric nano-antenna can be a fruitful platform to study 2D SPEs. The use of finer spectroscopy techniques , accessing nano-scale resolution of the SPEs emission, together with non-invasive characterization of the local TMD morphology, could open to a more profound understanding of these quantum states and their integration in next generation quantum technologies.

Chapter 8

Conclusions

8.1 Summary

In this thesis I have explored the light and matter interaction between high-refractive index dielectric nano-antennas and two-dimensional semiconductors. Both of these systems are novel platform in the fields of nano-photonics and nano-materials, respectively, and their integration can be fruitful in the understanding of their physical properties and to demonstrate novel photonic applications.

The physical properties of 2D semiconductors, and in particular the family of transition metal dichalcogenides, are introduced in Chapter 2. Their optical and electronic properties, and favourable integration approaches, have already made them one of the most flourishing platform for photonics in the last decade, leading to numerous studies on the coupling of 2D materials and light in different photonic architectures. On the other hand, dielectric nano-antennas are a novel platform in the field of nano-photonics, sharing many similarities with that of plasmonic excitations in noble metals. A description of the application of optical nano-antennas and the light-matter interaction between luminescent emitters and nano-antennas, and the relative figures of merit, is given in Chapter 3. Dielectric nano-antennas offer new perspectives in the engineering of light-matter interaction at the nano-scale, most of which have been readily demonstrated in the field of meta-surfaces. Here, arrays of transparent high-index nano-structures interacting between each other have been employed to tune the properties of the transmitted or reflected light. Another way to harness the optical properties of dielectric nano-structures is to engineer their interaction with luminescent emitters.

As discussed in Chapter 5, I have showed that such dielectric nano-structures can be readily used to enhance the PL, Raman scattering and radiative lifetime of coupled 2D semiconductors. This is achieved by closely placing an atomic layer of WSe_2 to the antenna

surface, by deterministic transfer of the 2D material on top of GaP nano-antennas. This improvement in the optical properties of 2D-TMDs at room temperature, related to an overall increase in their quantum efficiency, can be used in the enhancement of light emission and absorption in devices comprising atomically thin semiconductors and their heterostructures. Moreover, these results highlight high-index dielectrics as an efficient alternative to plasmonic structures for engineer light-matter coupling on the nano-scale, a field of research that is very young and where the integration with 2D materials have been demonstrated only recently [229, 260].

By exploiting the property of 2D materials, allowing their transfer on arbitrary substrates and onto non-planar structures, I have extended this study to the strain properties of 2D-TMDs interfaced with nano-photonic devices. The unique ability of a 2D crystals to stretch at almost 10% of their length is one of the most appealing properties of these class of materials. However, the platform used to study these effects shows either difficult integration in devices, or low strain values. In Chapter 6 I show how a nano-structure can be used to introduce strain in a 2D layer, and describe this deformation via a mechanical theory, starting from a classical picture of a deflected membrane. Via the optical signatures in the TMD photoluminescence I was able to demonstrate that even such a simple mechanical approximation can be used to describe the effect of strain in this system, allowing the tuning of their excitonic resonances and, moreover, a transition to direct band gap in bilayer TMDs. The most striking features of this approach is that the geometry of the nano-structure can be used to induce a controlled amount of strain, by tailoring its radius, leading to the possibility of engineering the deformation in a 2D membrane from the design of an underlying nano-structure. Moreover, I have proven that a bilayer does experience a larger strain that in the case of a monolayer, related to the higher rigidity, which results in a stronger deformation of the crystal structure when under the same distortion geometry, as in the case of tenting on the same size nano-antennas. An additional features of strained 2D semiconductors is the possibility of tuning the exciton motions by means of an inhomogeneous bandgap profile, resulting in the controlled motion and confinement of the luminescent species. I give evidences in the spatial distribution of the luminescence of coupled TMD/dielectric nano-antenna system where is confirmed that free excitons are captured into confinement potentials, in good agreement with the proposed theoretical model.

This approach to introduce strain in a 2D crystal demonstrated its potential in the creation of single photon emitters in atomically thin WSe_2 at cryogenic temperatures, as discussed in Chapter 7. These results open the way to the use of dielectric nano-antennas as a novel substrate for the creation of 2D quantum emitters, and to study their light-matter interaction.

While being a promising platform for quantum light emission, the lack of control over the optical properties is a standing problem in the development of 2D single photons. Here, we showed how a photonic nano-structure can be used to both position the quantum emitter and place it in very close proximity to confined electromagnetic modes in order to enhance their optical properties. However, for a more throughout study of these luminescent species a higher resolution in both the spectroscopy and morphology analysis is needed. For instance the implementation of AFM with near-field optics spectroscopic techniques could expand the understanding of such quantum emission and relate it to the local nano-scale morphology.

8.2 Outlook

The field of 2D materials is one of the most flourishing and fast-pacing research in the latest decade. The amount of future plans and possible applications increase every years, with possibly more to come in the future. This section will expand the results of this thesis work in the frame of more exciting prospects from the ones described in this work.

8.2.1 Dielectric nano-photonics and 2D materials

The research on dielectric nano-antenna is one of the youngest fields in nano-photonics and many of their qualities and applications are yet to be described. Coupling to the near-field of nano-antennas can be used to significantly enhance the quantum yield of 2D semiconductors, with potential for light emission and absorption enhancement in atomically thin structures made of van der Waals materials. Moreover, the presence of both an electric and magnetic response in dielectric nano-antennas can be theoretically use to promote dark transition which shows magnetic moments, as in spin forbidden transition in dark TMDs, a research path which has not been explored yet. The appealing spin-coupled valley degree of freedom in 2D-TMDs could also benefit in the integration with dielectric nano-photonics, as it have been recently shown in case of plasmonic nano-structures [229]. This approach could be expanded to dielectric nano-structures made of different high-index materials and coupling to more 2D materials compounds. This can be achieved by carefully engineering the resonances of nano-antennas together with the optical responses of the selected atomically thin structures. As previously stated, this approach can then be expanded to meta-surfaces where the 2D layers can be integrated as a gain medium for novel photonic applications. Novel van der Waals nano-photonics structures made from high refractive index multilayer TMDs [234]

could also be used in the coupling with 2D excitons, for the development of novel photonic application only with layered van der Waals nano-materials.

8.2.2 Strain effects induced by nano-photonic structures

The use of strain in a semiconductor coupled with nano-photonic structures is a novel concept which can implemented as an additional degree of freedom in the light-matter engineering with 2D materials. This approach could be readily used in studying 2D excitonic species in confined potentials, which theoretically could be expanded to host single excitons in a potential well, opening to novel physical insights as in strongly interacting excitons. On another hand, the presence of indirect excitons in heterostructures made from different TMD layers, could find applications in the use of both strain confinement and coupling to strong electromagnetic fields, in order to push the exciton population into localized sites and achieve Bose-Einstein condensation of the confined excitonic species. The continuum mechanical theoretical approach we have used shows a great feasibility and could be expanded to describe strain distributions, and relative distortion potential, for 2D-TMDs coupled to lower symmetric and more complex nano-structures geometries. By carefully designing the strain profiles of 2D crystals on complex nano-structures it is possible to tailor the local bandgap profile of the 2D layer, introducing interfaces which could be used for charge separation or even waveguiding excitons species via the funnel effect.

8.2.3 Quantum emission in 2D materials

Quantum emitters in 2D semiconductors are an attractive platform to study quantum physics at a single exciton level. However, the understating of their nature and the control over their optical properties is still the main obstacle when compared to more mature technologies and the required properties of single photon sources for real life quantum applications. Nonetheless, research is indeed meant to advance our understanding and provide new approaches in the study of nano-scale phenomena. The use of dielectric nano-antennas for positioning of single photon emitters in 2D TMDs shows promising results as in the ease of fabrication and possibility of tailoring many degree of freedom in the system, for instance optical resonances, strain magnitude and shape. The effort of developing more controllable fabrication schemes and higher resolution spectroscopy could lead to advances in this field and make 2D quantum emitters more competitive in the overall framework of quantum technologies.

Appendix A

GaP dimer nano-antennas simulations

This section covers the simulation of the GaP nano-antennas used throughout this work. The simulation were carried with a finite-difference time-domain (FDTD) method (Lumerical software) by Sandro Mignuzzi and Javier Cambiasso from the group of Riccardo Sapienza and Stefan A. Maier at Imperial College London.

A.1 Scattering cross sections

The scattering cross section of a nano-particle can be defined as the ratio between the power radiated by the nano-antenna over the incident power [165] $\sigma_{scatt}(\omega) = W_{rad}(\omega)/I_{exc}(\omega)$. The corresponding absorption efficiency can be estimated as $\sigma_{abs} = \sigma_{ext} - \sigma_{scatt}$, where σ_{ext} is the extinction cross section. The relative efficiency, $Q_{scatt}(Q_{abs})$, is calculated as the ratio between the relative cross section divided by the geometric area of the dimer, given by $A_{geom} = 2 \times \pi r^2$, where r is the nano-pillar radius. Fig.A.1 shows the calculated scattering efficiency for different radii GaP dimer nano-antennas, and for X and Y polarization geometries. As shown, the scattering response fully overlaps with the PL emission profile of monolayer WSe_2.

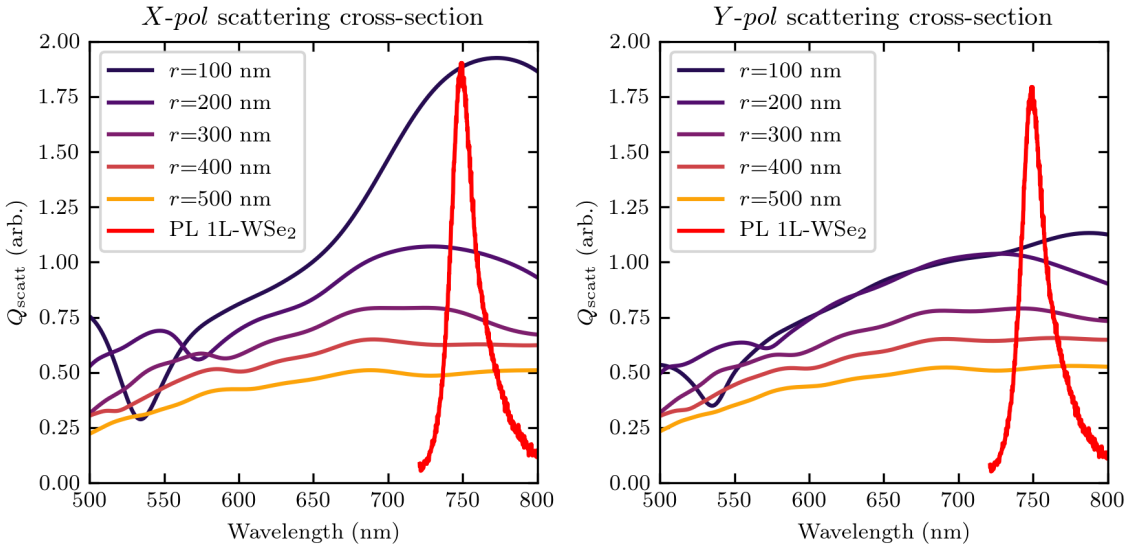

Fig. A.1 Simulated scattering cross section (Q_{scatt}) for different radii GaP dimer nano-antennas, with 65 nm gap width and excited at $\lambda_{exc} = 685$ nm, under different polarization geometries.

A.2 Calculation of the effective interaction area

The effective interaction area of the antenna near-field, $A_{eff}(\lambda_{exc})$, for different radius dimer antennas with h= 200 nm and g = 65 nm excited at $\lambda_{exc} = 685$ nm, is calculated by integrating a volume element over the regions of space where the electric field amplitude was enhanced, following the method outlined in Ref.[190]. Note, this does not mean that the whole top surface of the pillars contributes to the enhanced PL in the same way, as shown in the PL imaging in Chapter 5 where most of the emission is found to be localized around the edges and in the dimer gap. The effective interaction area is calculated where the field enhancement is larger than a threshold relative to the electric field maximum ($|\mathbf{E}_M|^2$), set equal to 1/2, on the topmost surface of the nano-antennas. With this threshold conditions, only the excitons inside this area experience the excitation enhancement, thus contributing to the effective PL enhancement, while the emitters outside this region are omitted due to the negligible contribution in the excitation enhancement. The effective area for the two pillars is calculated with the following formula:

$$A_{eff}(\lambda_{exc}) = 2 \times \pi r_{eff}^2(\lambda_{exc}) = 2 \times \int_0^R \int_0^{2\pi} \Theta[\frac{|\mathbf{E}(r,\theta,0;\lambda_{exc})|^2}{|\mathbf{E}_M|^2} - 1/2]\, r\, \mathrm{d}r\mathrm{d}\theta \qquad (A.1)$$

here, Θ represent the Heaviside step function (1 for $x \geqslant 0$, 0 for $x < 0$). The values of A_{eff} calculated using this method are shown in Fig.A.2, where they are compared with the geometric area of the dimers ($A_{dimer} = 2 \times \pi r^2$). As can be seen, both values have very close coincidence, with the only difference for the smallest pillar, where A_{dimer} is larger than A_{eff}.

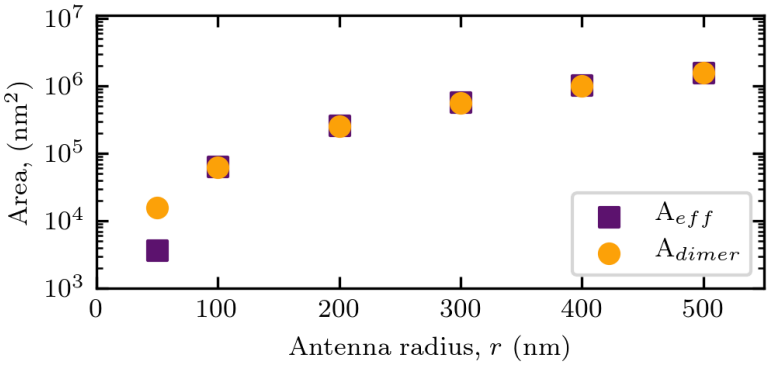

Fig. A.2 Comparison between the geometrical area of the top surface of a dimer (A_{dimer}) and the effective interaction area (A_{eff}).

A.3 Radiative emission pattern

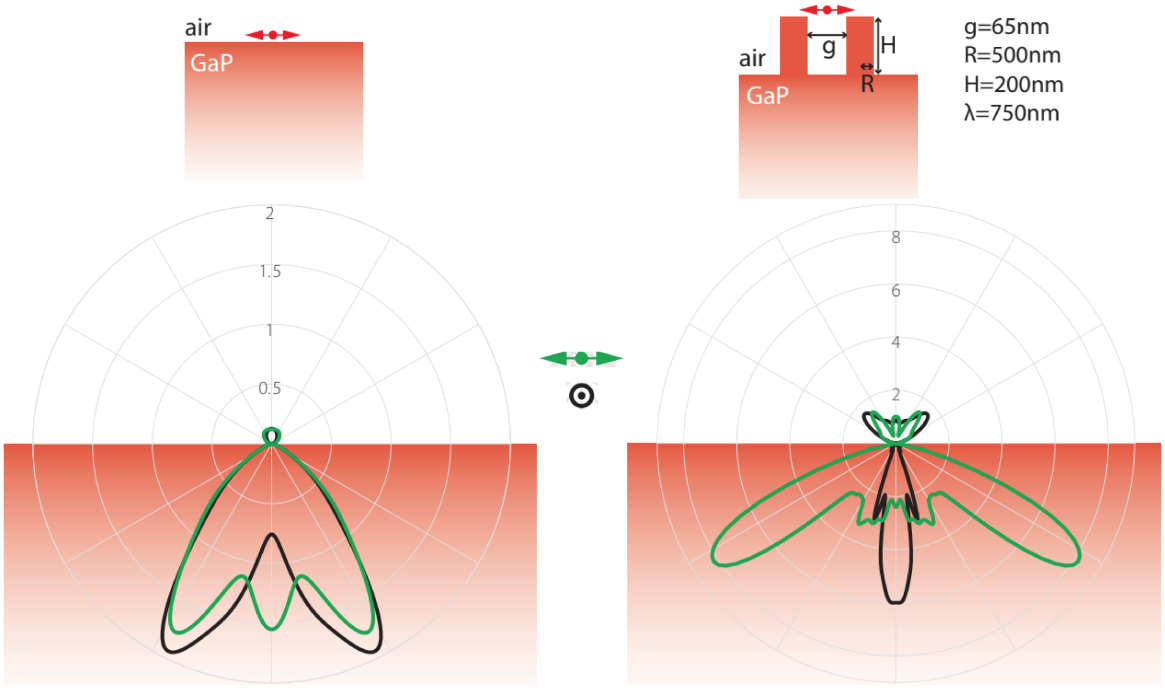

Fig. A.3 Radiative emission pattern for a dipole placed on planar GaP (left) and above the middle of the gap of a dimer nano-antenna (right) for a direction parallel (green) and perpendicular (black) to the line connecting the two nano-pillars. Although most of the emitted light is directed into the higher index substrate, the emission in air is strongly increased due to the presence of the dimer nano-structure.

A.4 Electric and magnetic field profiles

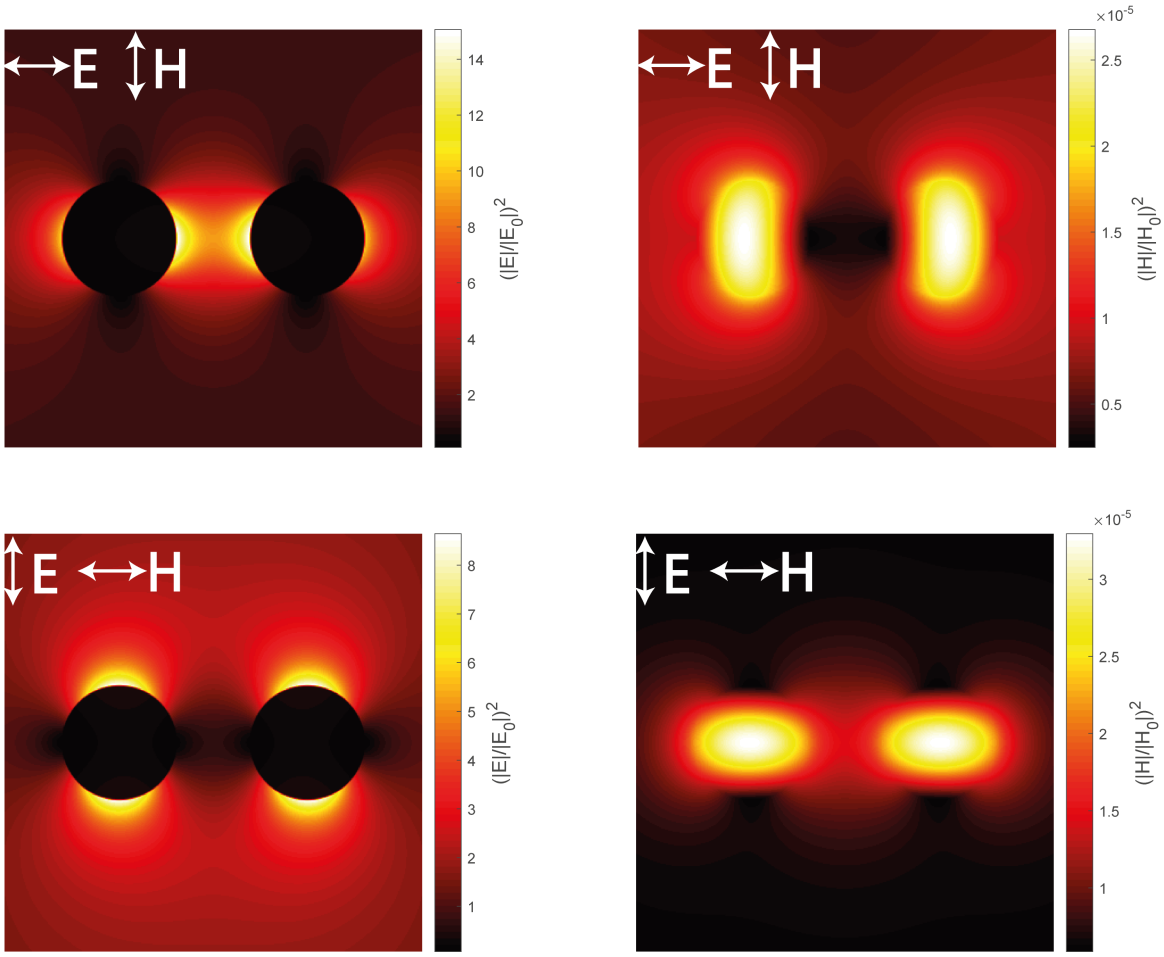

Fig. A.4 Electric (E) and magnetic (H) field distributions calculated for a GaP dimer nano-antenna (height 200 nm, radius 50 nm, gap 65 nm) illuminated with a normally incident plane wave (λ_{exc} = 685 nm). Relative field amplitudes are shown normalised by the amplitudes of the electric (E_0) and magnetic (H_0) fields in the incident wave. The polarisation of the incident light is shown with arrows. The distributions are calculated at half-height of the nano-antenna (z = 100 nm)

A.5 Purcell factor

The Purcell enhancement is calculated as the decay rate γ_r of an emitter coupled to the GaP nano-antenna, normalised with the decay rate γ_r^0 of an emitter on a planar GaP substrate. The decay rate enhancement γ_r/γ_r^0 corresponds to the enhancement of the rate of energy dissipation P/P_0. We have calculated the power P radiated by an electric dipole at 0.5 nm distance from the top surface of the GaP pillars, for different positions over the dimer, and compared that to the power P_0 radiated by the same dipole placed 0.5 nm above the surface of the planar substrate. In order to model our experimental system where photoluminescence in WSe_2 originates from the in-plane excitons, the dipole is placed parallel to the surface of the pillars or the substrate, polarised along the direction parallel or perpendicular to the dimer axis. Fig. A.5a plots the 2D maps of the Purcell enhancement around the dimer, for the two dipole orientations as indicated by the white arrow. In Fig. A.5b a dependence of γ_r/γ_r^0 on the position in the dimer gap is shown for a dimer with r=50 nm. Strong maxima are observed close to the edges of the pillars (marked with dotted lines in Fig. A.5a) with the Purcell enhancement values reaching 15. As Fig.A.5c shows, the maximum Purcell enhancement values increase as r is varied from 500 to 50 nm, while their positions remain the same in the proximity of the pillar edges.

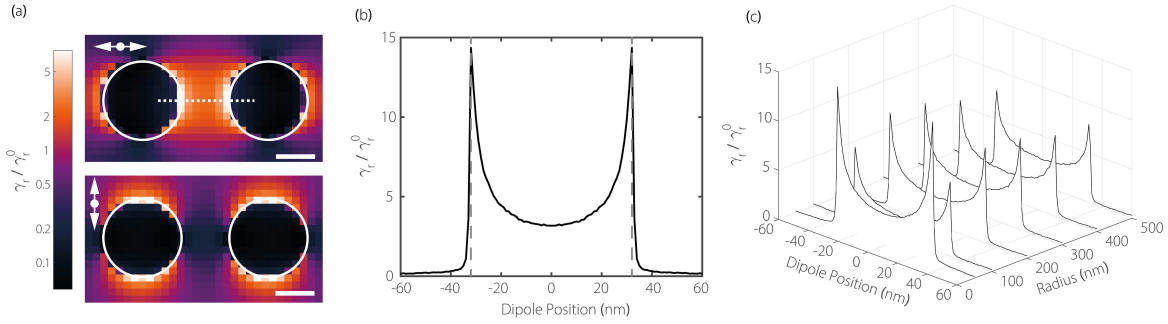

Fig. A.5 (a) Maps showing decay rate enhancement γ_r/γ_r^0 for a dipolar emitter orientated parallel and perpendicular to the dimer axis, with pillars of radius r=50 nm. Scale bar is 50 nm. Dependence of γ_r/γ_r^0 within the dimer gap for a dipolar emitter oriented parallel to the dimer axis shown by the dotted line in (a). The dotted line in (b) marks the edges of the pillars. (c) Dependences of γ_r/γ_r^0 as in (b) plotted for dimers with different r, with gap fixed at 65 nm.

Appendix B

Theoretical description of strained 2D layers

In this section is described the continuum theoretical model for the TMDs strain topography on top of dielectric nano-pillars used in the description of the results in Chapter 6. The model have been developed by Matthew Brooks from the group of Guido Burgkard at the University of Konstanz, based on the approach described in Ref.[124].

B.1 Strain topography theoretical modelling

The strain topography of stretched TMD layers is achieved by modelling the out-of-plane displacement relative to the underlying substrate. We applied a continuum-mechanical plate-theory approach [124] with the following reduced form of the Föppl-von Kármán equations, valid for such passively strained low-dimensional systems [261]:

$$D\Delta^2\zeta - P = 0 \tag{B.1}$$

where P is the pressure the atomic layer experiences, ζ is the height field, Δ^2 is the biharmonic operator, given by the square of the Laplacian Δ, and D is the flexural rigidity of the TMD layer defined as:

$$D = \frac{Eh^3}{12(1-\sigma^2)} \tag{B.2}$$

here E is the Young's modulus, σ is the Poisson's ratio and h is the TMD layer thickness.

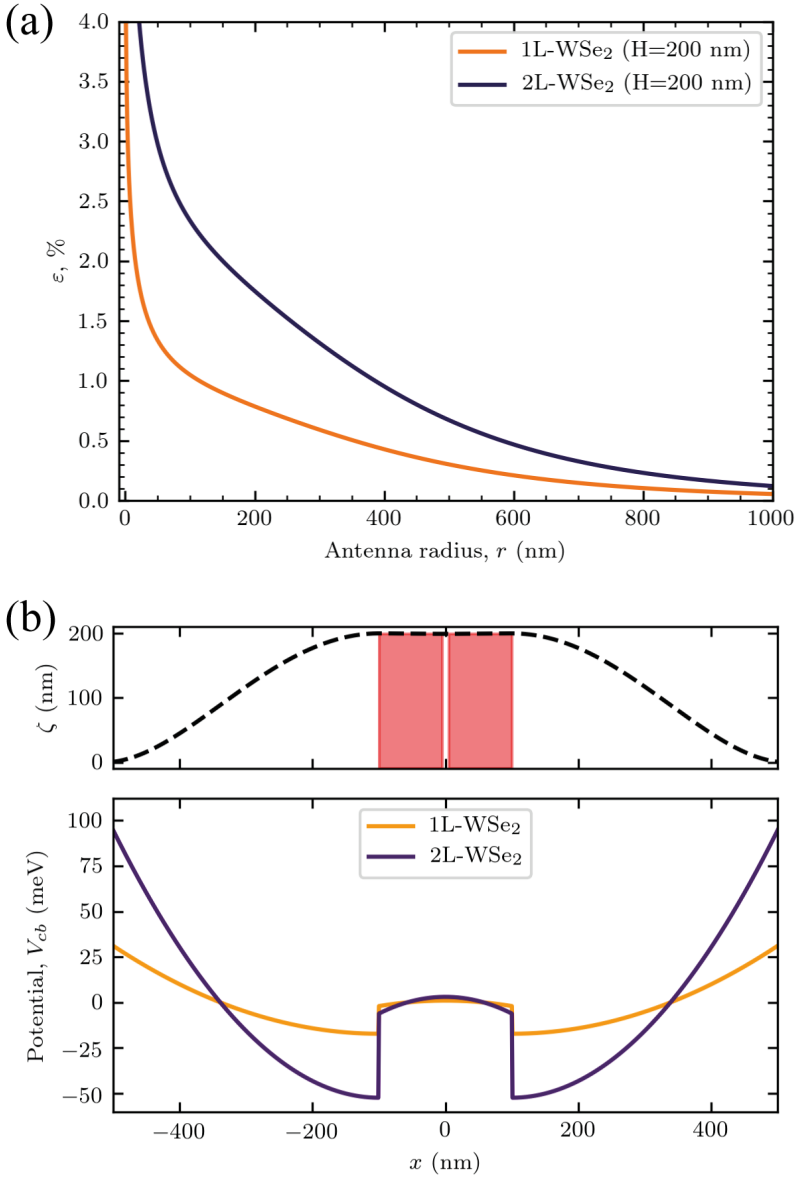

Fig. B.1 (a) Theoretical values of uniaxial tensile strain for single and double layer WSe_2 as a function of the dimer nano-pillar radius. The uniaxial tensile strain values are calculated around the topmost edge of a dimer nano-antenna (H = 200 nm), for both single and double layer WSe_2. (b) Theoretical model of the distortion potential profile. Top: Height field profile (black dashed line) for a dimer with $H = 200$ nm and $R_m = 50$ nm, schematically shown in red. Bottom: Value of the conduction band potential minimum (V_{cb}), at the K point of the Brillouin zone, calculated for both single (1L) and double (2L) layer WSe_2, relative the same height field profile shown on top. The compressive (tensile) strain region is correlated to an increase (decrease) in the V_{cb} value.

To model the WSe_2 strain topography above the dimer structure, we found a solution to Eq.B.1. The model of pressure adopted here, consistent with the microscopy measurements, is the P = 0 model [124] with boundary conditions:

$$\zeta_{P=0}(R_m) = H \tag{B.3}$$

$$\zeta_{P=0}(R) = 0 \tag{B.4}$$

$$\partial_r \zeta_{P=0}|_{R_m,R} = 0 \tag{B.5}$$

where H is the height of the dimer antenna, R_m is the nano-pillar radius and R is the tenting radius, the distance between the antenna pillars at the point where the WSe_2 meets the substrate at $H = 0$. We obtain the following analytical solution for the height field, relative to a single pillar, in rotational symmetry:

$$\zeta_{P=0}(r) = \frac{H}{(R^2 - R_m^2)^2 - 4R^2R_m^2 \ln^2\left[\frac{R}{R_m}\right]} \left\{ 2R^2 \ln[R] \left(R_m^2 + 2R_m^2 \ln\left[\frac{R_m}{R}\right] - r^2 \right) \right. \tag{B.6}$$

$$+ \left(r^2 - R^2\right)\left(R_m^2 + 2R_m^2 \ln[R_m] - R^2\right) \tag{B.7}$$

$$\left. +2\ln[r] \left(r^2\left(R^2 - R_m^2\right) + 2R^2R_m^2 \ln\left[\frac{R}{R_m}\right] \right) \right\} \tag{B.8}$$

Taking this approximation as a starting point, we obtain a numerically averaged height field over the dimer geometry by taking values of R from microscopy measurements, and interpolation in the gap region where the rational symmetry of the approximate model is violated. From a satisfactory model of the height field, the strain component responsible for the band gap renormalization is given by the trace $\mathscr{D}$ of the strain tensor ε_{ij}, given as [262]:

$$\mathscr{D} = Tr[\varepsilon_{ij}] = \frac{(2\sigma - 1)h}{1 - \sigma}\Delta\zeta \tag{B.9}$$

We resolved a relationship between the tensile strain maximum and the nano-pillars radius. Fig.B.1a shows the calculated strain values at the topmost edge of a nano-antenna ($H = 200$ nm), as a function of the nano-pillar radius. For both 1L and 2L-WSe_2 we observe an increased strain value as the nano-antenna radius decreases, with a stronger magnitude for the bilayer. This trend can be explained as the assumed model approaches a deflection of a

Dirac-delta like deformation, when $r \to 0$, giving an undefined pole in the strain value. An increased strain in bilayers is directly related to its larger rigidity (D).

B.2 Strain-induced deformation potential

After defining a strain topography, it is possible to calculate a strain-induced deformation potential in the WSe_2 band structure, following a tight-binding approach [262, 124], as:

$$V = \begin{pmatrix} \delta_v \mathscr{D} & 0 \\ 0 & \delta_c \mathscr{D} \end{pmatrix} \tag{B.10}$$

where δ_c and δ_v are the parameters governing the strain response for the conduction and valence band at the K/K' point, respectively. In Fig.B.1b is shown the calculated valence band deformation potential, calculated for both 1L and 2L-WSe_2, on a dimer structure with $r = 50$ nm, along the line connecting the centre of the two nano-pillars. We found a stronger modulation for the bilayer, as expected from the higher strain values shown in Fig.B.1a. The potential profile is correlated with the local reduction (increase) of WSe_2 bandgap under tensile (compressive) strain. As such, the maximum tensile deformation, located at the nano-antenna edges ($x \pm 100$ nm), corresponds to a decrease in the conduction band minimum. In correspondence with the compressive strain area, where the layers meet the substrate ($x \pm 500$ nm), the bandgap energy is increased, due to the lifting of V_{cb}, resulting in a potential barrier for trapped excitons. Due to the expected confinement of optically generated excitons in such a potential landscape, this modulation of the local WSe_2 band structure can trap excitons via the funnelling effect [128].

References

[1] Novoselov, K. S. Electric Field Effect in Atomically Thin Carbon Films. *Science (80-.).* **306**, 666–669 (2004). URL http://www.sciencemag.org/cgi/doi/10.1126/science.1102896. 0410550.

[2] Novoselov, K. S. *et al.* Two-dimensional atomic crystals. *Proc. Natl. Acad. Sci.* **102**, 10451–10453 (2005). URL http://www.pnas.org/cgi/doi/10.1073/pnas.0502848102. 0503533.

[3] Geim, A. K. & Novoselov, K. S. The rise of graphene. *Nat. Mater.* **6**, 183–191 (2007). URL http://www.nature.com/articles/nmat1849.

[4] Castellanos-Gomez, A. Why all the fuss about 2D semiconductors? *Nat. Photonics* **10**, 202–204 (2016). URL http://dx.doi.org/10.1038/nphoton.2016.53.

[5] Geim, A. K. & Grigorieva, I. V. Van der Waals heterostructures. *Nature* **499**, 419–425 (2013). URL http://www.nature.com/articles/nature12385.

[6] Xu, M., Liang, T., Shi, M. & Chen, H. Graphene-Like Two-Dimensional Materials. *Chem. Rev.* **113**, 3766–3798 (2013). URL http://pubs.acs.org/doi/abs/10.1021/cr300263a.

[7] Butler, S. Z. *et al.* Progress, Challenges, and Opportunities in Two-Dimensional Materials Beyond Graphene. *ACS Nano* **7**, 2898–2926 (2013). URL http://pubs.acs.org/doi/abs/10.1021/nn400280c.

[8] Fiori, G. *et al.* Electronics based on two-dimensional materials. *Nat. Nanotechnol.* **9**, 768–779 (2014). URL http://www.nature.com/articles/nnano.2014.207.

[9] Xia, F., Wang, H., Xiao, D., Dubey, M. & Ramasubramaniam, A. Two-dimensional material nanophotonics. *Nat. Photonics* **8**, 899–907 (2014). URL http://www.nature.com/articles/nphoton.2014.271. 1410.3882.

[10] Akinwande, D., Petrone, N. & Hone, J. Two-dimensional flexible nanoelectronics. *Nat. Commun.* **5**, 5678 (2014). URL http://www.nature.com/doifinder/10.1038/ncomms6678.

[11] Liu, Y., Huang, Y. & Duan, X. Van der Waals integration before and beyond two-dimensional materials. *Nature* **567**, 323–333 (2019). URL http://www.nature.com/articles/s41586-019-1013-x.

[12] Li, M.-Y., Su, S.-K., Wong, H.-S. P. & Li, L.-J. How 2D semiconductors could extend Moore's law. *Nature* **567**, 169–170 (2019). URL http://www.nature.com/articles/d41586-019-00793-8.

[13] Novoselov, K. S., Mishchenko, A., Carvalho, A. & Castro Neto, A. H. 2D materials and van der Waals heterostructures. *Science (80-.).* **353**, aac9439–aac9439 (2016). URL http://www.sciencemag.org/cgi/doi/10.1126/science.aac9439.

[14] Liu, Y. *et al.* Van der Waals heterostructures and devices. *Nat. Rev. Mater.* **1**, 16042 (2016). URL http://www.nature.com/articles/natrevmats201642.

[15] Withers, F. *et al.* Light-emitting diodes by band-structure engineering in van der Waals heterostructures. *Nat. Mater.* **14**, 301–306 (2015). URL http://www.nature.com/articles/nmat4205.

[16] Rivera, P. *et al.* Interlayer valley excitons in heterobilayers of transition metal dichalcogenides. *Nat. Nanotechnol.* **13**, 1004–1015 (2018). URL http://www.nature.com/articles/s41565-018-0193-0.

[17] Song, J. C. W. & Gabor, N. M. Electron quantum metamaterials in van der Waals heterostructures. *Nat. Nanotechnol.* **13**, 986–993 (2018). URL http://www.nature.com/articles/s41565-018-0294-9.

[18] Cao, Y. *et al.* Unconventional superconductivity in magic-angle graphene superlattices. *Nature* **556**, 43–50 (2018). URL http://www.nature.com/articles/nature26160.

[19] Jin, C. *et al.* Observation of moiré excitons in WSe_2/WS_2 heterostructure superlattices. *Nature* **567**, 76–80 (2019). URL http://www.nature.com/articles/s41586-019-0976-y.

[20] Alexeev, E. M. *et al.* Resonantly hybridized excitons in moiré superlattices in van der Waals heterostructures. *Nature* **567**, 81–86 (2019). URL http://www.nature.com/articles/s41586-019-0986-9.

[21] Burch, K. S., Mandrus, D. & Park, J.-G. Magnetism in two-dimensional van der Waals materials. *Nature* **563**, 47–52 (2018). URL http://www.nature.com/articles/s41586-018-0631-z.

[22] Gibertini, M., Koperski, M., Morpurgo, A. F. & Novoselov, K. S. Magnetic 2D materials and heterostructures. *Nat. Nanotechnol.* **14**, 408–419 (2019). URL http://www.nature.com/articles/s41565-019-0438-6.

[23] Li, P. *et al.* Evidence for topological type-II Weyl semimetal WTe_2. *Nat. Commun.* **8**, 2150 (2017). URL http://www.nature.com/articles/s41467-017-02237-1.

[24] Tran, T. T., Bray, K., Ford, M. J., Toth, M. & Aharonovich, I. Quantum emission from hexagonal boron nitride monolayers. *Nat. Nanotechnol.* **11**, 37–41 (2015). URL http://www.nature.com/doifinder/10.1038/nnano.2015.242. 1504.06521.

[25] Tonndorf, P. *et al.* Single-photon emission from localized excitons in an atomically thin semiconductor. *Optica* **2**, 347 (2015). URL https://www.osapublishing.org/abstract.cfm?URI=optica-2-4-347.

[26] Dirac, P. a. M. The Quantum Theory of the Emission and Absorption of Radiation. *Proc. R. Soc. A Math. Phys. Eng. Sci.* **114**, 243–265 (1927). URL http://rspa.royalsocietypublishing.org/cgi/doi/10.1098/rspa.1927.0039.

[27] Purcell, E. M., Torrey, H. C. & Pound, R. V. Resonance Absorption by Nuclear Magnetic Moments in a Solid. *Phys. Rev.* **69**, 37–38 (1946). URL https://link.aps.org/doi/10.1103/PhysRev.69.37.

[28] Vahala, K. J. Optical microcavities. *Nature* **424**, 839–846 (2003). URL http://www.nature.com/doifinder/10.1038/nature01939.

[29] Chikkaraddy, R. *et al.* Single-molecule strong coupling at room temperature in plasmonic nanocavities. *Nature* **535**, 127–130 (2016). URL http://dx.doi.org/10.1038/nature17974.

[30] Baranov, D. G., Wersäll, M., Cuadra, J., Antosiewicz, T. J. & Shegai, T. Novel Nanostructures and Materials for Strong Light-Matter Interactions. *ACS Photonics* **5**, 24–42 (2018). URL http://pubs.acs.org/doi/10.1021/acsphotonics.7b00674.

[31] Maier, S. A. *Plasmonics: Fundamentals and Applications* (Springer US, New York, NY, 2007). URL http://link.springer.com/10.1007/0-387-37825-1.

[32] Kuznetsov, A. I., Miroshnichenko, A. E., Brongersma, M. L., Kivshar, Y. S. & Luk'yanchuk, B. Optically resonant dielectric nanostructures. *Science (80-.).* **354**, aag2472 (2016). URL http://www.sciencemag.org/lookup/doi/10.1126/science.aag2472.

[33] Einstein, A., Podolsky, B. & Rosen, N. Can quantum-mechanical description of physical reality be considered complete? *Phys. Rev.* 2–5 (1935). URL http://prola.aps.org/abstract/PR/v47/i10/p777_1.

[34] DiVincenzo, D. P. The Physical Implementation of Quantum Computation. *Fortschritte der Phys.* **48**, 771–783 (2000). URL http://doi.wiley.com/10.1002/1521-3978%28200009%2948%3A9%2F11%3C771%3A%3AAID-PROP771%3E3.0.CO%3B2-E.

[35] Kimble, H. J. The quantum internet. *Nature* **453**, 1023–1030 (2008). URL http://www.nature.com/articles/nature07127.

[36] O'Brien, J. L., Furusawa, A. & Vučković, J. Photonic quantum technologies. *Nat. Photonics* **3**, 687–695 (2009). URL http://www.nature.com/articles/nphoton.2009.229.

[37] Kok, P. *et al.* Linear optical quantum computing with photonic qubits. *Rev. Mod. Phys.* **79**, 135–174 (2007). URL https://link.aps.org/doi/10.1103/RevModPhys.79.135.

[38] Politi, A., Cryan, M. J., Rarity, J. G., Yu, S. & O'Brien, J. L. Silica-on-Silicon Waveguide Quantum Circuits. *Science (80-.).* **320**, 646–649 (2008). URL http://www.sciencemag.org/cgi/doi/10.1126/science.1155441.

[39] Lounis, B. & Orrit, M. Single-photon sources. *Reports Prog. Phys.* **68**, 1129–1179 (2005). URL https://iopscience.iop.org/article/10.1088/0034-4885/68/5/R04.

[40] Hadfield, R. H. Single-photon detectors for optical quantum information applications. *Nat. Photonics* **3**, 696–705 (2009). URL http://www.nature.com/articles/nphoton.2009.230.

[41] Kimble, H. J., Dagenais, M. & Mandel, L. Photon Antibunching in Resonance Fluorescence. *Phys. Rev. Lett.* **39**, 691–695 (1977). URL https://link.aps.org/doi/10.1103/PhysRevLett.39.691.

[42] Shields, A. J. Semiconductor quantum light sources. *Nat. Photonics* **1**, 215–223 (2007). URL http://www.nature.com/articles/nphoton.2007.46.

[43] Aharonovich, I., Englund, D. & Toth, M. Solid-state single-photon emitters. *Nat. Photonics* **10**, 631–641 (2016). URL http://www.nature.com/doifinder/10.1038/nphoton.2016.186.

[44] Senellart, P., Solomon, G. & White, A. High-performance semiconductor quantum-dot single-photon sources. *Nat. Nanotechnol.* **12**, 1026–1039 (2017). URL http://www.nature.com/doifinder/10.1038/nnano.2017.218.

[45] Wilson, J. & Yoffe, A. The transition metal dichalcogenides discussion and interpretation of the observed optical, electrical and structural properties. *Adv. Phys.* **18**, 193–335 (1969). URL http://www.tandfonline.com/doi/abs/10.1080/00018736900101307.

[46] Dickinson, R. G. & Pauling, L. The crystal structure of molybdenite. *J. Am. Chem. Soc.* **45**, 1466–1471 (1923). 1601.07981.

[47] Manzeli, S., Ovchinnikov, D., Pasquier, D., Yazyev, O. V. & Kis, A. 2D transition metal dichalcogenides. *Nat. Rev. Mater.* **2** (2017). URL http://www.nature.com/articles/natrevmats201733.

[48] Wang, Q. H., Kalantar-Zadeh, K., Kis, A., Coleman, J. N. & Strano, M. S. Electronics and optoelectronics of two-dimensional transition metal dichalcogenides. *Nat. Nanotechnol.* **7**, 699–712 (2012). URL http://www.nature.com/articles/nnano.2012.193.

[49] Mak, K. F. & Shan, J. Photonics and optoelectronics of 2D semiconductor transition metal dichalcogenides. *Nat. Photonics* **10**, 216–226 (2016). URL http://www.nature.com/doifinder/10.1038/nphoton.2015.282.

[50] Chhowalla, M. *et al.* The chemistry of two-dimensional layered transition metal dichalcogenide nanosheets. *Nat. Chem.* **5**, 263–275 (2013). URL http://www.nature.com/doifinder/10.1038/nchem.1589.

[51] Radisavljevic, B., Radenovic, A., Brivio, J., Giacometti, V. & Kis, A. Single-layer MoS_2 transistors. *Nat. Nanotechnol.* **6**, 147–150 (2011). URL http://www.nature.com/articles/nnano.2010.279.

[52] Lopez-Sanchez, O., Lembke, D., Kayci, M., Radenovic, A. & Kis, A. Ultrasensitive photodetectors based on monolayer MoS_2. *Nat. Nanotechnol.* **8**, 497–501 (2013). URL http://www.nature.com/doifinder/10.1038/nnano.2013.100.

[53] Bertolazzi, S., Brivio, J. & Kis, A. Stretching and breaking of ultrathin MoS_2. *ACS Nano* **5**, 9703–9709 (2011). URL http://pubs.acs.org/doi/abs/10.1021/nn203879f.

[54] Zhang, Y. *et al.* Direct observation of the transition from indirect to direct bandgap in atomically thin epitaxial $MoSe_2$. *Nat. Nanotechnol.* **9**, 111–115 (2014). URL http://www.nature.com/articles/nnano.2013.277.

[55] Splendiani, A. *et al.* Emerging Photoluminescence in Monolayer MoS_2. *Nano Lett.* **10**, 1271–1275 (2010). URL http://pubs.acs.org/doi/abs/10.1021/nl903868w.

[56] Mak, K. F., Lee, C., Hone, J., Shan, J. & Heinz, T. F. Atomically Thin MoS_2 : A New Direct-Gap Semiconductor. *Phys. Rev. Lett.* **105**, 136805 (2010). URL https://link.aps.org/doi/10.1103/PhysRevLett.105.136805.

[57] Chang, C.-H., Fan, X., Lin, S.-H. & Kuo, J.-L. Orbital analysis of electronic structure and phonon dispersion in MoS_2, $MoSe_2$, WS_2 and WSe_2 monolayers under strain. *Phys. Rev. B* **88**, 195420 (2013). URL https://link.aps.org/doi/10.1103/PhysRevB.88.195420.

[58] Kormányos, A. *et al.* $\mathbf{k} \cdot \mathbf{p}$ theory for two-dimensional transition metal dichalcogenide semiconductors. *2D Mater.* **2**, 022001 (2015). URL https://iopscience.iop.org/article/10.1088/2053-1583/2/2/022001.

[59] Xiao, D., Liu, G.-B., Feng, W., Xu, X. & Yao, W. Coupled Spin and Valley Physics in Monolayers of MoS_2 and Other Group-VI Dichalcogenides. *Phys. Rev. Lett.* **108**, 196802 (2012). URL https://link.aps.org/doi/10.1103/PhysRevLett.108.196802.

[60] Castro Neto, A. H., Guinea, F., Peres, N. M. R., Novoselov, K. S. & Geim, A. K. The electronic properties of graphene. *Rev. Mod. Phys.* **81**, 109–162 (2009). URL https://link.aps.org/doi/10.1103/RevModPhys.81.109.

[61] Novoselov, K. S. *et al.* Two-dimensional gas of massless Dirac fermions in graphene. *Nature* **438**, 197–200 (2005). URL http://www.nature.com/articles/nature04233.0509330.

[62] Xiao, D., Yao, W. & Niu, Q. Valley-contrasting physics in graphene: Magnetic moment and topological transport. *Phys. Rev. Lett.* **99**, 236809 (2007). URL http://link.aps.org/doi/10.1103/PhysRevLett.99.236809.

[63] Zhu, Z. Y., Cheng, Y. C. & Schwingenschlögl, U. Giant spin-orbit-induced spin splitting in two-dimensional transition-metal dichalcogenide semiconductors. *Phys. Rev. B* **84**, 153402 (2011). URL http://link.aps.org/doi/10.1103/PhysRevB.84.153402.

[64] Xu, X., Yao, W., Xiao, D. & Heinz, T. F. Spin and pseudospins in layered transition metal dichalcogenides. *Nat. Phys.* **10**, 343–350 (2014). URL http://www.nature.com/doifinder/10.1038/nphys2942.

[65] Schaibley, J. R. *et al.* Valleytronics in 2D materials. *Nat. Rev. Mater.* **1**, 16055 (2016). URL http://www.nature.com/articles/natrevmats201655.

[66] Mak, K. F., Xiao, D. & Shan, J. Light–valley interactions in 2D semiconductors. *Nat. Photonics* **12**, 451–460 (2018). URL http://www.nature.com/articles/s41566-018-0204-6.

[67] Wang, G. *et al.* Colloquium : Excitons in atomically thin transition metal dichalcogenides. *Rev. Mod. Phys.* **90**, 021001 (2018). URL https://link.aps.org/doi/10.1103/RevModPhys.90.021001.

[68] Xiao, D., Chang, M.-C. & Niu, Q. Berry phase effects on electronic properties. *Rev. Mod. Phys.* **82**, 1959–2007 (2010). URL http://link.aps.org/doi/10.1103/RevModPhys.82.1959.

[69] Aivazian, G. *et al.* Magnetic Control of Valley Pseudospin in Monolayer WSe_2. *Nat. Phys.* **11**, 148–152 (2014). URL http://dx.doi.org/10.1038/nphys3201.

[70] Mak, K. F., McGill, K. L., Park, J. & McEuen, P. L. The valley Hall effect in MoS_2 transistors. *Science (80-.).* **344**, 1489–1492 (2014). URL http://www.sciencemag.org/cgi/doi/10.1126/science.1250140.

[71] Mak, K. F., He, K., Shan, J. & Heinz, T. F. Control of valley polarization in monolayer MoS_2 by optical helicity. *Nat. Nanotechnol.* **7**, 494–498 (2012). URL http://www.nature.com/articles/nnano.2012.96.

[72] Jones, A. M. *et al.* Optical generation of excitonic valley coherence in monolayer WSe_2. *Nat. Nanotechnol.* **8**, 634–638 (2013). URL http://www.nature.com/articles/nnano.2013.151.

[73] Zhang, X.-X., You, Y., Zhao, S. Y. F. & Heinz, T. F. Experimental Evidence for Dark Excitons in Monolayer WSe_2. *Phys. Rev. Lett.* **115**, 257403 (2015). URL http://link.aps.org/doi/10.1103/PhysRevLett.115.257403.

[74] Koperski, M. *et al.* Optical properties of atomically thin transition metal dichalcogenides: observations and puzzles. *Nanophotonics* **6**, 1289–1308 (2017). URL http://www.degruyter.com/view/j/nanoph.2017.6.issue-6/nanoph-2016-0165/nanoph-2016-0165.xml. 1612.05879.

[75] Joensen, P., Frindt, R. & Morrison, S. Single-layer MoS_2. *Mater. Res. Bull.* **21**, 457–461 (1986). URL https://linkinghub.elsevier.com/retrieve/pii/0025540886900115.

[76] Britnell, L. *et al.* Strong Light-Matter Interactions in Heterostructures of Atomically Thin Films. *Science (80-.).* **340**, 1311–1314 (2013). URL http://www.sciencemag.org/cgi/doi/10.1126/science.1235547.

[77] Chernikov, A. *et al.* Exciton Binding Energy and Nonhydrogenic Rydberg Series in Monolayer WS_2. *Phys. Rev. Lett.* **113**, 076802 (2014). URL http://link.aps.org/doi/10.1103/PhysRevLett.113.076802.

[78] Klingshirn, C. F. *Semiconductor Optics*. Graduate Texts in Physics (Springer Berlin Heidelberg, Berlin, Heidelberg, 2012). URL http://link.springer.com/10.1007/978-3-642-28362-8.

[79] Ugeda, M. M. *et al.* Giant bandgap renormalization and excitonic effects in a monolayer transition metal dichalcogenide semiconductor. *Nat. Mater.* **13**, 1091–1095 (2014). URL http://www.nature.com/doifinder/10.1038/nmat4061.

[80] Ye, Z. *et al.* Probing excitonic dark states in single-layer tungsten disulphide. *Nature* **513**, 214–218 (2014). URL http://www.nature.com/doifinder/10.1038/nature13734.

[81] Li, Y. *et al.* Measurement of the optical dielectric function of monolayer transition-metal dichalcogenides: MoS_2, $MoSe_2$, WS_2 and WSe_2. *Phys. Rev. B* **90**, 205422 (2014). URL https://link.aps.org/doi/10.1103/PhysRevB.90.205422.

[82] Shin, B. G. *et al.* Indirect Bandgap Puddles in Monolayer MoS 2 by Substrate-Induced Local Strain. *Adv. Mater.* **28**, 9378–9384 (2016). URL http://doi.wiley.com/10.1002/adma.201602626.

[83] Yankowitz, M., Ma, Q., Jarillo-Herrero, P. & LeRoy, B. J. van der Waals heterostructures combining graphene and hexagonal boron nitride. *Nat. Rev. Phys.* **1** (2019). URL www.nature.com/natrevphys.

[84] Raja, A. *et al.* Dielectric disorder in two-dimensional materials. *Nat. Nanotechnol.* **14**, 832–837 (2019). URL http://dx.doi.org/10.1038/s41565-019-0520-0http://www.nature.com/articles/s41565-019-0520-0.

[85] Rhodes, D., Chae, S. H., Ribeiro-Palau, R. & Hone, J. Disorder in van der Waals heterostructures of 2D materials. *Nat. Mater.* **18**, 541–549 (2019). URL http://dx.doi.org/10.1038/s41563-019-0366-8http://www.nature.com/articles/s41563-019-0366-8.

[86] Cadiz, F. *et al.* Excitonic linewidth approaching the homogeneous limit in MoS_2-based van der Waals heterostructures. *Phys. Rev. X* **7**, 1–12 (2017). 1702.00323.

[87] Woessner, A. *et al.* Highly confined low-loss plasmons in graphene-boron nitride heterostructures. *Nat. Mater.* **14**, 421–425 (2015).

[88] Mak, K. F. *et al.* Tightly bound trions in monolayer MoS_2. *Nat. Mater.* **12**, 207–211 (2012). URL http://www.nature.com/doifinder/10.1038/nmat3505.

[89] Ross, J. S. *et al.* Electrical control of neutral and charged excitons in a monolayer semiconductor. *Nat. Commun.* **4**, 1474 (2013). URL http://www.nature.com/doifinder/10.1038/ncomms2498.

[90] Courtade, E. *et al.* Charged excitons in monolayer WSe_2 : Experiment and theory. *Phys. Rev. B* **96**, 085302 (2017). URL http://link.aps.org/doi/10.1103/PhysRevB.96.085302.

[91] You, Y. *et al.* Observation of biexcitons in monolayer WSe_2. *Nat. Phys.* **11**, 477–481 (2015). URL http://www.nature.com/doifinder/10.1038/nphys3324.

[92] Barbone, M. *et al.* Charge-tuneable biexciton complexes in monolayer WSe_2. *Nat. Commun.* **9**, 3721 (2018). URL http://www.nature.com/articles/s41467-018-05632-4.

[93] Rivera, P. *et al.* Observation of long-lived interlayer excitons in monolayer MoSe2-WSe2 heterostructures. *Nat. Commun.* **6**, 6242 (2015). URL http://www.nature.com/ncomms/2015/150224/ncomms7242/full/ncomms7242.html. 1403.4985.

[94] Lindlau, J. *et al.* The role of momentum-dark excitons in the elementary optical response of bilayer WSe_2. *Nat. Commun.* **9**, 2586 (2018). URL http://www.nature.com/articles/s41467-018-04877-3.

[95] Wang, G. *et al.* In-Plane Propagation of Light in Transition Metal Dichalcogenide Monolayers: Optical Selection Rules. *Phys. Rev. Lett.* **119**, 047401 (2017). URL http://link.aps.org/doi/10.1103/PhysRevLett.119.047401.

[96] Robert, C. *et al.* Fine structure and lifetime of dark excitons in transition metal dichalcogenide monolayers. *Phys. Rev. B* **96**, 155423 (2017). URL https://link.aps.org/doi/10.1103/PhysRevB.96.155423.

[97] Zhang, X.-X. *et al.* Magnetic brightening and control of dark excitons in monolayer WSe_2. *Nat. Nanotechnol.* **12**, 883–888 (2017). URL http://www.nature.com/articles/nnano.2017.105.

[98] Zhou, Y. *et al.* Probing dark excitons in atomically thin semiconductors via near-field coupling to surface plasmon polaritons. *Nat. Nanotechnol.* **12**, 856–860 (2017). URL http://www.nature.com/articles/nnano.2017.106.

[99] Park, K.-D., Jiang, T., Clark, G., Xu, X. & Raschke, M. B. Radiative control of dark excitons at room temperature by nano-optical antenna-tip Purcell effect. *Nat. Nanotechnol.* **13**, 59–64 (2018). URL http://www.nature.com/articles/s41565-017-0003-0.

[100] Lindlau, J. *et al.* Identifying optical signatures of momentum-dark excitons in transition metal dichalcogenide monolayers. *arXiv* (2017). URL http://arxiv.org/abs/1710.00988.

[101] Brem, S. *et al.* Phonon-assisted Photoluminescence from Dark Excitons in Monolayers of Transition Metal Dichalcogenides. *arXiv* (2019). URL http://arxiv.org/abs/1904.04711.

[102] Andreani, L. C., Tassone, F. & Bassani, F. Radiative lifetime of free excitons in quantum wells. *Solid State Commun.* **77**, 641–645 (1991). URL http://linkinghub.elsevier.com/retrieve/pii/003810989190761J.

[103] Robert, C. *et al.* Exciton radiative lifetime in transition metal dichalcogenide monolayers. *Phys. Rev. B* **93**, 205423 (2016). URL https://link.aps.org/doi/10.1103/PhysRevB.93.205423.

[104] Palummo, M., Bernardi, M. & Grossman, J. C. Exciton Radiative Lifetimes in Two-Dimensional Transition Metal Dichalcogenides. *Nano Lett.* **15**, 2794–2800 (2015). URL http://pubs.acs.org/doi/abs/10.1021/nl503799t.

[105] Mouri, S. *et al.* Nonlinear photoluminescence in atomically thin layered WSe_2 arising from diffusion-assisted exciton-exciton annihilation. *Phys. Rev. B* **90**, 155449 (2014). URL https://link.aps.org/doi/10.1103/PhysRevB.90.155449.

[106] Sun, D. *et al.* Observation of Rapid Exciton–Exciton Annihilation in Monolayer Molybdenum Disulfide. *Nano Lett.* **14**, 5625–5629 (2014). URL https://pubs.acs.org/doi/10.1021/nl5021975.

[107] Sun, Y., Thompson, S. E. & Nishida, T. *Strain Effect in Semiconductors* (Springer US, Boston, MA, 2010). URL http://link.springer.com/10.1007/978-1-4419-0552-9.

[108] Lee, C., Wei, X., Kysar, J. W. & Hone, J. Measurement of the Elastic Properties and Intrinsic Strength of Monolayer Graphene. *Science (80-.).* **321**, 385–388 (2008). URL http://www.sciencemag.org/cgi/doi/10.1126/science.1157996.

[109] Guinea, F., Katsnelson, M. I. & Geim, A. K. Energy gaps and a zero-field quantum Hall effect in graphene by strain engineering. *Nat. Phys.* **6**, 30–33 (2010). URL http://www.nature.com/articles/nphys1420.

[110] Amorim, B. *et al.* Novel effects of strains in graphene and other two dimensional materials. *Phys. Rep.* **617**, 1–54 (2015). URL http://linkinghub.elsevier.com/retrieve/pii/S0370157315005402.

[111] Roldán, R., Castellanos-Gomez, A., Cappelluti, E. & Guinea, F. Strain engineering in semiconducting two-dimensional crystals. *J. Phys. Condens. Matter* **27**, 313201 (2015). URL http://stacks.iop.org/0953-8984/27/i=31/a=313201?key=crossref.907d8c88e752e6f3b5135d39592cc4e5.

[112] Mueller, T. & Malic, E. Exciton physics and device application of two-dimensional transition metal dichalcogenide semiconductors. *npj 2D Mater. Appl.* **2**, 29 (2018). URL http://www.nature.com/articles/s41699-018-0074-2.

[113] Castellanos-Gomez, A. *et al.* Local Strain Engineering in Atomically Thin MoS_2. *Nano Lett.* **13**, 5361–5366 (2013). URL http://pubs.acs.org/doi/abs/10.1021/nl402875m.

[114] Li, H. *et al.* Optoelectronic crystal of artificial atoms in strain-textured molybdenum disulphide. *Nat. Commun.* **6**, 7381 (2015). URL http://www.nature.com/doifinder/10.1038/ncomms8381.

[115] Yang, S. *et al.* Tuning the optical, magnetic, and electrical properties of $ReSe_2$ by nanoscale strain engineering. *Nano Lett.* **15**, 1660–1666 (2015). URL http://pubs.acs.org/doi/10.1021/nl504276u.

[116] Quereda, J. *et al.* Strong Modulation of Optical Properties in Black Phosphorus through Strain-Engineered Rippling. *Nano Lett.* **16**, 2931–2937 (2016). URL http://pubs.acs.org/doi/10.1021/acs.nanolett.5b04670.

[117] Li, Y. *et al.* Giant Anisotropic Raman Response of Encapsulated Ultrathin Black Phosphorus by Uniaxial Strain. *Adv. Funct. Mater.* **27**, 1600986 (2017). URL http://doi.wiley.com/10.1002/adfm.201600986.

[118] Duerloo, K.-A. N., Ong, M. T. & Reed, E. J. Intrinsic Piezoelectricity in Two-Dimensional Materials. *J. Phys. Chem. Lett.* **3**, 2871–2876 (2012). URL http://pubs.acs.org/doi/10.1021/jz3012436.

[119] Zhu, H. *et al.* Observation of piezoelectricity in free-standing monolayer MoS_2. *Nat. Nanotechnol.* **10**, 151–155 (2015). URL http://www.nature.com/articles/nnano.2014.309.

[120] Wu, W. *et al.* Piezoelectricity of single-atomic-layer MoS_2 for energy conversion and piezotronics. *Nature* **514**, 470–474 (2014). URL http://www.nature.com/articles/nature13792.

[121] Conley, H. J. *et al.* Bandgap Engineering of Strained Monolayer and Bilayer MoS_2. *Nano Lett.* **13**, 3626–3630 (2013). URL http://pubs.acs.org/doi/10.1021/nl4014748.

[122] Scalise, E., Houssa, M., Pourtois, G., Afanas'ev, V. & Stesmans, A. Strain-induced semiconductor to metal transition in the two-dimensional honeycomb structure of MoS_2. *Nano Res.* **5**, 43–48 (2012). URL http://link.springer.com/10.1007/s12274-011-0183-0.

[123] Yun, W. S., Han, S. W., Hong, S. C., Kim, I. G. & Lee, J. D. Thickness and strain effects on electronic structures of transition metal dichalcogenides: 2H-MX_2 semiconductors (M=Mo,W;X=S,Se,Te). *Phys. Rev. B* **85**, 033305 (2012). URL https://link.aps.org/doi/10.1103/PhysRevB.85.033305.

[124] Brooks, M. & Burkard, G. Theory of strain-induced confinement in transition metal dichalcogenide monolayers. *Phys. Rev. B* **97**, 195454 (2018). URL https://link.aps.org/doi/10.1103/PhysRevB.97.195454.

[125] Desai, S. B. *et al.* Strain-Induced Indirect to Direct Bandgap Transition in Multilayer WSe_2. *Nano Lett.* **14**, 4592–4597 (2014). URL http://pubs.acs.org/doi/abs/10.1021/nl501638a.

[126] Wu, W. *et al.* Giant Mechano-Optoelectronic Effect in an Atomically Thin Semiconductor. *Nano Lett.* **18**, 2351–2357 (2018). URL http://pubs.acs.org/doi/10.1021/acs.nanolett.7b05229.

[127] Feng, J., Qian, X., Huang, C.-W. & Li, J. Strain-engineered artificial atom as a broad-spectrum solar energy funnel. *Nat. Photonics* **6**, 866–872 (2012). URL http://www.nature.com/articles/nphoton.2012.285.

[128] San-Jose, P., Parente, V., Guinea, F., Roldán, R. & Prada, E. Inverse Funnel Effect of Excitons in Strained Black Phosphorus. *Phys. Rev. X* **6**, 031046 (2016). URL https://link.aps.org/doi/10.1103/PhysRevX.6.031046.

[129] De Sanctis, A., Amit, I., Hepplestone, S. P., Craciun, M. F. & Russo, S. Strain-engineered inverse charge-funnelling in layered semiconductors. *Nat. Commun.* **9**, 1652 (2018). URL http://www.nature.com/articles/s41467-018-04099-7.

[130] Somaschi, N. *et al.* Near-optimal single-photon sources in the solid state. *Nat. Photonics* **10**, 340–345 (2016). URL http://www.nature.com/articles/nphoton.2016.23.

[131] Srivastava, A. *et al.* Optically active quantum dots in monolayer WSe_2. *Nat. Nanotechnol.* **10**, 491–496 (2015). URL http://www.nature.com/articles/nnano.2015.60.

[132] Koperski, M. *et al.* Single photon emitters in exfoliated WSe_2 structures. *Nat. Nanotechnol.* **10**, 503–506 (2015). URL http://www.nature.com/doifinder/10.1038/nnano.2015.67.

[133] He, Y.-M. *et al.* Single quantum emitters in monolayer semiconductors. *Nat. Nanotechnol.* **10**, 497–502 (2015). URL http://www.nature.com/articles/nnano.2015.75.

[134] Chakraborty, C., Kinnischtzke, L., Goodfellow, K. M., Beams, R. & Vamivakas, a. N. Voltage-controlled quantum light from an atomically thin semiconductor. *Nat. Nanotechnol.* **10**, 507–511 (2015). URL http://www.nature.com/doifinder/10.1038/nnano.2015.79.

[135] Palacios-Berraquero, C. *et al.* Atomically thin quantum light-emitting diodes. *Nat. Commun.* **7**, 12978 (2016). URL http://www.nature.com/articles/ncomms12978.

[136] Tran, T. T. *et al.* Room-Temperature Single-Photon Emission from Oxidized Tungsten Disulfide Multilayers. *Adv. Opt. Mater.* **5**, 1600939 (2017). URL http://doi.wiley.com/10.1002/adom.201600939.

[137] Branny, A. *et al.* Discrete quantum dot like emitters in monolayer $MoSe_2$: Spatial mapping, magneto-optics, and charge tuning. *Appl. Phys. Lett.* **108**, 142101 (2016). URL http://aip.scitation.org/doi/10.1063/1.4945268.

[138] Chakraborty, C., Goodfellow, K. M. & Nick Vamivakas, A. Localized emission from defects in $MoSe_2$ layers. *Opt. Mater. Express* **6**, 2081 (2016). URL https://www.osapublishing.org/abstract.cfm?URI=ome-6-6-2081.

[139] Tonndorf, P. *et al.* Single-photon emitters in GaSe. *2D Mater.* **4**, 021010 (2017). URL https://iopscience.iop.org/article/10.1088/2053-1583/aa525b.

[140] Schwarz, S. *et al.* Electrically pumped single-defect light emitters in WSe_2. *2D Mater.* **3**, 025038 (2016). URL http://iopscience.iop.org/2053-1583/3/2/025038.

[141] Clark, G. *et al.* Single Defect Light-Emitting Diode in a van der Waals Heterostructure. *Nano Lett.* **16**, 3944–3948 (2016). URL http://pubs.acs.org/doi/abs/10.1021/acs.nanolett.6b01580.

[142] Brotons-Gisbert, M. *et al.* Coulomb blockade in an atomically thin quantum dot coupled to a tunable Fermi reservoir. *Nat. Nanotechnol.* (2019). URL http://www.nature.com/articles/s41565-019-0402-5.

[143] Tonndorf, P. *et al.* On-Chip Waveguide Coupling of a Layered Semiconductor Single-Photon Source. *Nano Lett.* **17**, 5446–5451 (2017). URL https://pubs.acs.org/doi/10.1021/acs.nanolett.7b02092.

[144] Blauth, M. *et al.* Coupling Single Photons from Discrete Quantum Emitters in WSe_2 to Lithographically Defined Plasmonic Slot Waveguides. *Nano Lett.* **18**, 6812–6819 (2018). URL https://pubs.acs.org/doi/10.1021/acs.nanolett.8b02687.

[145] Flatten, L. C. *et al.* Microcavity enhanced single photon emission from two-dimensional WSe_2. *Appl. Phys. Lett.* **112**, 191105 (2018). URL http://aip.scitation.org/doi/10.1063/1.5026779.

[146] Luo, Y. *et al.* Deterministic coupling of site-controlled quantum emitters in monolayer WSe_2 to plasmonic nanocavities. *Nat. Nanotechnol.* **13**, 1137–1142 (2018). URL http://www.nature.com/articles/s41565-018-0275-z.

[147] He, Y.-M. *et al.* Cascaded emission of single photons from the biexciton in monolayered WSe_2. *Nat. Commun.* **7**, 13409 (2016). URL http://www.nature.com/articles/ncomms13409.

[148] Zhang, S. *et al.* Defect Structure of Localized Excitons in a WSe_2 Monolayer. *Phys. Rev. Lett.* **119**, 046101 (2017). URL http://link.aps.org/doi/10.1103/PhysRevLett.119.046101.

[149] Zheng, Y. J. *et al.* Point Defects and Localized Excitons in 2D WSe_2. *ACS Nano* **13**, 6050–6059 (2019). URL http://pubs.acs.org/doi/10.1021/acsnano.9b02316.

[150] Kumar, S. *et al.* Resonant laser spectroscopy of localized excitons in monolayer WSe_2. *Optica* **3**, 882 (2016). URL https://www.osapublishing.org/abstract.cfm?URI=optica-3-8-882.

[151] Dass, C. K. *et al.* Ultra-Long Lifetimes of Single Quantum Emitters in Monolayer WSe_2/hBN Heterostructures. *Adv. Quantum Technol.* **1900022**, 1900022 (2019). URL https://onlinelibrary.wiley.com/doi/abs/10.1002/qute.201900022.

[152] Bayer, M. *et al.* Fine structure of neutral and charged excitons in self-assembled In(Ga)As/(Al)GaAs quantum dots. *Phys. Rev. B* **65**, 195315 (2002). URL http://link.aps.org/doi/10.1103/PhysRevB.65.195315.

[153] Chakraborty, C., Jungwirth, N. R., Fuchs, G. D. & Vamivakas, A. N. Electrical manipulation of the fine-structure splitting of WSe_2 quantum emitters. *Phys. Rev. B* **99**, 045308 (2019). URL https://link.aps.org/doi/10.1103/PhysRevB.99.045308.

[154] Kumar, S., Kaczmarczyk, A. & Gerardot, B. D. Strain-Induced Spatial and Spectral Isolation of Quantum Emitters in Mono- and Bilayer WSe_2. *Nano Lett.* **15**, 7567–7573 (2015). URL http://pubs.acs.org/doi/10.1021/acs.nanolett.5b03312.

[155] Kern, J. *et al.* Nanoscale Positioning of Single-Photon Emitters in Atomically Thin WSe_2. *Adv. Mater.* **28**, 7101–7105 (2016). URL http://doi.wiley.com/10.1002/adma.201600560.

[156] Branny, A., Kumar, S., Proux, R. & Gerardot, B. D. Deterministic strain-induced arrays of quantum emitters in a two-dimensional semiconductor. *Nat. Commun.* **8**, 15053 (2017). URL http://www.nature.com/articles/ncomms15053.

[157] Palacios-Berraquero, C. *et al.* Large-scale quantum-emitter arrays in atomically thin semiconductors. *Nat. Commun.* **8**, 15093 (2017). URL http://www.nature.com/doifinder/10.1038/ncomms15093.

[158] Klein, J. *et al.* Site-selectively generated photon emitters in monolayer MoS_2 via local helium ion irradiation. *Nat. Commun.* **10**, 2755 (2019). URL http://www.nature.com/articles/s41467-019-10632-z.

[159] Feierabend, M., Brem, S. & Malic, E. Optical fingerprint of bright and dark localized excitonic states in atomically thin 2D materials. *arXiv* (2019). URL http://arxiv.org/abs/1908.05071.

[160] Chirolli, L., Prada, E., Guinea, F., Roldán, R. & San-Jose, P. Strain-induced bound states in transition-metal dichalcogenide bubbles. *2D Mater.* **6**, 025010 (2019). URL https://iopscience.iop.org/article/10.1088/2053-1583/ab0113.

[161] Linhart, L. *et al.* Localized Intervalley Defect Excitons as Single-Photon Emitters in WSe2. *Phys. Rev. Lett.* **123**, 146401 (2019). URL https://doi.org/10.1103/PhysRevLett.123.146401. 1904.03217.

[162] Bharadwaj, P., Deutsch, B. & Novotny, L. Optical Antennas. *Adv. Opt. Photonics* **1**, 438 (2009). URL https://www.osapublishing.org/aop/abstract.cfm?uri=aop-1-3-438.

[163] Novotny, L. & van Hulst, N. Antennas for light. *Nat. Photonics* **5**, 83–90 (2011). URL http://www.nature.com/articles/nphoton.2010.237.

[164] Biagioni, P., Huang, J.-S. & Hecht, B. Nanoantennas for visible and infrared radiation. *Reports Prog. Phys.* **75**, 024402 (2012). URL https://iopscience.iop.org/article/10.1088/0034-4885/75/2/024402.

[165] Novotny, L. & Hecht, B. *Principles of Nano-Optics* (Cambridge University Press, Cambridge, 2006). URL http://ebooks.cambridge.org/ref/id/CBO9780511813535.

[166] Hartschuh, A., Sánchez, E. J., Xie, X. S. & Novotny, L. High-Resolution Near-Field Raman Microscopy of Single-Walled Carbon Nanotubes. *Phys. Rev. Lett.* **90**, 095503 (2003). URL https://link.aps.org/doi/10.1103/PhysRevLett.90.095503.

[167] Schuller, J. A. *et al.* Plasmonics for extreme light concentration and manipulation. *Nat. Mater.* **9**, 193–204 (2010). URL http://www.nature.com/articles/nmat2630.

[168] Tame, M. S. *et al.* Quantum plasmonics. *Nat. Phys.* **9**, 329–340 (2013). URL http://www.nature.com/articles/nphys2615.

[169] Maier, S. A. *et al.* Local detection of electromagnetic energy transport below the diffraction limit in metal nanoparticle plasmon waveguides. *Nat. Mater.* **2**, 229–232 (2003). URL http://www.nature.com/articles/nmat852.

[170] Low, T. *et al.* Polaritons in layered two-dimensional materials. *Nat. Mater.* **16**, 182–194 (2017). URL http://www.nature.com/articles/nmat4792.

[171] Alcaraz Iranzo, D. *et al.* Probing the ultimate plasmon confinement limits with a van der Waals heterostructure. *Science (80-.).* **360**, 291–295 (2018). URL http://www.sciencemag.org/lookup/doi/10.1126/science.aar8438.

[172] Giannini, V., Fernandez-Dominguez, A. I., Heck, S. C. & Maier, S. A. Plasmonic Nanoantennas: Fundamentals and Their Use in Controlling the Radiative Properties of Nanoemitters. *Chem. Rev.* **111**, 3888–3912 (2011). URL https://pubs.acs.org/doi/10.1021/cr1002672.

[173] Ghenuche, P., Cherukulappurath, S., Taminiau, T. H., van Hulst, N. F. & Quidant, R. Spectroscopic Mode Mapping of Resonant Plasmon Nanoantennas. *Phys. Rev. Lett.* **101**, 116805 (2008). URL https://link.aps.org/doi/10.1103/PhysRevLett.101.116805.

[174] Curto, A. G. *et al.* Unidirectional Emission of a Quantum Dot Coupled to a Nanoantenna. *Science (80-.).* **329**, 930–933 (2010). URL http://www.sciencemag.org/cgi/doi/10.1126/science.1191922.

[175] Baumberg, J. J., Aizpurua, J., Mikkelsen, M. H. & Smith, D. R. Extreme nanophotonics from ultrathin metallic gaps. *Nat. Mater.* **18**, 668–678 (2019). URL http://www.nature.com/articles/s41563-019-0290-y.

[176] Akselrod, G. M. *et al.* Probing the mechanisms of large Purcell enhancement in plasmonic nanoantennas. *Nat. Photonics* **8**, 835–840 (2014). URL http://www.nature.com/articles/nphoton.2014.228.

[177] Kleemann, M.-E. *et al.* Strong-coupling of WSe_2 in ultra-compact plasmonic nanocavities at room temperature. *Nat. Commun.* **8**, 1296 (2017). URL http://www.nature.com/articles/s41467-017-01398-3.

[178] Khurgin, J. B. How to deal with the loss in plasmonics and metamaterials. *Nat. Nanotechnol.* **10**, 2–6 (2015). URL http://www.nature.com/articles/nnano.2014.310.

[179] Anger, P., Bharadwaj, P. & Novotny, L. Enhancement and Quenching of Single-Molecule Fluorescence. *Phys. Rev. Lett.* **96**, 113002 (2006). URL https://link.aps.org/doi/10.1103/PhysRevLett.96.113002.

[180] Mie, G. Beiträge zur Optik trüber Medien, speziell kolloidaler Metallösungen. *Ann. Phys.* **330**, 377–445 (1908). URL http://doi.wiley.com/10.1002/andp.19083300302.

[181] Kuznetsov, A. I., Miroshnichenko, A. E., Fu, Y. H., Zhang, J. & Luk'yanchuk, B. Magnetic light. *Sci. Rep.* **2**, 492 (2012). URL http://www.nature.com/articles/srep00492. 1205.1610.

[182] Fu, Y. H., Kuznetsov, A. I., Miroshnichenko, A. E., Yu, Y. F. & Luk'yanchuk, B. Directional visible light scattering by silicon nanoparticles. *Nat. Commun.* **4**, 1527 (2013). URL http://www.nature.com/articles/ncomms2538.

[183] García-Etxarri, A. *et al.* Strong magnetic response of submicron Silicon particles in the infrared. *Opt. Express* **19**, 4815 (2011). URL http://dx.doi.org/10.1364/OE.19.004815.

[184] Bakker, R. M. *et al.* Magnetic and Electric Hotspots with Silicon Nanodimers. *Nano Lett.* **15**, 2137–2142 (2015). URL https://pubs.acs.org/doi/10.1021/acs.nanolett.5b00128.

[185] Decker, M. *et al.* High-Efficiency Dielectric Huygens' Surfaces. *Adv. Opt. Mater.* **3**, 813–820 (2015). URL http://doi.wiley.com/10.1002/adom.201400584.

[186] Caldarola, M. *et al.* Non-plasmonic nanoantennas for surface enhanced spectroscopies with ultra-low heat conversion. *Nat. Commun.* **6**, 7915 (2015). URL http://www.nature.com/articles/ncomms8915.

[187] Regmi, R. *et al.* All-Dielectric Silicon Nanogap Antennas To Enhance the Fluorescence of Single Molecules. *Nano Lett.* **16**, 5143–5151 (2016). URL http://pubs.acs.org/doi/10.1021/acs.nanolett.6b02076.

[188] Albella, P. *et al.* Low-Loss Electric and Magnetic Field-Enhanced Spectroscopy with Subwavelength Silicon Dimers. *J. Phys. Chem. C* **117**, 13573–13584 (2013). URL http://pubs.acs.org/doi/10.1021/jp4027018.

[189] Yang, Y., Miller, O. D., Christensen, T., Joannopoulos, J. D. & Soljačić, M. Low-Loss Plasmonic Dielectric Nanoresonators. *Nano Lett.* **17**, 3238–3245 (2017). URL https://pubs.acs.org/doi/10.1021/acs.nanolett.7b00852.

[190] Cambiasso, J., König, M., Cortés, E., Schlücker, S. & Maier, S. A. Surface-Enhanced Spectroscopies of a Molecular Monolayer in an All-Dielectric Nanoantenna. *ACS Photonics* **5**, 1546–1557 (2018). URL http://pubs.acs.org/doi/10.1021/acsphotonics.7b01604.

[191] Albella, P., Alcaraz de la Osa, R., Moreno, F. & Maier, S. A. Electric and Magnetic Field Enhancement with Ultralow Heat Radiation Dielectric Nanoantennas: Considerations for Surface-Enhanced Spectroscopies. *ACS Photonics* **1**, 524–529 (2014). URL http://pubs.acs.org/doi/10.1021/ph500060s.

[192] Krasnok, A., Caldarola, M., Bonod, N. & Alú, A. Spectroscopy and Biosensing with Optically Resonant Dielectric Nanostructures. *Adv. Opt. Mater.* **6**, 1701094 (2018). URL http://doi.wiley.com/10.1002/adom.201701094.

[193] Baranov, D. G. *et al.* All-dielectric nanophotonics: the quest for better materials and fabrication techniques. *Optica* **4**, 814 (2017). URL https://www.osapublishing.org/abstract.cfm?URI=optica-4-7-814.

[194] Cambiasso, J. *et al.* Bridging the Gap between Dielectric Nanophotonics and the Visible Regime with Effectively Lossless Gallium Phosphide Antennas. *Nano Lett.* **17**, 1219–1225 (2017). URL https://pubs.acs.org/doi/10.1021/acs.nanolett.6b05026.

[195] Staude, I. *et al.* Tailoring directional scattering through magnetic and electric resonances in subwavelength silicon nanodisks. *ACS Nano* **7**, 7824–7832 (2013). URL https://pubs.acs.org/doi/10.1021/nn402736f.

[196] Miroshnichenko, A. E. *et al.* Nonradiating anapole modes in dielectric nanoparticles. *Nat. Commun.* **6**, 8069 (2015). URL http://www.nature.com/articles/ncomms9069.

[197] Mignuzzi, S. *et al.* Nanoscale Design of the Local Density of Optical States. *Nano Lett.* **19**, 1613–1617 (2019). URL http://pubs.acs.org/doi/10.1021/acs.nanolett.8b04515.

[198] Krasnok, A. *et al.* Demonstration of the enhanced Purcell factor in all-dielectric structures. *Appl. Phys. Lett.* **108**, 211105 (2016). URL http://aip.scitation.org/doi/10.1063/1.4952740.

[199] Kravets, V. G., Kabashin, A. V., Barnes, W. L. & Grigorenko, A. N. Plasmonic Surface Lattice Resonances: A Review of Properties and Applications. *Chem. Rev.* **118**, 5912–5951 (2018). URL http://pubs.acs.org/doi/10.1021/acs.chemrev.8b00243.

[200] Hsu, C. W., Zhen, B., Stone, A. D., Joannopoulos, J. D. & Soljačić, M. Bound states in the continuum. *Nat. Rev. Mater.* **1**, 16048 (2016). URL http://www.nature.com/articles/natrevmats201648.

[201] Jahani, S. & Jacob, Z. All-dielectric metamaterials. *Nat. Nanotechnol.* **11**, 23–36 (2016). URL http://www.nature.com/articles/nnano.2015.304.

[202] Staude, I. & Schilling, J. Metamaterial-inspired silicon nanophotonics. *Nat. Photonics* **11**, 274–284 (2017). URL http://dx.doi.org/10.1038/nphoton.2017.39.

[203] Cheben, P., Halir, R., Schmid, J. H., Atwater, H. A. & Smith, D. R. Subwavelength integrated photonics. *Nature* **560**, 565–572 (2018). URL http://www.nature.com/articles/s41586-018-0421-7.

[204] Koenderink, A. F. On the use of Purcell factors for plasmon antennas. *Opt. Lett.* **35**, 4208 (2010). URL https://www.osapublishing.org/abstract.cfm?URI=ol-35-24-4208.

[205] Pelton, M. Modified spontaneous emission in nanophotonic structures. *Nat. Photonics* **9**, 427–435 (2015). URL http://dx.doi.org/10.1038/nphoton.2015.103.

[206] Bohren, C. F. & Huffman, D. R. (eds.) *Absorption and Scattering of Light by Small Particles* (Wiley-VCH Verlag GmbH, Weinheim, Germany, 1998). URL http://doi.wiley.com/10.1002/9783527618156.

[207] Kerker, M., Wang, D.-S. & Giles, C. L. Electromagnetic scattering by magnetic spheres. *J. Opt. Soc. Am.* **73**, 765 (1983). URL https://www.osapublishing.org/abstract.cfm?URI=josa-73-6-765.

[208] Decker, M. & Staude, I. Resonant dielectric nanostructures: A low-loss platform for functional nanophotonics. *J. Opt. (United Kingdom)* **18**, 1–31 (2016). URL http://dx.doi.org/10.1088/2040-8978/18/10/103001. arXiv:1011.1669v3.

[209] Koenderink, A. F. Single-Photon Nanoantennas. *ACS Photonics* **4**, 710–722 (2017). URL http://pubs.acs.org/doi/10.1021/acsphotonics.7b00061.

[210] Amani, M. *et al.* Near-unity photoluminescence quantum yield in MoS_2. *Science (80-.).* **350**, 1065–1068 (2015). URL http://www.sciencemag.org/cgi/doi/10.1126/science.aad2114.

[211] Campion, A. & Kambhampati, P. Surface-enhanced Raman scattering. *Chem. Soc. Rev.* **27**, 241 (1998). URL http://xlink.rsc.org/?DOI=a827241z.

[212] Alessandri, I. & Lombardi, J. R. Enhanced Raman Scattering with Dielectrics. *Chem. Rev.* **116**, 14921–14981 (2016). URL https://pubs.acs.org/doi/10.1021/acs.chemrev.6b00365.

[213] Le Ru, E. C., Blackie, E., Meyer, M. & Etchegoin, P. G. Surface Enhanced Raman Scattering Enhancement Factors: A Comprehensive Study. *J. Phys. Chem. C* **111**, 13794–13803 (2007). URL http://pubs.acs.org/doi/10.1021/jp0687908.

[214] Zhou, J. *et al.* A library of atomically thin metal chalcogenides. *Nature* **556**, 355–359 (2018). URL http://www.nature.com/articles/s41586-018-0008-3.

[215] Coleman, J. N. *et al.* Two-Dimensional Nanosheets Produced by Liquid Exfoliation of Layered Materials. *Science (80-.).* **331**, 568–571 (2011). URL http://www.sciencemag.org/cgi/doi/10.1126/science.1194975.

[216] Frisenda, R. *et al.* Recent progress in the assembly of nanodevices and van der Waals heterostructures by deterministic placement of 2D materials. *Chem. Soc. Rev.* **47**, 53–68 (2018). URL http://xlink.rsc.org/?DOI=C7CS00556C.

[217] Alexeev, E. M. *et al.* Imaging of Interlayer Coupling in van der Waals Heterostructures Using a Bright-Field Optical Microscope. *Nano Lett.* **17**, 5342–5349 (2017). URL http://pubs.acs.org/doi/10.1021/acs.nanolett.7b01763.

[218] Benameur, M. M. *et al.* Visibility of dichalcogenide nanolayers. *Nanotechnology* **22**, 125706 (2011). URL https://iopscience.iop.org/article/10.1088/0957-4484/22/12/125706.

[219] Castellanos-Gomez, A. *et al.* Deterministic transfer of two-dimensional materials by all-dry viscoelastic stamping. *2D Mater.* **1**, 011002 (2014). URL https://iopscience.iop.org/article/10.1088/2053-1583/1/1/011002.

[220] Zhao, Y. *et al.* Interlayer Breathing and Shear Modes in Few-Trilayer MoS_2 and WSe_2. *Nano Lett.* **13**, 1007–1015 (2013). URL https://pubs.acs.org/doi/10.1021/nl304169w.

[221] Lakowicz, J. R. *Principles of Fluorescence Spectroscopy* (Springer US, Boston, MA, 2006). URL http://link.springer.com/10.1007/978-0-387-46312-4.

[222] Wu, S. *et al.* Monolayer semiconductor nanocavity lasers with ultralow thresholds. *Nature* **520**, 69–72 (2015). URL http://www.nature.com/articles/nature14290.

[223] Zhang, L., Gogna, R., Burg, W., Tutuc, E. & Deng, H. Photonic-crystal exciton-polaritons in monolayer semiconductors. *Nat. Commun.* **9**, 1–8 (2018). URL http://dx.doi.org/10.1038/s41467-018-03188-x.

[224] Li, Y. *et al.* Room-temperature continuous-wave lasing from monolayer molybdenum ditelluride integrated with a silicon nanobeam cavity. *Nat. Nanotechnol.* **12**, 987–992 (2017). URL http://www.nature.com/doifinder/10.1038/nnano.2017.128.

[225] Salehzadeh, O., Djavid, M., Tran, N. H., Shih, I. & Mi, Z. Optically Pumped Two-Dimensional MoS_2 Lasers Operating at Room-Temperature. *Nano Lett.* **15**, 5302–5306 (2015). URL https://pubs.acs.org/doi/10.1021/acs.nanolett.5b01665.

[226] Dufferwiel, S. *et al.* Exciton–polaritons in van der Waals heterostructures embedded in tunable microcavities. *Nat. Commun.* **6**, 8579 (2015). URL http://www.nature.com/doifinder/10.1038/ncomms9579.

[227] Sidler, M. *et al.* Fermi polaron-polaritons in charge-tunable atomically thin semiconductors. *Nat. Phys.* **13**, 255–261 (2016). URL http://www.nature.com/doifinder/10.1038/nphys3949.

[228] Wang, Z. *et al.* Giant photoluminescence enhancement in tungsten-diselenide–gold plasmonic hybrid structures. *Nat. Commun.* **7**, 11283 (2016). URL http://www.nature.com/articles/ncomms11283.

[229] Krasnok, A., Lepeshov, S. & Alú, A. Nanophotonics with 2D transition metal dichalcogenides. *Opt. Express* **26**, 15972 (2018). URL https://www.osapublishing.org/abstract.cfm?URI=oe-26-12-15972.

[230] Tahersima, M. H. *et al.* Testbeds for Transition Metal Dichalcogenide Photonics: Efficacy of Light Emission Enhancement in Monomer vs Dimer Nanoscale Antennae. *ACS Photonics* **4**, 1713–1721 (2017). URL http://pubs.acs.org/doi/10.1021/acsphotonics.7b00208.

[231] Cai, T. *et al.* Radiative Enhancement of Single Quantum Emitters in WSe_2 Monolayers Using Site-Controlled Metallic Nanopillars. *ACS Photonics* **5**, 3466–3471 (2018). URL http://pubs.acs.org/doi/10.1021/acsphotonics.8b00580. 1803.09358.

[232] Cihan, A. F., Curto, A. G., Raza, S., Kik, P. G. & Brongersma, M. L. Silicon Mie resonators for highly directional light emission from monolayer MoS_2. *Nat. Photonics* **12**, 284–290 (2018). URL http://www.nature.com/articles/s41566-018-0155-y.

[233] Lepeshov, S. *et al.* Tunable Resonance Coupling in Single Si Nanoparticle–Monolayer WS_2 Structures. *ACS Appl. Mater. Interfaces* **10**, 16690–16697 (2018). URL http://pubs.acs.org/doi/10.1021/acsami.7b17112.

[234] Verre, R. *et al.* Transition metal dichalcogenide nanodisks as high-index dielectric Mie nanoresonators. *Nat. Nanotechnol.* (2019). URL http://www.nature.com/articles/s41565-019-0442-x.

[235] Godde, T. *et al.* Exciton and trion dynamics in atomically thin $MoSe_2$ and WSe_2 : Effect of localization. *Phys. Rev. B* **94**, 165301 (2016). URL https://link.aps.org/doi/10.1103/PhysRevB.94.165301.

[236] Tonndorf, P. *et al.* Photoluminescence emission and Raman response of monolayer MoS_2, $MoSe_2$, and WSe_2. *Opt. Express* **21**, 4908 (2013). URL https://www.osapublishing.org/oe/abstract.cfm?uri=oe-21-4-4908.

[237] Hayashi, S., Koh, R., Ichiyama, Y. & Yamamoto, K. Evidence for surface-enhanced Raman scattering on nonmetallic surfaces: Copper phthalocyanine molecules on GaP small particles. *Phys. Rev. Lett.* **60**, 1085–1088 (1988). URL https://link.aps.org/doi/10.1103/PhysRevLett.60.1085.

[238] Johari, P. & Shenoy, V. B. Tuning the Electronic Properties of Semiconducting Transition Metal Dichalcogenides by Applying Mechanical Strains. *ACS Nano* **6**, 5449–5456 (2012). URL https://pubs.acs.org/doi/10.1021/nn301320r.

[239] Guzman, D. M. & Strachan, A. Role of strain on electronic and mechanical response of semiconducting transition-metal dichalcogenide monolayers: An ab-initio study. *J. Appl. Phys.* **115**, 243701 (2014). URL http://aip.scitation.org/doi/10.1063/1.4883995.1312.1275.

[240] Feierabend, M., Morlet, A., Berghäuser, G. & Malic, E. Impact of strain on the optical fingerprint of monolayer transition-metal dichalcogenides. *Phys. Rev. B* **96**, 045425 (2017). URL http://link.aps.org/doi/10.1103/PhysRevB.96.045425.

[241] Aslan, O. B., Deng, M. & Heinz, T. F. Strain tuning of excitons in monolayer WSe_2. *Phys. Rev. B* **98**, 115308 (2018). URL https://link.aps.org/doi/10.1103/PhysRevB.98.115308.

[242] Schmidt, R. *et al.* Reversible uniaxial strain tuning in atomically thin WSe_2. *2D Mater.* **3**, 021011 (2016). URL https://iopscience.iop.org/article/10.1088/2053-1583/3/2/021011.

[243] Liu, T. *et al.* Crested two-dimensional transistors. *Nat. Nanotechnol.* **1**, 1 (2019). URL http://www.nature.com/articles/s41565-019-0361-x.

[244] Manzeli, S., Allain, A., Ghadimi, A. & Kis, A. Piezoresistivity and Strain-induced Band Gap Tuning in Atomically Thin MoS_2. *Nano Lett.* **15**, 5330–5335 (2015). URL https://pubs.acs.org/doi/10.1021/acs.nanolett.5b01689.

[245] Gant, P. *et al.* A strain tunable single-layer MoS_2 photodetector. *Mater. Today* **27**, 8–13 (2019). URL https://linkinghub.elsevier.com/retrieve/pii/S1369702119301762.

[246] Shiue, R.-J. *et al.* Active 2D materials for on-chip nanophotonics and quantum optics. *Nanophotonics* **6**, 1329–1342 (2017). URL http://www.degruyter.com/view/j/nanoph.2017.6.issue-6/nanoph-2016-0172/nanoph-2016-0172.xml.

[247] Schneider, C., Glazov, M. M., Korn, T., Höfling, S. & Urbaszek, B. Two-dimensional semiconductors in the regime of strong light-matter coupling. *Nat. Commun.* **9**, 2695 (2018). URL http://www.nature.com/articles/s41467-018-04866-6.

[248] Sortino, L. *et al.* Enhanced light-matter interaction in an atomically thin semiconductor coupled with dielectric nano-antennas. *Nat. Commun.* **10**, 5119 (2019). URL http://www.nature.com/articles/s41467-019-12963-3.

[249] Niehues, I. *et al.* Strain Control of Exciton–Phonon Coupling in Atomically Thin Semiconductors. *Nano Lett.* **18**, 1751–1757 (2018). URL http://pubs.acs.org/doi/10.1021/acs.nanolett.7b04868.

[250] Zhao, W. *et al.* Origin of Indirect Optical Transitions in Few-Layer MoS_2 , WS_2 , and WSe_2. *Nano Lett.* **13**, 5627–5634 (2013). URL https://pubs.acs.org/doi/10.1021/nl403270k.

[251] Atatüre, M., Englund, D., Vamivakas, N., Lee, S.-Y. & Wrachtrup, J. Material platforms for spin-based photonic quantum technologies. *Nat. Rev. Mater.* **3**, 38–51 (2018). URL http://www.nature.com/articles/s41578-018-0008-9.

[252] Ye, Z. *et al.* Efficient generation of neutral and charged biexcitons in encapsulated WSe_2 monolayers. *Nat. Commun.* **9**, 3718 (2018). URL http://www.nature.com/articles/s41467-018-05917-8.

[253] Barjon, J. Luminescence Spectroscopy of Bound Excitons in Diamond. *Phys. status solidi* **214**, 1700402 (2017). URL http://doi.wiley.com/10.1002/pssa.201700402.

[254] Gammon, D., Snow, E. S., Shanabrook, B. V., Katzer, D. S. & Park, D. Fine Structure Splitting in the Optical Spectra of Single GaAs Quantum Dots. *Phys. Rev. Lett.* **76**, 3005–3008 (1996). URL http://link.aps.org/doi/10.1103/PhysRevLett.76.3005.

[255] Iff, O. *et al.* Strain-Tunable Single Photon Sources in WSe_2 Monolayers. *Nano Lett.* acs.nanolett.9b02221 (2019). URL http://pubs.acs.org/doi/10.1021/acs.nanolett.9b02221.

[256] Kim, H., Moon, J. S., Noh, G., Lee, J. & Kim, J.-H. Position and Frequency Control of Strain-Induced Quantum Emitters in WSe_2 Monolayers. *Nano Lett.* acs.nanolett.9b03421 (2019). URL http://pubs.acs.org/doi/10.1021/acs.nanolett.9b03421.

[257] Corfdir, P. *et al.* Low-temperature time-resolved cathodoluminescence study of exciton dynamics involving basal stacking faults in a-plane GaN. *Appl. Phys. Lett.* **94**, 201115 (2009). URL http://aip.scitation.org/doi/10.1063/1.3142396.

[258] Singh, R. & Bester, G. Lower Bound for the Excitonic Fine Structure Splitting in Self-Assembled Quantum Dots. *Phys. Rev. Lett.* **104**, 196803 (2010). URL https://link.aps.org/doi/10.1103/PhysRevLett.104.196803.

[259] Bryant, G. W. *et al.* Effect of Mechanical Strain on the Optical Properties of Quantum Dots: Controlling Exciton Shape, Orientation, and Phase with a Mechanical Strain. *Phys. Rev. Lett.* **105**, 067404 (2010). URL https://link.aps.org/doi/10.1103/PhysRevLett.105.067404.

[260] Staude, I., Pertsch, T. & Kivshar, Y. S. All-Dielectric Resonant Meta-Optics Lightens up. *ACS Photonics* **6**, 802–814 (2019). URL http://pubs.acs.org/doi/10.1021/acsphotonics.8b01326.

[261] Landau, L., Lifshitz, E., Kosevich, A. & Pitaevski, L. Course of Theoretical Physics: Volume 7, Theory of Elasticity (1975).

[262] Pearce, A. J., Mariani, E. & Burkard, G. Tight-binding approach to strain and curvature in monolayer transition-metal dichalcogenides. *Phys. Rev. B* **94**, 155416 (2016). URL https://link.aps.org/doi/10.1103/PhysRevB.94.155416.